Maximization of permanent trapping of CO_2 and co-contaminants in the highest-porosity formations of the Rock Springs Uplift (Southwest Wyoming): experimentation and multi-scale modeling

DOE award number: DE-FE0004832

Final Report

October 01, 2010 - March 31, 2014

Award recipient: University of Wyoming

Prepared by: Project Director Mohammad Piri
Department of Chemical and Petroleum Engineering
College of Engineering and Applied Science
University of Wyoming
Tel: 1-307-766-3954 (Office)
Fax: 1-307-766-6777
Email: mpiri@uwyo.edu

Submitted to: Project Manager William W. Aljoe
U.S. Department of Energy
National Energy Technology Laboratory
626 Cochrans Mill Road
PO Box 10940
Pittsburgh, PA 15236-0940

JUNE 30, 2014

DISCLAIMER

ABSTRACT

Under this project, a multidisciplinary team of researchers at the University of Wyoming combined state-of-the-art experimental studies, numerical pore- and reservoir-scale modeling, and high performance computing to investigate trapping mechanisms relevant to geologic storage of mixed $scCO_2$ in deep saline aquifers. The research included investigations in three fundamental areas: (i) the experimental determination of two-phase flow relative permeability functions, relative permeability hysteresis, and residual trapping under reservoir conditions for mixed $scCO_2$-brine systems; (ii) improved understanding of permanent trapping mechanisms; (iii) scientifically correct, fine grid numerical simulations of CO_2 storage in deep saline aquifers taking into account the underlying rock heterogeneity. The specific activities included: (1) Measurement of reservoir-conditions drainage and imbibition relative permeabilities, irreducible brine and residual mixed $scCO_2$ saturations, and relative permeability scanning curves (hysteresis) in rock samples from RSU; (2) Characterization of wettability through measurements of contact angles and interfacial tensions under reservoir conditions; (3) Development of physically-based dynamic core-scale pore network model; (4) Development of new, improved high-performance modules for the UW-team simulator to provide new capabilities to the existing model to include hysteresis in the relative permeability functions, geomechanical deformation and an equilibrium calculation (Both pore- and core-scale models were rigorously validated against well-characterized core-flooding experiments); and (5) An analysis of long term permanent trapping of mixed $scCO_2$ through high-resolution numerical experiments and analytical solutions. The analysis takes into account formation heterogeneity, capillary trapping, and relative permeability hysteresis.

TABLE OF CONTENTS

Executive Summary

This research project span over 42 months and included fourteen (14) faculty members, research associates, and graduate students. They focused their efforts on eight (8) project tasks each related to a different aspect of this research initiative.

The following items are among the main accomplishments of each of the technical tasks:

- Task 2: In this task scientists completed two extensive groups of reservoir-conditions flow experiments. In the first group, they considered $scCO_2$/brine and gCO_2/brine fluid systems. They studied relative permeabilities hysteresis (using steady-state technique), residual trapping, and trapped CO_2 dissolution for a wide range of flow scenarios. The experiments include full drainage and imbibition cycles in addition to several scanning cycles for the measurement of hysteresis effects and residual saturations of the non wetting (supercritical CO_2) phase. In the second group, they performed flow experiments with brine and $scCO_2$+SO_2. They carried out two sets of relative permeability experiments on Madison Limestone rock sample from RSU at about 2780 psi and 60°C. They investigated relative permeability hysteresis (using steady-state technique), residual trapping of $scCO_2$+SO_2, remaining brine saturation due to $scCO_2$+SO_2 injection, drainage and imbibition capillary pressures, and impact of dynamic effects on trapping.
- Task 3: Under this task the scientists built and integrated a state-of-the-art reservoir conditions interfacial tensions and contact angle measurement system. The apparatus is built out of Hastelloy (to handle corrosive fluids) and includes closed-loop equilibration system. It uses a highly-accurate heating system to heat the main IFT/CA cell with ±0. 1°C accuracy and is capable of handling captive bubble and sessile drop configurations. The group successfully validated the HPHT IFT/CA set-up and procedure with fluid/fluid/solid systems for which experimentally-measured values for IFT/CA were reported in the literature. The system was then used to study IFT and CA hysteresis for $scCO_2$/brine/quartz and $scCO_2$+SO_2/brine/quartz systems over wide ranges of temperature and pressure conditions.
- Task 4: In this task the researchers developed a truly unique dynamic pore-scale network model that can be used to perform direct pore-to-core up-scaling of displacement two-phase flow processes. In this model, pore-scale displacements are performed based on the combined magnitude of capillary, viscous, and gravitational pressure drops. Therefore, this dynamic model can be used to study two-phase flow over wide ranges of capillary and Bond numbers. Furthermore, wetting-phase corner flow is included in this model. The location of fluid/fluid interfaces in the corners (wetting layers) are determined and updated based on local capillary pressures. Another important feature of this model is the realistic boundary conditions used during simulations. In order to reproduce the same conditions as experiments and study steady-state two-phase flow processes, the wetting and non-wetting fluids are injected simultaneously at constant flow rates from the inlet of the medium. Constant pressure boundary condition is enforced at the outlet of the medium. The model is heavily parallelized and runs on large computer clusters. The model was extensively validated against experimental data generated at the University of Wyoming. The validated model was then used to study impact of low IFT, high flow rate, and high viscosity on trapping and relative permeabilities.
- Task 5: Under this task the scientists worked on two categories of items: 1) Relative permeability hysteresis and 2) Thermodynamic equilibrium. In the first category, they world on the mathematical analysis of the physically-based two-phase flow model with hysteresis. This model was built upon a set of experimentally-measured two-phase relative permeabilities (generated under to Task 2) for the brine/$scCO_2$ system. The resulting mathematical model comprises a system of two equations (one mass conservation equation for one of the phases and one equation for the dynamics of the

hysteresis parameter) and displays a rich (mathematical) structure: Its characteristicspeeds are both real (hyperbolicity) but not always distinct (nonstrict hyperbolicity), coinciding along a curve in state space. One of the characteristic fields is linearly degenerate with zero characteristic speed so that the waves associated to this field are stationary discontinuities. Theother characteristic field is nonlinear, but not genuinely nonlinear, so that the corresponding waves generically comprise wave groups involving both rarefaction and shock waves. Thus the analysis of this system falls outside the scope of the classical theory of hyperbolic systems of conservation laws. Their analysis, performed in terms of Riemann solutions, reveals that this systempossess sound mathematical properties as an evolutionary system: Riemann problems have unique solutions (within the class of discontinuities that satisfy an appropriate admissibility (entropy) criterion), which depend continuously on the Riemann data. They also exhaustively tested an explicitcentral-upwind finite difference scheme for the numerical simulation of this system, verifying its solutions against the (analytic) Riemann solutions. In all tests the scheme was able to compute the correct (admissible) solution with small numerical dissipation and no spurious oscillations. However, the occurrence of very fast propagating waves and the explicit nature of the numerical scheme dictate, in some cases, very restrictive time steps for stable computations. This suggests the investigation of implicit techniques for the time discretization, which we plan to perform in the next quarter. In the second category, the researchers developed PC-SAFT thermodynamic models for dissolution of $scCO_2$, $scCO_2$+SO_2, and NO_2 in brine and water over wide ranges of temperature and pressure conditions. The thermodynamic models were then used to develop flash codes for integration with compositional reservoir simulators developed under Tasks 6-8.

- Task 6**:** Researchers working in this task have developed the UW-team compositional simulator. At the beginning of this project we had a two-phase simulator for incompressible fluids. In order to handle supercritical CO_2 the UW-team simulator has been developed in several directions. New modules have been developed to solve a parabolic pressure equation (that arises in the modeling of compressible fluids), flash calculations, and hysteresis. The overall simulator can take advantage of state-of-the-art supercomputers, including CPU-GPU clusters. The new simulator has been applied to validate a standard compositional model for CO_2 injection in brine-saturated porous media. This was a non-trivial accomplishment because an uncertainty quantification method had to be designed to handle uncertainty in the absolute permeability of rock samples.
- Task 7**:** The group working in this task was concerned with the understanding of a coupled nonlinear model that describes the injection of CO_2 in deformable brine aquifers. We describe the development a mathematical model as well as the development of the UW-team simulator to include a high-performance, high resolution module for the solution of a comprehensive, 3D geomechanical subsystem coupled to multi-phase flow in highly heterogenous, deformable porous media. The implementation is based in an operator-splitting technique that allows us to use distinct and appropriate numerical methods and time-steps for subsystems describing distinct physical processes.
- Task 8**:** We have developed a flexible uncertainty quantification and reduction framework for field scale problems. The framework uses Bayesian statistics to combine information obtained from different sources (such as monitoring wells, huff-puff tests, etc) in determining permeability and porosity fields that are consistent with such measurements. We refer to the new procedure as the Multi-Physics Markov-Chain Monte Carlo Method. The procedure was tested for some simple fluid flow problems (using the simulator developed in Tasks 6 and 7) and has been applied to a test problem involving CO_2 injection in a saline aquifer.

Per-Task Report

Task 1: Project management and planning
PI: Dr. Mohammad Piri and Dr. Felipe Pereira

Key activities and accomplishments:

- Project Director, Dr. Piri, finalized Project Management Plan (Milestone 1) before the planned completion date of October 31, 2010.
- Professors Piri and Pereira organized and moderated the project kickoff meeting that included 14 people. All the task PIs, post-docs, and graduate students involved in the project attended the meeting.
- Professors Piri and Pereira prepared and submitted monthly progress reports as required by the DOE.
- Professors Piri and Pereira prepared and submitted thirteen quarterly progress reports as required by the DOE.
- Throughout project duration projects meetings were held every other week with PIs of all tasks where difficulties, progress, findings, and plans for the next steps were carefully discussed.
- Numerous meetings were held between Project Director, Dr. Piri, with Project Manager, Dr. Pereira, to discuss progress and our strategy to continue our active and dynamic support of research activities in various tasks.
- Professors Piri and Pereira organized and moderated four workshops at the Hilton Garden Inn (April 19-22/2011, September 27-29/2011, May 8-10/2012 and May 19-21/2014, Laramie, WY) on experimentation, modeling and numerical simulation of multiphase flows on topics directly related to the activities of this project. This was an opportunity that the PIs of this project had to discuss several issues related to the injection of CO_2 in saline aquifers.
- Professors Piri and Pereira held meetings with the Director of the Carbon Management Institute, Dr. Ronald C. Surdam, regarding the coordination of efforts between various CO_2 projects at UW.
- Within the period January 01/2012 – March 31/2012 Dr. Piri worked with CMI to coordinate acquisition of RSU rock samples for Task 2 and RSU reservoir brine composition report for task 2 and 3.
- Professors Piri and Pereira participated in the 10th Annual Conference on Carbon Capture & Sequestration, Pittsburgh, Pennsylvania, May 2-5 (2011). One of the research scientists involved in the project, Dr. Arunasalam Rahunanthan, also participated in this conference.
- Researchers of this project participated in the project Peer Review meeting of DOE's Carbon Storage program, October 22-26/2012, Pittsburgh, PA.
- Professors Piri and Pereira organized a meeting with our DOE project manager William Aljoe during his visit to the University of Wyoming in September 26, 2012. A tour of experimental facilities used in this project was carried out. Furthermore, a set of short seminars on progress made on each task was presented to Mr. Aljoe after the above-mentioned tours.
- Professor Piri made a required presentation at the *2013 Carbon Storage Review Meeting* that took place in Pittsburgh, August 20-22/2013.
- A *Final Project Briefing* was presented by Professors Piri and Pereira to Mr. William Aljoe in a WebEx meeting, April 22/2014.
- A no-cost extension of this project until March 31-2014 was requested by the PI and approved by the DOE.

Task 2: Measurement of mixed $scCO_2$/brine steady-state drainage and imbibition relative permeabilities in samples from the RSU at reservoir condition.

PI: Dr. Mohammad Piri

A) CO_2 /brine fluid system

1 Introduction

We present the results of an experimental study that, for the first time, carefully characterizes relative permeability hysteresis of $scCO_2$/brine fluid system in sandstone cores using steady-state method. We also use unsteady-state technique to investigate sensitivity of residual CO_2 trapping to variations in initial brine saturation at different flow conditions and fluid properties ($scCO_2$ and gCO_2). We study drainage and imbibition flow experiments in three different outcrop sandstone core samples using a reservoir-conditions core-flooding apparatus. All the experiments were performed through vertically-placed cores while a CT scanner is used to measure in-situ saturations.

2 Experiments

In this section, we present detailed information regarding the material and experimental conditions, setup, and procedure used in the first series of this task.

2.1 Rock samples, Fluids, and Experimental Conditions

The flow experiments included two categories of tests: A) series of unsteady-state CO_2 (drainage) and brine flooding (imbibition) tests in two different core samples, low permeability Berea and Nugget sandstone cores (Samples 1 & 2) and, B) series of steady-state drainage and imbibition experiments in a high permeability Berea sandstone core (Sample 3). As we will explain in more details later, the experiments in category A were designed and carried out to study capillary trapping of CO_2 while the flow tests in category B were mainly focused on characterization of relative permeability hysteresis. In both categories, the imbibition tests were followed by in-situ dissolution process to dissolve trapped CO_2 and re-establish S_w=1 state.

Table 1 lists dimensions and other petrophysical properties of the core samples. Nugget sandstone core was obtained from SW Wyoming, while the Berea cores were cut from two blocks obtained from a quarry in Ohio. Core samples were characterized using various techniques. Porosity was measured using both Boyle's law and x-ray imaging technique, generating similar values. Brine absolute permeability was also measured. Table 2 lists the number of experiments along with their conditions and procedures.

Table 1: Dimensions and petrophysical properties of the cores used in this study.

Sample	Diameter (cm)	Length (cm)	ϕ (X-ray) (%)	K_{abs} (Brine) (mD)	Pore Volume (cm^3)
01-Berea sandstone	3.81	15.0	20.08	50	34.34
02-Nugget sandstone	3.81	14.8	14.28	312	24.09
03-Berea sandstone	3.76	15.4	21.2	612	36.3

In category A of the flow tests, two groups of experiments were performed. In the first group, we used gCO_2 and brine with 10 wt% NaI, 5 wt% NaCl, and 0.5 wt% $CaCl_2$ composition. The experiments were carried out in Sample 1 at ambient temperature and 3.46 MPa back pressure. These conditions fall within the gaseous region of the pressure-temperature diagram of CO_2 [1]. In this group, we performed nine drainage and nine imbibition experiments. Each experiment was started with a brine saturated core (S_w=1). CO_2 was injected (drainage) to establish an initial brine saturation. Each drainage experiment was carried out with a pre-specified maximum CO_2 flow rate. We increased the flow rate gradually until the pre-specified maximum value was reached. The initial brine saturation was then measured repeatedly. The measurements were considered final when the difference between two consecutive saturation profiles and pressure drop data were less than 1%. We used a wide range of maximum flow rates, i.e., 0.125-120 cm^3/min, to create a broad range of initial brine saturations. All the flow rates used are listed in Table 3.

Table 2: Number of experiments along with the experimental conditions and procedures that have been performed on different rock samples.

Sample	Exp. numbers	Temp.(°C)/Press.(MPa)	Fluids	Experimental procedure
01-Berea sandstone	1-9	20.0/3.45	gCO_2/Brine	Unsteady-state
01-Berea sandstone	10-17	55.0/11.0	$scCO_2$/Brine	Unsteady-state
02-Nugget sandstone	18-23	55.0/11.0	$scCO_2$/Brine	Unsteady-state
03-Berea sandstone	24-31	55.0/11.0	$scCO_2$/Brine	Steady-state

Table 3: Maximum CO_2 flow rates used in unsteady-state drainage experiments (1-23). gCO_2 was used at 20°C temperature and 3.46 MPa pressure, while $scCO_2$ was at 55°C and 11 MPa. The NWP and WP stand for non-wetting and wetting phases, respectively.

Sample	NWP	WP	0.125 (cm^3/min)	0.25	0.5	1.0	2.5	5	10	15	20	30	60	100	120
Berea SS	$scCO_2$	Brine		•	•	•	•	•	•	•	•				
Berea SS	gCO_2	Brine	•	•	•		•		•			•	•	•	•
Nugget SS	$scCO_2$	Brine		•	•	•	•	•	•						

It is important to note that all the experiments presented in this paper were carried out in a closed-loop system. This means that the fluids were fully recirculated even at high flow rates, e.g., 120 cm^3/min. Full recirculation allowed us to achieve and maintain equilibrium between the aqueous and CO_2-rich phases at the pressure and temperature of the experiments and hence minimize mass transfer between them in the cores. We performed this procedure with minimum variations in the pressure of different parts of the experimental apparatus, e.g., core back pressure, core upstream pressure, and separator pressure. This is particularly important as large variations in pressure can impact miscibility of fluids in each other as well as displacements in the core samples. The details of this system and its operation principles are explained in section 2.2.

After establishing an initial brine saturation at the end of each drainage experiment, brine was injected into the core to displace and trap CO_2 (imbibition). The maximum brine flow rate in all the imbibition experiments in category A was 0.375 cm^3/min. The brine flow rate was first increased to 0.1 cm^3/min

and then gradually to a maximum of 0.375 in 0.025 cm^3/min increments. It is critical to increase the flow rate gradually as sudden increase could lead to dynamic effects and hence affect the trapping results. Our purpose in this category was to study trapping of CO_2 under capillary dominated conditions. When changes in brine flow rate did not reduce CO_2 saturation and the variations in the pressure drop across the core were less than 1% the experiment was considered complete.

In order to perform a new set of drainage and imbibition flow experiments, an in-situ re-saturation technique was used to re-establish S_w=1. This allowed us to avoid disassembling and re-assembling of the core holder and the fluid lines. During this step, brine was injected at relatively high flow rates, e.g., 0.4-14 cm^3/min, to dissolve the trapped CO_2. As we will explain in section 3.1.3, equilibrated brine always has *very small* capacity left for dissolution of more CO_2 due to minute deviations from equilibrium. This is regardless of the technique used to equilibrate the fluids. We took advantage of this in order to re-saturate the core with brine by dissolving the trapped CO_2. And since brine is very close to equilibrium state, the dissolution of trapped CO_2 was an extremely slow process. The re-saturation step took up to 72 hrs depending on brine flow rate and CO_2 density. One should note that dissolution is a very slow process not only because brine is almost fully saturated with CO_2 but also due to the fact that a unit volume brine that enters the core will initially dissolve a very small amount of CO_2 at the inlet of the core and become fully saturated preventing it from dissolving any more CO_2 during the rest of its residence time in the core. We will explain this further later in section 3.1.3. After full re-saturation of the core is confirmed by a complete scan, a new drainage experiment with a new maximum CO_2 flow rate was initiated.

In the second group of category A, we used higher pressure and temperature conditions, i.e., 55°C and 11 MPa back pressure, leading to a supercritical state for CO_2, and carried out the experiments in two samples, Berea and Nugget cores (Samples 1 & 2). Similar to the first group of the experiments, we performed drainage experiments followed by brine floods. Due to higher viscosity and density of $scCO_2$ compared to those of gCO_2, see Table 4, the maximum $scCO_2$ flow rate used during the drainage experiments was 20 cm^3/min. A total of eight and six drainage and imbibition experiment sets were performed in Berea and Nugget cores, respectively, see Table 3 for flow rates. We were able to establish initial brine saturations comparable to those in the first group of experiments with gCO_2.

Table 4: Properties of fluids used in this study [1-4].

Fluid	Pressure MPa	Temperature (°C)	Viscosity (cP)	Density (gr/cm^3)	CO_2/Brine IFT (mN/m)
Supercritical CO_2	11.0	55	0.044	0.393	38.15
Gaseous CO_2	3.46	20	0.016	0.081	51.24
Brine	3.46	20	1.57	1.125	—
Brine	11.0	55	0.91	1.126	—

In the steady-state category of the tests (category B), seven different cycles of drainage and imbibition flow experiments were performed to obtain steady-state relative permeability scanning curves. Various cycles were performed using monotonically increasing and decreasing fractional flows. The range of flow rates used in this approach are listed in Table 5. They included three full cycles, two half cycles, and one quarter, one-eighth, and one-sixteenth cycles. The initial condition was the same for all these experiments (i.e., S_w=1), while the $scCO_2$ saturation reached during drainage, and consequently the initial brine saturation at which the subsequent brine injection was started, was different from one cycle

to another. For instance, for full cycle tests, at the end of drainage the $scCO_2$ saturation was at its highest value, i.e., 0.475, leading to an initial brine saturation of 0.525 for imbibition step of this cycle. Whereas for half cycle tests, these were 0.32 and 0.68, respectively.

All the experiments reported in this study were performed under capillary dominated displacement regime with $N_c \leq 10^{-5}$, where N_c is the capillary number and is given by:

$$N_c = \frac{\mu_w \times u_w}{\phi \times \sigma_{gw}} \qquad (1)$$

where μ_w, u_w, ϕ, and σ_{gw} are, for imbibition tests, brine viscosity, brine velocity, porosity, and interfacial tension between CO_2 and brine, respectively. Table 6 lists the typical values of capillary number for both Berea and Nugget cores (Samples 1, 2, and 3) during unsteady- and steady-state imbibition experiments.

Table 5: Brine and $scCO_2$ flow rates (cm^3/min) and fractional flows used during steady-state experiments (24-31).

Item	Drainage	Imbibition
$scCO_2$ flow rates	0-5.0	0-5.0
Brine flow rates	0-0.45	0-0.2
Fractional flows	0.18-1.0	1.0-0.33

Table 6: Capillary numbers of imbibition flow experiments.

Sample	NWP	WP	max N_{Ca}
01-Berea sandstone	$scCO_2$	Brine	1.037×10^{-5}
01-Berea sandstone	gCO_2	Brine	1.34×10^{-5}
02-Nugget sandstone	$scCO_2$	Brine	1.468×10^{-5}
03-Berea sandstone	$scCO_2$	Brine	2.5×10^{-6}

2.2 Experimental Setup and Procedure

The experimental setup used in this work is a reservoir-conditions multiphase core-flooding systems that includes a nine-cylinder Quizix pumping system (5000 and 6000 series), two compensation accumulators, an acoustic three-phase separator, air-operated valves, differential pressure transducers, a Hassler type core holder, and three mechanical convection ovens, see Figure 1 for a schematic flow diagram [5]. All the wetted parts of the apparatus are made of Hastelloy and other corrosion resistant materials. The experimental setup is a closed-loop system that allows fluids to be co-injected into the core at elevated temperatures and pressures.

We used dual-cylinder 5000 and 6000 Quizix pumps for injection of brine and CO_2, respectively. Each cylinder of the brine pump has 9.3 cm^3 volume, while that is 275 cm^3 in the CO_2 pump. Maximum possible flow rates for these pumps were 15 and 200 cm^3/min, respectively. In order to maintain back

pressure, we use a dual-cylinder 6000 Quizix pump instead of a common dome-loaded back pressure regulator. This allowed us to maintain a fixed back pressure, even at very high flow rates, leading to a stable equilibrium between the phases (i.e., amounts of CO_2 dissolution in brine and water evaporation to CO_2) as we will explain later [5]. All these six cylinders were located inside a large mechanical convection oven from which fluids were sent to, and received from, the core holder.

The effluent of the core was sent to a large 3,500 cm^3 acoustic three-phase separator, located in another oven, close to the back pressure regulation pump. The separator is made of Hastelloy and the level of fluids in it are monitored carefully. As we mentioned earlier, the apparatus is closed-loop system and we performed full-recirculation experiments. Therefore, the pumps that injected fluids to the core, retracted fluids from the separator. And hence it was critical to monitor fluid levels in the separator to avoid retraction of wrong fluids to the injection pumps particularly at high flow rates. The pressure of the separator is controlled by a compensation module that in turn includes a dual-cylinder 6000 Quizix pump and two 2,000 cm^3 compensation accumulators. This pump was also heated using heating tapes and carefully insulated using efficient insulation material. The accumulators were placed in a third mechanical oven. We installed special ultra high molecular weight seals in Quizix cylinders to prevent any leakage when working with $scCO_2$.

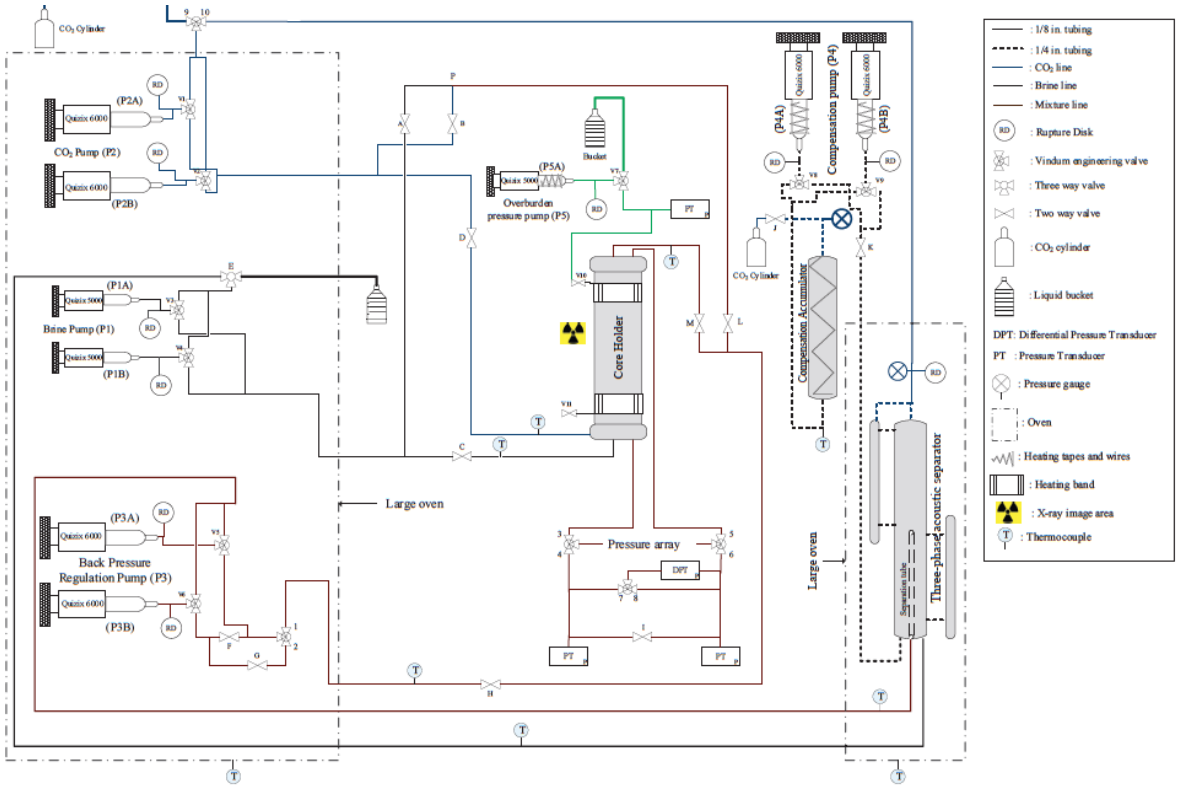

Figure 1: Schematic flow diagram of the experimental setup used in this work. The apparatus includes a medical CT scanner and a Vertical Positioning System, nine Quizix Hastelloy cylinders, a Hastelloy three-phase acoustic separator, an Aluminium Hassler core-holder, differential and gauge pressure transducers, a compensation accumulator, and several temperature measurement devices [5]

The overburden pressure was maintained using a single cylinder 5000 Quizix pump. This allows automatic adjustment of the overburden pressure with variations in the pore pressure. This is critical in experiments with rock samples that show significant sensitivity to overburden pressure such as tight gas sandstones. The overburden pressure for Berea samples 1 and 3 and Nugget were kept at 13.45, 13.1, and 13.65 MPa, respectively. This was 5.5 MPa for experiments with $gcCO_2$.

The setup also includes a medical CT scanner tuned for petrophysical applications. The scanner is rotated to the horizontal orientation allowing us to perform the experiments through vertically-placed rock samples. A vertical positioning system (VPS) was used to move the core holder vertically from bottom into the gantry. During an experiment with a core sample, the VPS was synchronized with the horizontal table of the scanner.

Next we explain the details of the experimental procedure used to perform the flow experiments in the above-mentioned categories of the tests.

For each set of unsteady-state experiments (category A), a core was placed in a Hassler type core holder with a sleeve. The core and also sleeve were wrapped with several layers of Aluminium foil and Teflon tape to prevent CO_2 penetration through the sleeve and ultimately into the overburden fluid. The core holder was then wrapped with highly efficient insulation material and located on the VPS system and moved into the CT scanner's gantry. The core holder assembly was then flushed with gCO_2 from a pressurized bottle and then vacuumed for several hours. At this stage, the entire core was scanned with 1 , 2, and 4 mm slice thicknesses generating about 140-150, 70-77, and 35-37 slices, respectively.

The core-flooding apparatus was first saturated with brine and CO_2. The system was then pressurized (with additional CO_2) and heated to 11 MPa and 55°C. A total approximate amount of 1,500 cm^3 of brine was introduced into the separator and 2,000 cm^3 into the compensation accumulators. The remaining volumes of these vessels were occupied by $scCO_2$. At this point, brine pump (P1A and P1B) and CO_2 pump (P2A and P2B) were used to retract brine and CO_2, respectively, from the separator and inject into junction P, see Figure 1, with valves D and C closed. This allowed brine and CO_2 to mix at the junction and flow *together*, by-passing the core holder, toward the back pressure pump (P3A and P3B). Brine and CO_2 pumps were operated under paired constant flow rate mode allowing them to create continuous flow of these fluids. The fluids by-passing the core holder were received by the back pressure pump under paired constant pressure receive mode. The pressure at which the pump was set to receive the fluids was 11 MPa for experiments with $scCO_2$. This allowed us to have a high quality back pressure regulation at the outlet of the core leading to very stable pressures and hence better equilibrium maintenance. Figure 2 demonstrates the stability of the back pressure during unsteady-state experiments in Berea and Nugget cores (Samples 1 and 2). During the steady-state experiments, we experienced similar stability for back pressure. Back pressure pump injected its contents into the bottom of the separator whose pressure was also accurately regulated using a sophisticated pressure regulation system (see Figure 1). The large volume of the separator (3,500 cm^3) also helped prevent drastic fluctuations in its pressure during this process. The CO_2 in the mixture received by the separator was distributed into the brine in the vessel through a distribution cap with numerous small holes generating small CO_2 bubbles for more effective mass transfer between the phases.

The above-mentioned full recirculation of the fluids was continued (bypassing the core) for up to 72 hours under the pressure and temperature of the experiment. This technique was used to achieve equilibrium between the phases before the core flood was started. The fluids were in continuous

contact (while flowing) in the separator, accumulator, flow lines, and back pressure pump during this process. During the steady-state tests, we added a 6000 dual cylinder Quizix pump to continuously retract brine from the bottom of the separator and inject it to the top of the separator through a multi-hole injection tube mounted inside the separator. This was done in addition to CO_2 bubbled into the brine at the bottom of the separator.

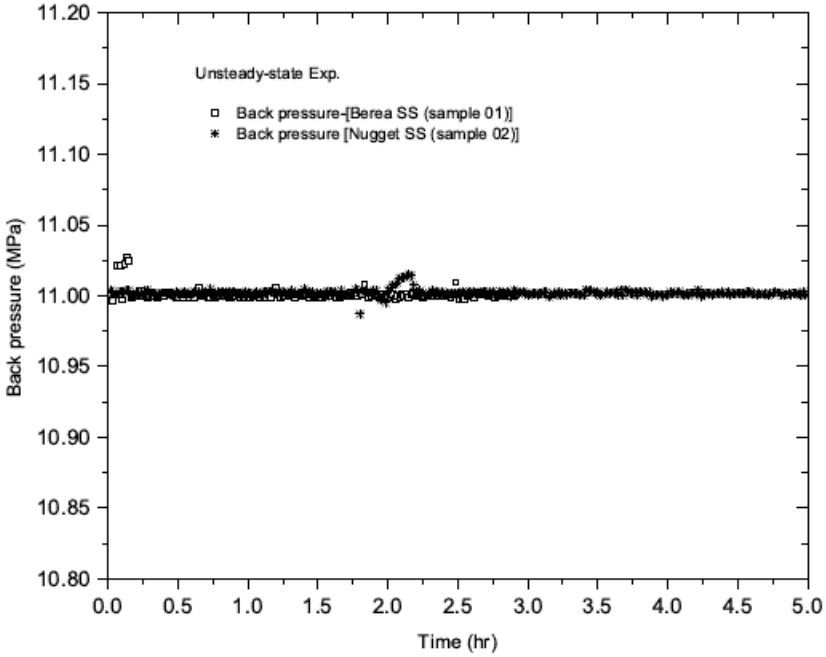

Figure 2: Variations of back pressure of Berea (Sample 1) and Nugget (Sample 2) sandstone cores during unsteady-state experiments with scCO2 and brine.

At this point, the core was saturated with $scCO_2$. The core-holder was heated at its two ends using two highly efficient heat bands and manual controllers. For the steady-state experiments, they were replaced by a thin heating foil, wrapped around the core holder. The level of heat was adjusted to obtain the desired temperature at the outlet of the core. The fluid temperature at the inlet was also monitored and controlled using heating tapes utilized on all the tubings outside the ovens. Temperature was monitored in other locations of the systems as well, e.g., inside the separator, inside both ovens, and inside the large compensation accumulator. Flow of $scCO_2$ through the core was continued for a few hours before it was scanned to acquire CO_2-saturated reference image of the core. During this period, CO_2 leaving the core, similar to what we explained earlier, was received by the back pressure pump and injected into the bottom of the separator from which CO_2 was again retracted by P2.

After acquisition of CO_2-saturated image of the core, brine was injected into the core using P1, which again retracted it from the separator, to establish S_w=1 state. This step took a very long time (e.g., 80 hrs) as brine was almost fully saturated. The effluent CO_2 and brine were received by the back pressure pump at the set pressure and injected into the separator. Then the entire core was scanned to obtain a brine-saturated image of the sample. The flow of brine was continued for additional 24 hrs and the core was scanned repeatedly. The brine-saturated image was called final when we did not have "free" CO_2 in the core. At this point, the core was ready for the first drainage (CO_2 injection) experiment.

For unsteady-state experiments (category A), CO_2 was injected into the brine saturated core (drainage). The flow rate was gradually increased to reach the maximum and maintained at that point until the variations in pressure drop and saturation distribution along the length of the core were less than 1%. The brine saturation at that point was reported as initial brine saturation for the maximum CO_2 flow rate used. The core at the end of drainage was then subjected to brine injection (imbibition). The maximum brine flow rate for all imbibition experiments in this category was 0.375 cm^3/min. The flow rate was increased gradually to reach this maximum and kept under this condition until all the CO_2 was either displaced or trapped. Slight increase in flow rate did not lead to further reduction in CO_2 saturation. The core was then scanned to report residual CO_2 saturation. As it was discussed earlier, the sample at this point was resaturated with brine with extensive (e.g., ~200 pore volumes) injection of brine at high flow rates (e.g., 12 cm^3/min) to reach S_w=1. This process took up to 72 hrs, which was then followed by a new set of drainage and imbibition experiments.

In order to prepare the core for the steady-state flow tests (category B), we followed a slightly different procedure. After establishing a brine-saturated core, the $scCO_2$ and brine were co-injected with monotonically increasing Q_{CO2}/Q_b ratio to perform a drainage test. This was done by increasing the $scCO_2$ flow rate or decreasing the brine flow rate carefully maintaining capillary dominated ($N_c \leq 10^{-5}$) displacement regime. This threshold is where the trapping results start to be significantly affected by N_c [6]. Capillary number here was calculated using measured pressure drop from the previous step:

$$N_c = \frac{k_{rw} * K_{abs} * \Delta P}{\phi * \sigma_{gw} * L} \qquad (2)$$

where k_{rw}, K_{abs}, ϕ, σ_{gw}, and L are relative permeability, absolute permeability, porosity, interfacial tension between CO_2 and brine, and length of the core sample, respectively. The range of flow rates used in this procedure are listed in Table 5. During this process, for each value of fractional flow we recorded pressure drop and in-situ saturations after reaching steady-state. These were then used to calculate relative permeability curves.

After completing the drainage process and determining the initial brine saturation, we reversed the process to perform an imbibition experiment. The procedure was similar to drainage with this difference that the flow rate ratio was monotonically decreased. This step allowed us to determine S_{CO2r} as well as the respective relative permeabilities. In order to perform the next set of experiments, core was re-saturated through dissolution of the trapped CO_2.

2.3 Porosity and In-situ Saturation Measurements

The scanner provided 250 μm resolutions per slice and a minimum slice thickness of 1 mm. Porosity was calculated from

$$\phi = (CT^*_{wc} - CT^*_{gc})/(CT_w - CT_g) \qquad (3)$$

where *w* and *g* represent brine and CO_2, CT^*_{wc} and CT^*_{gc} are CT numbers of the core fully saturated with brine at 3.46 MPa and with CO_2 at 0.14 MPa, respectively, and at ambient temperature. We assume that the impact of pressure on CT_{wc} is negligible. CT_w and CT_g are generated by scanning the core holder

without the core while it is filled with brine and CO_2, respectively. Figure 3 shows the porosity distribution along the core for Berea and Nugget sandstone cores (Samples 1, 2, and 3). The blank spaces between the points of Sample 3 are related to the pressure taps along the core holder, which made the scans at those locations unusable.

To calculate two in-situ fluid phase saturations, the core was scanned at one energy level (130 kV, 100 mA) during the experiment and also when it was fully saturated with each of the fluids to obtain the reference scans. The saturations were determined by using the following equations:

$$S_w = (CT_c - CT_{gc})/(CT_{wc} - CT_{gc}) \quad (4)$$

$$S_g = 1 - S_w \quad (5)$$

where CT_c is the CT number of the core containing two phases during the experiment. CT_{wc} and CT_{gc} are the CT numbers of the core fully saturated with brine and $scCO_2$ at temperature and pressure of the experiment, respectively.

In order to obtain CT_{wc} and CT_{gc}, core samples were first flushed with dry CO_2 and then vacuumed to remove air. While the entire apparatus was being heated and pressurized to maintain the required pressure and temperature, CO_2 and brine were being recirculated for several days bypassing the core to reach equilibrium. At this point, the $scCO_2$ saturated with water vapor was injected into the core at experimental conditions to create fully $scCO_2$-saturated core. $scCO_2$ was re-circulated through the core for one day during which several scans of the core was obtained. When the difference between two consecutive scans was negligible the scan was reported as CT_{gc}. This was followed by injection of $scCO_2$-saturated brine to create fully brine-saturated core, which was then scanned to find CT_{wc}. As we mentioned earlier, this step took about 3.5 days as brine was almost fully saturated with $scCO_2$.

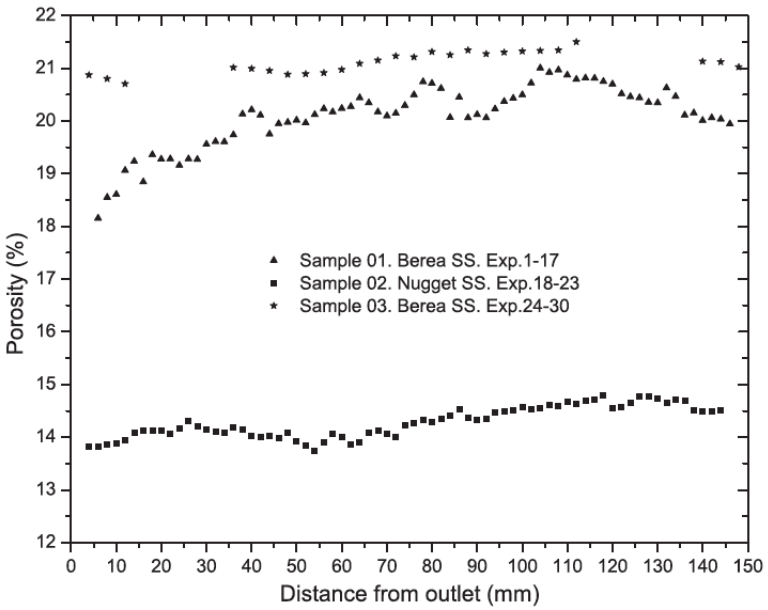

Figure 3: Porosity distribution along the length of the Berea (Samples 1 and 3) and Nugget (sample 2) sandstone cores used in this work.

3 Results

In this section we present results of the two categories of flow experiments mentioned earlier, i.e., A) Unsteady-state, and B) Steady-state tests. Table 2 lists the number of experiments that were performed along with their corresponding experimental conditions.

3.1 Unsteady-state Experiments

In this set of experiments we present results for several flow cycles with each involving three processes: 1) injection of CO_2 to establish S_{wi}, 2) injection of chase brine to reach S_{CO2r}, and 3) dissolution of residual CO_2 to re-establish S_w=1 state. We first discuss the injection of CO_2 into brine-saturated core (drainage). This is then followed by discussions on the injection of chase brine into a core at initial brine saturation (imbibition) and in-situ dissolution of trapped CO_2. The latter is used to re-establish brine-saturated state in the core before a new cycle is started. All the saturation results presented in this category are, unless stated otherwise, averaged over 70% central part of the core samples.

3.1.1 Injection of CO_2

Figure 4 depicts variations of maximum CO_2 saturation reached during CO_2 primary drainage versus maximum Darcy velocity used for experiments with supercritical and gaseous CO_2 in the Berea (Sample 1) and Nugget (Sample 2) sandstone cores. Each data point represent an independent experiment and shows the values reached at steady-state at a given maximum CO_2 flow rate (see Table 3). Maximum $scCO_2$ saturation increases sharply in lower flow rates and then gradually stabilizes at higher flow rates. This is expected as it becomes more difficult to displace brine from smaller pores and crevices as brine saturation decreases. But the wide range of maximum $scCO_2$ flow rates allowed us to create a relatively wide range of initial brine saturations (S_{wi}) for the subsequent chase brine injection (imbibition) experiments. Initial brine saturation ranged between 0.68 and 0.40 for flow rates between 0.25 and 20 cm^3/min under supercritical conditions.

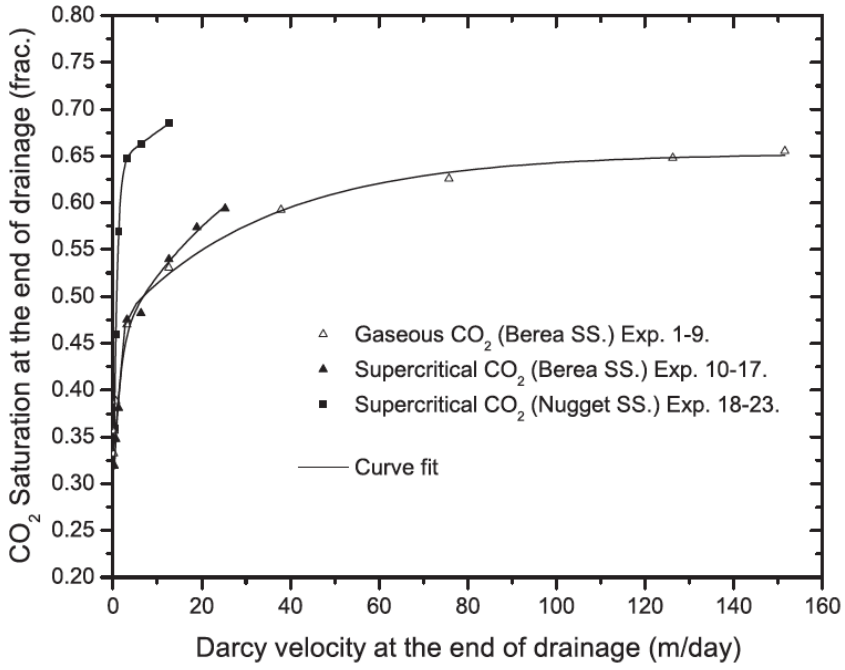

Figure 4: Variation of CO2 saturation with maximum Darcy velocity reached at the end of drainage in Berea (Sample 1) and Nugget sandstone (Sample 2) cores.

To obtain a similar range of initial brine saturations with gCO_2, we performed gCO_2 injection experiments with flow rates as high as 120 cm^3/min, which were much higher than those in $scCO_2$ experiments (see Table 3). This is mainly because gCO_2 is about four times less viscous than $scCO_2$ (see Table 4) and therefore less effective in displacing brine at a given flow rate. Initial brine saturations ranged between 0.67 and 0.35 for flow rates between 0.125 and 120 cm^3/min (see Figure 4). We performed experiments with gCO_2 to allow us to study the possible effects of wetting on trapping of CO_2 as we will discuss in the next section. As we mentioned earlier, all the experiments (regardless of flow rate) were performed under full-recirculation conditions and with equilibrated fluids.

As it is shown in Figure 4, for a given flow rate, displacement of brine in Nugget sandstone (Sample 2) led to lower initial brine saturation than in Berea core (Sample 1). Further analysis of the results shown in Figure 4 with the associated pressure drop data (not included here), suggests that pores in the Nugget core are larger with lower drainage threshold capillary pressure and therefore they are invaded by $scCO_2$ more easily. We were able to obtain an average of 68 % $scCO_2$ saturation at 10 cm^3/min $scCO_2$ flow rate in Nugget versus about 54 % in Berea core with the same flow rate.

Figures 5 and 6 include CT slices that show the variation of in-situ $scCO_2$ saturation in different locations along the length of Berea and Nugget sandstone cores, respectively. $scCO_2$ and brine are distributed more evenly in Berea than in Nugget as the former is more homogenous.

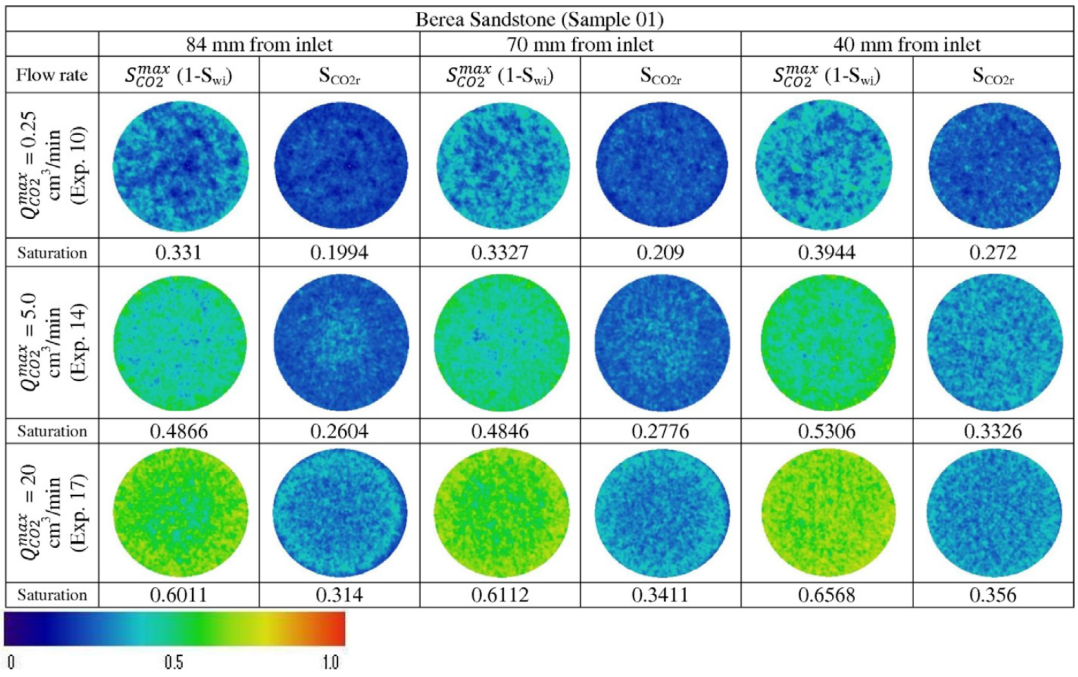

Figure 5: scCO2 saturation in Berea sandstone core (Sample 1) at different locations from inlet. The values are reported at the end of drainage and imbibition for three different experiments.

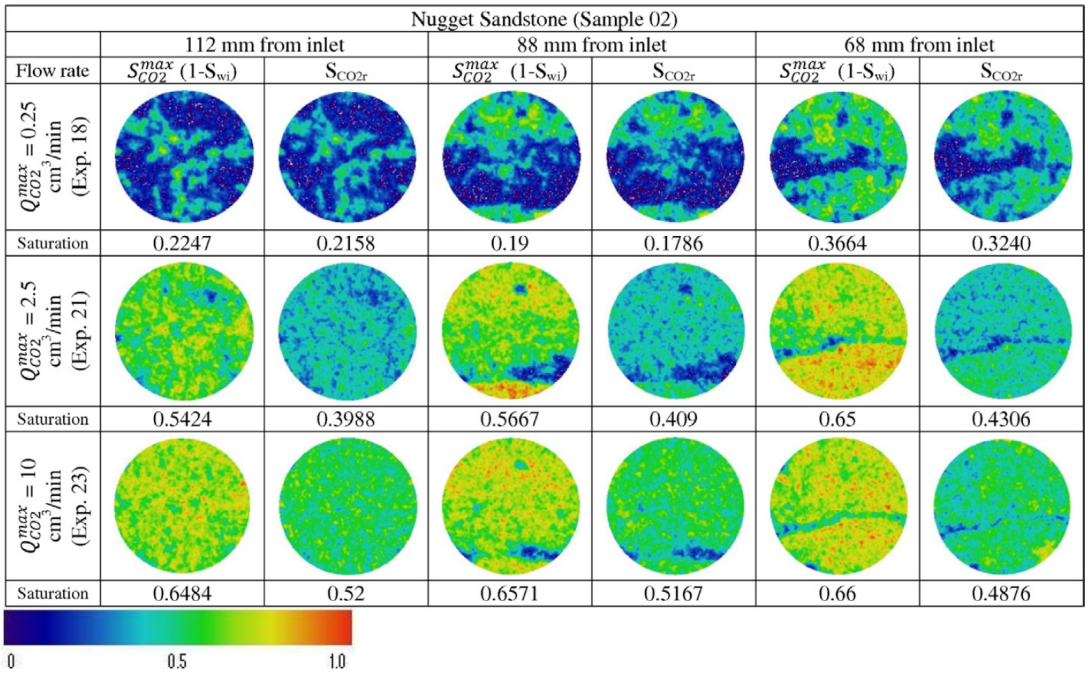

Figure 6: scCO2 saturation in Nugget sandstone core (Sample 2) at different locations from inlet.The values are reported at the end of drainage and imbibition for three different experiments.

3.1.2 Injection of Chase Brine

After reaching the steady-state at the end of each CO_2 injection experiment, chase brine was injected at about 0.1 cm^3/min and gradually increased to 0.375 cm^3/min. The brine was saturated with CO_2 under the conditions of the experiments before injection. The injection was continued until residual CO_2 saturation was reached. At this point, slight changes in flow rate did not alter the saturation. Multiple scans of the core during this process allowed us to determine this point. We then recorded the in-situ saturation and pressure drop across the core. This process was carried out after every CO_2 injection experiment discussed in the previous section creating a wide range of residual CO_2 saturations.
Figures 7 and 8 show the variation of slice-averaged trapped CO_2 saturation with S_{CO2}^{max} under supercritical and gaseous conditions in Berea core (Sample 1) and under supercritical condition in Nugget (Sample 2), respectively.

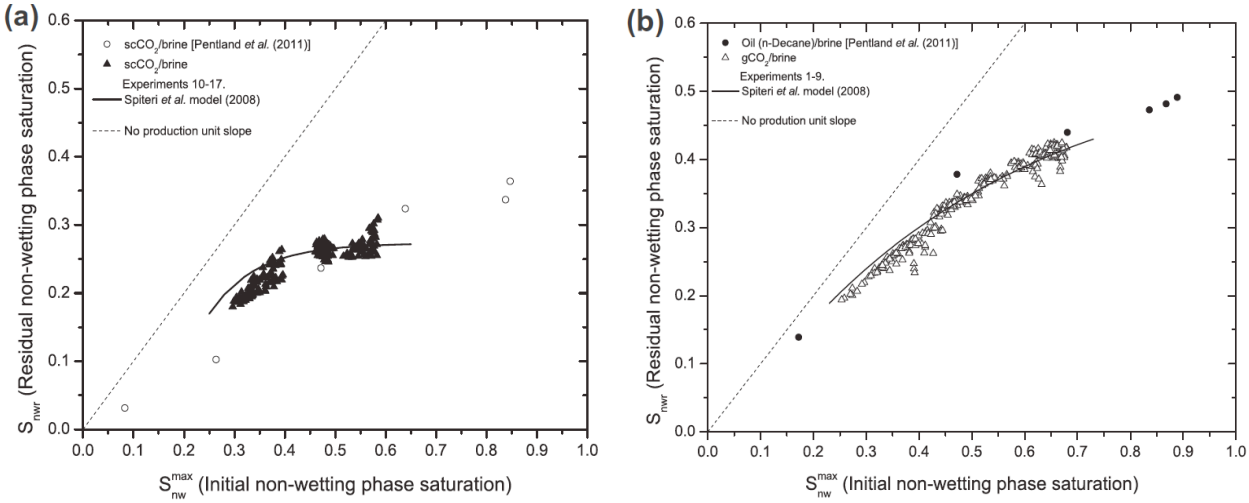

Figure 7: Variation of slice-averaged residual trapped CO2 saturation with CO2 saturation at the end of drainage for Berea sandstone core (Sample 1) under (a) supercritical and (b) gaseous conditions.

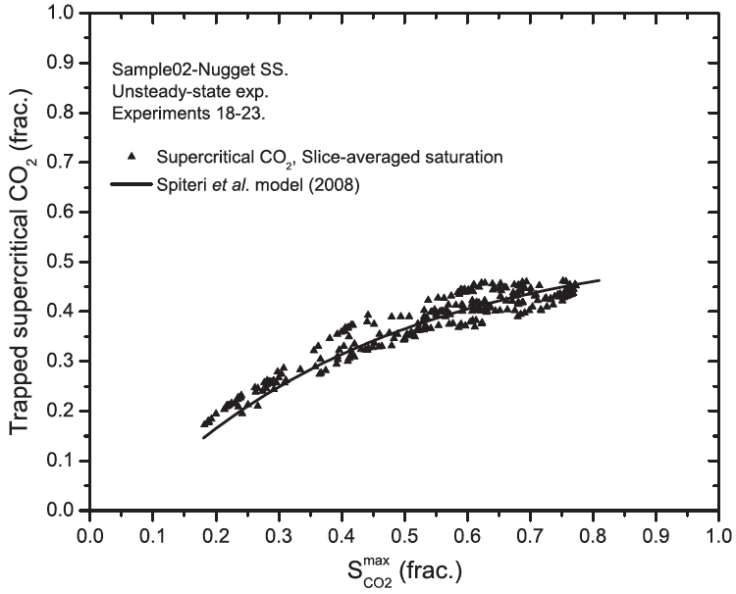

Figure 8: Variation of slice-averaged residual trapped scCO2 saturation with scCO2 saturation at the end

of drainage for Nugget sandstone core (Sample 2).
It is clear that for a given initial CO_2 saturation, trapped gCO_2 saturation is greater than $scCO_2$ saturation in Sample 1. We think this might have been caused by brine being less wetting in the presence of $scCO_2$ than in the presence of gCO_2 in the Berea sample. Recent measurements by Saraji *et al.* [7] of advancing CO_2/brine contact angles on quartz surfaces under gaseous and supercritical conditions supports this explanation. On a given surface, advancing gCO_2/brine contact angle was lower than that for $scCO_2$/brine fluid system. Furthermore, the residual $scCO_2$ saturation in Nugget is higher than those in Berea for a given initial brine saturation. This may have been caused by a number of possible factors such as different levels of connectivity and tortuosity that can strongly affect residual CO_2 saturation. These data indicate that residual $scCO_2$ saturations varies between 20 % and 32 % in Berea and 28 to 46 % in Nugget. In Figures 7 and 8, the experimental results are compared with those given by an empirical correlation for trapping developed by Spiteri *et al.* [8]. The correlation provides a relationship between trapped non-wetting phase saturation, S_{nwr}, at the end of imbibition and initial wetting phase saturation, S_{wi}, at the end of drainage. The agreement between the model and our experimental data is satisfactory. The parameters that were used with the Spiteri *et al.* model are listed in Table 7. In Figure 7 our $scCO_2$/brine and gCO_2/brine results in Berea sandstone core are compared with the results of Pentland *et al.* [9] for (a) $scCO_2$/brine and (b) oil (n-Decane)/brine experiments in Berea sandstone core. The agreements in both groups are encouraging. One should note that these two groups of experiments have been carried out independently using different techniques, therefore the agreements are significant.

Table 7: Parameters used with Spiteri *et al.* [8] empirical correlation.

Sample	Fluid system	max S_{CO2r}	α	β
01-Berea	$scCO_2$/Brine	0.2772	1	0.94
01-Berea	gCO_2/Brine	0.40526	0.95	0.5
02-Nugget	$scCO_2$/Brine	0.48216	1	0.54
03-Berea	$scCO_2$/Brine	0.34	1	0.6

The resulted presented in Figures 7 and 8 can be used to calculate the trapping efficiency - the ratio of trapped CO_2 saturation at the end of imbibition to the CO_2 saturation at the end of drainage (S_{CO2r}/S_{CO2}^{max}) - for Berea and Nugget sandstone cores under supercritical conditions. The trapping efficiency varies between 50 to 60 % for Berea and 65 to 78 % for Nugget. These are significant fractions of the CO_2 that were initially placed in the cores. Note that as S_{wi} increases trapping efficiency increases. This might be due to more efficient pore-level trapping mechanisms when there are more brine-filled elements present, i.e., at higher initial brine saturations. In other words, presence of more brine-filled elements translates to a greater number of main terminal menisci [10], which are the invading menisci at the pore-throat junctions separating brine and CO_2. And when imbibition is started, brine is able to initiate more brine-to-CO_2 piston-like and pore-body filling displacements across the medium rapidly trapping CO_2. At lower initial brine saturations, fewer brine filled-elements are present and therefore the process *initially* relies more on snap-off displacements until more brine-filled elements are formed [11].

At the end of imbibition, the pore space is filled with CO_2 and brine. Therefore the amount of CO_2 that is stored in the core permanently is the summation of trapped and dissolved CO_2. Table 8 lists the amount of CO_2 that can dissolve in brine under the experimental conditions in this study. Figures 9(a) and (b) present the mass of CO_2 stored in Berea and Nugget sandstone cores. They include both trapped and

dissolved CO_2 for both total and 1 cm^3 of the pore volume of the cores. The amount of trapped and dissolved $scCO_2$ in Nugget is greater than Berea for a given S_{CO2}^{max}. The results for Berea sandstone show that greater quantities of CO_2 can be stored when CO_2 is in supercritical condition and this is expected as the $scCO_2$ is about five times denser than gCO_2 (see Table 4) under the experimental conditions used in this work.

Table 8: Solubility of CO_2 under different conditions in 1.86 m brine used in this study [12].

Unit	Gaseous CO_2	Supercritical CO_2
kg CO_2 /kg brine	0.02665	0.03366

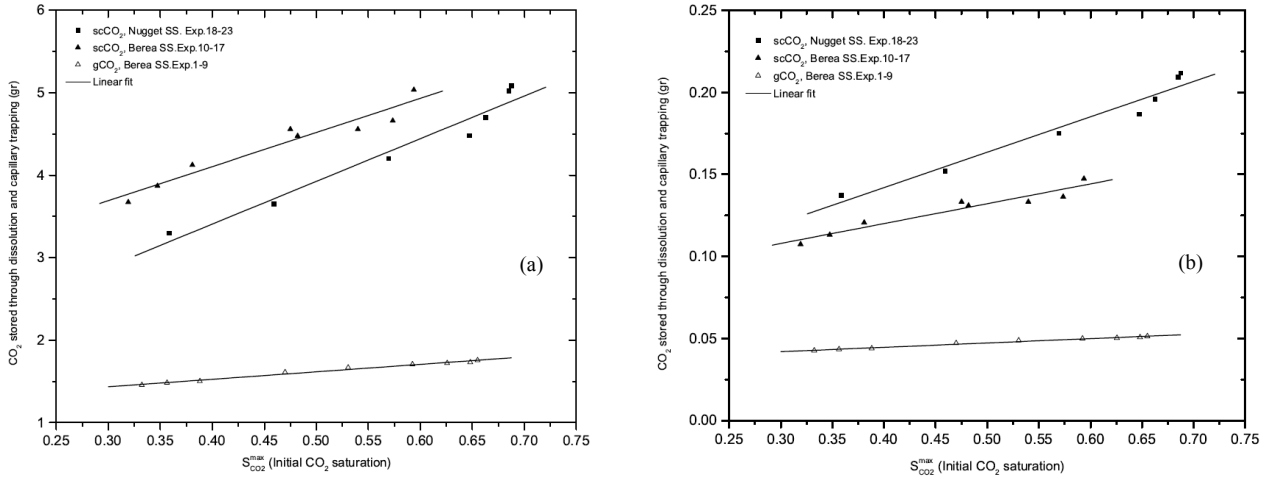

Figure 9: The amount of CO2 stored through capillary trapping and dissolution in Berea and Nugget SS cores (samples 1 and 2) in (a) 1 pore volume, and (b) 1 cm3 of pore volume.

3.1.3 Dissolution of Trapped CO_2

At the end of each imbibition, the trapped CO_2 was dissolved in brine to re-establish S_w=1 state before starting a new drainage/imbibition cycle. In other words, we injected brine into the core with residual $scCO_2$ until all the $scCO_2$ was dissolved. This was a lengthy process; it took up to 72 hrs using different brine flow rates. In most cases we had to inject more than 180 pore volumes of brine to completely dissolve the trapped CO_2.

For each of the samples, we selected one of the dissolution steps for additional investigations. In-situ brine and CO_2 saturations and pressure drop data were frequently recorded until the core was fully saturated with brine. Figures 10 illustrates the relative permeability of brine during dissolution of trapped $scCO_2$. At the beginning of this process, trapped $scCO_2$ creates significant blockage for the flow of brine leading to small brine relative permeability. With injection of brine, trapped clusters of $scCO_2$ start shrinking gradually. This reduces the blockage and improves the flow of brine, which manifests itself in lower brine pressure drop and higher brine relative permeability. Figure 11 shows two-dimensional visualizations of $scCO_2$ saturation distribution along the length of the (a) Berea and (b) Nugget cores during the dissolution process. It shows that, for instance, in Berea core, after injection of about 184 pore volumes of brine, we could re-establish S_w =1 and prepare the core for the next cycle of experiments.

It is important to mention that we carefully monitored variation of $scCO_2$ saturation along the cores during this process and did not observe mobilization of trapped $scCO_2$ clusters even at the advanced stages of dissolution process. Figure 12 shows variation of $scCO_2$ saturation along the length of the Berea and Nugget sandstone cores at different steps of this process and formation of dissolution front. This figure demonstrates one complete dissolution sequence that we followed in each cycle of this category of experiments.

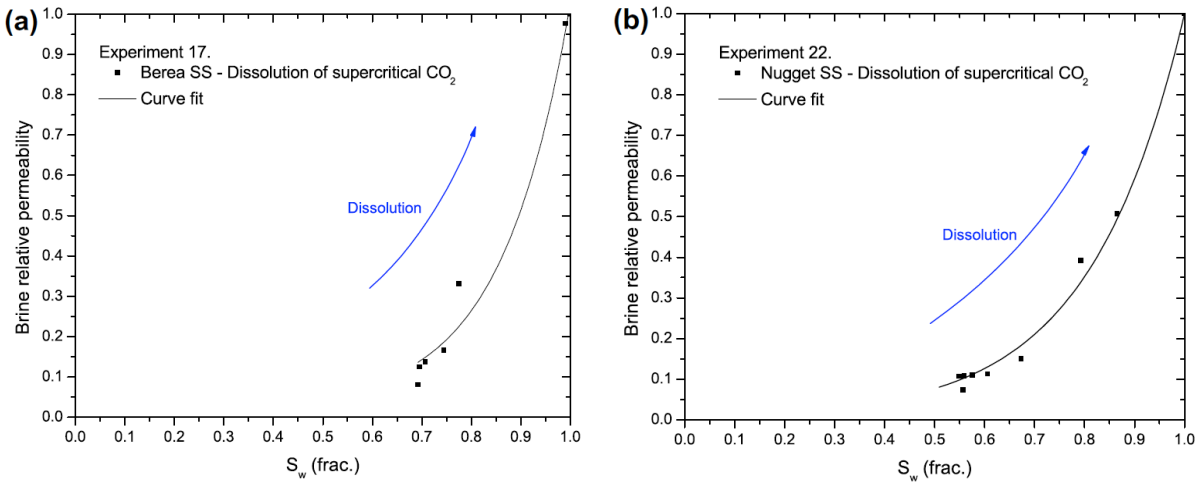

Figure 10: Brine relative permeability during dissolution process in Berea and Nugget sandstone cores (Samples 1 and 2).

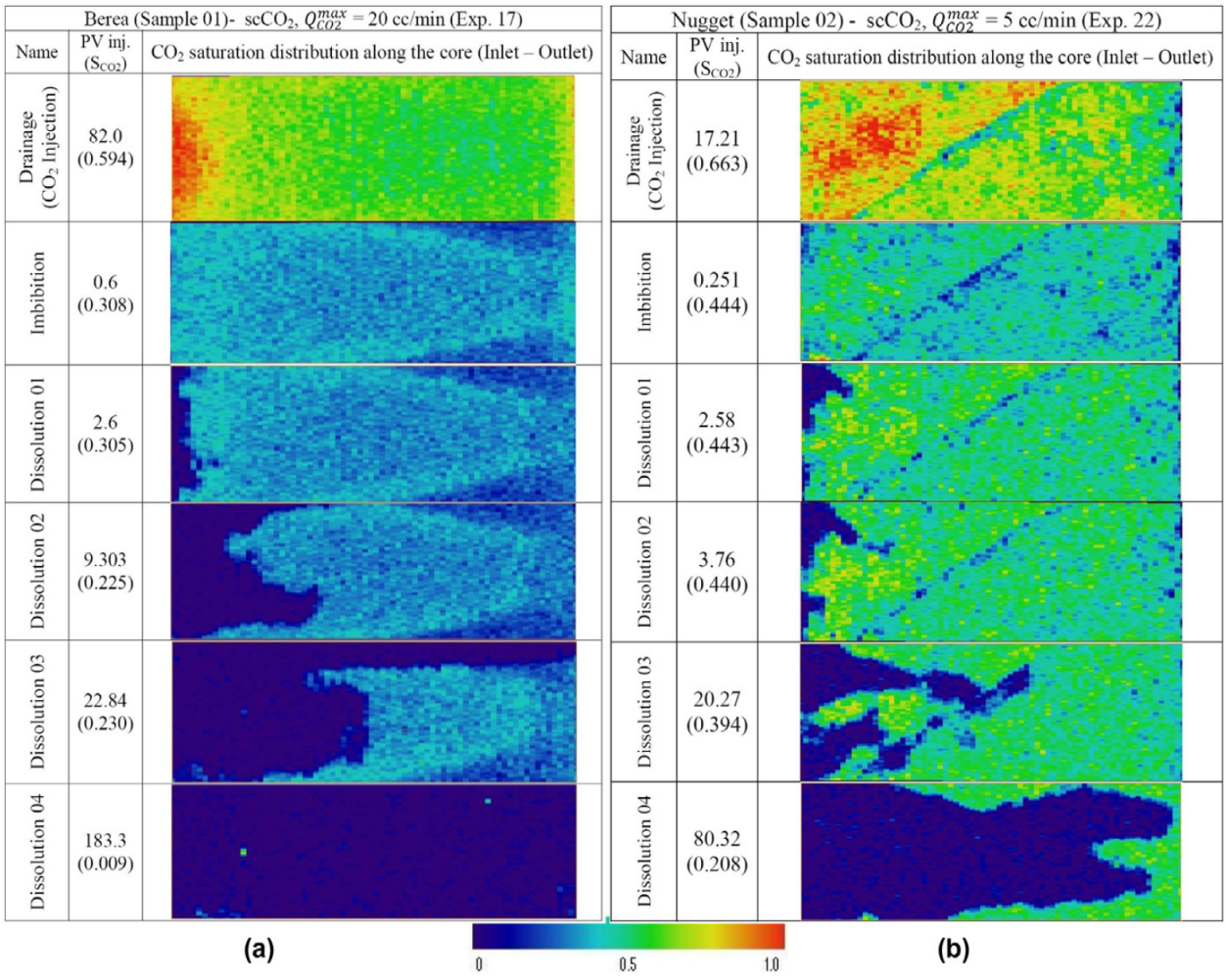

Figure 11: Two-dimensional visualizations of fluids distribution along the length of core samples during dissolution experiments in (left) Berea (Sample 2) and (right) Nugget sandstone cores.

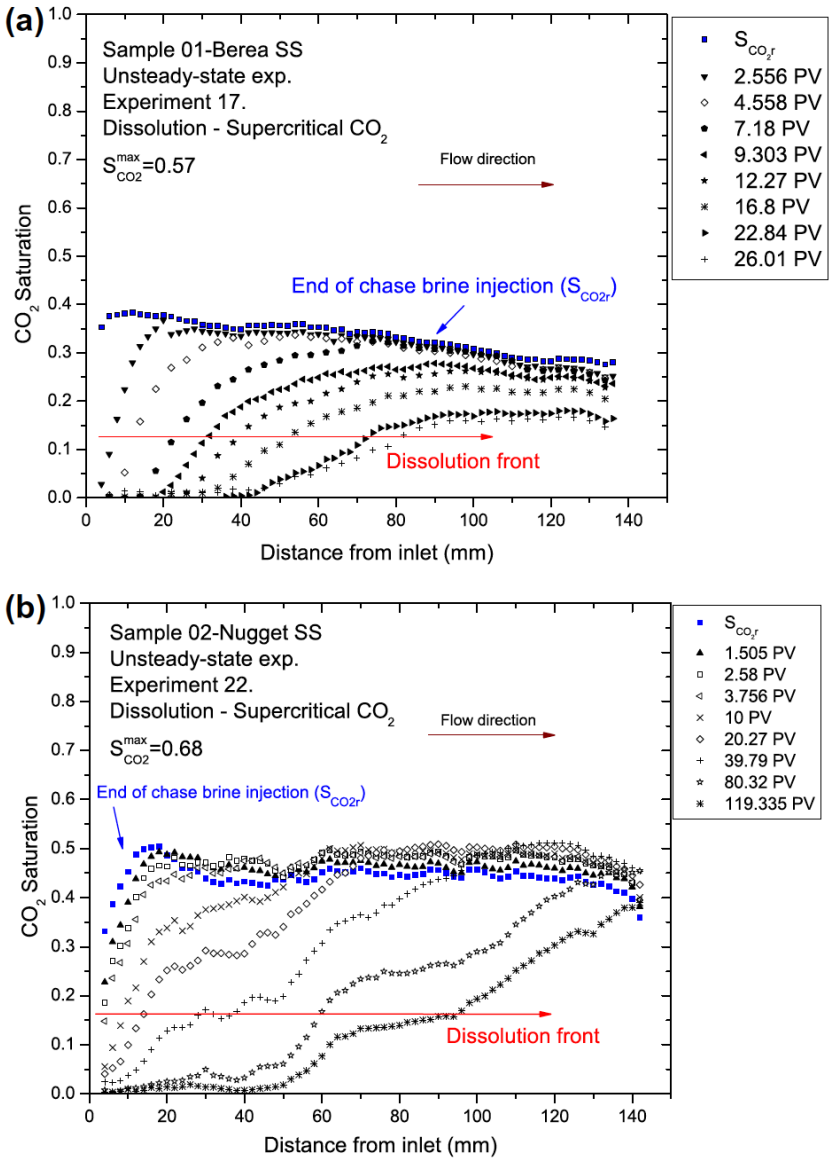

Figure 12: Advancement of dissolution front along the length of the core sample during a dissolution experiment in (a) Berea (Sample 2) and (b) Nugget sandstone cores.

3.2 Steady-state Experiments

In this set of experiments, we perform steady-state drainage and imbibition flow tests to obtain relative permeabilities. This is achieved by monotonically increasing or decreasing fractional flow of fluids. Similar to the previous category of experiments, we use in-situ dissolution of trapped CO_2 at the end of imbibition to re-establish S_w=1 state before initiating a new cycle of drainage and imbibition. In each cycle we establish a different level of S_{wi} generating relative permeability curves with different saturation spans. This results in characterization of both "full-cycle" drainage and imbibition relative permeabilities (with the widest saturation span) and relative permeability hysteresis for $scCO_2$/brine systems through scanning curves (shorter saturation spans). We performed seven steady-state (SS) drainage and imbibition experiments. All the saturation results presented in this category are, unless

stated otherwise, averaged over the whole core.

Figures 13(a) and (b) show the full-cycle SS drainage and imbibition relative permeability curves with the same range of fractional flows. As it can be seen, the results are quite similar, which is an indication of the reproducibility of our experimental results. The results show a relatively low average initial brine saturation of about 0.53. The $scCO_2$ saturation at this point, 0.47, is not as high as the maximum values reported for the other Berea core (Sample 1) in figure 21. This is mainly due to the fact that maximum $scCO_2$ flow rate at the end of drainage in Sample 3 was 5 cm^3/min compared to 20 cm^3/min in Sample 1. Brine relative permeability of drainage process initially exhibits a very rapid decline followed by a gradual reduction with decrease in brine saturation. This is attributed to large and well connected brine-filled elements getting quickly invaded by $scCO_2$, significantly reducing brine hydraulic conductivity of the core. The increase in $scCO_2$ relative permeability during drainage, on the other hand, is gradual and reaches to about 0.2 at brine saturation of 0.53. This is comparable with the drainage non-wetting phase relative permeability at the same wetting phase saturation reported by Oak [13] for Berea sandstone.

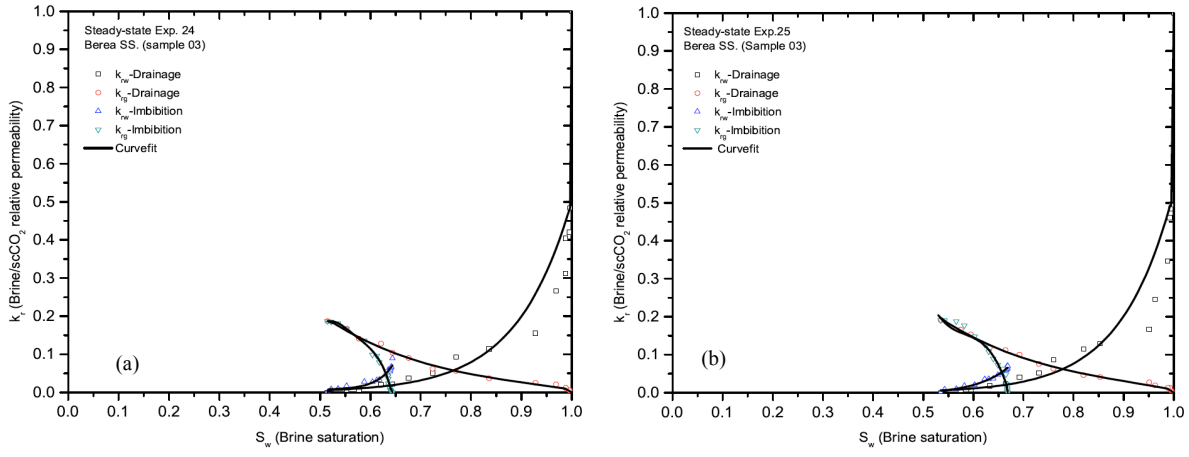

Figure 13: Full cycle steady-state drainage and imbibition relative permeabilities for Berea sandstone core (Sample 3) generated by two separate experiments performed with identical fractional flows.

Imbibition process carried out after drainage led to an average residual $scCO_2$ saturation of about 0.34, which is about 72 % of the initial $scCO_2$ saturation. During this step a very rapid reduction in $scCO_2$ relative permeability is seen that is partly responsible for trapping a significant fraction of the initial $scCO_2$ in place. We also observe that for a given brine saturation, imbibition brine relative permeability is greater than its drainage value. This might be attributed to certain pore-level displacement physics responsible for re-distribution of fluids between floods. This behavior has also been observed by Oak [14] for oil/water flow in Berea sandstone.

As we mentioned earlier, the $scCO_2$ trapped at the end of imbibition was dissolved by injection of hundreds of pore volumes of brine to re-establish S_w=1 state. This allowed us to start a new set of drainage and imbibition tests but with different end points. Figures 14 to 17 demonstrate the relative permeability curves for different cycles. Figures 14 includes the results of two half-cycle tests with encouraging reproducibility. Characteristics similar to those of the full-cycle tests were observed. Rapid trapping of $scCO_2$ due to imbibition is particularly important within the context of permanent CO_2 storage.

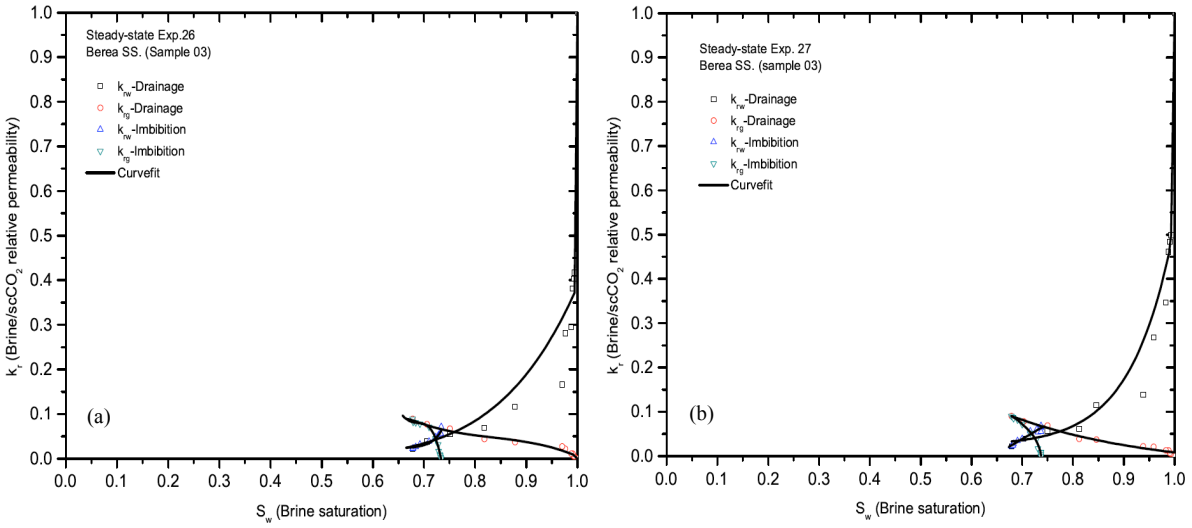

Figure 14: Quarter cycle steady-state drainage and imbibition relative permeabilities for Berea sandstone core (Sample 3).

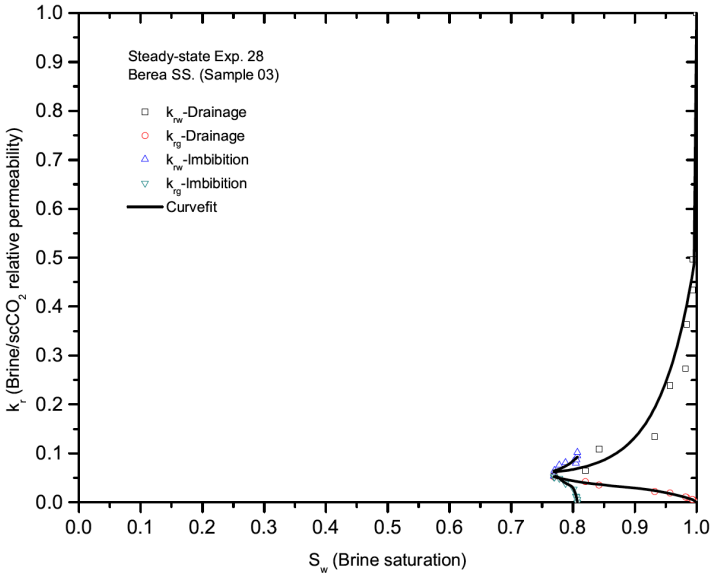

Figure 15: Quarter cycle steady-state drainage and imbibition relative permeabilities for Berea sandstone core (Sample 3).

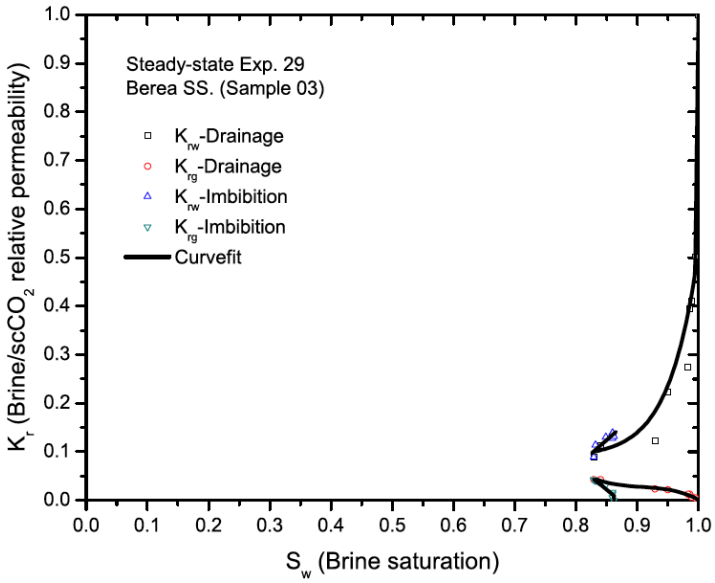

Figure 16: One-eighth cycle steady-state drainage and imbibition relative permeabilities for Berea sandstone core (Sample 3).

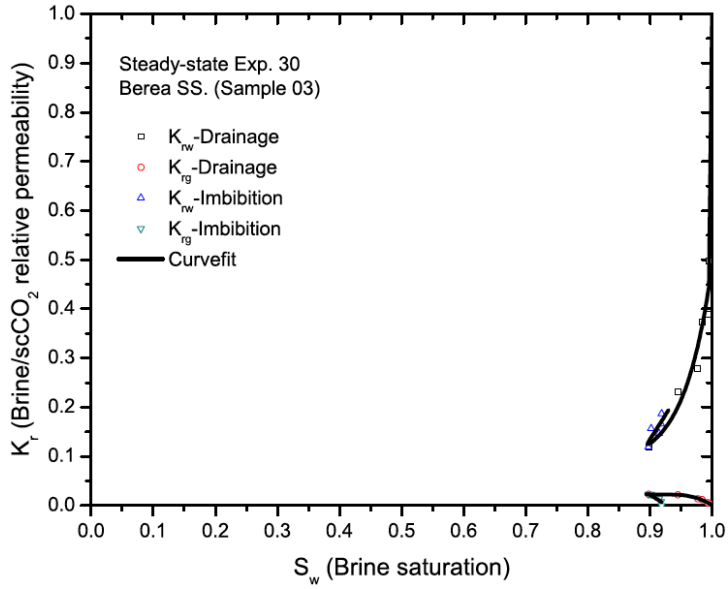

Figure 17: One-sixteenth cycle steady-state drainage and imbibition relative permeabilities for Berea sandstone core (Sample 3).

As we mentioned earlier, the minimum initial brine saturation established at the end of steady-state drainage tests is higher than that of unsteady-state tests. This leads to formation of shorter saturation spans for the steady-state experiments, which might be more relevant to reservoir modeling applications. This is because factors such as heterogeneity and well placement at reservoir scale often limit the maximum CO_2 saturation that can be reached in reservoir blocks away from injection wells,

which in turn reduces the saturation span the block experiences during drainage and imbibition processes. Furthermore, we have shown that this leads to improved trapping efficiencies.

In Figure 18, all cycles have been combined to depict the relative permeability hysteresis of $scCO_2$ and brine in Berea (Sample 3).

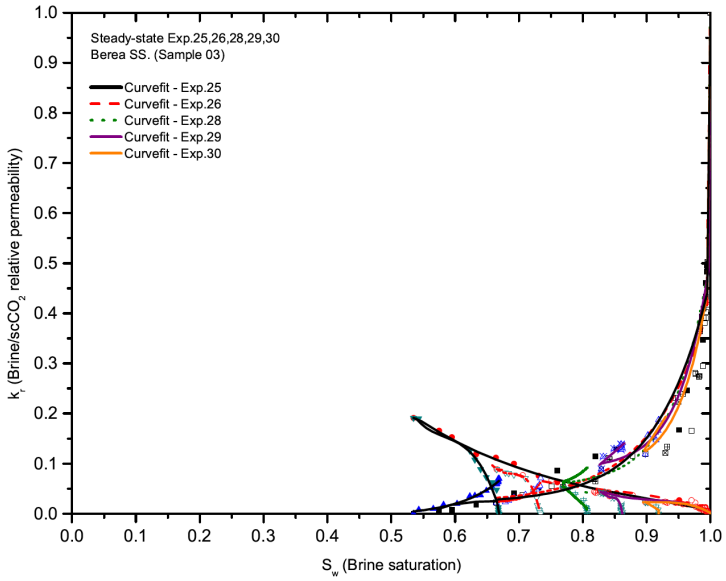

Figure 18: Steady-state drainage and imbibition relative permeabilities for Berea sandstone core (Sample 3) generated in this study.

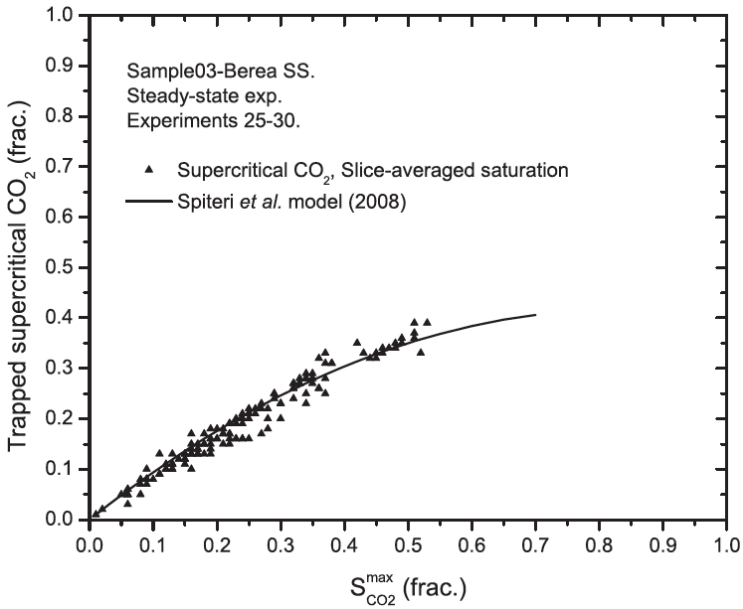

Figure 19: Variation of S_{CO2r} with S_{CO2}^{max} for Berea sandstone core (Sample 3) during steady-state flow tests.

Two major observations can be reported from this figure, (a) similar to the unsteady-state experiments, different initial brine saturations expectedly lead to different residual $scCO_2$ saturations, and (b) the higher initial brine saturation results in higher trapping efficiency. Figure 19 indicates the variation of trapped $scCO_2$ with S_{CO2}^{max}. We also include the trend generated by Spiteri *et al.* [21] model, which agrees well with our measured values. Numerical values of measured steady-state relative permeabilities for experiments 24 to 31 are listed in tables 9 through 13.

Table 9: Steady-state relative permeability data for experiments 24 and 25.

	Experiment 24			Experiment 25		
	S_w	k_{rw}	k_{rg}	S_w	k_{rw}	k_{rg}
Drainage	1.000	1.000	0.000	1.000	1.000	0.000
	0.997	0.484	0.005	0.995	0.494	0.005
	0.995	0.420	0.006	0.994	0.484	0.007
	0.988	0.404	0.011	0.992	0.461	0.013
	0.986	0.312	0.012	0.988	0.347	0.013
	0.969	0.266	0.021	0.963	0.246	0.019
	0.928	0.155	0.025	0.951	0.167	0.027
	0.836	0.114	0.037	0.853	0.129	0.041
	0.770	0.093	0.056	0.820	0.115	0.046
	0.724	0.051	0.062	0.760	0.086	0.063
	0.676	0.037	0.090	0.731	0.052	0.076
	0.644	0.022	0.104	0.692	0.041	0.100
	0.621	0.020	0.128	0.664	0.023	0.112
	0.577	0.007	0.141	0.633	0.018	0.119
	0.553	0.007	0.167	0.595	0.008	0.153
	0.515	0.000	0.187	0.575	0.007	0.166
				0.535	0.000	0.191
Imbibition	0.522	0.008	0.185	0.543	0.008	0.190
	0.536	0.009	0.181	0.566	0.010	0.188
	0.553	0.017	0.167	0.582	0.018	0.177
	0.588	0.028	0.136	0.603	0.020	0.148
	0.604	0.027	0.099	0.623	0.035	0.126
	0.613	0.032	0.096	0.631	0.036	0.108
	0.618	0.033	0.079	0.640	0.037	0.089
	0.633	0.046	0.056	0.649	0.046	0.073
	0.635	0.048	0.043	0.659	0.052	0.063
	0.636	0.059	0.036	0.665	0.059	0.048
	0.636	0.057	0.023	0.666	0.060	0.024
	0.639	0.055	0.011	0.668	0.063	0.013
	0.640	0.060	0.006	0.668	0.066	0.008
	0.641	0.065	0.004	0.668	0.070	0.003
	0.642	0.067	0.002	0.669	0.070	0.000
	0.644	0.089	0.000			

Table 10: Steady-state relative permeability data for experiments 26 and 27.

	Experiment 26			Experiment 27		
	S_w	k_{rw}	k_{rg}	S_w	k_{rw}	k_{rg}
Drainage	1.000	1.000	0.000	1.000	1.000	0.000
	0.994	0.417	0.004	0.993	0.499	0.005
	0.993	0.403	0.006	0.991	0.484	0.007
	0.991	0.381	0.011	0.988	0.461	0.013
	0.988	0.295	0.011	0.983	0.347	0.013
	0.976	0.281	0.022	0.959	0.268	0.021
	0.970	0.166	0.027	0.938	0.138	0.022
	0.878	0.116	0.037	0.846	0.115	0.037
	0.818	0.069	0.044	0.812	0.061	0.039
	0.751	0.055	0.067	0.750	0.057	0.069
	0.706	0.038	0.077	0.703	0.039	0.078
	0.678	0.022	0.089	0.679	0.022	0.090
Imbibition	0.679	0.023	0.082	0.682	0.024	0.088
	0.684	0.026	0.081	0.683	0.028	0.085
	0.692	0.032	0.078	0.691	0.034	0.082
	0.710	0.038	0.071	0.700	0.039	0.072
	0.723	0.048	0.045	0.716	0.056	0.052
	0.728	0.049	0.032	0.729	0.060	0.039
	0.729	0.053	0.017	0.731	0.054	0.017
	0.731	0.054	0.009	0.737	0.055	0.009
	0.732	0.058	0.007	0.737	0.064	0.008
	0.733	0.056	0.003	0.737	0.066	0.004
	0.734	0.071	0.000	0.737	0.068	0.000

Table 11: Steady-state relative permeability data for experiment 28.

	S_w	k_{rw}	k_{rg}
Drainage	1.000	1.000	0.000
	0.994	0.496	0.005
	0.993	0.434	0.006
	0.984	0.364	0.010
	0.982	0.273	0.011
	0.957	0.239	0.019
	0.932	0.134	0.022
	0.842	0.109	0.035
	0.820	0.065	0.042
	0.769	0.054	0.052
Imbibition	0.770	0.065	0.052
	0.778	0.076	0.049
	0.788	0.081	0.039
	0.801	0.083	0.027
	0.805	0.080	0.013
	0.806	0.087	0.011
	0.807	0.095	0.006
	0.807	0.102	0.000

Table 12: Steady-state relative permeability data for experiment 29.

	S_w	k_{rw}	k_{rg}
Drainage	1.000	1.000	0.000
	0.995	0.502	0.005
	0.989	0.410	0.007
	0.986	0.394	0.013
	0.983	0.275	0.013
	0.950	0.223	0.022
	0.929	0.122	0.024
	0.840	0.112	0.043
	0.829	0.089	0.043
Imbibition	0.832	0.114	0.041
	0.849	0.130	0.032
	0.860	0.138	0.017
	0.860	0.139	0.013
	0.860	0.128	0.006
	0.862	0.132	0.000

Table 13: Steady-state relative permeability data for experiment 30.

	S_w	k_{rw}	k_{rg}
Drainage	1.000	1.000	0.000
	0.995	0.498	0.005
	0.993	0.390	0.006
	0.984	0.373	0.012
	0.977	0.279	0.014
	0.945	0.231	0.022
	0.898	0.119	0.023
Imbibition	0.902	0.157	0.023
	0.915	0.147	0.014
	0.918	0.166	0.008
	0.919	0.187	0.000

4 Conclusions

We used a robust full-recirculation core-flooding system to perform thirty drainage and imbibition CO_2/brine flow experiments at reservoir conditions in three different sandstone core samples. The flow test were performed at various flow conditions and fluid properties (gCO_2 and $scCO_2$). Both unsteady- and steady-state core-flooding techniques were employed. We used a medical CT scanner to measure in-situ saturations during the experiments and developed a specific technique to maintain an unchanging back pressure resulting in stable thermodynamic equilibrium between the phases. The experiments were perfumed with thoroughly equilibrated fluids.

We presented two large categories of results each related to a separate group of experiments. In category A, unsteady-state technique was used to establish a wide range of initial brine saturations by injection of CO_2 to brine saturated samples. This allowed us to study the sensitivity of residual CO_2 trapping to variations in initial brine saturation, when chase brine was injected. The observed trends for $scCO_2$ and gCO_2 were successfully compared with the data in the literature. We were able to use Spiteri *et al.* model to reproduce the above-mentioned sensitivity in all cases. The results indicated that significant quantities of injected CO_2 can be trapped by capillary forces. Trapping efficiency was between 49 to 78 % of CO_2 in place. Trapping efficiency was higher at lower initial CO_2 saturations. For a given initial brine saturation, residual gCO_2 saturation was higher than residual $scCO_2$ saturation in the same sample. We attributed this to brine being less wetting in the presence of $scCO_2$ than in the presence of gCO_2. Recent measurements of advancing contact angle under gaseous and supercritical conditions confirms this explanation.

In this category, we also investigated the dissolution of residual trapped CO_2 after imbibition. This was performed by extensive injection (hundreds of pore volumes) of brine. We showed the formation of dissolution front and characteristic of its movement across the sample during this process. We also presented endpoint brine relative permeability for this process. We showed that brine relative permeability dramatic increases owing to reduced blockage to flow of brine as CO_2 dissolves. We did not observe any noticeable entrainment of trapped CO_2 even at late stage of dissolution. We showed that

this was an extremely slow process but an effective method to re-establish S_w=1 state.

In category B, we employed the steady-state approach to study relative permeability trends of drainage and imbibition processes. A wide rage of fractional flows leading to different end points was used. We reported seven sets of curves each covering a different saturation span. Shorter saturation spans in the relative permeability curves were considered to be more relevant to reservoir modeling applications as factors such as reservoir scale heterogeneity and well-placement limit the maximum CO_2 saturation that can be established in reservoir blocks away from injection wells.

The results fully characterized relative permeability hysteresis for this system and revealed some potentially critical trends. We observed that $scCO_2$ imbibition relative permeability decreased rapidly with increase in brine saturation trapping significant portions of the $scCO_2$ in place. This was considered to be an important characteristics from sequestration point of view as it improved trapping efficiency. Brine relative permeability during imbibition was higher than its drainage counterpart indicating a possible rearrangement of fluids at the pore scale during floods. This trend was consistent with those reported in the literature for Berea sandstone. Sensitivity of residual CO_2 trapping to initial brine saturation in these tests was successfully reproduced by the Spiteri *et al.* model. S_{wi} and S_{CO2r} and trapping efficiency for different cycles varied from 0.525 to 0.9, 0.34 to 0.081, and 60 % to 85 %, respectively.

In both categories of the experiments, i.e., steady- and unsteady-state, the ratio of S_{CO2r} to initial CO_2 saturation (1- S_{wi}) was very significant, i.e., about 50 to 85 %. This means that greater fractions of injected CO_2 can be permanently trapped at higher initial brine saturations. This was attributed to more efficient trapping at the pore-scale due to presences of more brine-filled elements and main terminal menisci at higher initial brine saturations.

B) Supercritical CO_2 +SO_2/brine fluid system

1 Introduction

In the second series of experiments performed under task 2, we investigate capillary trapping of $scCO_2$ in the presence of SO_2 as an impurity. We exclude the effect of mineral trapping by equilibrating the aqueous and $scCO_2$-rich phases with the minerals of the rock sample. We examine relative permeability and capillary pressure of the $scCO_2$/brine system in the presence of SO_2. In addition to these properties, we study the impact of dynamic effects on trapping of $scCO_2$ +SO_2 mixture using high flow rate imbibition tests.

2 Experiments

In this work, we performed three categories of experiments. In category A, we investigated relative permeability hysteresis of $scCO_2$ -rich/brine fluid system in a Madison limestone sample in the presence of SO_2 as a co-contaminant, using the steady-state method. In category B, we used an unsteady-state (uss) technique to characterize the $scCO_2$+SO_2 /brine capillary pressure. In categories A and B, we also examined trapping of the $scCO_2$+SO_2 mixture with variations in initial brine saturation (S_{wi}). In category C, we explored the impact of high brine flow rate displacement regime on the trapping of the $scCO_2$+SO_2 mixture. Table 1 lists all the experiments performed under this study. It also includes the technique used to carry out each experiment.

In the remainder of this section, we include information about the rock sample, fluids, and experimental conditions, apparatus, and procedure.

Table 1: Experiments performed in this study; RP: relative permeability.

Item	Experiment No.-Category No.	Process	Experiment	Technique
1	Exp.1-A	Drainage	1st RP cycle	ss
2	Exp.2-A	Imbibition	1st RP cycle	ss
3	Exp.3-A	Dissolution	1st RP cycle	uss
4	Exp.4-A	Drainage	2nd RP cycle	ss
5	Exp.5-A	Imbibition	2nd RP cycle	ss
6	Exp.6-A	Dissolution	2nd RP cycle	uss
7	Exp.7-B	Drainage	Capillary pressure	uss
8	Exp.8-B	Imbibition	Capillary pressure	uss
9	Exp.9-B	Drainage	Capillary pressure	uss
10	Exp.10-C	Imbibition	Dynamic effects	uss
11	Exp.11-C	Drainage	Dynamic effects	uss
12	Exp.12-C	Imbibition	Dynamic effects	uss

2.1 Rock Sample, fluids, and experimental conditions

The experiments were performed on a Madison limestone rock sample acquired from the Rock Springs Uplift in southwest Wyoming. This formation is currently being targeted as a potential site for storage of large quantities of CO_2. The layers of interest in this reservoir are Pennsylvanian Weber sandstone (equivalent to Tensleep sandstone) and Mississippian Madison limestone [15]. The core sample used in this study was 3.77 cm in diameter and 17.4 cm long. The porosity of the sample was measured 19.03% using an X-ray CT scanner. The other petrophysical properties of the sample are summarized in Table 2. The core was heterogeneous, and variation of porosity along the length of the sample was considerable (see Figure 1). Before performing the main experiments listed in Table 1, a sacrificial core was used to equilibrate the fluids with the minerals of the rock. The details of this step are presented later in this paper. The main and sacrificial cores were cut from the same Madison limestone sample.

The main core was wrapped with a layer of Teflon shrink tube and several layers of Teflon tape. The sleeve used in this work was manufactured from a highly impermeable AFLAS material specifically manufactured for this study. The sleeve was wrapped with several layers of Teflon tape and Aluminum foil to provide further assurance against possible penetration of the $scCO_2$+SO_2 mixture. The experiments were performed at 60°C and 19.16 MPa. At these experimental conditions, CO_2 and SO_2 were at the supercritical [16] and liquid states [17], respectively. We used a brine with 36500 ppm NaCl and 50000 ppm NaI salt concentrations as well as highly pure CO_2 and SO_2 gases for the flow tests.

Table 2: Dimensions and petrophysical properties of the Madison limestone core sample used in this study.

Sample	Length (cm)	Diameter (cm^3)	Avg. porosity (%) (X-ray)	$K_{abs,brine}$ (mD)	Pore volume (cm^3)
Madison limestone	17.4	3.77	19.03	13.6	36.96

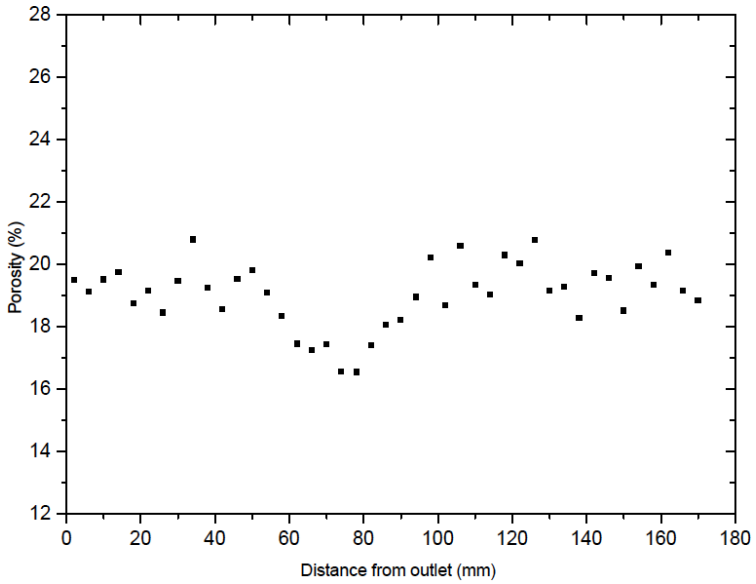

Figure 1: Porosity distribution of the Madison limestone core sample measured using an X-ray CT scanner.

Table 3: Properties of the fluid phases used in this study at 60°C and 19.16 MPa [16,22-28].

Fluids	Density ρ (kg/m^3)	Viscosity μ (m.Pa.s (cP))	$scCO_2$ /Brine IFT (mN/m)
$scCO_2$-rich phase	0.70	0.0692	28.1
Aqueous phase	1.05	0.635	-
$scCO_2$	0.70	0.0582	29.8
Brine	1.05	0.597	-

The concentration of SO_2 in the $scCO_2$-rich phase was selected according to the maximum concentration of SO_2 in flue gas streams from the coal-fired power plants in North America [18]. For instance, flue gas from Jim Bridger coal power plant in southwest Wyoming contains an average of 800-1200 ppm of SO_2 [18-20]. We introduced 1200 ppm of SO_2 into the $scCO_2$-rich phase in our experiments. The solubility of SO_2 in brine is extremely high [21], and a thermodynamic flash calculation indicated that we had formed a two-phase system [22], i.e., 1) a $scCO_2$-rich phase, including CO_2, SO_2, and water vapor and 2) an aqueous phase, containing water, salts, CO_2, and SO_2. Throughout the text we will refer to these phases as $scCO_2$-rich and aqueous phases, respectively.

Table 3 shows the estimated physical properties of the fluid phases used in this work at experimental conditions with and without impurity. The values were obtained from literature and also thermodynamic flash calculations [22].

2.2 Core-flooding apparatus

The experiments were carried out using a reservoir-conditions core-flooding system that includes a ten cylinders Hastelloy Quizix pumping system, a medical CT scanner (Universal HD-350E-V) modified for petrophysical applications, a Hassler-type Aluminum core holder, 3500 cm^3 three-phase separator, two 2000 cm^3 Hastelloy accumulators, and a pressure array system with Rosemount differential pressure transducers. To maintain a uniform temperature throughout the setup, three mechanical convection ovens were used to contain the pumps, the separator, and the accumulators. Several thermocouples were inserted at different locations of the apparatus, such as the inlet and the outlet of the core holder, to monitor the temperature. The wetted parts of the set up are made of Hastelloy to minimize corrosion. We also used special AFLAS seal kits with the equipment to leakproof the system at high pressure and temperature with the fluids mentioned earlier. Figure 2 presents a schematic diagram of the core-flooding system 15.

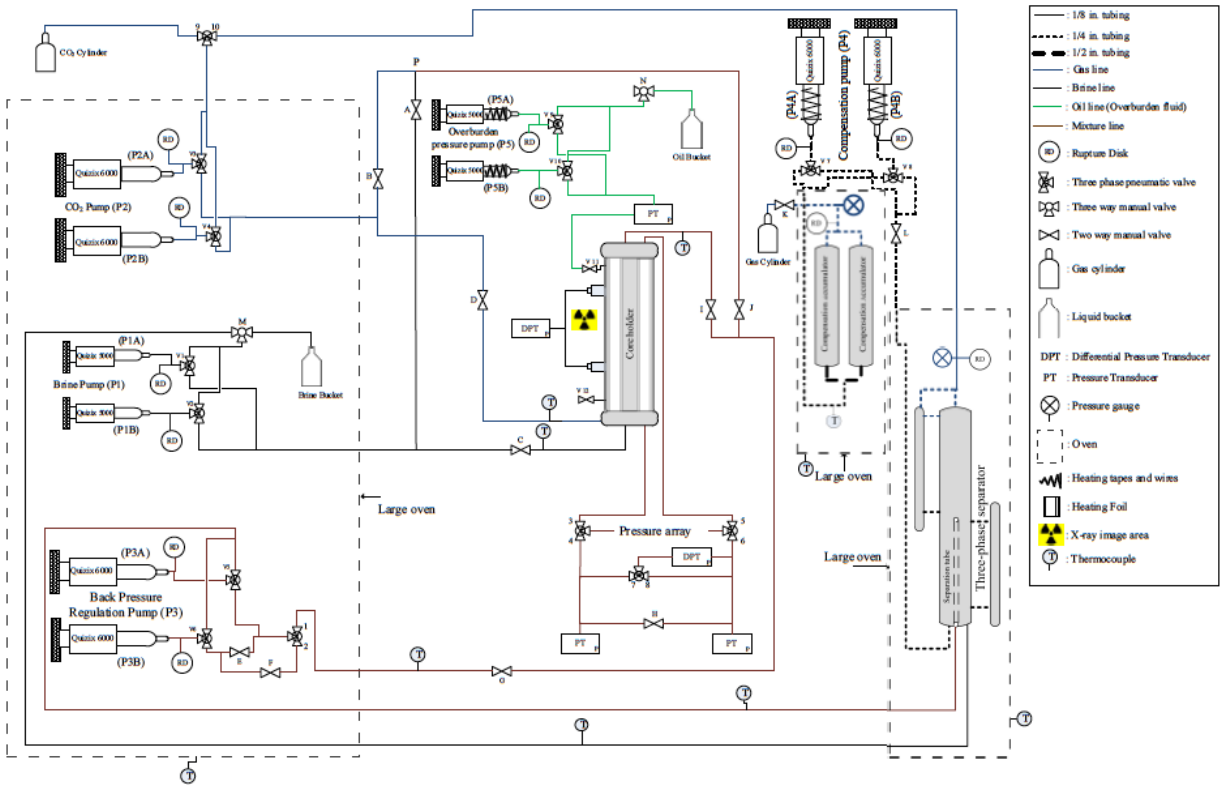

Figure 2: Schematic flow diagram of the experimental setup used in this work. The apparatus includes a medical CT scanner and a Vertical Positioning System, ten Quizix Hastelloy cylinders, a three-phase separator, an Aluminum Hassler core holder, differential pressure transducers, two compensation accumulators, and several temperature measurement devices [29].

To prepare for the experiments, the apparatus was thoroughly cleaned and vacuumed for several hours to remove any trapped air in the lines. The separator and accumulators were then filled with brine using pump 3 (P3), see Figure 2. We added 1200 ppm SO_2 to the separator and accumulators using the brine pump (P1). After saturating the setup with the appropriate fluids, the system was pressurized by injecting CO_2 using pump 2 (P2). At the same time, the ovens were turned on to heat the equipment to

60°C. This also helped with pressurization of the system.
After establishing the pre-specified temperature and pressure, the fluids were re-circulated (by-passing the core sample) to achieve thermodynamic equilibrium. P1 and P2 were retracting brine and $scCO_2$+SO_2 mixture from the separator, respectively, and injecting them at constant flow rate to point P (see Figure 2) at which two phases were mixed and retracted by the back pressure regulation (BPR) pump (P3). We used the Constant Pressure Receive mode in P3 to retract effluent mixture from the core holder at a constant back pressure. This mode allowed us to establish a very stable boundary condition, which was essential for the experiments as the fluids were highly miscible. Variations in the back pressure could introduce inaccuracies into the experimental results (e.g., in-situ saturations).

It is important to note that all the experiments listed in Table 1 were carried out in a closed-loop system in which we maintained the equilibrium between the phases and minimized the amount of mass transfer between them in the core. A dual cylinder 5000 Quizix pump was utilized to adjust the overburden pressure on the core at 21.37 MPa. Additional details about the core-flooding setup can be found elsewhere [30].

2.3 Experimental procedure

As it is listed in Table 1, steady- and unsteady-state techniques were used to carry out different series of experiments. In this section, first, we explain the preparation steps taken prior to the main tests. We then describe the procedures used to perform three different categories of flow experiments.

Before initiating the main experiments, a sacrificial core was prepared to equilibrate the fluids with the minerals of the limestone core. The fluids (i.e., $scCO_2$+SO_2 mixture and brine) were injected into the sacrificial core and re-circulated throughout the system to achieve the thermodynamic equilibrium. This stage was necessary as the interactions between the minerals of the carbonate rock and the acidic fluids prevented matrix dissolution during the main core-flooding experiments. Therefore, the core used in the main experiments remained intact.

The main core was placed in the core holder and flushed with dry CO_2 to displace trapped air in the pore space and lines. The sample was then vacuumed for several hours and pressurized using P2 by injecting pure CO_2. At this stage, when temperature and pressure were 60°C and 19.16 MPa, respectively, the outlet of the core was connected to the BPR pump (P3). We then started, using P2, to inject water-saturated $scCO_2$ into the core while P3 was retracting the effluent mixture from the core holder. After injecting about 15 pore volumes of $scCO_2$-rich phase, the core was imaged to obtain the reference scan (CT_{gc}) for saturation calculations. Thereafter, the core was flushed with fresh brine.

A 1000 cm^3 of fresh brine was prepared and equilibrated with the minerals of the crushed Madison limestone rock in a separate cell placed in an oven maintained at 60°C and 19.16 MPa. The fresh brine was re-circulated through the crushed minerals at the pressure and temperature of the experiments. It was then injected into the core using a 6000 Quizix cylinder. More than 20 pore volumes of the brine was injected to displace and dissolve all the $scCO_2$+SO_2 mixture to establish S_w=1; the core was then scanned. The main goal of this step was to obtain a reference scan (CT_{fb}) for comparison in later stages of the study. The core was then subjected to injection of $scCO_2$-saturated brine using P1. After injection of about 20 pore volumes of the brine, the core was imaged to find another reference scan (CT_{wc}). CT_{wc} was identical to CT_{fb}. At this point, the first drainage-imbibition cycle was started.

2.3.1 Porosity, permeability, and in-situ saturation measurements

The resolution per slice of the scanner was 250 µm. Throughout the experiments, the core was scanned with 4 mm slice thickness and 2 mm spacing, producing 44 slices. The porosity was calculated using the CT numbers obtained from the scanner:

$$\phi = (CT^*_{wc} - CT^*_{gc})/(CT_w - CT_g) \quad (1)$$

where CT^*_{wc} and CT^*_{gc} are the CT numbers of the core fully saturated with fresh brine and CO_2 at ambient temperature and 0.14 MPa pressure, respectively, whereas CT_w and CT_g were obtained by scanning the core holder while it was filled with brine and CO_2, respectively.

The permeability of the sample was calculated using the relationship between flow rate and pressure drop in Darcy's law. To measure the absolute permeability, when the core was saturated with $scCO_2$-saturated brine, we recorded steady-state pressure drops at several brine flow rates. The permeability was obtained by calculating the slope of the line generated by plotting the pressure drop data versus the flow rate values.

To calculate two in-situ fluid phase saturations, the core was scanned at one energy level (130 kV, 100 mA) during the experiments, and also when it was fully saturated with each of the fluids to obtain the reference scans. The saturations were determined using:

$$S_w = (CT_c - CT_{gc})/(CT_{wc} - CT_{gc}) \quad (2)$$

$$S_g = 1 - S_w \quad (3)$$

where CT_c is the CT number of the core containing two fluid phases during the experiments, and CT_{wc} and CT_{gc} are the CT numbers of the core fully saturated with aqueous and $scCO_2$-rich phases at the temperature and pressure of the experiments, respectively.

2.3.2 Relative permeability, capillary pressure, and dynamic-effects experiments

To perform the category A of the experiments, fully brine-saturated core was flooded with both fluid phases simultaneously to perform a test using the steady-state technique. In this approach, the ratio of $scCO_2$-rich and aqueous phase flow rates (Q_{CO2}/Q_w) was monotonically increased and decreased during drainage and imbibition processes, respectively. At each fractional flow, the saturation distribution was carefully monitored and pressure difference along the length of the core was recorded. When the difference between two consecutive measurements of the saturation distribution and pressure difference were less than 1%, the step was considered at steady state. The core was scanned, and the flow rates were changed. Meanwhile, we used capillary number at each step to select the flow rates in such a way that the process was always under the capillary-dominated displacement regime (i.e., $N_c \leq 10^{-5}$). It was calculated using:

$$N_c = \frac{k_{rw} * K_{abs} * \Delta P}{\phi * \sigma_{gw} * L} \quad (4)$$

where k_{rw}, K_{abs}, ϕ, σ_{gw}, ΔP, and L are relative permeability, absolute permeability, porosity, interfacial tension between $scCO_2$ and brine, pressure drop, and length of the core, respectively. The flow rates of each phase and the fractional flows used in this study during steady-state experiments are listed in Table 4.

Table 4: Aqueous and $scCO_2$-rich phases flow rates (cm^3/min) and the fractional flows used during steady-state experiments (1, 2, 4, and 5).

Item	Drainage	Imbibition
Aqueous phase flow rate	0.03-0.2	0.03-0.16
$scCO_2$-rich phase flow rate	0-0.1	0-0.08
Fractional flow	0.05-3.33	0.06-2.67

After establishing the maximum $scCO_2$ saturation (S_{CO2}^{max}=1-S) at the end of drainage test, the imbibition experiment was started. It was performed analogous to the drainage test with this difference that the Q_{CO2}/Q_w was monotonically decreased during the experiment until Q_{CO2} became zero. At this point, small increases in Q_w did not affect the saturations. After completing the imbibition and determining the residual $scCO_2$ saturation (S_{CO2r}), the Q_w was increased gradually to dissolve all the trapped $scCO_2$+SO_2, and re-establish S_w=1. We then started a new drainage-imbibition cycle with shorter saturation span. After the second cycle, the dissolution process was carried out again. As a result of the thermodynamic equilibrium established between the phases, the dissolution was a time-consuming process. Each dissolution run took about 7 days to be completed. About 250 pore volumes of brine were injected to re-create a fully brine-saturated core. After the second steady-state drainage-imbibition cycle, the capillary pressure measurement experiments (category B) were performed. This category included primary drainage, imbibition, and secondary drainage tests using the unsteady-state approach.

In category B, to accomplish primary drainage, $scCO_2$-rich phase was injected at a low flow rate, i.e., 0.025 cm^3/min into a fully brine saturated core. After reaching the steady state, the brine saturation was measured. The pressure difference was also recorded throughout the whole process. This information was then processed to obtain capillary pressure as we will explain later in this document. For the next point, the $scCO_2$ flow rate was increased, and similar procedure was repeated until upon increasing the $scCO_2$ flow rate, no significant decrease in brine saturation was observed. At this point, we had constructed a full drainage capillary pressure curve.

To establish an imbibition capillary pressure curve, one can use two different methods: 1) spontaneous imbibition in which the capillary pressure is decreased gradually to zero to allow the wetting phase to imbibe and 2) forced imbibition that can be created by decreasing the capillary pressure from zero to a potentially large negative number [31]. In this study, we used the latter where the imbibition process was started just after the primary drainage step with a very low brine flow rate (0.005 cm^3/min). This process was continued by increasing the brine flow rate in small increments. When slight increase in brine flow rate did not change the saturation profile, the imbibition process was considered complete, and the residual $scCO_2$ saturation was determined. This allowed us to build an imbibition capillary pressure curve. After accomplishing the imbibition test, the secondary drainage was started by injecting $scCO_2$ at a much lower flow rate, i.e., 0.005 cm^3/min, compared to that of the primary drainage. The procedure was identical to the primary drainage process to construct the capillary pressure curve an ultimately establish the same S_{wi} as primary drainage (i.e., ~0.49).

Following the secondary drainage, in order to perform the last group of experiments (category C), an imbibition test was started with a relatively high brine flow rate of 1.01 cm^3/min, which corresponded to $N_c=1.3\times10^{-5}$. After reaching the steady-state condition, we recorded the pressure drop and measured the S_{CO2r}. This imbibition test was then followed by another set of drainage and imbibition experiments, with this difference that we used an even higher brine flow rate, i.e., 2.02 cm^3/min. Before each imbibition test, we made sure that S_{wi} was similar to previous imbibition tests. All the saturation values used in this study were averaged over the entire length of the core, unless stated otherwise.

3 Results and discussions

In this section, first, we present the capillary trapping results obtained from experiments 1-8, see 2, followed by the results of the relative permeability tests using steady- and unsteady-state methods (exp.1-9); then we explain the characteristics of the capillary pressure curves (exp.7-9), and finally we demonstrate the results of the high brine flow rate imbibition experiments (exp.9-12).

3.1 Capillary trapping

Two steady-state (experiments 1, 2, 4, and 5) and one unsteady-state drainage-imbibition cycles (experiments 7 and 8) were performed on the Madison limestone core sample under capillary-dominated displacement regime.

Figure 3 demonstrates the variation of the CO_2 saturations across the core sample during steady-state experiment. This figure also shows the effect of heterogeneity on the saturation profiles along the length of the core sample.

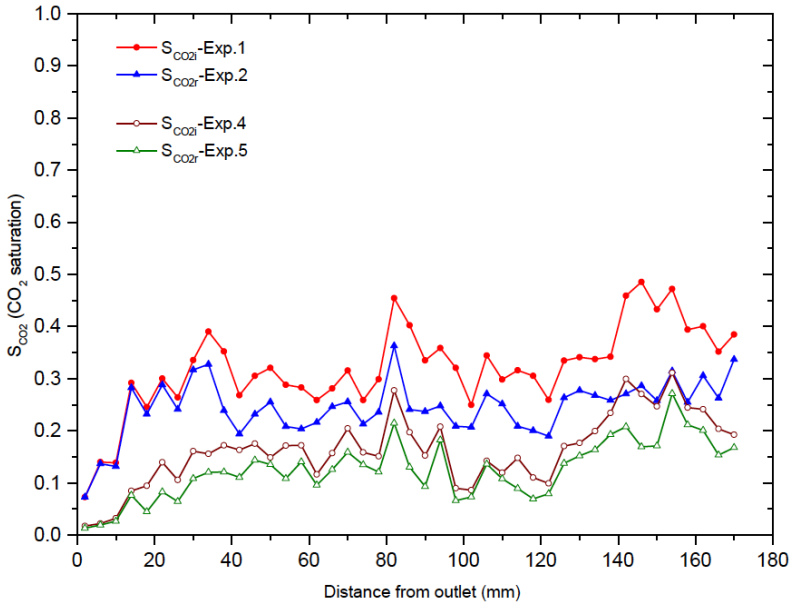

Figure 3: $scCO_2$ saturation profiles along the length of the Madison limestone core sample at the end of Experiments 1, 2, 4, and 5.

Figure 4 exhibits the variation of the S_{CO2r} with S_{CO2}^{max} for these series of experiments. In this figure, the results are compared with the Spiteri et al. [32] empirical correlation and Land model [33], which

provide a relationship between initial and residual non-wetting phase saturations. The results compare well using the model parameters listed in Table 5. The coefficients α and β were calculated through fitting the experimental data into the quadratic equation provided by Spiteri et al. [32].

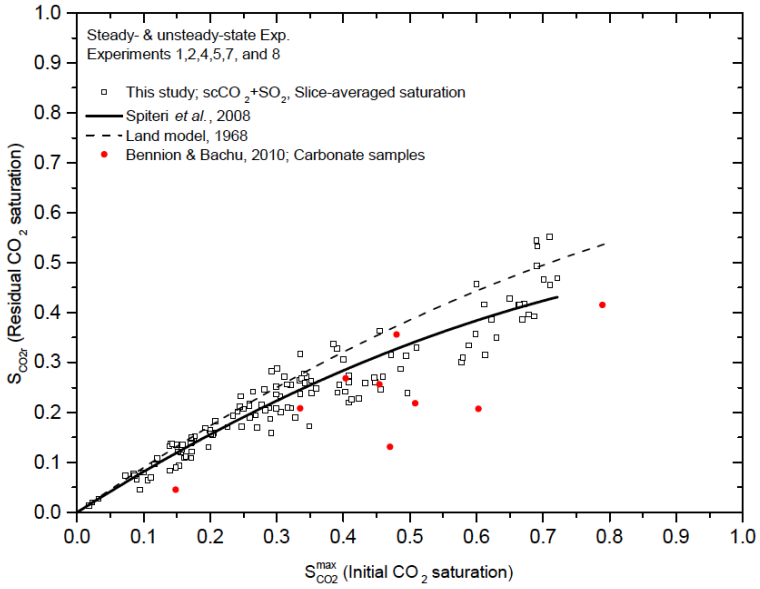

Figure 4: Variation of S_{CO2r} with S_{CO2}^{max} for capillary-dominated experiments on the Madison limestone core sample.

Note that each point in this figure represents the slice-averaged saturations obtained along the length of the core sample. For the first steady-state drainage-imbibition cycle, the S_{CO2}^{max} was about 0.32. The subsequent waterflood led to S_{CO2r} of about 0.245, meaning that approximately 76.3% of the initial $scCO_2$ was trapped permanently through capillary trapping. The S_{CO2}^{max}, S_{CO2r}, and trapping efficiency (S_{CO2r} /S_{CO2}^{max}) for the second cycle were 0.164, 0.126, and 76.8%, respectively. For the last drainage and imbibition cycle, i.e., experiments 7 and 8, these values were 0.525, 0.329, and 62.7%, respectively. Figure 5 illustrates the trapping efficiency obtained from each slice along the length of the Madison limestone core sample. It indicates that significant fractions of $scCO_2$-rich phase can be trapped, i.e., from 62.7 to 76.8%, due to chase brine flooding. It also shows that as the initial brine saturation increases, the trapping efficiency improves. The scatter in the data is attributed to the heterogeneity of the sample. The trapping results obtained from the second cycle of steady-state experiments with low S_{CO2}^{max} are particularly significant due to the fact that at reservoir scale, initial CO_2 saturation in grid blocks away from the injection wells may not be high. This reduces the saturation span that those blocks experience during a drainage-imbibition cycle.

Table 5: Parameters used with Spiteri [32] empirical correlation and Land model [33].

Sample	Experiment	Fluid system	α	β	S_{CO2}^{max}	C
Madison limestone	Exp.1,2,4,5,7, and 8	$scCO_2$+SO_2/Brine	0.85	0.35	0.62	0.613
Madison limestone	Exp. 9 and 10	$scCO_2$+SO_2/Brine	0.80	0.42	-	-
Madison limestone	Exp. 11 and 12	$scCO_2$+SO_2/Brine	0.70	0.40	-	-

These results show that the maximum initial $scCO_2$-rich phase saturation obtained at the end of

unsteady-state experiments (i.e., 0.525) is less than its counterparts in Berea and Nugget SS cores, i.e., 0.59 and 0.68, respectively [30]. The lower initial saturation may be attributed to higher drainage capillary pressure needed. Furthermore, compared to sandstone rock samples, less amount of $scCO_2$-rich phase is trapped in the Madison limestone, which might be attributed to the latter being less water wet leading to better hydraulic conductivity of the $scCO_2$-rich phase. In Figure 4, we also plot our data against the trapping results of the various carbonate rock samples reported in the literature. In some cases, higher residual trapping observed in our study may be attributed to heterogeneity [34], lower viscosity ratio between two phases under our experimental conditions as well as different pore-space topologies impacting pore-scale displacement mechanisms responsible for trapping. In Table 6, the initial and residual $scCO_2$ saturations measured on different carbonate rock samples presented in the literature are compared to those of this study. It can be seen that our results lie within the range of data that have been reported by other researchers (see also Figure 4). This could be in part owing to the fact that small amount of SO_2 did not affect parameters such as IFT and contact angle, significantly, [27] and hence SO_2+$scCO_2$ trapping results compare favorably with those without SO_2. This is consistent with the results of another study suggesting that small amount of SO_2 does not decrease the volume of $scCO_2$-rich phase trapped in the rock sample [35]. Note that in this work, the fluid phases were equilibrated with the minerals of the rock sample to minimize the impact of acidic brine on the trapping of $scCO_2$-rich phase, for instance, by altering the pore and matrix structures.

3.2 Relative permeability measurements

In this section, we demonstrate the results of two sets of drainage-imbibition relative permeability experiments with different saturation spans in the Madison limestone core sample (category A). We also present the relative permeability results generated through unsteady-state technique (category B), see Table 1.

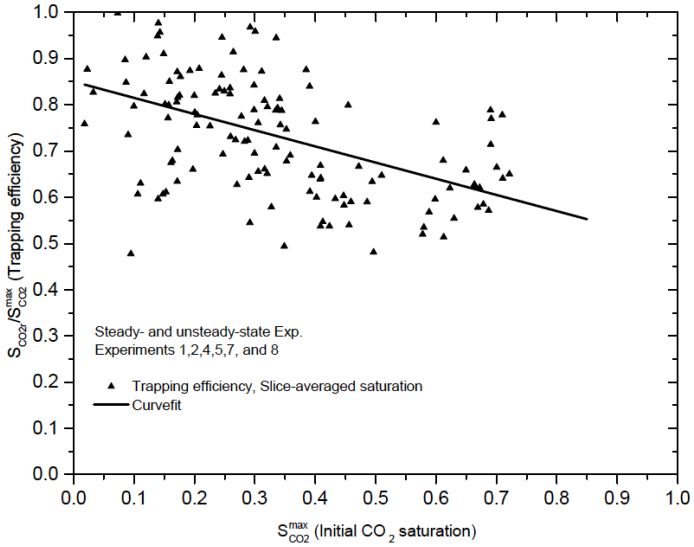

Figure 5: Variation of trapping efficiency with S^{max}_{CO2} for capillary-dominated experiments on the Madison limestone core sample.

Table 6: Initial and residual $scCO_2$ saturations measured in various carbonate rock samples obtained

from the literature.

Rock sample	Porosity (%)	K_{abs} (mD)	Temperature (°C)	Pressure (MPa)	Viscosity ratio (μ_w/μ_{nw})	Initial $scCO_2$ saturation	Residual $scCO_2$ saturation	Reference
Wabamun#3	15.4	54.3	41	11.9	15.41	0.148	0.045	[36, 37]
Nisku#2	10.4	21.02	56	17.4	11.80	0.508	0.218	[36, 37]
Nisku#3	10.9	74.4	56	17.4	11.80	0.603	0.207	[36, 37]
Grosmont	11.8	153.9	41	11.9	-	0.480	0.365	[36, 37]
Morinville Leduc	11.6	371.9	40	11.4	-	0.470	0.131	[36, 37]
Redwater Leduc	16.8	353.6	36	9.2	-	0.335	0.208	[36, 37]
Cooking Lake#2	16.7	4.87	55	15.5	15.43	0.431	0.268	[36, 37]
Slave Point	9.9	0.217	43	18.8	-	0.454	0.256	[36, 37]
Winnipegosis	14.8	3.09	36	8.73	-	0.789	0.415	[36, 37]
Carbonate from Middle East	14.0	6.7	40	9.8	-	0.400	0.230	[38]
Indiana	19.7	244	50	9.0	3.0	0.730	0.230	[39]
Madison	19.03	13.6	60	19.16	9.18	0.475	0.329	This study

3.2.1 Steady-state experiments

Figure 6 illustrates the results of the drainage-imbibition relative permeability tests for both cycles. As it is shown in this figure, the initial and residual $scCO_2$ saturations for the first and second cycles were 0.321, 0.245 and 0.164, 0.136, respectively. We observe rather rapid reduction of $scCO_2$-rich phase relative permeability during imbibition. Furthermore, $scCO_2$+SO_2 relative permeability at the end of drainage reaches relatively small values, e.g., 0.04. This is consistent with the results reported by various research groups in the literature [30,40-44].

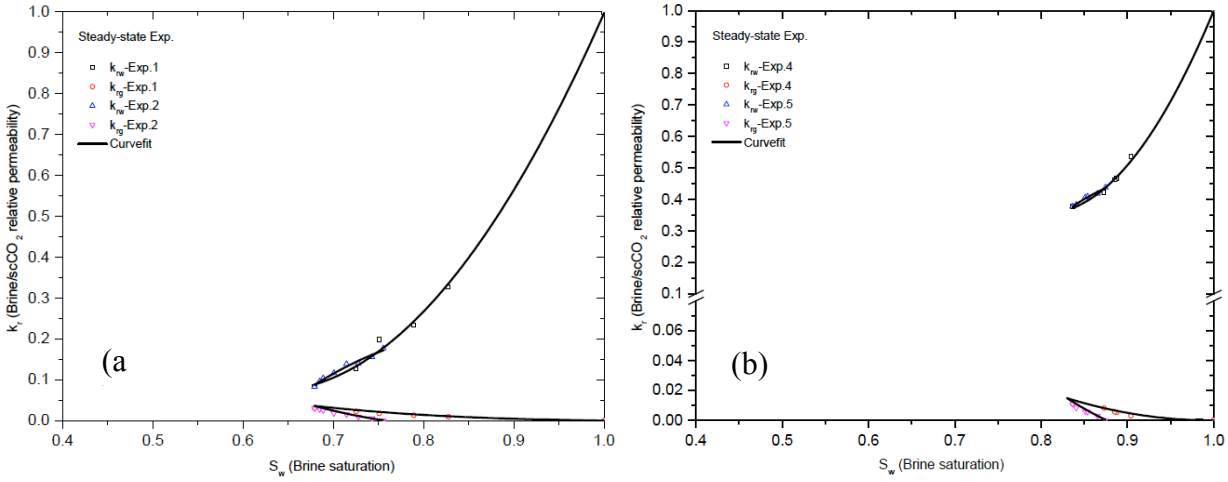

Figure 6: $scCO_2$+SO_2/brine drainage-imbibition relative permeability results generated using steady-state method on the Madison limestone sample for (a) first (b) second cycles.

It is clear that unlike the results of the drainage-imbibition relative permeability experiments on, for instance, Berea sandstone core [30], we do not observe a sharp decrease in brine relative permeability

during drainage. This might be attributed to poor pore-level connectivity of large brine-filled elements that get invaded by $scCO_2$+SO_2 compared to those of the $scCO_2$/brine system in the Berea SS core. This figure suggests that the brine maintained a good hydraulic conductivity while the non-wetting phase gradually invaded the pores. The trends observed in this category agree well with those of the carbonate core samples published in the literature [37,44].

For the imbibition process we noticed that for a given brine saturation, the drainage brine relative permeability is slightly smaller than that of the imbibition. This phenomenon was also observed in the results presented by Akbarabadi and Piri [30], Bennion and Bachu [37,44], and Oak et al. [45] and might have been caused by slight re-configuration of pore fluid occupancy. Numerical values of the measured steady-state relative permeabilities for experiments 1, 2, 4, and 5 are listed in Table 7.

Table 7: Steady-state relative permeability data of experiments 1, 2, 4, and 5.

	Experiments 1,2			Experiments 4,5		
	S_w	k_{rw}	k_{rg}	S_w	k_{rw}	k_{rg}
Drainage	1.000	1.000	0.000	1.000	1.000	0.000
	0.8274	0.32712	0.0106	0.9039	0.5361	0.0035
	0.7892	0.2340	0.0152	0.8873	0.4669	0.0061
	0.7509	0.1980	0.0205	0.885	0.4629	0.0067
	0.7254	0.1266	0.0263	0.8727	0.4213	0.0096
	0.6792	0.0825	0.0357	0.8364	0.3779	0.0131
Imbibition	0.6792	0.0825	0.0357	0.8407	0.3830	0.0099
	0.6848	0.0958	0.0331	0.8511	0.4063	0.0070
	0.6887	0.1035	0.0307	0.8539	0.4093	0.0066
	0.7004	0.1161	0.0215	0.8653	0.4181	0.0034
	0.7145	0.1383	0.0179	0.8744	0.4381	0.0000
	0.7278	0.1400	0.0109			
	0.7429	0.1556	0.0061			
	0.7554	0.1797	0.0000			

3.2.2 Unsteady-state experiments

We performed one set of primary drainage and imbibition experiments followed by a secondary drainage using the unsteady-state method. For each step during drainage and imbibition tests, end-point relative permeability data were calculated using the pressure drop values. To illustrate the agreement between the steady- and unsteady-state relative permeabilities, all data are combined and presented in Figure 7. From this figure, it is evident that the steady- and unsteady-state data compare well with each other. Numerical values of the measured unsteady-state end-point relative permeabilities for experiments 7 to 9 are listed in Table 8.

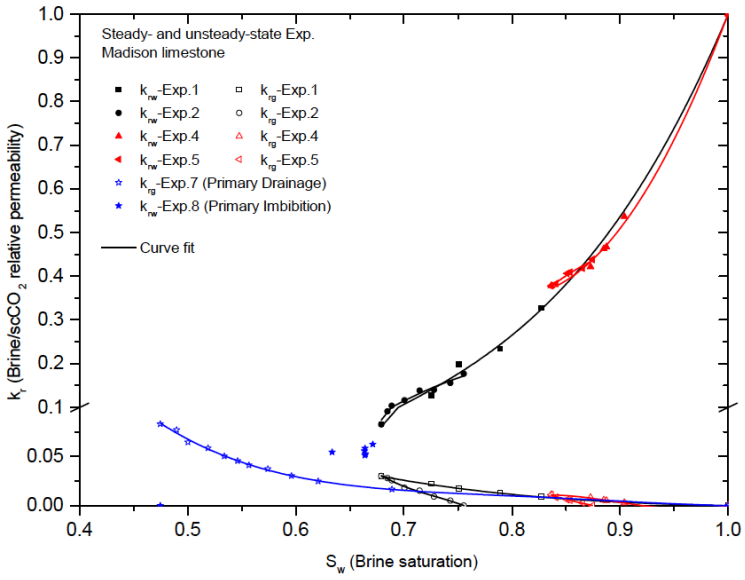

Figure 7: $scCO_2$+SO_2/brine relative permeability data generated using steady- and unsteady-state experiments performed on the Madison limestone core sample.

Table 8: End-point relative permeability data of experiments 7 to 9.

Primary drainage		Imbibition		Secondary drainage	
S_w	k_{rg}	S_w	k_{rw}	S_w	k_{rg}
.0000	0.0000	0.6337	0.0511	0.5992	0.0066
.6889	0.0197	0.6640	0.0526	0.5649	0.0096
.6207	0.0295	0.6645	0.0556	0.5561	0.0140
.5959	0.0362	0.6640	0.0583	0.5438	0.0169
.5741	0.0444	0.6640	0.0624	0.5416	0.0201
.5567	0.0489	0.6712	0.0629	0.5259	0.0262
.5461	0.0541			0.5249	0.0298
.5339	0.0599			0.5171	0.0329
.5189	0.0697			0.5128	0.0362
.5003	0.0767			0.5029	0.0413
.4896	0.0916			0.5014	0.0463
.4750	0.0988				

In Figure 8, the relative permeability data obtained in this study using steady- and unsteady-state experiments on Madison limestone are compared to those of the pure $scCO_2$/brine/carbonate studies from the literature. As it is shown, the results are in good agreement. This figure indicates that the end point $scCO_2$-rich phase drainage relative permeabilities are below 0.1, which is consistent with our results. The low end-point relative permeability in $scCO_2$/brine system might be attributed to several factors, such as heterogeneity of the sample, viscosity ratio, interfacial tension, and wettability of the rock [46].

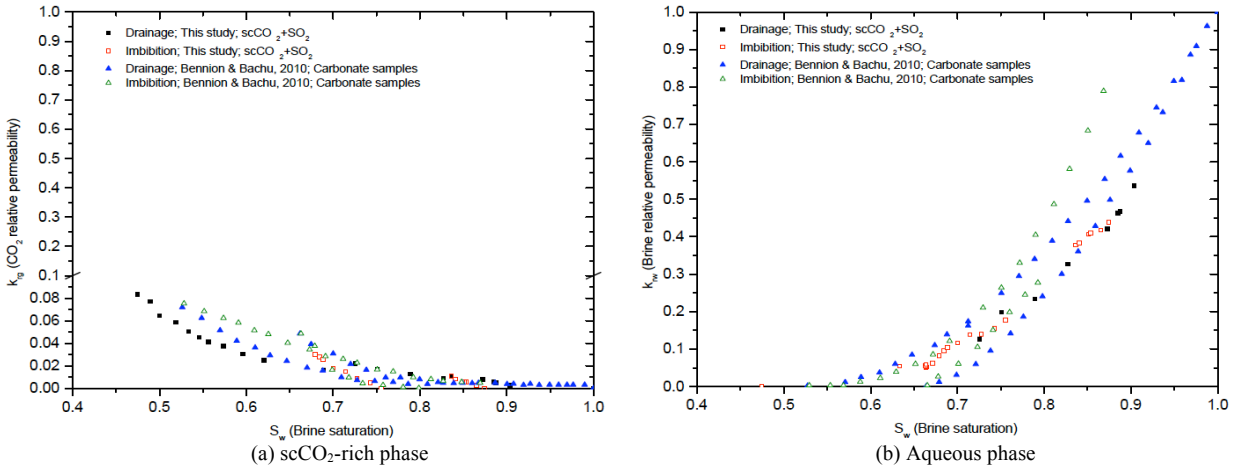

(a) $scCO_2$-rich phase (b) Aqueous phase

Figure 8: Comparison between the relative permeability data of this study and those from the literature.

An unsteady-state dissolution step was performed as an approach to re-establish S_w=1, and initiate a new set of experiments. At the end of each dissolution test, the core was fully scanned and CT numbers were compared with both CT_{fb} and CT_{wc}. Comparing the scans showed that we had successfully re-established S_w=1. The end-point dissolution brine relative permeability for both cycles are demonstrated in Figure 9. The slight difference between the results of the two dissolution experiments might have been caused by the vastly different brine flow rates used for dissolution in experiment 3 compared to those in test 6. The difference in brine flow rate may have resulted in a slightly different order by which $scCO_2$+SO_2-filled pores were invaded by brine through dissolution of the mixture. This may have then led to a different fluid occupancy at the pore scale for a given saturation producing different relative permeability.

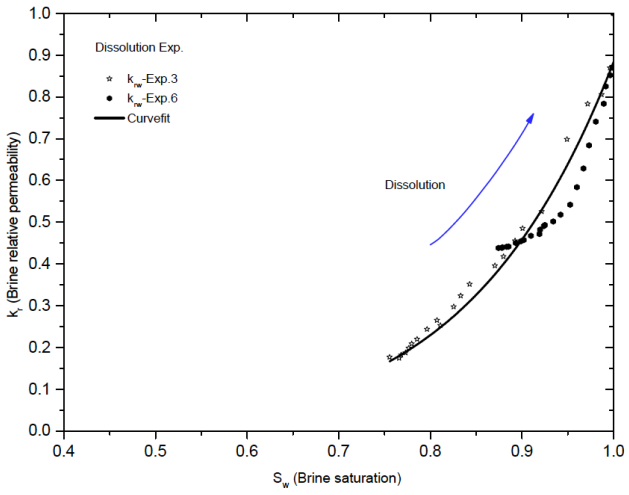

Figure 9: End-point dissolution brine relative permeability for experiments 3 and 6 performed on the Madison limestone core sample.

3.3 Capillary pressure

In this section, we present the results of the capillary pressure measurement experiments performed on the Madison limestone core using the unsteady-state method. We used *inlet* saturations to characterize the capillary pressure behavior of the rock sample. The method of using the inlet saturations during the

100% non-wetting phase injection to calculate relative permeability and capillary pressure was first introduced by Leas [47] and Ramakrishnan and Capiello [48], and then adopted by Pini et al. [34,49] to study the capillary pressure versus saturation of the $scCO_2$/brine core-flooding experiments.

During unsteady-state core-flooding experiments, $scCO_2$-rich phase is injected at a constant flow rate (Q_{CO2}) into the fully brine-saturated core. The boundary conditions are: 1) $P|_{x=L} = P_{backpressure}$ = constant (Back pressure is kept constant using back pressure regulation pump) and 2) $Q_{CO2}|_{inlet}$ = constant (Inlet flow rate is constant). Therefore, a pressure gradient exists along the length of the core. The inlet and outlet pressures, as well as pressure drops, are carefully monitored and recorded. At the steady state, there is no brine production and the pressure drop is constant. This means that brine pressure in the core reaches to a fixed value, i.e., $dP_w/dx = 0$, and $P_w|_{x=0} = P_w|_{x=L}$. As long as brine remains a continuous phase across the outlet face of the core, which is a valid assumption for the wetting phase, the CO_2 flow creates the pressure drop across the core. At this point, if CO_2 stays as a continuous phase across the upstream of the core, it can be assumed that $P_{inlet} = P_{CO2}$ and $P_{outlet} = P_{brine}$. This means that before reaching to zero capillary pressure outside outlet face of the core, P_c takes a finite value at the end faces, i.e., $P_c|_{x=0}$ and $P_c|_{x=L} \neq 0$.

For a CO_2/brine system, the capillary pressure is calculated using:

$$P_c = P_{CO2} - P_{brine} \quad (5)$$

Using the above-mentioned boundary conditions with equation 5, the final P_c^{dra} can be found through pressure drop measurement:

$$P_c^{dra}|_{x=0} = P_{inlet} - P_{outlet} = \Delta P \quad (6)$$

To calculate the capillary pressure during the imbibition process, we only injected brine and implemented the following procedure: at the steady-state condition, we use equation 5 where the pressures are measured at the inlet face of the core. Considering the pore-scale physics of the displacement mechanism during the imbibition tests: $P_{CO2}^{inlet} = P_{backpressure} + \Delta P_{max}^{dra}$ and $P_{brine}^{inlet} = P_{backpressure} + \Delta P^{imb}$, where ΔP_{max}^{dra} is the maximum pressure drop at the end of the primary drainage process preceding imbibition and ΔP^{imb} is the pressure drop at the end of each imbibition step. Hence, the final equation would be:

$$P_c^{imb}|_{x=0} = \Delta P_{max}^{dra} - \Delta P^{imb} \quad (7)$$

Therefore, through measuring the inlet saturation using the CT scanner and repeating this procedure for various CO_2 and brine flow rates, the capillary pressure versus saturation curves can be constructed [49].

Two sets of experiments were performed on the Madison limestone core sample to characterize the $scCO_2$+SO_2/brine primary drainage, imbibition, and secondary drainage capillary pressures versus

saturation. In category C, to obtain more accurate values for the saturations, the inlet face of the core was scanned 20 times after reaching steady state, and the final value was calculated through averaging.

Figure 10 depicts the results of the $scCO_2$+SO_2/brine capillary pressure data obtained using the core-flooding apparatus. As it is illustrated, the maximum initial and residual $scCO_2$ saturations are 0.692 and 0.532, respectively. These values agree well with the trend shown in Figure 4.

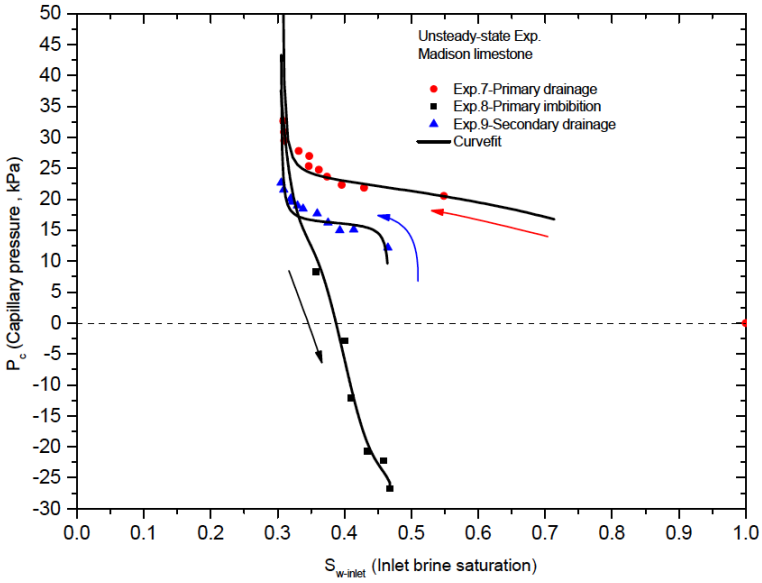

Figure 10: $scCO_2$+SO_2/brine capillary pressure versus saturation curves for the Madison limestone core sample.

During the imbibition process, if the sample was strongly water-wet, imbibition would establish the final residual CO_2 saturation at capillary pressures close to zero; otherwise, additional CO_2 could be displaced by more brine injection [17]. This phenomenon was observed in the Madison limestone core sample. Our results show that the wettability of the core sample might have been altered due to being in contact with $scCO_2$+SO_2 mixture. This is consistent with the observations reported in Chiquet et al. [50], Chalbaud et al. [51], and Be [52]. The numerical values of the primary drainage, imbibition, and secondary drainage capillary pressure versus saturation are presented in Table 9.

3.4 Dynamic effects

To investigate the impact of dynamic effects, corresponding to viscous-dominated displacement regime, on the trapping of the $scCO_2$-rich phase, two separate imbibition tests with relatively high brine flow rates (i.e., 1.01 and 2.02 cm^3/min) were conducted. The initial $scCO_2$ saturation for both tests were identical (i.e., ~0.49). Figure 11 displays the $scCO_2$+SO_2 trapping results for each individual slices for both experiments in the Madison limestone core. We also compared these results with those obtained from the capillary-dominated experiments as well as the Spiteri et al. [32] empirical correlation. The results compare well utilizing the models parameters listed in Table 5. We observed that the $scCO_2$-rich phase saturation was significantly reduced because of the dynamic effects. The average residual $scCO_2$ saturation decreased from 0.329 at the end of experiment 8 to 0.291 and 0.262 at the end of experiments 10 and 12, respectively. It means that the residual $scCO_2$-rich phase dropped about 11.5% for the first and 20.4% for the second imbibition test. This decline is attributed to high brine flow rates

producing a considerable pressure drop across the core. Under these conditions, brine invades accessible $scCO_2$-filled pores not only based on the pore threshold capillary pressure, but also the viscous pressure drops associated with each displacement. This creates displacements similar to frontal piston-like advance, which significantly reduces trapping. These reductions were more significant specifically through the first half of the core. One could imagine the possibility of high pressure brine, created by high flow rate, at the inlet side of the core dissolving some of the $scCO_2$-rich phase and releasing it at the second half of the core, which was at a much lower pressure due to considerable heterogeneity. This phenomenon, however, is expected to have negligible impact on the saturation difference observed in the first half of the core, because the difference in pressure values could not create a meaningful difference in additional dissolution and hence saturations. Flash calculations [22] showed that only 0.3% and 0.5% (saturation percentage) reductions in residual saturation during the above-mentioned experiments were due to additional dissolution of $scCO_2$-rich phase in brine as a result of pressure increase. Note that this amount represents the maximum dissolution when the pressure is at its highest value, i.e., at the inlet of the core sample. This pressure gradient decreases significantly towards the outlet of the sample, leading to even less additional dissolution of the $scCO_2$+SO_2 in brine. Furthermore, the reservoir core sample used in this study had a lower porosity and permeability in the middle (see Figure 1); therefore, this created a significant pressure gradient in the first half of the core sample while the rest of the sample did not experience large pressure drop. This led to more decrease in saturation through the first half of the core.

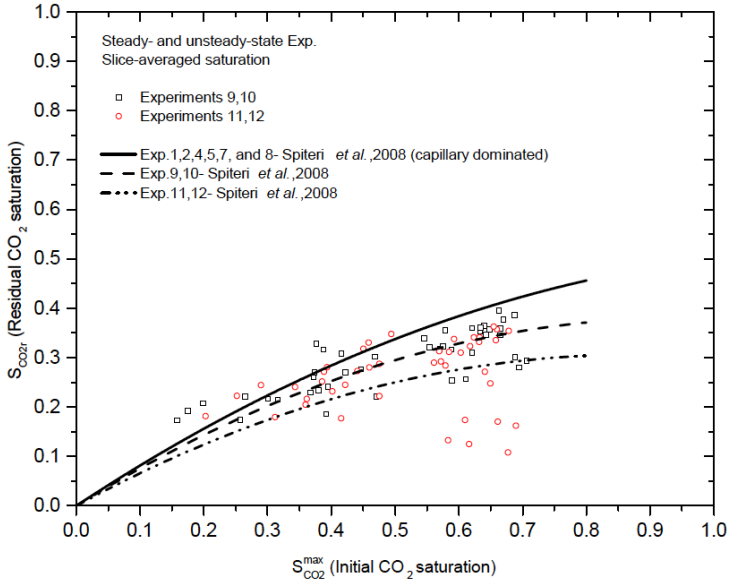

Figure 11: Variation of S_{CO2r} with S_{CO2}^{max} for high flow rate brine floods and comparison with the capillary-dominated counterparts.

3.5 Conclusions

A heterogeneous Madison limestone core sample acquired from Rock Springs Uplift in southwest Wyoming was used to perform reservoir-conditions core-flooding experiments with $scCO_2$+SO_2/brine fluid system at 60°C temperature and 19.16 MPa pressure. A state-of-the-art experimental apparatus was utilized to carry out three categories of flow tests to characterize relative permeability, capillary pressure, and capillary trapping of $scCO_2$+SO_2 mixture using steady- and unsteady-state techniques. We

also investigated the impact of dynamic effects on capillary trapping of the above-mentioned mixture due to chase brine injection.

The results of three different categories of experiments were presented and discussed. In category A, we employed a steady-state method to perform two drainage-imbibition relative permeability cycles. At the end of each cycle, a dissolution process was implemented to re-establish S_w=1. The comparison between the dissolution scans and the fresh brine scans confirmed the S_w=1 state. Different ranges of fractional flow during drainage experiments were applied to establish various initial $scCO_2$-rich phase saturations for the subsequent imbibition process. The results showed that 62.7% to 76.8% of the initial $scCO_2$+SO_2 volume was trapped through capillary trapping, meaning that significant portion of the CO_2 in-placed at the end of the drainage process will be trapped permanently due to chase brine injection with the lowest risk of leakage. The amount of $scCO_2$-rich phase trapping was comparable to those of pure CO_2 in other carbonates reported in the literature. This might be in part due to the fact that small amount of SO_2 did not affect IFT, contact angles, and storage capacity of the rock sample, which was also reported by other researchers. Note that in this study, the impact of mineral dissolution into the acidified brine caused by SO_2 disproportionation was almost eliminated as we equilibrated the fluid phases with the minerals of the rock sample.

The results show that the higher initial brine saturations led to higher trapping efficiencies. We found that the final $scCO_2$-rich phase drainage relative permeability was very low, i.e., 0.04, which is consistent with the results that have been reported by other research studies. We observed a rapid reduction in imbibition relative permeability of the $scCO_2$-rich phase, resulting in high residual trapping. For the imbibition process, we noticed that for a given brine saturation, the imbibition brine relative permeability is higher than that of the drainage. This might be due to the re-configuration of the fluid occupancy. The end-point dissolution brine relative permeabilities were also obtained for two dissolution experiments. A slight difference between the dissolution results may be attributed to difference in brine flow rates used, resulting in a different order by which $scCO_2$+SO_2-filled pores were invaded by brine through dissolution of the mixture, in turn leading to a different fluid occupancy at the pore scale for a given saturation. This result indicates that dissolution plays an effective role on the permanent mitigation of the $scCO_2$-rich phase at the later stages of the geological storage process.

In category B of the experiments, unsteady-state technique was used to perform primary drainage, imbibition, and secondary drainage tests to measure $scCO_2$+SO_2/brine capillary pressures. The results showed that the lowest initial brine saturation we could establish in the Madison limestone core sample was 0.475. The subsequent imbibition process resulted in 0.329 residual $scCO_2$ saturation, meaning that more than 62% of the $scCO_2$-rich phase was trapped through capillary trapping mechanism. By comparing the trapping results (i.e., initial and residual saturations, and trapping efficiency) obtained from both categories (A and B) of experiments in this study to those available in the literature for other rock samples (e.g., Berea and Nugget sandstones and different carbonates), it can be concluded that the capacity of the rock sample to receive $scCO_2$-rich phase during the drainage was slightly lower in the Madison limestone compared to those of the sandstones, furthermore, the residual saturations of the $scCO_2$-rich phase also decreased. This could be due to the fact that Madison limestone is less water wet than the above-mentioned sandstone rock samples. However, in comparison with the results of carbonate cores, our data showed slightly higher residual $scCO_2$-rich phase saturations. This might be attributed to heterogeneity, different viscosity ratio, and dissimilar pore-space topologies impacting pore-scale displacement mechanisms responsible for trapping. The imbibition capillary pressure curve showed a negative value at the residual $scCO_2$ saturation, which is an indication of wettability alteration

of the rock sample. This was consistent with findings of other authors reported in the literature. The end-point $scCO_2$-rich phase and brine relative permeabilities were also obtained, which agreed well with those of the steady-state method.

In category C, two imbibition tests with relatively high brine flow rates were conducted to study the impact of dynamic effects on capillary trapping. Brine flow rates during the first and second fast imbibition tests were 1.01 and 2.02 cm^3/min. Residual $scCO_2$ saturations at the end of each imbibition test were reduced by 11.5% (0.291) and 20.4% (0.262) compared to 0.329 obtained under capillary-dominated displacement regime. This phenomenon can be attributed to the large viscous pressure drop, created by high brine flow rate, along the core, causing the sweeping of the $scCO_2$-rich phase from the pores. The extra $scCO_2$ was produced by weakening the non-wetting phase trapping processes. This was done by changing the order by which the displacement mechanisms take place at the pore scale, which in turn is achieved by changing their relative threshold pressure values. Flash calculations showed that only 0.3% and 0.5% (saturation percentage) of the reductions in residual saturation during the first and second fast imbibition tests were due to high pressures created by high brine flow rates. Therefore, the contribution of the dissolution to the overall reduction in trapping was relatively insignificant.

Task 3: Measurement of mixed scCO$_2$/brine interfacial tension and contact angles at reservoir conditions with relevant fluid compositions
PI: Dr. Lamia Goual

1 Introduction

The final storage capacity and total amount of capillary-trapped CO_2 inside an aquifer are affected by the interfacial tension between the fluids and the contact angle between the fluids and the rock mineral surface. A thorough study of these parameters and their variations with temperature and pressure will provide a better understanding of the carbon sequestration process and thus improve predictions of the sequestration efficiency. Successful implementation of CO_2 sequestration projects via the structural trapping mechanism requires minimal CO_2 leakage through the cap rock. One possible cause of rapid leakage is capillary failure of the cap rock, which is to a large extent controlled by the CO_2/brine interfacial tension (IFT) and water advancing angle in CO_2/brine/cap rock mineral as shown by the Equation 1 [53]:

$$Pc_{th} = \frac{2\gamma\cos(\theta)}{r}, \quad (1)$$

where γ is the IFT between CO_2 and brine, θ is the contact angle between these fluids on the rock surface, and r is the characteristic diameter of rock pores. Rapid leakage occurs when the pressure build-up in the reservoir due to CO_2 injection is more than the threshold value. If the wettability of the cap rock changes during CO_2 sequestration from strongly water-wet to weakly water-wet, the capillary threshold pressure reduces. This will affect the design and planning of any CO_2 injection and storage project as it sets a limit on both the injection pressure and the storage capacity [53]. On the other hand, the capillary trapping of carbon dioxide is desired for higher storage efficiencies and reduced risk of leakage through the cap rock. Capillary trapping is governed by relative permeability and capillary pressure of the rock, which in turn depend on CO_2/brine IFT and wettability (or contact angle) of the reservoir rock minerals. Thus, carefully measured IFT and CA data that are consistent with reservoir pressure, temperature, and fluid compositions will reduce the uncertainties associated with the prediction of flow properties that directly affect the estimation of storage capacity and the fate of the CO_2 plume.

The wettability of minerals in the presence of water and carbon dioxide has become a controversial issue in recent years. While some studies [54]–[56] reported no effect of CO_2 phase change (or pressure) on the wettability of minerals, others [57]–[65] found a gradual or sudden wettability change towards less water-wet conditions as pressure increased. Espinoza and Santamarina [54] conducted sessile drop experiments in the pressure range of 0-1500 psi at ambient temperature and found that contact angles are independent of pressure. Bikkina [55] used the same method and did not observe any clear trends with pressure (200-3000 psi) or temperature ranging from 25 to 50 °C. Dickson et al. [57], Yang et al. [58], Sutjiadi-Sia et al. [59], Wang et al. [60], and Farokhpoor et al. [65] reported an increase in contact angles with increasing pressure. Plung and Bruining [62] and Plung et al. [61] performed capillary pressure measurements on sand and coal samples. They noticed that the wettability of these samples was altered from water-wet to intermediate-wet in the presence of CO_2 under supercritical conditions. Recently, Jung and Wan [64] observed about 18° increase in the static contact angles from subcritical to supercritical pressures. The increase occurred only in a small pressure range close to the phase change region of CO_2, while contact angles were almost constant at lower and higher pressures. Another recent study by Farokhpoor et al. [65] reported a sudden increase in contact angles around the carbon dioxide

critical pressure. Chiquet et al. [53] and Broseta et al. [66] used a different approach and measured both water advancing and receding contact angles in a quasi-static mode. In the first study, the authors found a gradual increase in receding contact angle with pressure. In the subsequent study, they reported very small variations in the receding angles while the water advancing angles showed a clear increase with pressure. Kim et al. [63] studied the dewetting of silica surfaces using a water-wet glass micromodel. They observed thinning of the water film and growth of the water droplets during drainage of the initially water-saturated model with carbon dioxide. They also noticed an increase in the apparent contact angles up to 80 degrees. These findings contradict the study performed by Chalbaud and co-workers [56].

The brine salinity is an important parameter that affects the solubility of CO_2, the interfacial tension between fluids, the wettability of reservoir and caprock, and hence the storage capacity of aquifers. The effect of brine salinity on wettability or contact angle of quartz and glass surfaces in CO_2/brine/quartz systems have been recently studied by a few research groups [53], [54], [60], [64]–[66]. While some studies have not observed any significant effect of brine salinity [54], [60], others have reported a clear decrease in water-wetness of quartz surface by increasing brine salinity [53], [64]–[66]. The salinity of the sedimentary basins that have been used for CO_2 storage varies considerably from 7,000 ppm to the maximum salt solubilty in water which is about 360,000 ppm [67]. However in the United States, the EPA regulations do not permit any CO_2 injection in aquifers with total dissolved solids (TDS) of less than 10,000 ppm [68]. In this study, a broad range of brine salinity (0.2-5 M NaCl), compatible with EPA regulations and currently active CO_2 sequestration projects, was investigated.

Another important factor to consider is the presence of co-contaminants such as SO_2 in CO_2 phase. There are very limited data in the literature on the solubility of CO_2/SO_2 mixtures in brines and there are no interfacial tension data between this gas mixture and brine. Furthermore, the wettability state of the reservoir or caprock in the presence of SO_2 as co-contaminant has not been studied in the past. There are very few data on interfacial tension and contact angle of pure H_2S acid gas at reservoir conditions. Shah et al. [75] measured the interfacial tension between pure H_2S and 30 mole% of H_2S/CO_2 mixture with water. They reported a considerable reduction in IFT by increase in concentration of H_2S. Also, Broseta et al. [66] compared the contact angle of CO_2/brine and H_2S/brine on mica and quartz surfaces. They did not observe any significant difference between the contact angles of these two fluid systems. A report by Miller and Van Atten [76] listed the annual emissions of about 700 power plants across North America. They have reported 2400 million tons of CO_2 emission into the atmosphere per year from these power plants. Other gases such as Sulfur Dioxide or SO_2 (11.5 million tons per year) and Nitrogen Oxides or NO_x (4.5 million tons per year) are also present in the emission stream. These gases (co-cotaminants) can be co-injected with CO_2 for geological storage, and thereby avoiding extra cost of separation process. For the first time, the effect of SO_2 as a co-contaminant in supercritical CO_2 (sc-CO_2) on IFT and dynamic contant angles of a representative system for geological storage of carbon dioxide were examined in this study.

Figure 1 shows the most likely ranges of pressure and temperature at which saline aquifers are found underground. This graph is created considering the earth's surface temperature ranging from 15 to 25 °C, the geothermal gradient between 20 to 30 °C/km, and hydrostatic pressure gradient of about 1500 psi/km. Although there are possible cases of cold reservoirs, for example in the Arctic [80], or extremely hot reservoirs [66], it is expected that this range to be valid for most of the saline aquifers. The phase diagram of carbon dioxide is also superimposed on the same graph, demonstrating that CO_2 is most likely to be in supercritical state in underground aquifers (shaded area in Figure 1). For the purpose of

carbon sequestration, it is desirable to find an aquifer having a pressure and temperature where CO_2 has the highest density so that a maximum mass of carbon dioxide can be stored per unit volume. For pressures higher than 4000 psig (or reservoirs deeper than about 3 km), the density change of CO_2 phase becomes minimal and the cost of compression and injection of CO_2 becomes uneconomical [80]. Also, in agreement with the above argument, the reported CO_2 injection depths for sixteen active carbon dioxide storage operations in saline aquifers are between 0.7 and 3 km [67]. Therefore, we selected pressure and temperature ranges that were not explored in the past and can be considered more practical for carbon sequestration in deep saline aquifers (filled blue circle symboles in Figure 1).

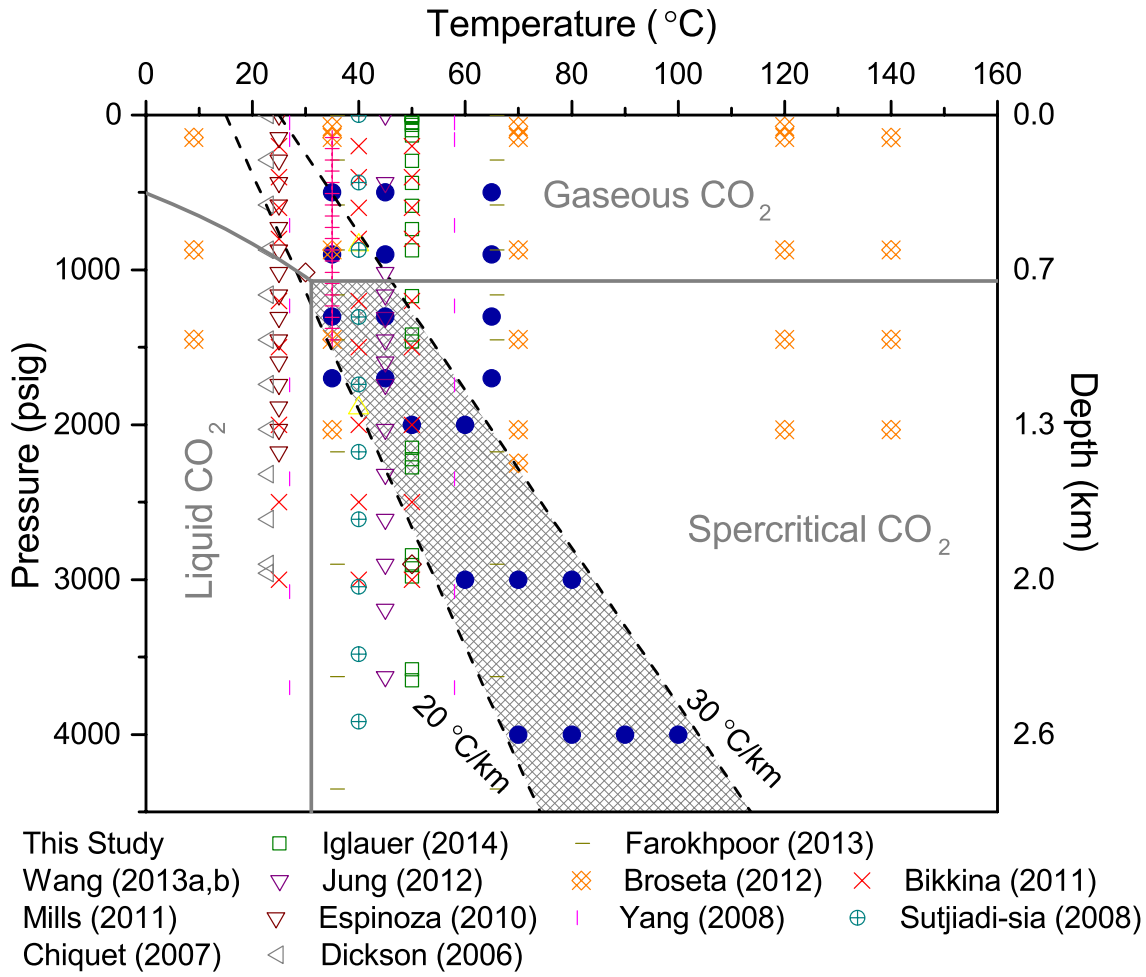

Figure 1: Pressure and temperature conditions used in this study and in the literature [53], [54], [57]–[60], [64]–[66], [70], [81]–[84].

2 Experimental methods

HPHT IFT/CA apparatus

A state-of-the-art IFT/CA measurement system was designed and constructed to perform measurements under extreme conditions such as those encountered in geological sequestration of carbon dioxide in deep saline aquifers (Figure 2). The setup can handle high pressure (up to 7500 psi),

high temperature (up to 200 °C), and highly corrosive fluids. All the wetted parts in the high-pressure/high-temperature (HPHT) setup were constructed from Hastelloy C-276, polyether ether ketone (PEEK), Sapphire glass, and AFLAS O-rings. A few parts (valves and some fittings) were made out of 316-stainless steel. The main components of the apparatus are a HPHT measurement cell, an imaging module, a fluid equilibration module, a density measurement module, a temperature control module, and a data acquisition and analysis module. A schematic of the entire experimental setup is also illustrated in Figure 2.

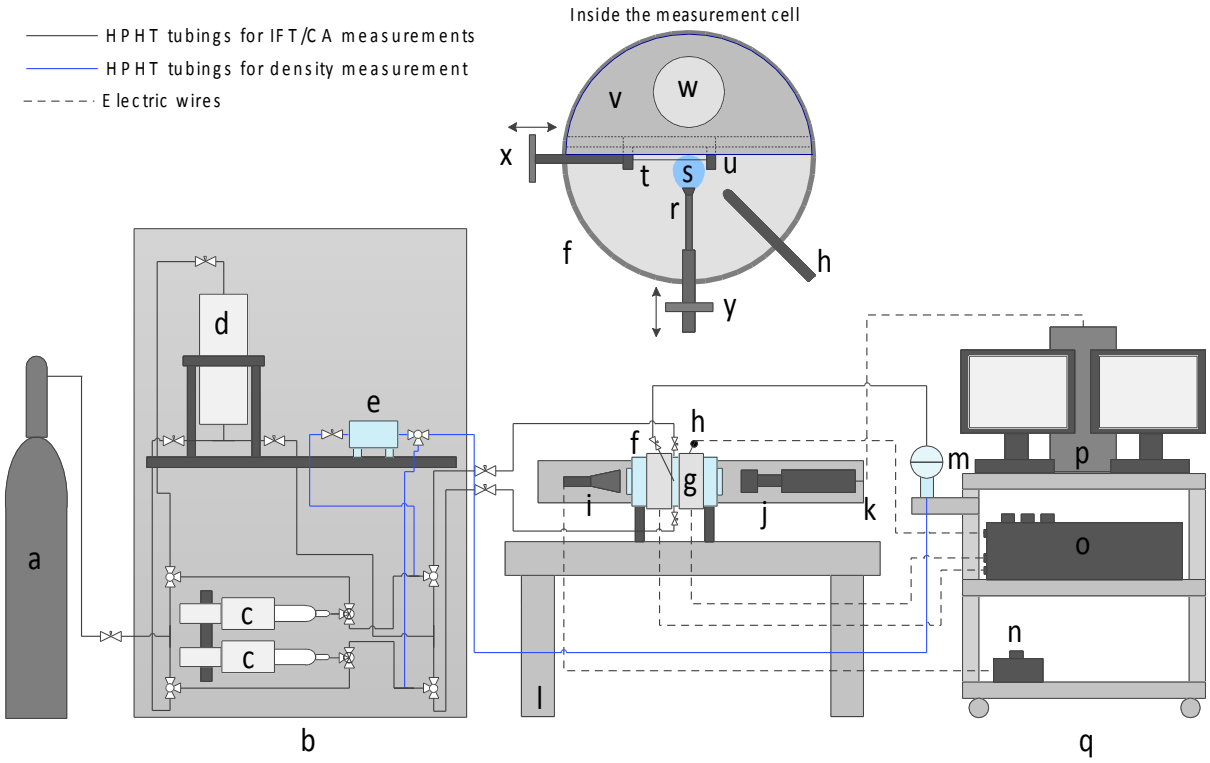

Figure 2: Schematic of the experimental setup used in this study; (a) CO_2 cylinder, (b) mechanical convection oven, (c) dual-cylinder Quizix pump, (d) equilibration cell, (e) density meter, (f) measurement cell, (g) heating jackets, (h) RTD, (i) light source, (j) apochromatically-corrected lenses and CCD camera, (k) adjustable stand, (l) anti-vibration table, (m) Rosemount pressure sensor, (n) current source, (o) temperature control system, (p) data acquisition computer, (q) shelf cart, (r) IFT/CA needle, (s) fluid bubble, (t) solid substrate, (u) movable tray, (v) crystal holder, (w) fluid level observation opening, (x) horizontal drive shaft, and (y) vertical drive shaft.

IFT/CA measurement cell

The cell is made of Hastelloy C-276 and is considered as the main part of the experimental setup. A schematic of the interior of the cell is also provided in Figure 3. The crystal holder located inside the measurement cell contains a movable tray that holds the crystal and an opening to observe the level of the fluids inside the cell. Two drive shafts mounted on the cell facilitate the measurement of CA and IFT. The shafts move the needle and crystal tray in the vertical and horizontal directions, respectively. Two

high-pressure Sapphire windows are located at two ends of the measurement cell for observing drop/bubble images generated during the measurements (Figure 3c).

Imaging module

This module has two components: a light source and a microscope attached to a digital camera (Figure 4a). The light source (Edmund Optics Inc.) consists of a blue LED, a telecentric backlight illuminator that increases edge contrast and measurement accuracy by decreasing diffuse reflections from the object under inspection, and a polarizing filter that directs blue light in the range of 400-700 nm wavelength into the cell. The microscope has a fully apochromatically corrected lens (Leica Z16 APO) that minimizes the chromatic aberration and color fringing and therefore results in high-contrast edges and high-resolution image. The microscope is attached to a high-resolution CCD digital color camera (Leica DFC295) with a c-mount interface. It offers a standard resolution of 2048 x 1536 pixels (3 Megapixels) and produces high-quality color images. These components are mounted to an adjustable stand that pivots to provide independent, adjustable vertical angles for two arms holding the microscope/camera and the light source (Figure 4b). The measurement cell and the imaging module are fastened on an anti-vibration air table to minimize image distortion due to the mechanical noises from the environment.

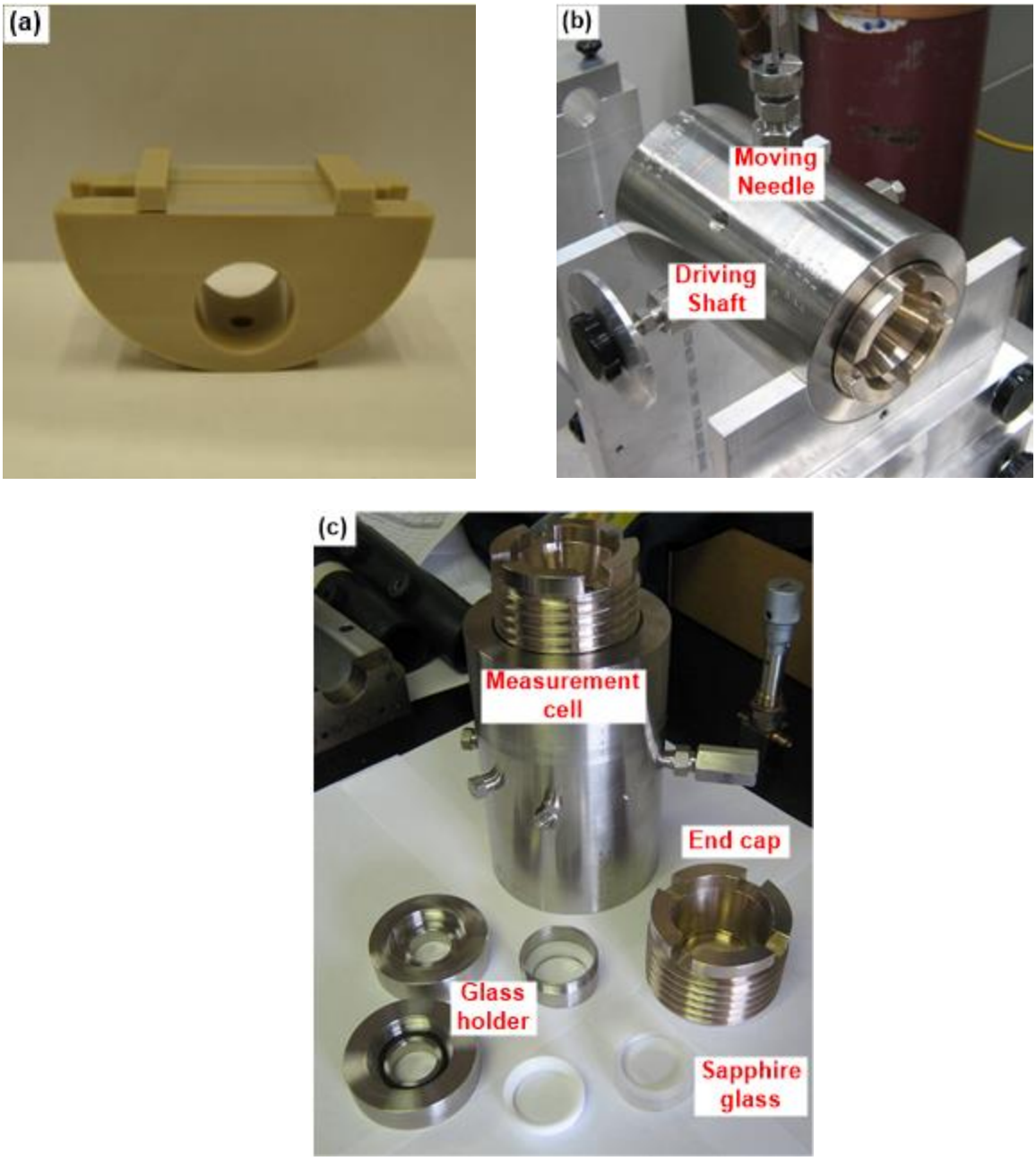

Figure 3: IFT/CA measurement cell: (a) crystal holder, (b) driving shafts, (c) the cell components.

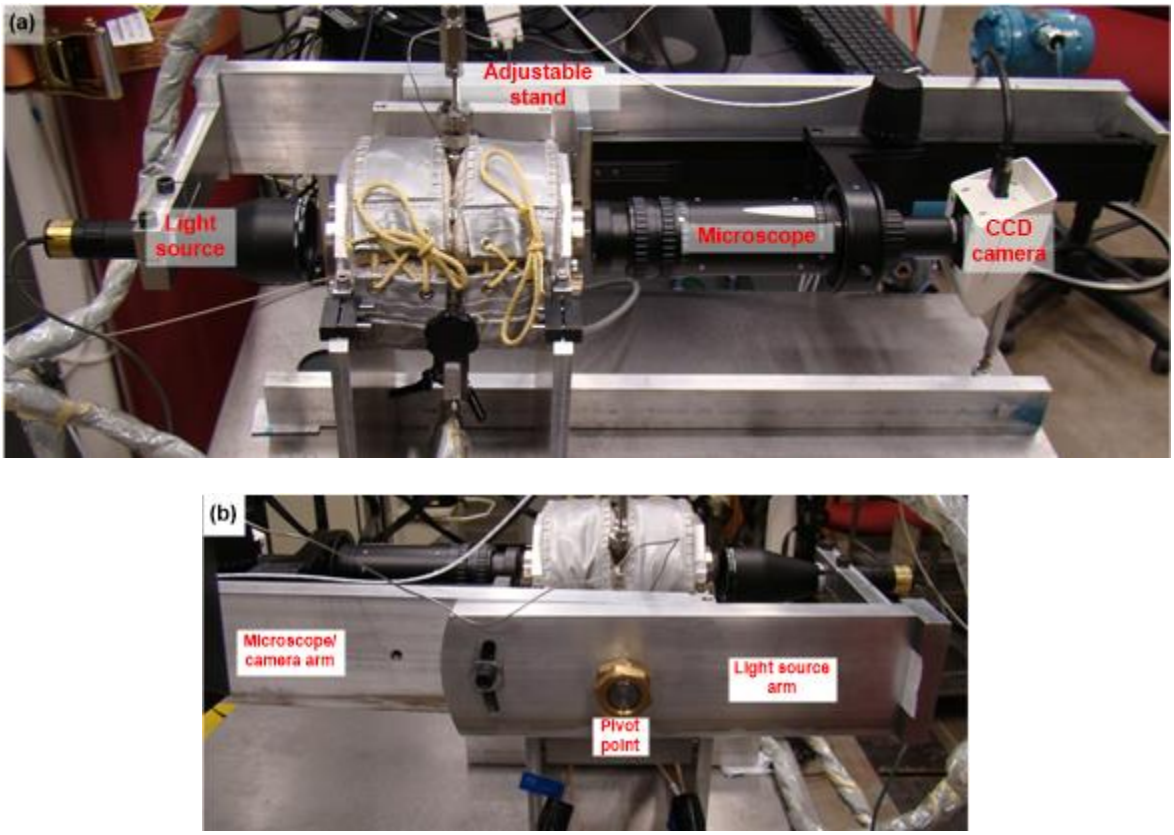

Figure 4: Imaging module: (a) front view, (b) rear view.

Fluid equilibration module

A mechanical convection Yamato oven was modified to accommodate a dual-cylinder pulse-free Quizix pump and a fluid equilibration cell (Figure 5). The pump, made out of Hastelloy C-276, provides precise and stable flow rates and pressures. It is also used for transferring gas or liquid phase to the other parts of the setup and to equilibrate the fluids in the equilibration cell (also made of Hastelloy C-276). The fluid equilibration was performed by retracting the lighter fluid from the top of the cell and injecting it into the bottom of the cell for a given period of time.

Density measurement module

An Anton Paar DMA HPM density meter is used to measure the equilibrium density of phases at elevated pressures and temperatures (Figure 5c). The measurement device is a U-shaped Hastelloy C-276 tube that is excited to vibrate at its characteristic frequency, which depends on the density of the fluid. The density meter was located inside the oven and connected to a Rosemount pressure transducer. The operating specifications for DMA HPM are -10 to +200 °C and 0 to 20300 psi.

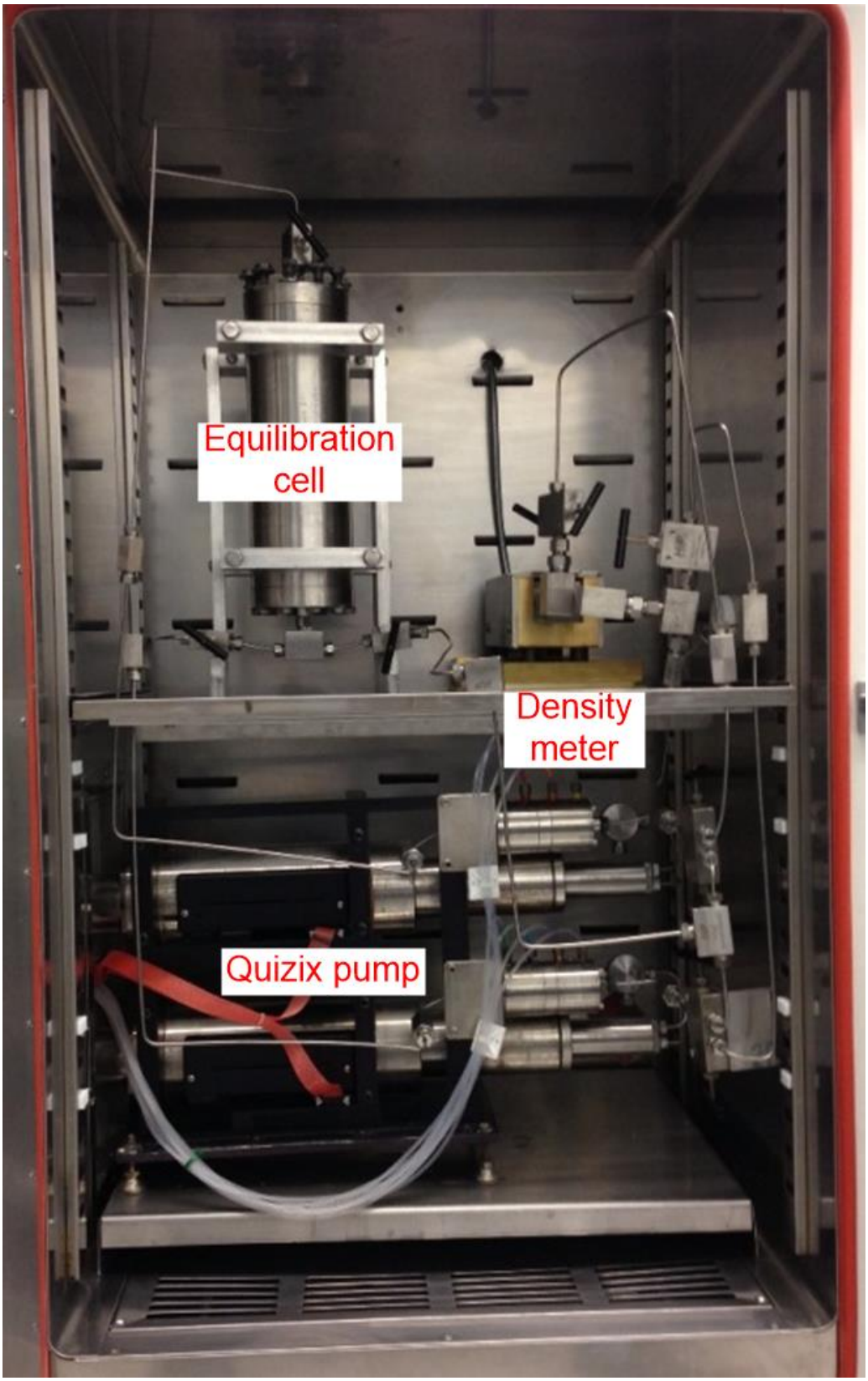

Figure 5: Fluid equilibration module: (a) equilibration cell, (b) Quizix pump, (c) density meter.

Temperature control module

This module consists of a resistance temperature device (RTD) (Figure 6a) sealed in a Hastelloy Sheet (Conax Technologies), heating jackets (Glas-col, LLC) (Figure 6b), and a temperature control system (Figure 6c). The module uses proportional-integral-derivative (PID) control concept (Watlo Electric Manufacturing, Co.) to maintain an accurate and stable temperature inside the measurement cell. There are three parameters involved in the PID controlling: The heat proportional band that is responsible for stability of temperature, the time integral is manipulating the temperature shift to reach to a desired value, and the time derivative that controls overshooting for a new set point. A LabVIEW program, coupled with this control system, was specifically developed to read, plot, and adjust set points for the temperature, the three PID parameters, and to monitor the heat output needed for manual tuning (Figure 7a). The controller was fine-tuned to stabilize the process temperature, reduce the temperature over-shoot, and decrease the time interval to reach a new set point. This fine-tuning procedure allows the temperature inside the measurement cell to stay within ± 0.05 °C of the set-point temperature during the measurements for as long as 10 hours (Figure 7b).

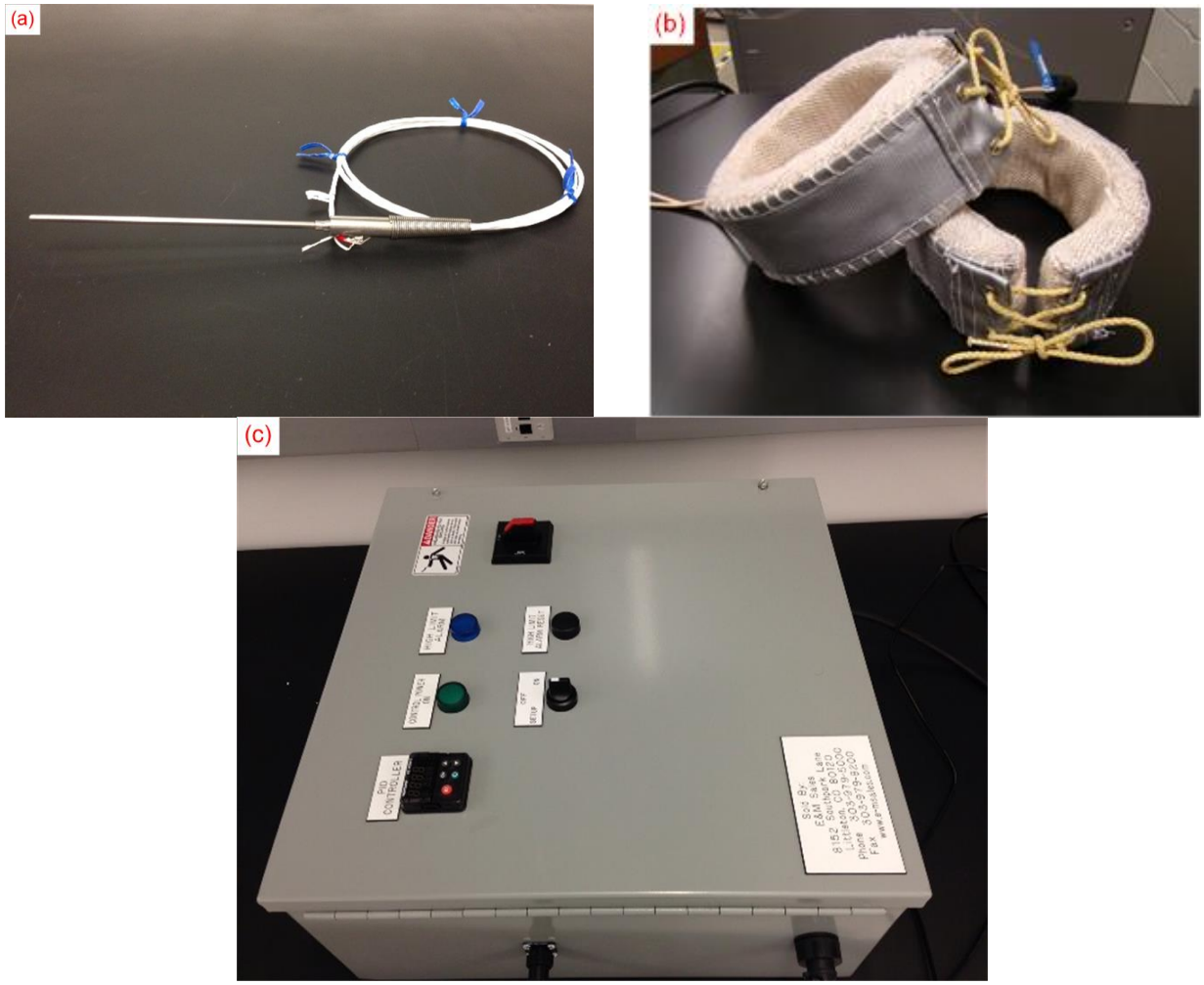

Figure 6: Temperature control module: (a) RTD, (b) heating jackets, (c) temperature control system.

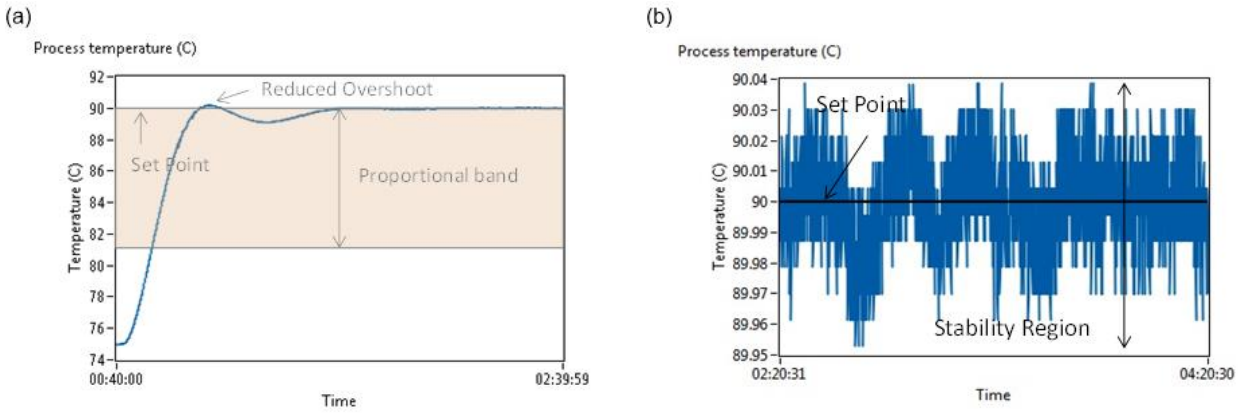

Figure 7: Application of the temperature control module: (a) system response to set point increase from 75 °C to 90 °C, (b) temperature stability.

Data acquisition and analysis module

This includes Leica LAS software, LabVIEW program, and IFT/CA analysis program. These programs were used to capture and analyze images, and to record temperature and pressure. The IFT/CA analysis program uses a well-established method, Axisymmetric Drop Shape Analysis with No Apex (ADSA-NA) to calculate interfacial tension and contact angle simultaneously.

2.1 Substrate preparation

Silicon wafers (Silicon sense, Inc.) and smooth quartz slides (0.5 nm surface roughness, SPI supplies) were diced into 19.3 mm x 15.7 mm rectangular pieces compatible with the crystal holder. Each piece of silicon wafer was coated with a layer of Teflon by spin-coating 3% Teflon solution (AF 1600 solution, DuPont) at 1000 rpm according to a procedure by Tavana et al. [85]. The quartz pieces were used as substrate in the CO_2/water/quartz experiments. All the substrates were handled from their edges with clean tweezers to avoid surface contamination. In order to generate strongly water-wet quartz surfaces, the following cleaning procedure was adopted: (1) the quartz substrates were rinsed with Isopropyl alcohol (HPLC grade, Sigma-Aldrich), (2) they were immersed in sulfuric acid solution (95-98%, ACS grade, Sigma-Aldrich) containing 10% NOCROMIX (Godax Laboratories, Inc.) and sonicated for 30 minutes, (3) the substrates were then soaked inside this solution overnight, (4) they were washed thoroughly with water and boiled in distilled water for about 2 hours, and (5) the quartz pieces were subsequently rinsed and stored inside fresh distilled water. A few minutes before each test, the substrates were dried by absorbing their bulk water (from edges) with a filter paper and then blow-dried with ultra high pure (UHP) nitrogen (instrumental grade, Praxair, Inc.).

2.2 Substrate surface detection

The contact angle is defined as the angle between a tangent line on a drop/bubble profile and the horizontal plane at the substrate surface. Therefore, precise identification of the solid surface position in a sessile drop or captive bubble image is essential for contact angle measurements. The drop/bubble profiles near the solid surface are sometimes fuzzy and obscure especially for systems with very large (>160°) or very small (<20°) angles. Uncertainties in the identification of the exact position of the drop/bubble contact with the solid surface may cause significant errors in measured CA. This is the case for strongly water-wet surfaces such as quartz in CO_2/water/quartz systems with typical contact angles less than 30°. Figure 8a shows a portion of a CO_2 bubble on quartz in water at 500 psi and 35 °C with a contact angle of 9°. Various cut off levels (presumed solid surface) on this bubble image were used to

calculate contact angle with ADSA-NA program. Only a few pixel differences in the cutoff level will change contact angle values significantly as demonstrated in Figure 8b. For example, displacing the solid surface line below the actual solid level (line in Figure 8a) by only 21 pixels (each pixel is about 2.2 x 10^{-4} cm), the contact angle changes 11° (the angle was initially only 9° at line 1). In order to facilitate detection of the substrate surface, the camera was tilted 1-2° with respect to the horizontal line, downwards for sessile drops and upwards for captive bubbles. This procedure allowed the mirror image of the drop/bubble in the substrate to be seen. A simple mathematical criterion was used to determine the cut-off pixel (substrate surface) in all of the images. A few hundred points were considered on the bubble surface near the contact line (BS) together with their mirror image (MI). The substrate surface was defined as the average mid-point between vertically aligned BS and MI points. This algorithm was run on the two sides of the bubble and the two cut-off values were used as input in the ADSA-NA program for contact angle determination.

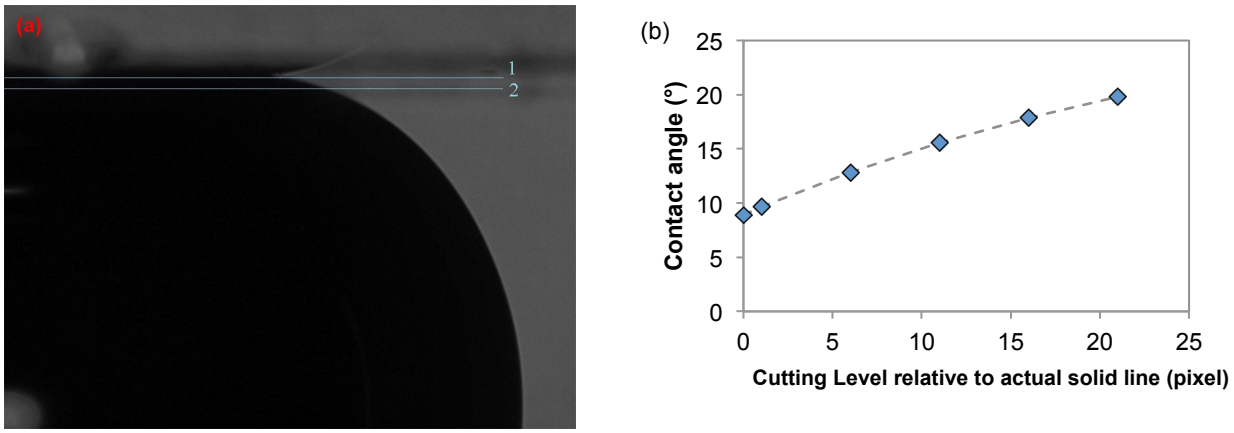

Figure 8: Effect of different cut-off points on contact angle values of a CO_2 bubble in a CO_2/water/quartz system.

2.3 Axisymmetric drop shape analysis with no apex (ADSA-NA)

The IFT/CA analysis program uses well-established shape analysis technique and the Laplace equation of capillarity to calculate the IFT and CA of drops or bubbles. This equation is the balance between surface tension and gravity. It relates the pressure difference across a curved interface to the surface tension and the curvature of the interface:

$$\Delta P = \gamma \left(\frac{1}{R_1} + \frac{1}{R_2}\right), \tag{2}$$

where γ is the interfacial tension between two fluids and R_1 and R_2 are principal radii of curvature in the plane of the paper and in a plane perpendicular to the paper (Figure 9), respectively. The pressure difference is a function of elevation:

$$\Delta P = \Delta P_0 + \Delta \rho g z, \tag{3}$$

where ΔP0 is the pressure difference at a selected reference plane, Δρ is the density difference between two phases, g is the gravitational acceleration, and z is the vertical distance from the reference plane. Assuming an axisymmetric drop/bubble (Figure 9), results in:

$$R_2 = \frac{x}{\sin(\phi)}, \tag{4}$$

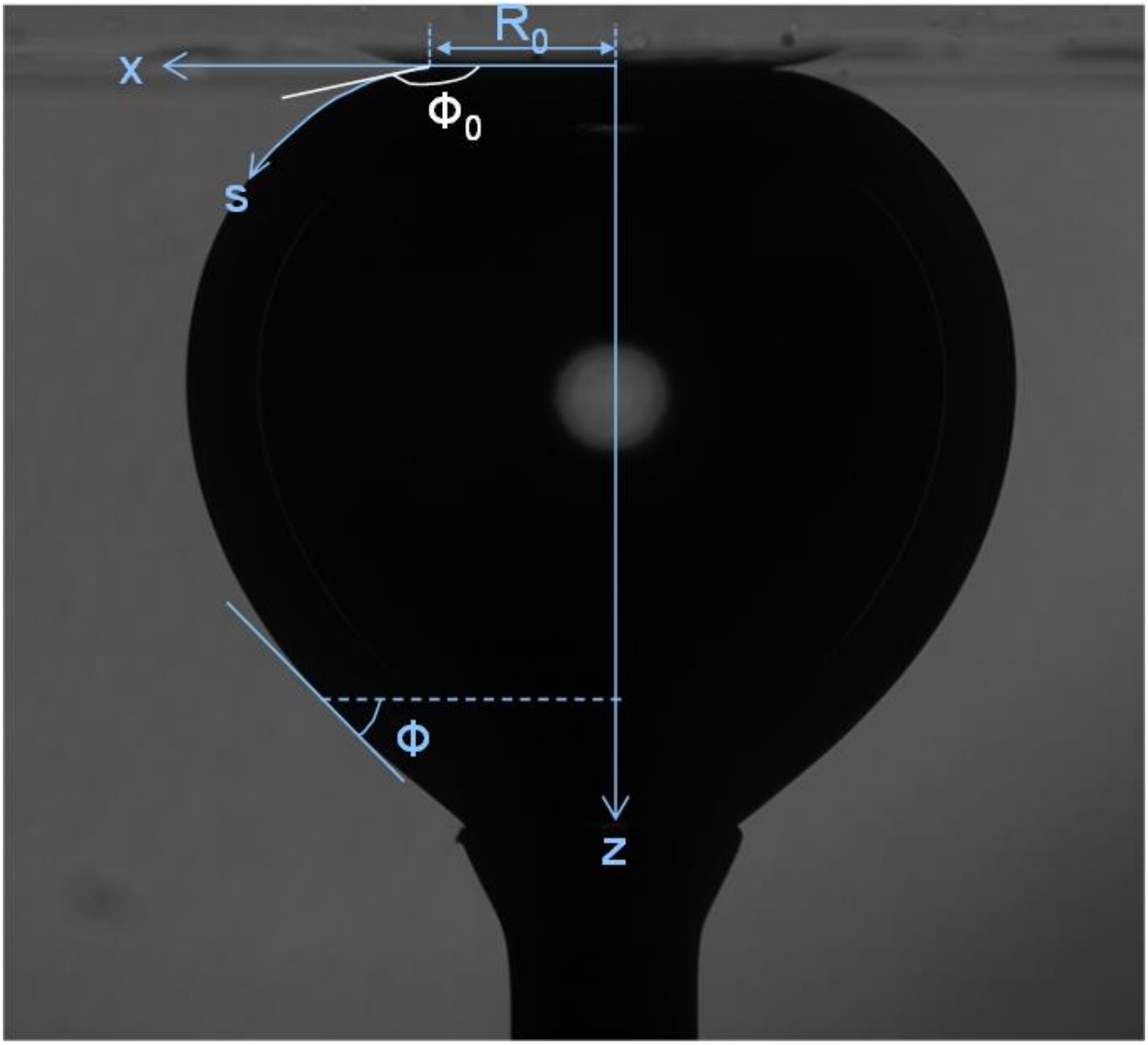

Figure 9: Definition of the coordinate system in Laplace equation for a captive bubble.

Incorporating Equations 3 and 4 in 2:

$$\gamma\left(\frac{1}{R_1}+\frac{\sin(\phi)}{x}\right)=\frac{2\gamma}{R_0}+\Delta\rho g z, \tag{5}$$

where R_0 is the radius of the interface at the origin and φ is the turning angle measured between the tangent to the interface and reference plane. Note that when the reference plane passes through the three-phase contact point, φ is the contact angle (φ_0). Considering s as the arc length measured from the origin:

$$\frac{dx}{ds}=\cos(\phi), \tag{6}$$

$$\frac{dz}{ds}=\sin(\phi), \tag{7}$$

And

$$\frac{1}{R_1} = \frac{d\phi}{ds}, \tag{8}$$

Combining Equations 8 and 5 and rearranging yields:

$$\frac{d\phi}{ds} = \frac{2}{R_0} + \frac{\Delta\rho}{\gamma} gz - \frac{\sin(\phi)}{x}, \tag{9}$$

Equations 6, 7, and 9 and the boundary conditions:

$$x(0) = z(0) = \phi(0) = 0, \tag{10}$$

form a set of differential equations that can be integrated simultaneously to find the value of interfacial tension (γ) and contact angle (φ0).

In axisymmetric drop shape analysis technique, theoretical Laplacian curve is fit to the digitized image of drop/bubble of fluids. A typical calculation procedure is as follows: (1) An image of drop/bubble of one fluid in another is taken (Figure 10a), (2) the profile of a drop/bubble image is extracted using an edge detection method (Figure 10b), (3) the program then fits a theoretical Laplacian curve to the experimental profile extracted from the image assuming an axisymmetric drop/bubble (Figure 10c), (4) The value of IFT is determined from the best match between these two profiles. A recent improvement in shape analysis techniques, Axisymmetric Drop Shape Analysis with No Apex (ADSA-NA), allows IFT/CA calculations without the drop apex information. This means that dynamic contact angles of a drop/bubble can be measured while a protruding needle is attached to it. In this method, first, IFT of the system were calculated by the same procedure as mentioned above except in this case the drop/bubble profile does not have an apex. It then uses the final optimum theoretical profile to find the contact angle at the solid surface level. It has been shown that contact angles can be measured with an accuracy of 0.2° with this method [86]. This technique also allows accurate and simultaneous measurement of IFT and CA of drops/bubbles.

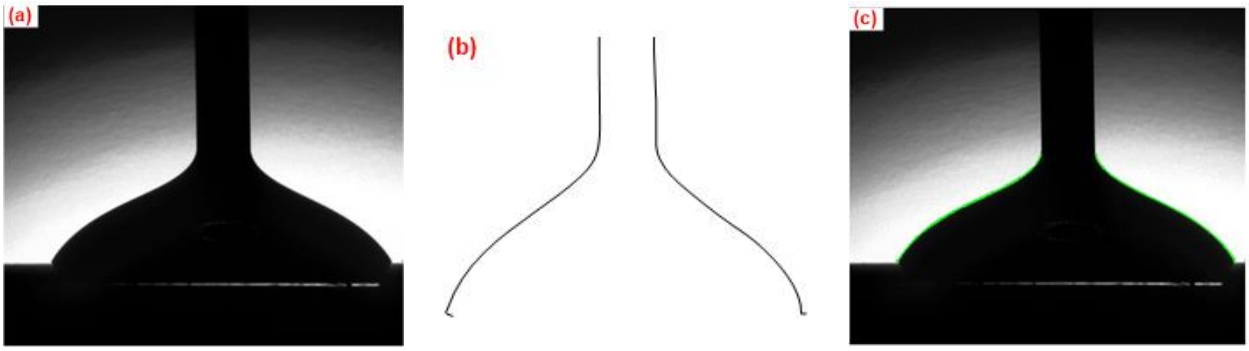

Figure 10: Calculation procedure in ADSA method: (a) drop image, (b) digitized perimeter of the drop, (c) match between the theoretical Laplace curve and the experimental drop image.

2.4 Simultaneous measurement of density, interfacial tension and contact angle

A leak test of the Quizix pump system, equilibration cell, measurement cell, and transfer lines, at experimental temperature and pressure, was followed by an equilibration step in the equilibration cell for about 10-12 hours to produce mutually saturated CO_2 and aqueous phases. All the transfer lines

outside the oven were wrapped with thermocouples, heating tapes, and insulations to monitor and control the temperature of the fluids inside the lines. The density difference between the two equilibrated phases (water-humidified CO_2 and CO_2-saturated distilled water) is one of the required input parameters in the ADSA-NA method for the calculation of IFT and CA. Since the final IFT value is very sensitive to this parameter, the densities of both saturated phases were measured at the same pressure and temperature conditions as the IFT/CA experiments. The density meter was initially calibrated using high purity carbon dioxide and distilled water in the range of 100-5000 psi and 35-100 °C. A minimum of 70 calibration points were measured and recorded for each fluid to maximize the accuracy of the density values. The total deviation in density measurement was less than 0.0005 g/cc. At each experimental condition, multiple samples of the water-saturated CO_2 were obtained from the top of the equilibration cell and transferred to the density measurement unit at a constant pressure and temperature. To complete a series of density measurements under the same experimental condition, several samples of distilled CO_2-saturated water were also taken from the bottom of the cell and analyzed by the density meter.

Prior to IFT/CA measurements, the measurement cell was pressurized with dry CO_2 and the temperature was adjusted to the desired experimental condition. Dry CO_2 was then replaced with water-saturated CO_2 by recycling gases between the two cells (equilibration and measurement) using a Quizix pump. The CO_2-saturated water was then retracted from the bottom of the equilibration cell and injected into the measurement cell at a constant pressure until the solid substrate (quartz) was fully immersed in water. The pressure inside the cell was kept constant using the pump's constant pressure mode during fluid transfer and measurement. The fluids and solid remained inside the measurement cell for about 2 hours before making IFT and CA measurements.

There are two general configurations for conducting IFT/CA measurements: either the solid substrate is immersed in CO_2 and a drop of water is placed on top of it (sessile drop method), or the substrate is immersed in the aqueous phase while a bubble of CO_2 is positioned beneath it (captive bubble method). Both methods were evaluated in this study. In the sessile drop mode, a condensed phase accumulated gradually on the Sapphire windows, which resulted in fuzzy drop images and hence caused a systematic error in the measured contact angles. This effect became more significant at higher pressures and temperatures (supercritical region of CO_2). Due to the heat lost to the outside environment, there was a small temperature gradient from the center of the cell toward the sapphire windows. This gradient caused super-saturation of carbon dioxide phase close to the observation windows and led to water condensation on the windows. The captive bubble method does not exhibit the condensation problem and is in fact more representative of the process that is encountered during the geological sequestration of carbon dioxide in saline aquifers, i.e., the mineral is initially immersed in the aqueous phase before coming in contact with the CO_2 phase. Thus, the captive bubble configuration was selected for our experiments.

The Camera was tilted 1-2° with respect to the horizontal quartz substrate and the magnification was set at 2x. A pedestal-shaped needle with 1.37 mm outer diameter (Figure 11) was used to form a CO_2 bubble beneath the quartz substrate while the needle tip was located 3-4 mm from the quartz surface. With this configuration, it was possible to conduct 3-4 measurements on different parts of the same quartz surface by moving the substrate tray on the crystal holder horizontally (Figure 11a). Each substrate was used only once to avoid any complications due to possible reaction of quartz with fluids. Images of the CO_2 bubble were taken repeatedly while growing the bubble (water receding contact angle) or shrinking it (water advancing contact angle) at intervals of 5-20 seconds. When the CO_2 bubble

is growing and its contact area on the mineral is increasing, water recedes from the quartz surface. Therefore, the angle is called CO_2-advancing angle when measured through the carbon dioxide phase or water-receding angle when measured through the water phase.

When water replaces CO_2 on the solid surface (that is, the CO_2 bubble is shrinking and receding), the measured angle through saturated CO_2 phase is referred to as CO_2-receding angle and the corresponding angle in the aqueous phase is called water-advancing angle (see Figure 11b). The ADSA-NA software was used to calculate both IFT and CA from the same images of captive bubbles [86]. The primary input parameters required for the calculations were the density difference between the phases, acceleration of gravity, scale of the images, and location of the solid surface.

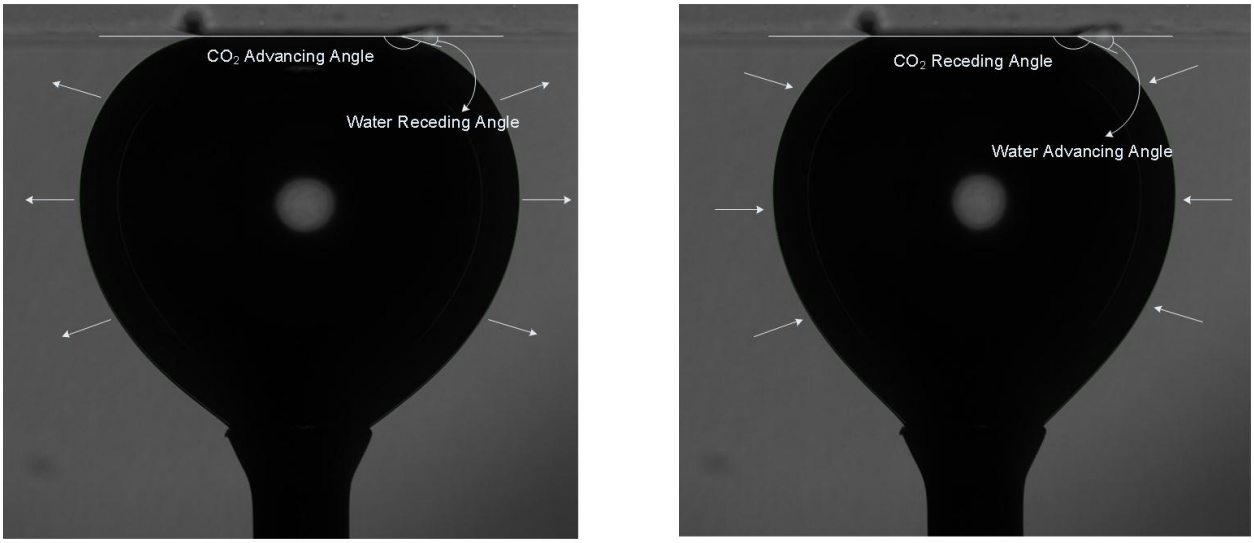

Figure 11: Representative images of supercritical CO_2 bubbles in distilled water at 45 °C and 1700 psi; (a) water receding angle, (b) water advancing angle.

2.5 Water analysis

Carbon dioxide dissolution in water produces carbonic acid, an aqueous solution that becomes more corrosive at high pressures and temperatures [70]. The potential effects of corrosion and dissolution of some metal ions from vessels, valves, and connections in the experimental apparatus, prompted an investigation into whether the test fluids become contaminated during the equilibration or measurement periods. Three water samples were analyzed by Inductively Coupled Plasma (ICP) mass spectrometry (1 part per billion accuracy): (1) freshly distilled water from the all-glass water distiller, (2) a certified HPLC grade de-ionized water (VWR international), and (3) the distilled water after being used to make contact angle measurements. The last sample was equilibrated with CO_2 by re-circulation through the equilibration cell and associated transfer lines for about one week prior to transferring it to the measurement cell for an additional 10 hours of measurement. The Hastelloy C-276 re-circulation system also contained some stainless steel valves and fittings. Figure 12 shows ICP results for the distilled water, the HPLC grade de-ionized water, the CO_2 equilibrated water, and typical chemical compositions of Hastelloy C-276 and stainless steel. We found that the distilled water quality from an in-house all-glass water distiller (in terms of dissolved ion concentrations) is comparable to the certified HPLC grade de-ionized water purchased from VWR international (Figure 12a). Moreover, the

concentrations of ions in the equilibrated water (less than 1 ppm in total) are slightly higher than those in the distilled water (Figure 12b). This was probably caused by the dissolution of metallic components in the system into the CO_2 equilibrated water (Figure 12c). However, this insignificant amount of total ion concentration is not expected to have a significant effect on IFT and CA values reported in this study.

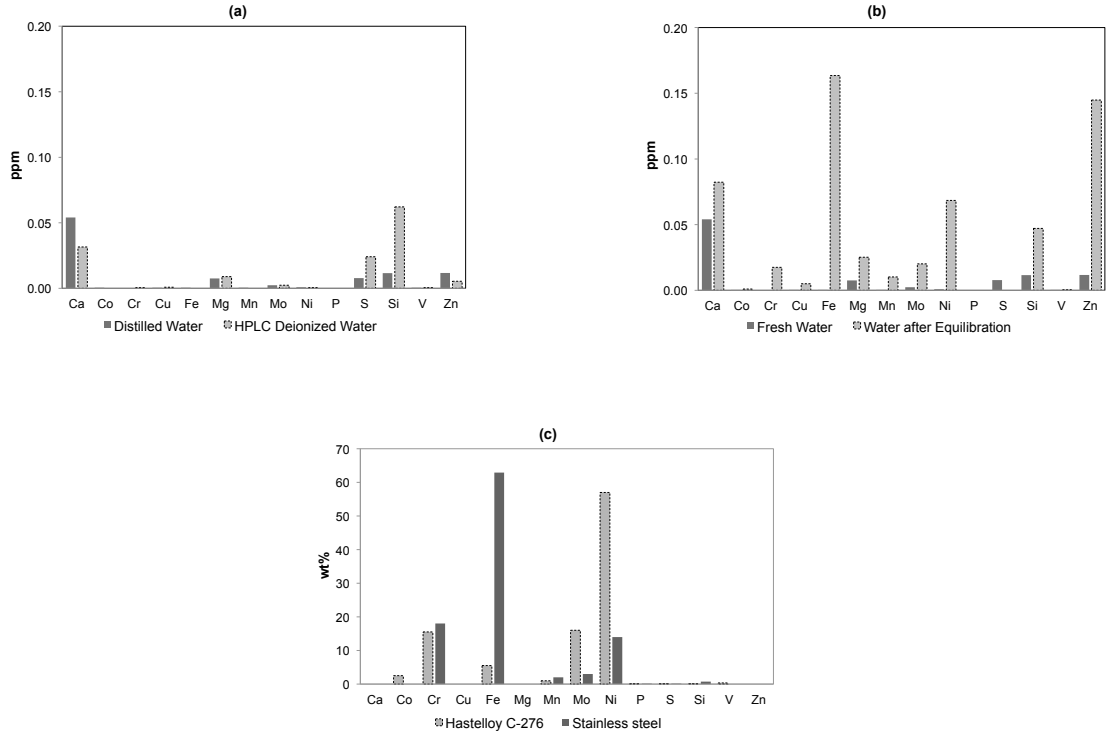

Figure 12: ICP analysis of water samples and typical elemental composition of Hastelloy C-276 [87] and stainless steel [87].

3 Validation

The n-decane/air/Teflon system was selected for contact angle validation purposes because Teflon has a lower surface energy than quartz and it is less sensitive to contamination. Prior to measuring contact angles, a freshly prepared Teflon-coated solid substrate was mounted on the crystal holder inside the measurement cell and the camera angle was set to 2° above the solid surface. The liquid was slowly injected through either a straight or pedestal-shaped needle at ambient condition until a symmetric drop touched the Teflon surface. At this point the flow rate was further reduced to a low, fixed value. Multiple images of the drop contacting the Teflon-coated surface were automatically taken every 20 seconds as the drop size increased (advancing) or decreased (receding) by injection or retraction of n-decane.

Three sets of experiments were conducted in this study to validate our experimental setup and procedures, and to check the reproducibility of CA measurements. Table 1 lists the selected parameters and results for each test. The first series, V1-3, investigated the effect of drop advancing rate on the

advancing contact angle. Three different flow rates were selected in a way that the advancing rate of the contact line in all the tests was smaller than the proposed critical value i.e., 5 mm/min [79]. It has been shown that if the rate of motion of the three-phase contact line is above the critical value, dynamic contact angles will be affected by viscous forces [79]. There is a good agreement between the measured contact angles (Figure 13) and the average value reported in the literature 59.43°± 0.02 [86]. This result indicates that small changes in flow rate do not affect the contact angle values.

The second series, V4-6, evaluated the effect of decrease in needle size and image resolution on the contact angle results. The flow rate was kept constant to check the reproducibility of the data. Three pairs of advancing-receding contact angles were measured from this series. Figure 14 depicts the advancing/receding contact angles and contact radius of an n-decane drop on the solid substrate versus time for Test V5. The results confirm the reproducibility of CA measurements. In the third series, V7-8, the straight at-ended needle (Figure 15a) used in the first two series, was replaced with a pedestal-shaped needle (Figure 15b and c). The latter needle helps to generate a well-deformed (symmetric) drop and improves the accuracy of interfacial tension in simultaneous measurement of CA and IFT [86]. The difference between the last two tests (V7 and V8) is the clearance between the needle tip and the solid surface. The clearance for Test V7 was small (2.08 mm), but the clearance was increased for Test V8 (3.10 mm) to make the drop well stretched. Figures 15b and c show the needles and drops for these two tests. It is evident that the second drop is well deformed. The measured angles from this test are shown in Figure 3.20. The comparison of the results between the first two series and the last one demonstrates that the pedestal-shaped needle reduced the standard deviation for CA measurement. Also, a well-deformed drop can produce IFT value that is comparable to the literature value (23.70 mN/m [86]).

Table 1- Specification and results for validation tests.

Test	Magnification	Flow Rate (cc/min)	Needle OD (mm)	Advancing CA	Receding CA	IFT (mN/m)
V1	1.6x	0.001	1.194	59.55 ± 0.21	NA	NA
V2	1.6x	0.0001	1.194	59.48 ± 0.11	NA	NA
V3	1.6x	0.0005	1.194	59.66 ± 0.07	NA	NA
V4	1.25x	0.0005	0.838	59.51 ± 0.33	52.86 ± 0.26	NA
V5	1.25x	0.0005	0.838	59.36 ± 0.31	52.86 ± 0.40	NA
V6	1.25x	0.0005	0.838	59.45 ± 0.37	53.28 ± 0.29	NA
V7	1.25x	0.0005	3.220	59.78 ± 0.24	53.39 ± 0.22	22.84 ± 0.33
V8	1.25x	0.0005	3.220	59.34 ± 0.09	53.29 ± 0.24	23.96 ± 0.28

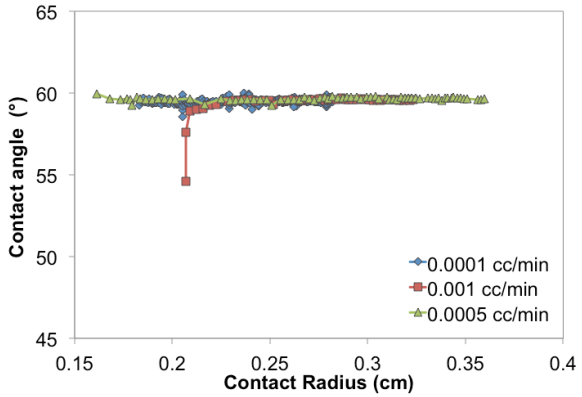

Figure 13: Advancing contact angles during Tests V1-V3.

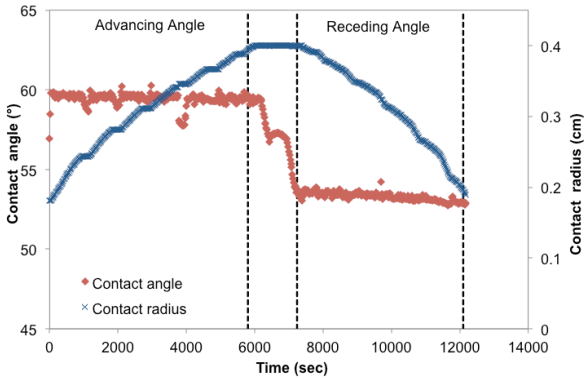

Figure 14: Advancing and receding contact angles during Test V5.

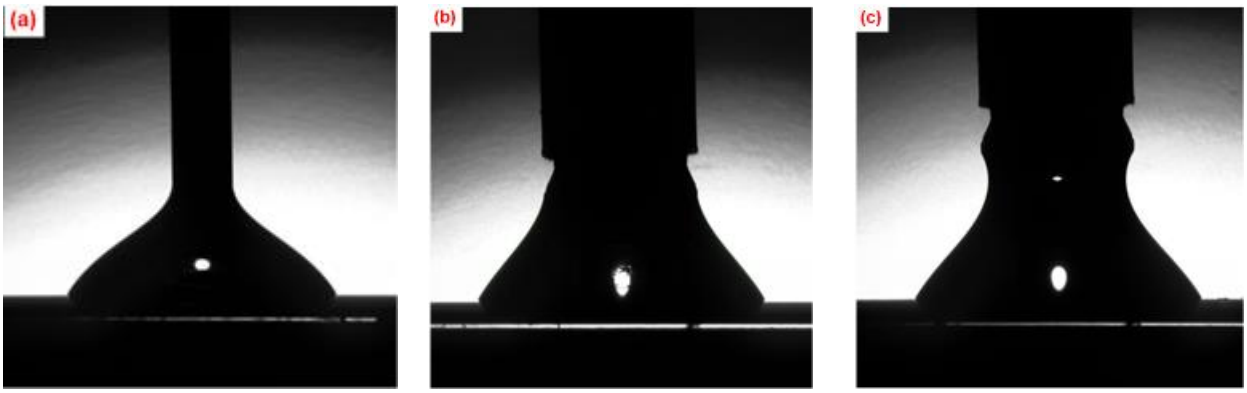

Figure 15: Different needles used in the validation experiments: (a) straight needle (TestV5), (b) pedestal-shaped needle with low clearance (Test V7), (c) pedestal-shaped needle with high clearance (Test V8).

4 Results and Discussions

There are two sets of experiments performed in this study to investigate the effect of pressure, temperature, brine salinities and co-contaminant in CO_2 phase on densities, interfacial tensions, and dynamic contact angles of the mutually saturated fluids. In the first set (Series A), the controversial concept of wettability alteration of quartz surfaces in the presence of supercritical CO_2 was systematically investigated. For this purpose, pure distilled water was used as aqueous phase and the effect of CO_2 phase change from subcritical to supercritical at pressures ranging from 500 to 1700 psi and temperatures ranging from 35 to 60 °C were studied. Also, wettability was assessed by measuring apparent water advancing and receding contact angles. The apparent contact angle is defined as the angle of the macroscopic meniscus when extrapolated to zero thickness of the thin film [88], [89]. In the second set (Series B) densities, interfacial tensions, and dynamic contact angles of mutually equilibrated brine and CO_2 phases on quartz surface were measured at reservoir conditions. Measurements were performed at different pressures (2000-4000 psi), temperatures (50-100 °C), and brine salinities (0.2 to 5 M) that are practical for carbon sequestration in deep saline aquifers, which were not explored in the past. The effect of SO_2 co-contaminant (0-6 wt.%) on these parameters was also investigated and possible implications on different CO_2 trapping mechanisms were discussed.

4.1 Natural wettability of quartz surface

The effect of surface contamination on contact angle measurements in CO_2/brine/quartz systems was first addressed in a communication between Bikkina [73], [74] and Mahandavan [75]. Later, Saraji et al. [71] pointed out the possibility of contamination as a major source of discrepancy in the reported contact angles for such systems. They proposed an extensive substrate cleaning procedure, storage in distilled water before use, and drying the surface with ultrahigh-purity Nitrogen as necessary steps to avoid surface contamination. Most recently, Iglauer et al. [76] investigated the effect of cleaning procedure on contact angle of CO_2/brine on quartz/glass surfaces and concluded that inappropriate cleaning methods could result in artificially high contact angles. They reported relatively low contact angles (0-30°) for clean surfaces, which is consistent with the values reported by Saraji et al. [71]. However, using oxidizing solutions such as Piranha [76] and NOCROMIX in sulfuric acid solution [71] may cause hydroxylation of the quartz surface and hence change its wettability. Therefore, it is important to understand the natural wettability of quartz surface at conditions relevant to carbon sequestration before coming into contact with CO_2 phase.

The previous studies on the surface chemistry of silica suggest that the wettability of silica surface is largely determined by the arrangement and distribution of surface groups such as silanol (Si-OH) and siloxane (Si-O-Si) [77], [78]. For instance, a recent molecular dynamics simulation study reported approximately 10° increase in contact angle by increasing the silanol surface density on quartz from 1.7 to 4.5 (OH/nm^2) [64]. The reason for this behavior is the preferential adsorption of water molecules on hydrophilic silanols rather than hydrophobic siloxanes [77]. Moreover, thermal treatment of silica at very high temperatures (> 400 °C) is shown to cause dehydroxylation of its surface, meaning conversion of silanols to siloxanes [78]. For example, Horn et al. [79] reported a relatively high contact angle (i.e. 45 °) on freshly prepared high-purity silica surface by the melting method (the melting point of silica is around 1600 °C). In contrast, soaking silica in water is believed to result in rehydroxylation of silica surface [78]. This process is exceedingly slow at 25 °C, and it is recommended to heat silica in water at 95 °C for several hours to rehydroxylate the surface [77]. This is also in accord with the reported water contact angles on hydrophilic quartz/glass surfaces (< 10°) measured by different methods such as Wilhelmy plate [80], capillary rise [81], and sessile drop [82].

Therefore, the surface of quartz minerals in contact with aquifer at subsurface conditions, in extended geological time scales, is expected to be hydroxylated. Although one can argue that the quartz grains in reservoir rocks are partly covered by omnipresent clays, the clean pure hydroxylated quartz surface (strongly water-wet) provides a practical baseline for fundamental research on fluid-mineral interactions during geological sequestration of carbon dioxide.

4.2 Effect of supercritical CO_2

The density of equilibrated pure water and carbon dioxide were measured at twelve different conditions in Series A measurements. Results from multiple consecutive measurements showed that the density values became stable after a short time and final values were comparable to the expected equilibrium values. The final results are listed in Table 2. A comparison between the density data measured in this study and those available in the literature is presented in Figures 16a and b. The density of both phases increases with pressure and decreases with temperature. Also, the IFT measurements in this study were performed at least three times under each experimental condition and the results are listed in Table 2. There are two groups of IFT values reported for each temperature and pressure condition in this Table. The first group, called IFT_{ind}, was measured independently using a regular rising bubble technique and analyzed by ADSA method. These data are provided here for comparison purposes only. The second group, called IFT_{dep}, was calculated simultaneously during contact angle measurements using ADSA-NA

method. The IFT_{dep} results at various temperatures and pressures are plotted in Figure 17. This Figure shows that the measured interfacial tensions are comparable to the literature values (shown in the same Figure) and follow the same trend, i.e., sharp decrease with pressure increase in the subcritical region and then stabilization of IFTs in the supercritical region. Additionally, IFT_{dep} is comparable to IFT_{ind} within 1-2 mN/m (see Table 2). However our IFT_{dep} data are valid only during water receding angle measurements.

Figures 18b and 19b show a clear decrease in IFT_{dep} during water advancing angle measurement that is more pronounced at HPHT conditions. This behavior did not occur during the validation experiment (Tests V7 and V8 in the Validation Section) for n-decane drops on Teflon surface. Several plausible explanations can be provided to elucidate the decrease in IFT_{dep} during water advancing angle measurements (as seen in Figures 18b and 19b). The first one is the possible reaction between CO_2 and Silanol groups on the quartz surface that leave some reaction products on the surface. When the bubble is retracting, these products may detach from the solid and adsorb on the bubble and thus alter the interfacial tension. However, we performed Scanning Electron Microscopy (SEM) tests on a few quartz samples that were contacted with CO_2-saturated water and water-saturated CO_2 at pressures and temperatures used in this study. There was no visible physical heterogeneity on the surface in the scale of 10 nm (the resolution of SEM instrument) that does not support a change in solid surface due to reaction between CO_2 molecules and quartz surface. In addition, chemical reaction between Silanol groups and CO_2 molecules is not well supported in the literature. Another explanation for the observed IFT decrease might be due to the rate of three-phase contact line movement during the CO_2 phase retraction. Neumann et al. [79] pointed out that dynamic effects possibly deform the shape of the bubble so that the underlying Laplace equation is no longer valid. In this case, ADSA-NA responds by finding an IFT value that satisfies the error function regardless of the validity of Laplace equation. Although the rates of bubble contact line motion were less than 0.1 mm/min in this study, the rate of water advancing was slightly higher than water receding. For example, the rate of the test shown in Figure 19 was 0.04 mm/min during the water advancing angle and 0.06 mm/min during the water receding angle measurement. This may explain why we only see dynamic effects in the water-advancing zone. Moreover, this effect is more pronounced in Figure 19b than in Figure 18b possibly because higher density fluids (supercritical CO_2) have much more momentum (dynamic effects) than lower density fluids (gaseous CO_2). It should be noted that although the software gives erroneous IFT values in the water-advancing zone, these values would not affect the water advancing contact angles. As explained earlier, ADSA-NA utilizes the final optimum theoretical profile, regardless of the actual IFT value, to find the contact angle at the solid surface level. It was discussed previously that a pedestal-shaped needle facilitates interfacial tension calculation while measuring contact angle. This type of needle also generates stable bubbles for measuring both water advancing and receding contact angles. Therefore, a pedestal-shaped needle with 1.37 mm outer diameter was used for all the measurements in this section.

Figure 18 shows a series of contact angle images spanning over 100 to 2050 seconds of a CO_2 bubble at the gaseous state (500 psi and 35 °C). The computed contact angles in Figure 18a reveal a water receding and advancing angle of 8° and 12°, respectively. Also in Figure 19a, which presents the same measurement for a supercritical CO_2 bubble at 1700 psi and 60°C, the water receding and advancing angles are 13° and 30°, respectively. The results for other temperatures and pressures are summarized in Table 2. The standard deviation for these measurements was typically ±1°. All the contact angle data at various temperatures and pressure are plotted in Figure 20. The critical pressure of CO_2 is about 1070 psi, shown as vertical lines in this Figure. Therefore, these isotherms undergo phase change from the subcritical fluid (gas) to the supercritical fluid. The contact angles are almost constant in the subcritical

region for all of the isotherms suggesting that small pressure changes in this region do not have any significant effect on the wettability of quartz surface. However, there is a jump in the contact angle values across the CO_2 phase change line, which is more pronounced in the water advancing than receding angles. Figure 20b shows that only the isotherm at 60 °C follows this behavior and any change in the angles on the other two isotherms are within the experimental error range. Similar to the subcritical region, in the supercritical region there is no significant change in the contact angle with pressure increase. The temperature had the same effect on the contact angles of CO_2 bubbles on quartz surface. Both water advancing and receding contact angles increased with increasing temperature except for the receding angles at the subcritical region where changes in the contact angles are within the experimental error. One reason for this behavior may be the inability of the Axisymmetric drop shape analysis technique to measure extremely small angles (< 10°), as stated by Neumann et al. [79]. The last column in Table 2 lists the contact angle hysteresis (that is, differences between advancing and receding angles). This quantity follows the same behavior as the water advancing angles since the receding angles were not changing significantly. For instance, the contact angle hysteresis was about 20° at the highest pressure and temperature (1700 psi and 60 °C) compared to only 2-3° at 500 psi and 35 °C. The contact angle data measured in this study can be used to interpret the wettability of the quartz surface in contact with carbon dioxide. The water advancing contact angle typically increases by 7-10° from the subcritical to supercritical CO_2 region. There is also a slight increase in the receding angle at 60 °C, which is in accord with reports by Chiquet et al. [93] and Broseta et al. [66] Surprisingly, this change is not gradual but rather steep around the phase change region. Jung and Wan [94] and Farokhpoor et al. [65] also observed a sudden increase in the equilibrium contact angles at the phase change region.

Table 2- Density, interfacial tension, and dynamic contact angles of CO_2/pure water/Quartz system.

Test	Pressure (psi)	Temperature (°C)	ρ_{CO2} (kg/m^3)	ρ_{H2O} (kg/m^3)	$\Delta\rho$ (kg/m^3)	IFT_{ind} (mN/m)	IFT_{dep} (mN/m)	θ_a (°)	θ_r (°)	$\Delta\theta$ (°)
A1	1700	60	412.9	997.2	584.3	31.16 ±0.45	33.28 ±0.24	30.38 ±0.37	13.23 ±0.85	17.14
A2	1300	60	233.4	995.4	762.0	31.98 ±0.06	33.73 ±1.04	34.03 ±1.49	11.24 ±1.04	22.79
A3	900	60	130.1	992.3	862.2	42.31 ±1.99	42.96 ±0.57	22.97 ±1.06	8.22 ±0.91	14.76
A4	500	60	62.5	988.6	926.1	50.78 ±1.00	52.47 ±0.42	20.59 ±0.53	9.08 ±1.47	11.51
A5	1700	45	645.4	1004.3	359.0	NA	31.35 ±0.49	24.63 ±1.14	9.43 ±0.73	15.20
A6	1300	45	332.3	1002.8	670.5	NA	34.59 ±0.17	25.22 ±2.17	10.14 ±0.40	15.08
A7	900	45	147.9	999.9	852.0	NA	41.09 ±0.27	12.61 ±1.37	8.84 ±0.86	3.77
A8	500	45	66.2	995.4	929.2	NA	51.67 ±0.16	16.12 ±0.46	9.11 ±0.61	7.01
A9	1700	35	762.2	1011.5	249.3	32.29 ±0.39	32.68 ±0.54	19.47 ±2.17	8.58 ±0.97	10.90
A10	1300	35	661.3	1010.4	349.2	32.84 ±1.00	31.16 ±0.24	18.13 ±0.91	7.93 ±1.28	10.20
A11	900	35	170.1	1007.9	837.8	38.26 ±0.56	39.40 ±1.45	11.91 ±0.62	9.05 ±0.84	2.86
A12	500	35	71.5	1003.3	931.7	51.09 ±0.52	50.62 ±0.27	12.11 ±1.09	8.22 ±0.65	3.89

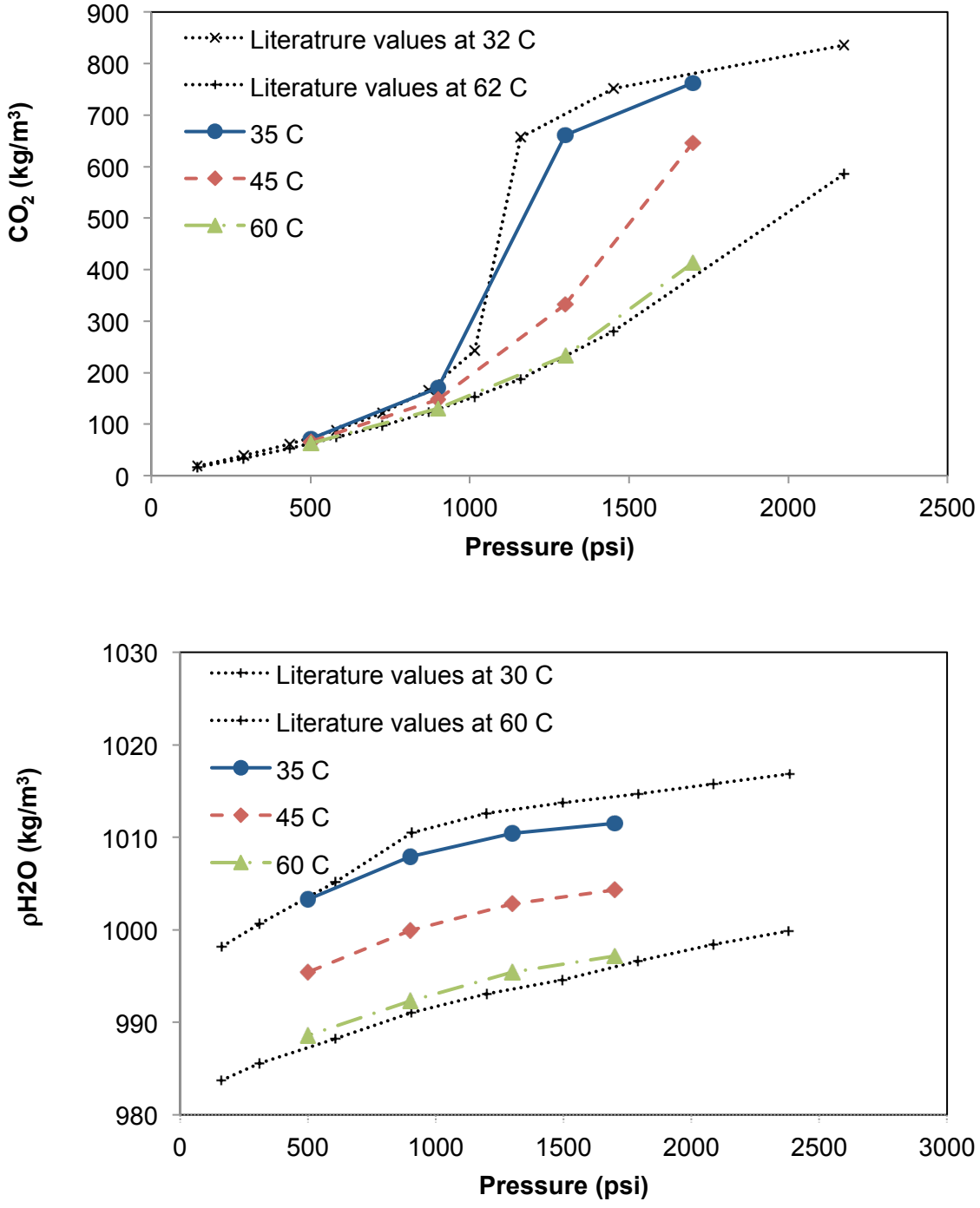

Figure 16: Comparison between density values measured in this study with values reported in the literature: (a) water-humidified CO_2 phase density [90], (b) CO_2-saturated water phase density [91].

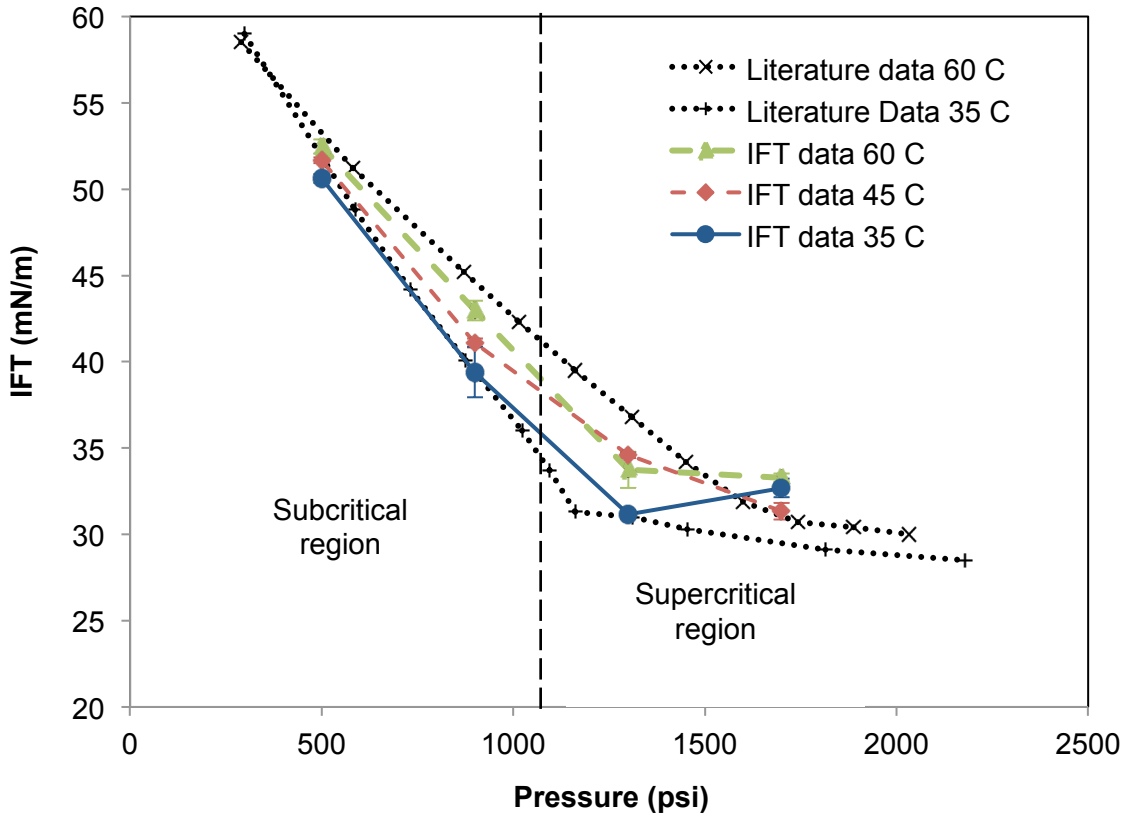

Figure 17: Comparison of IFT results with literature values [92].

This suggests that, in the presence of supercritical carbon dioxide, the wettability of quartz surface is altered towards less water-wet conditions. The water advancing and receding contact angles did not change significantly in the supercritical region ranging between 1300-1700 psi. It is generally believed that once the temperature is above the critical point of CO_2 (≈ 31 °C), the temperature does not have any prominent effect on the wettability of minerals. However, this study shows that increasing temperature from 35 °C to 60 °C leads to an increase of water advancing and receding contact angles by 10° and 4°, respectively. These results indicate less water-wet quartz surfaces at higher temperatures in both supercritical and subcritical regions. Several explanations have been proposed for the observed wettability change of quartz or glass surfaces in contact with supercritical CO_2 [57], [93], [95]. Dissolution of carbon dioxide in water can reduce the pH values from 7 to 3 [93]. The surface charge of silica particles is sensitive to the water solution pH. It is negative at pH = 7 and reduces to almost zero at pH = 3 [96]. Therefore, the electrostatic repulsions due to electric double layer effects that are responsible for the stability of water films will reduce [97], [98]. The effect of pH on the thickness of water films confined between CO_2 and rock mineral was studied by Tokunaga through a theoretical calculation of DLVO theory [96] Chiquet et al. [93] suggested that this effect causes alteration of surface wettability and hence an increase in contact angle. In addition to the pH effect, there may be other interactions between CO_2 and quartz that promote changes in surface wettability. For example, capping of the Silanol groups on quartz surface by CO_2 molecules through physisorption was proposed by Dickson et al. [57] or hydrogen bonding of supercritical CO_2 molecules with the Silanol groups was suggested by Vishnyakov and co-workers [95]. These proposed reactions can deter the water-wetness of quartz by reducing the interactions between water molecules and SiO groups on the quartz surface.

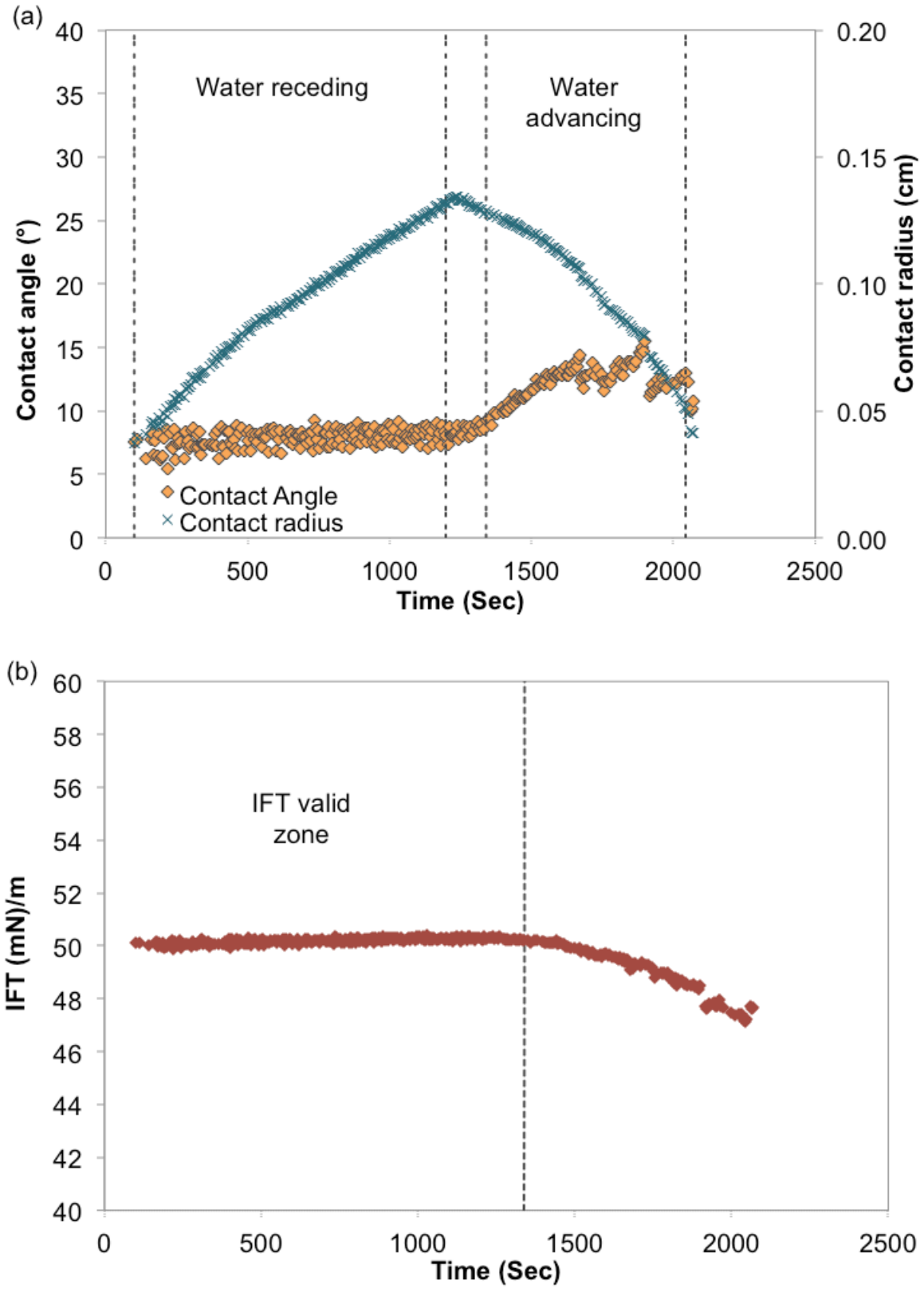

Figure 18: Contact angle, radius (a) and IFT (b) results for CO_2 bubble on quartz in water at 500 psi and 35 °C.

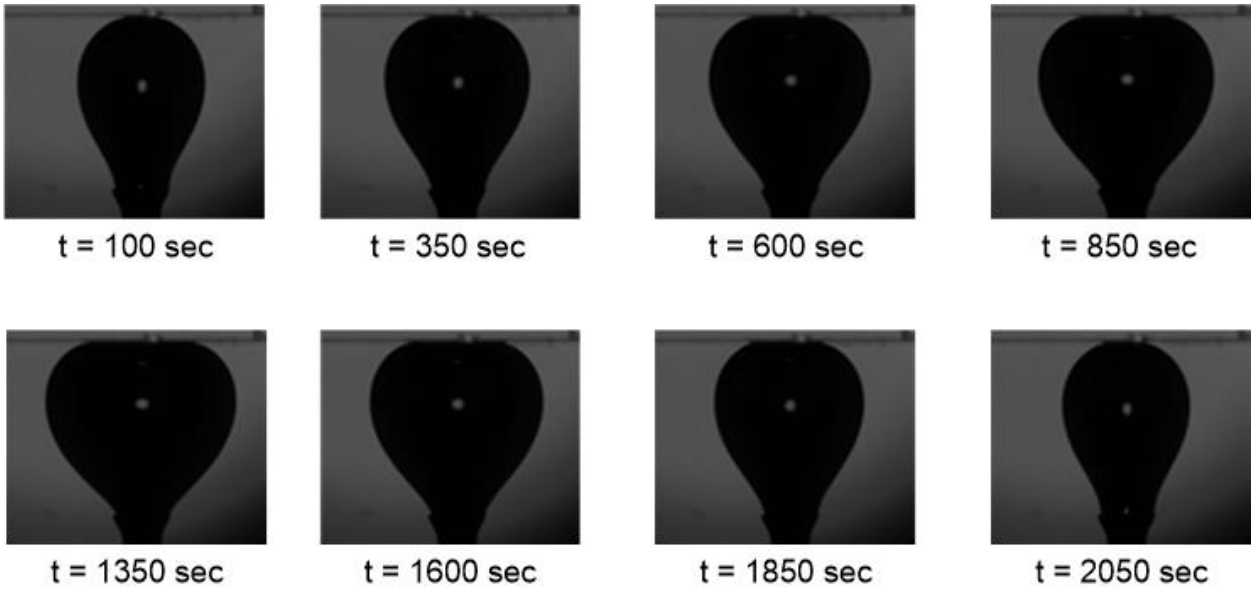

Figure 18: Continued.

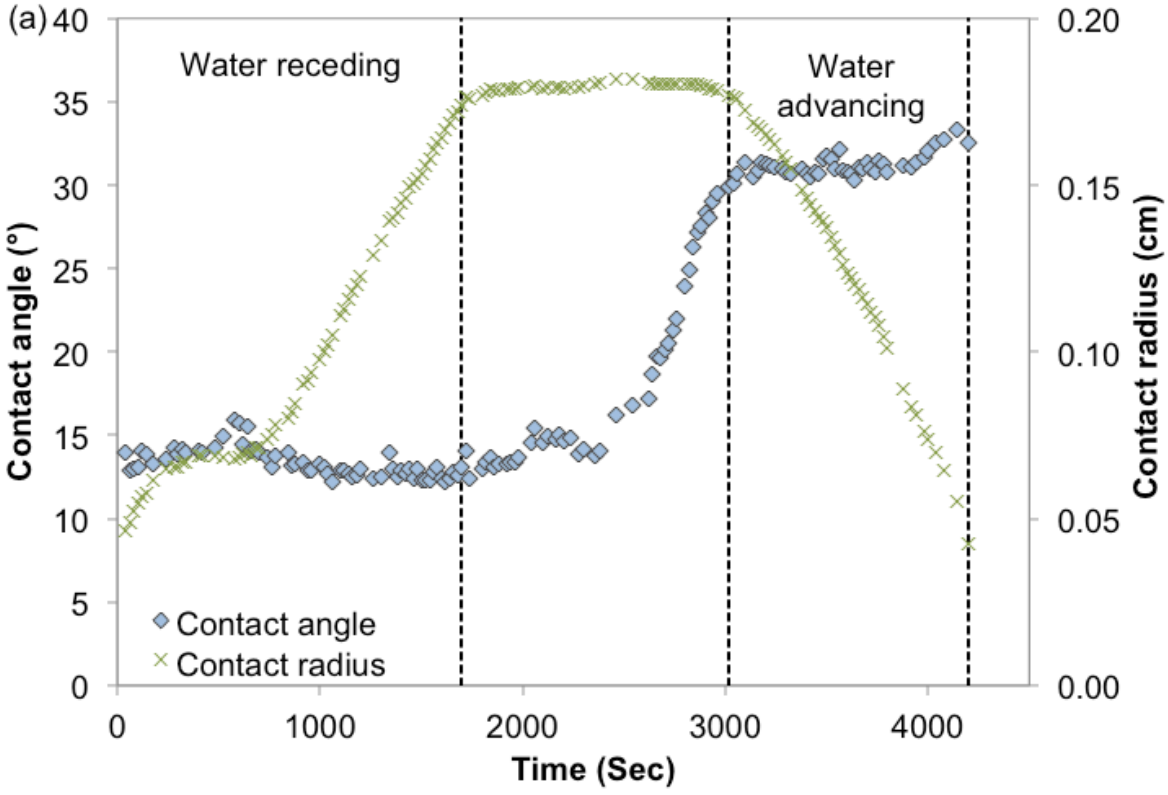

Figure 19: Contact angle, radius (a) and IFT (b) results for CO_2 bubble on quartz in water at 1700 psi and 60 °C.

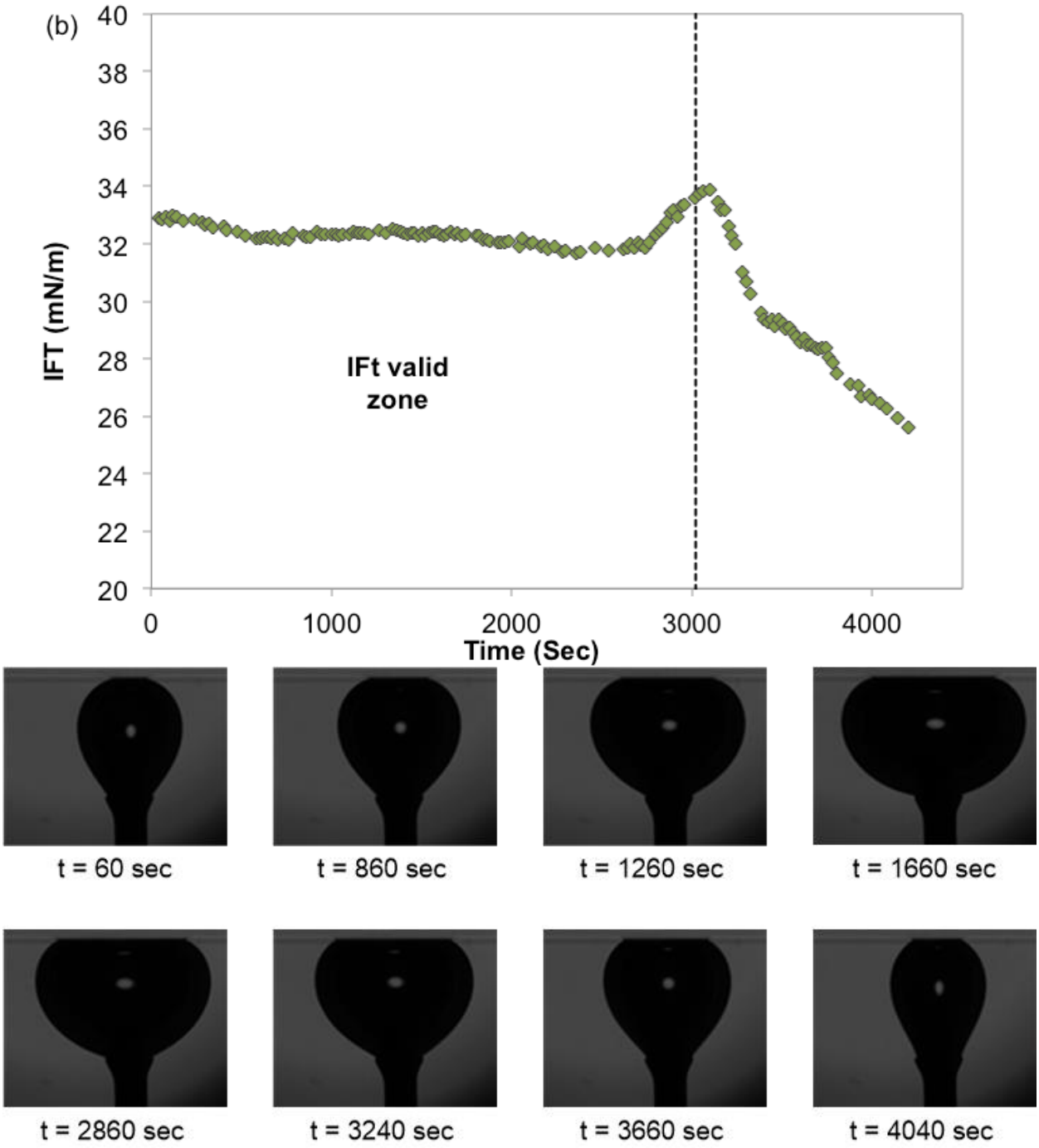

Figure 19: Continued.

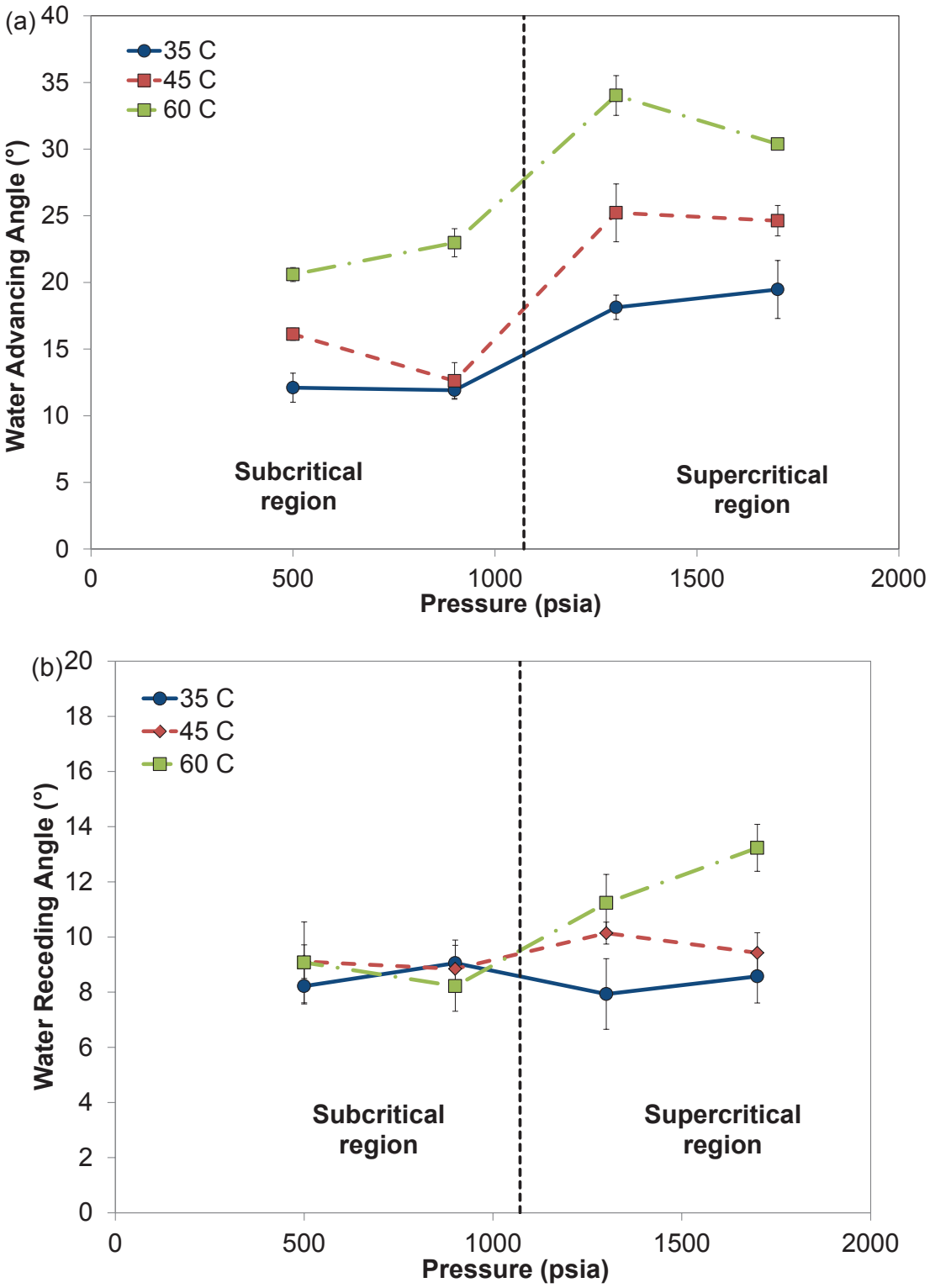

Figure 20: Effect of pressure on water advancing (a) and receding (b) contact angles.

4.3 Effect of Pressure and Temperature

The pressure and temperature ranges used in Series B are 2000-4000 psig and 50-100 °C, respectively, as shown in Figure 1. Experiments were performed at nine different conditions, all with a brine salinity of 1 M. Because brine is largely incompressible in the pressure and temperature range of these experiments, its density was not affected by pressure change; although it slightly decreased when temperature was increased (Figure 21a). On the other hand, supercritical carbon dioxide (sc-CO_2) is a compressible fluid and its density increased with increasing pressure and decreased with increasing temperature (Figure 21a). The interfacial tension between equilibrated CO_2-rich and aqueous phases at various temperatures and pressures are plotted in Figure 21b. As shown in this figure, variations in pressure did not have a significant effect on the IFT, but an increase in temperature slightly reduced the IFT values. Figure 22a shows the experimental CO_2 solubility data in 1M brine and its variations with P and T reported in Koschel et al. [99]. The relative insensitivity of IFT to P and T in the supercritical region of CO_2 may stem from the fact that the solubility of CO_2 in brine (1M) does not drastically change in the P and T ranges studied here. Similar to the IFT data, the dynamic contact angles also did not change drastically with P and T (Figure 21c). There was only a slight increase in the water angles and contact angle hysteresis ($\Delta\theta$) by the increase in pressure (the last column of Table 3 and Figure 21d). However, due to the lack of enough temperature overlap in the presented data a general trend cannot be deducted.

4.4 Effect of brine salinity

In a recent publication by Michael et al. [67], the authors summarized the operational conditions for sixteen active sequestration sites worldwide with brine salinities ranging from 7,000 to 340,000 ppm. Therefore, three different salinities were chosen for our studies that are in the range of 0.2 to 5 M NaCl (~11,500 to 300,000 ppm) to cover the spectrum of brine salinities observed in underground aquifers. All the measurements in this section were performed at 3000 psig.

The densities of CO_2-rich and aqueous phases at various NaCl concentrations are plotted in Figure 23a. As expected, the density of CO_2 was insensitive to the changes in salt concentration, however brines with higher ionic strength had larger densities. Figure 23b depicts the variations of IFT with ionic strength. There was a significant increase in IFT with increase in ionic strength. For example, IFT between equilibrated sc-CO_2 and brine at 3000 psig and 60 °C increased from 26 to 39 mN/m by changing the ionic strength from 0.2 to 5 M. This behavior is partly due to the decrease in CO_2 solubility in brine with higher salinities, as shown in Figure 22b, and partly because of hydration of ions that leads to an ion-free layer at the water interface [100]. Figure 23c depicts the water receding and advancing contact angles of the CO_2/brine/quartz system. There was a consistent increase in both dynamic contact angles with the increase in ionic strength. The observed trend is consistent with the reported data in several studies [53], [64]–[66]. Furthermore, the hysteresis in contact angle was much larger at higher salinities (Figure 23d). For instance, $\Delta\theta$ increased from 6° to 22° with the increase in brine ionic strength from 0.2 to 5 M at 80 °C.

Table 3- Density, interfacial tension, and water advancing and receding contact angles of CO_2/brine/quartz systems measured in this study. (The reported errors in this table are the standard deviation of the mean value)

Test	P (psig)	T (°C)	Ionic Strength (M)	SO_2 (wt.%)	ρ_{CO2} (kg/m^3)	ρ_{Brine} (kg/m^3)	$\Delta\rho$ (kg/m^3)	IFT (mN/m)	θ_{WR} (°)	θ_{WA} (°)	$\Delta\theta$ (°)
B1	2000	50	1	0	672	1040	369	31.4 ±0.1	14.6 ±0.9	25.9 ±0.9	11.3 ±0.9
B2	2000	60	1	0	561	1034	473	28.7 ±0.2	13.6 ±1.0	23.5 ±1.0	9.9 ±1.0
B3	3000	60	1	0	742	1036	294	28.7 ±0.1	14.6 ±1.0	29.3 ±0.5	14.7 ±0.7
B4	3000	70	1	0	687	1031	345	27.0 ±0.1	11.6 ±0.7	29.0 ±0.6	17.4 ±0.6
B5	3000	80	1	0	612	1024	412	25.0 ±0.4	13.3 ±0.7	25.4 ±1.8	12.0 ±1.3
B6	4000	70	1	0	771	1034	264	26.7 ±0.4	12.1 ±0.5	33.0 ±1.4	20.9 ±0.9
B7	4000	80	1	0	721	1028	307	27.9 ±0.1	10.5 ±0.8	27.1 ±0.7	16.6 ±0.7
B8	4000	90	1	0	679	1021	342	26.3 ±0.1	11.5 ±0.7	25.5 ±0.8	14.0 ±0.7
B9	4000	100	1	0	636	1012	377	28.6 ±0.2	8.8 ±0.6	27.0 ±0.2	18.2 ±0.4
B10	3000	60	0.2	0	740	1010	270	26.0 ±0.3	10.0 ±0.2	20.5 ±0.9	10.5 ±0.5
B11	3000	70	0.2	0	674	1003	329	23.9 ±0.2	9.8 ±0.7	16.5 ±1.0	6.7 ±0.8
B12	3000	80	0.2	0	614	996	382	23.6 ±0.2	11.0 ±0.7	17.0 ±1.9	6.0 ±1.3
B13	3000	60	5	0	739	1166	427	39.2 ±0.2	17.3 ±0.9	35.7 ±0.7	18.4 ±0.8
B14	3000	70	5	0	674	1162	488	39.2 ±0.7	19.8 ±1.2	44.1 ±1.5	24.2 ±1.4
B15	3000	80	5	0	613	1147	534	38.3 ±0.8	20.0 ±1.4	42.2 ±2.1	22.2 ±1.7
B16	3000	60	1	1	739	1022	283	27.0 ±0.4	14.0 ±0.1	27.0 ±0.2	13.0 ±0.2
B17	3000	60	1	6	778	1023	245	18.4 ±0.7	12.9 ±1.0	27.6 ±2.5	14.7 ±1.7

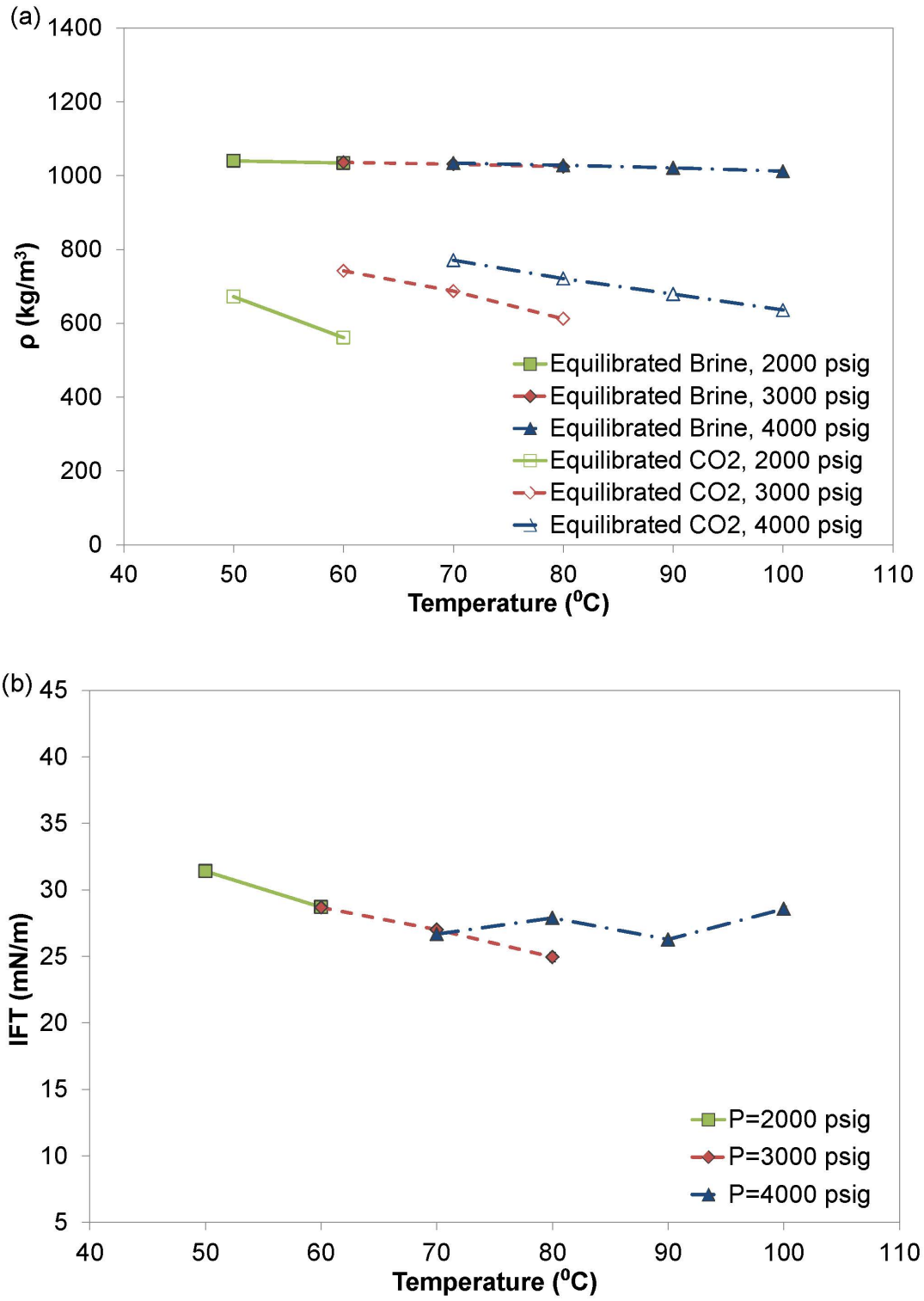

Figure 21: Effects of pressure and temperature on (a) density, (b) interfacial tension, (c) dynamic contact angles (WR: water receding, WA: water advancing), and (d) contact angle hysteresis (Δθ) of CO_2/brine/quartz system.

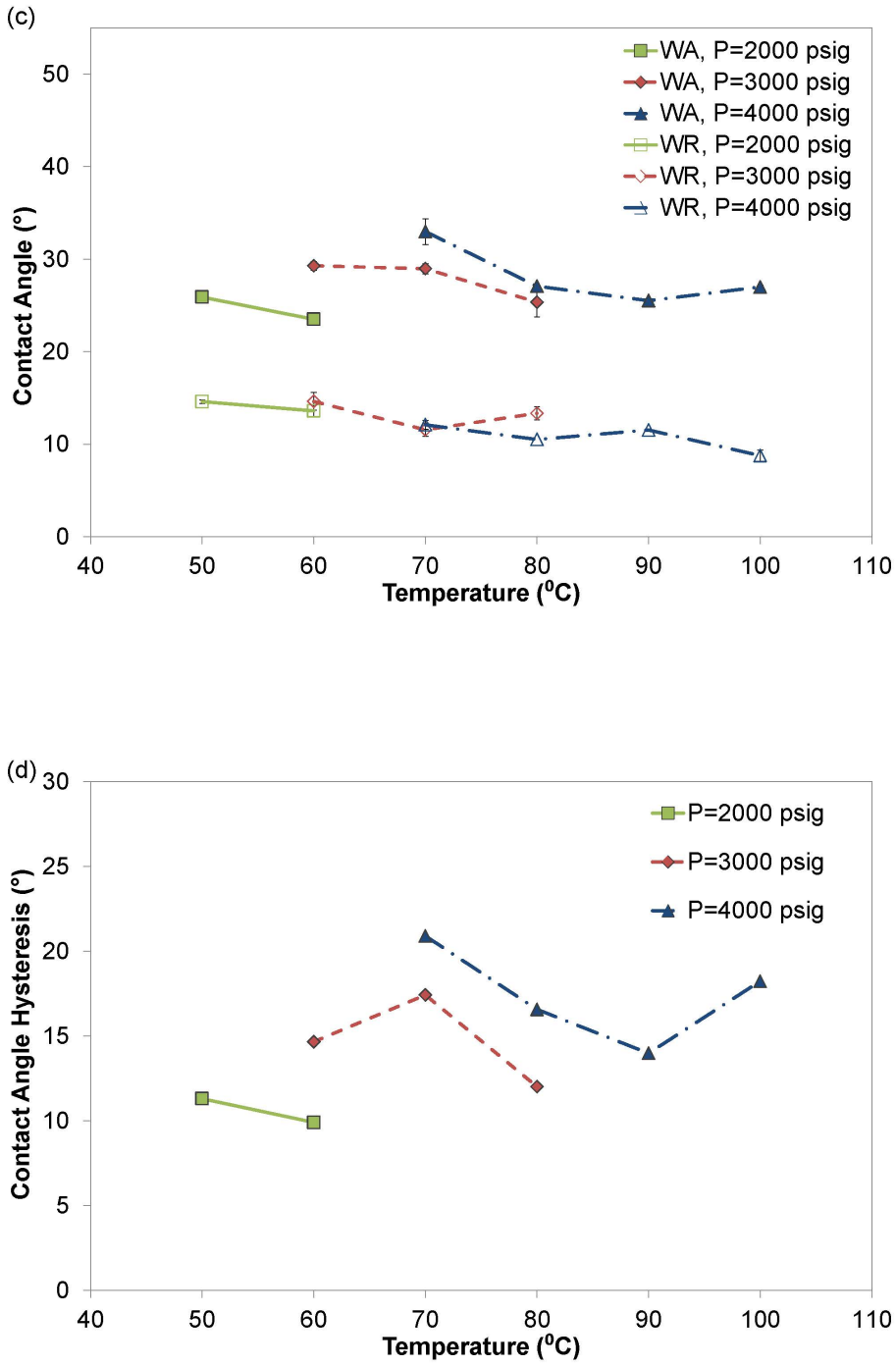

Figure 21: Continued.

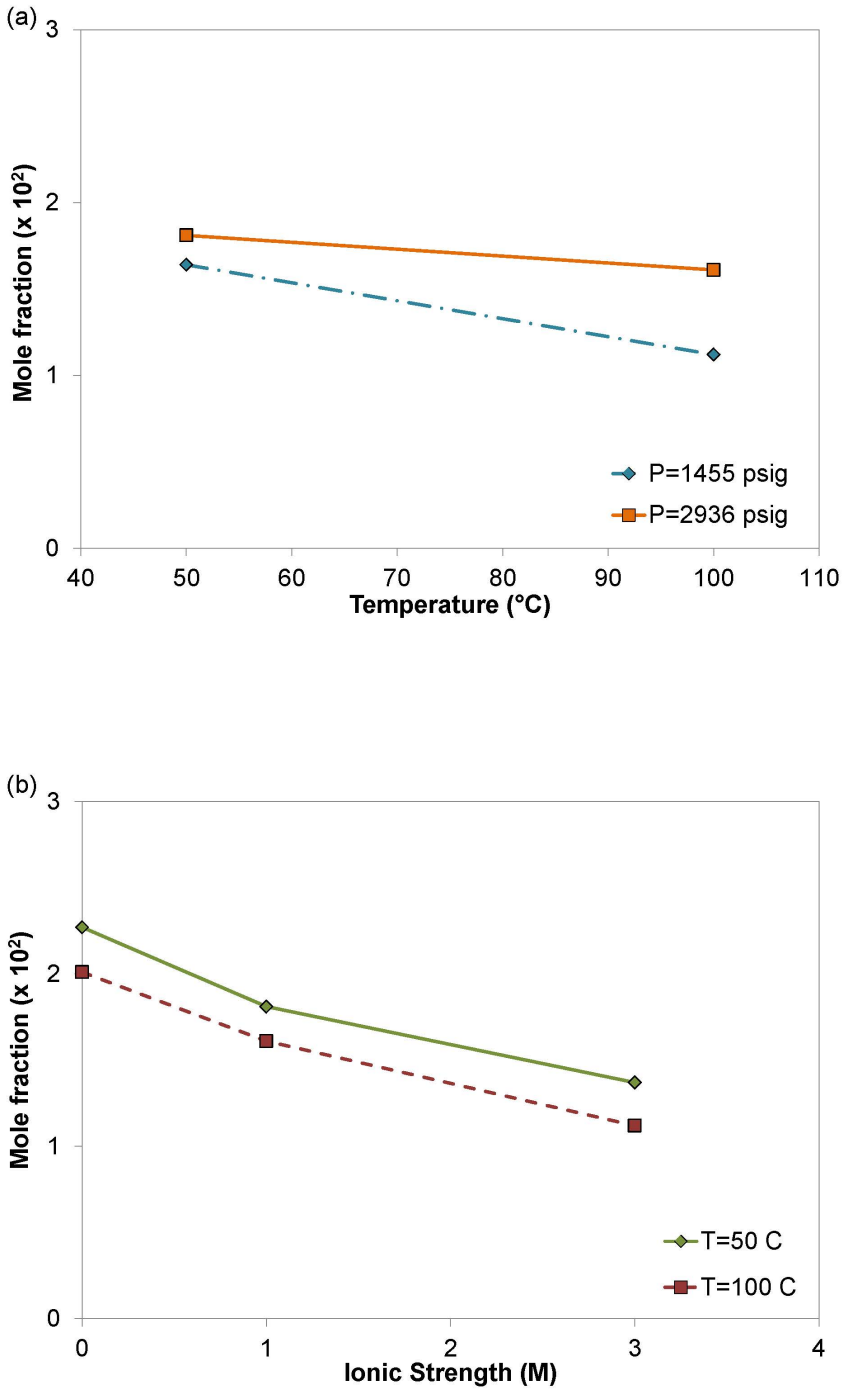

Figure 22: Variations in CO_2 solubility in brine with (a) pressure and temperature (1M brine), and (b) brine salinity (at 3000 psig) (data from Koschel et al. [99]).

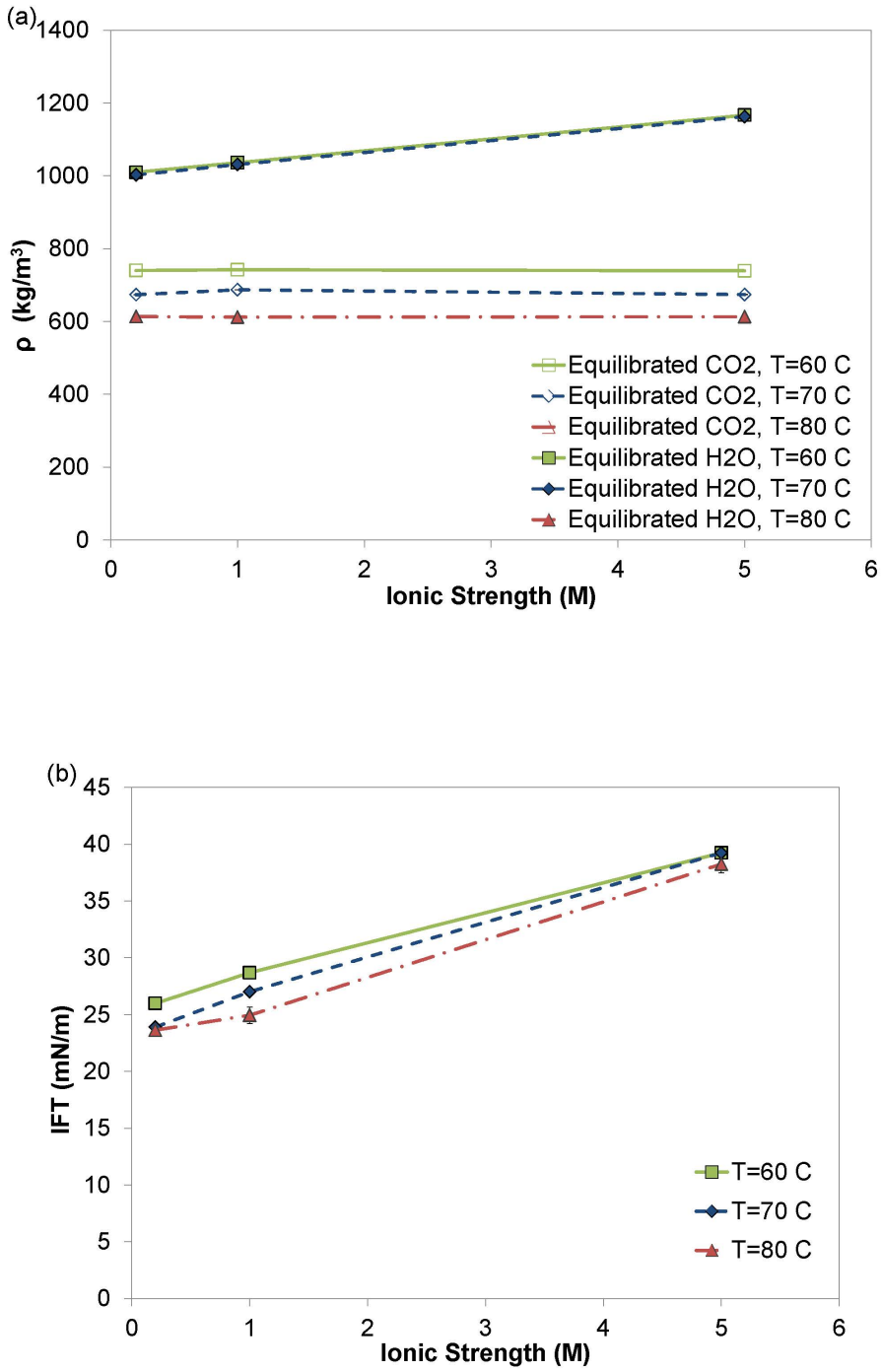

Figure 23: Effects of brine salinity on (a) density, (b) interfacial tension, (c) dynamic contact angles (WR: water receding, WA: water advancing) and (d) contact angle hysteresis (Δθ) of CO_2/brine/quartz system. (All the measurements were performed at 3000 psig)

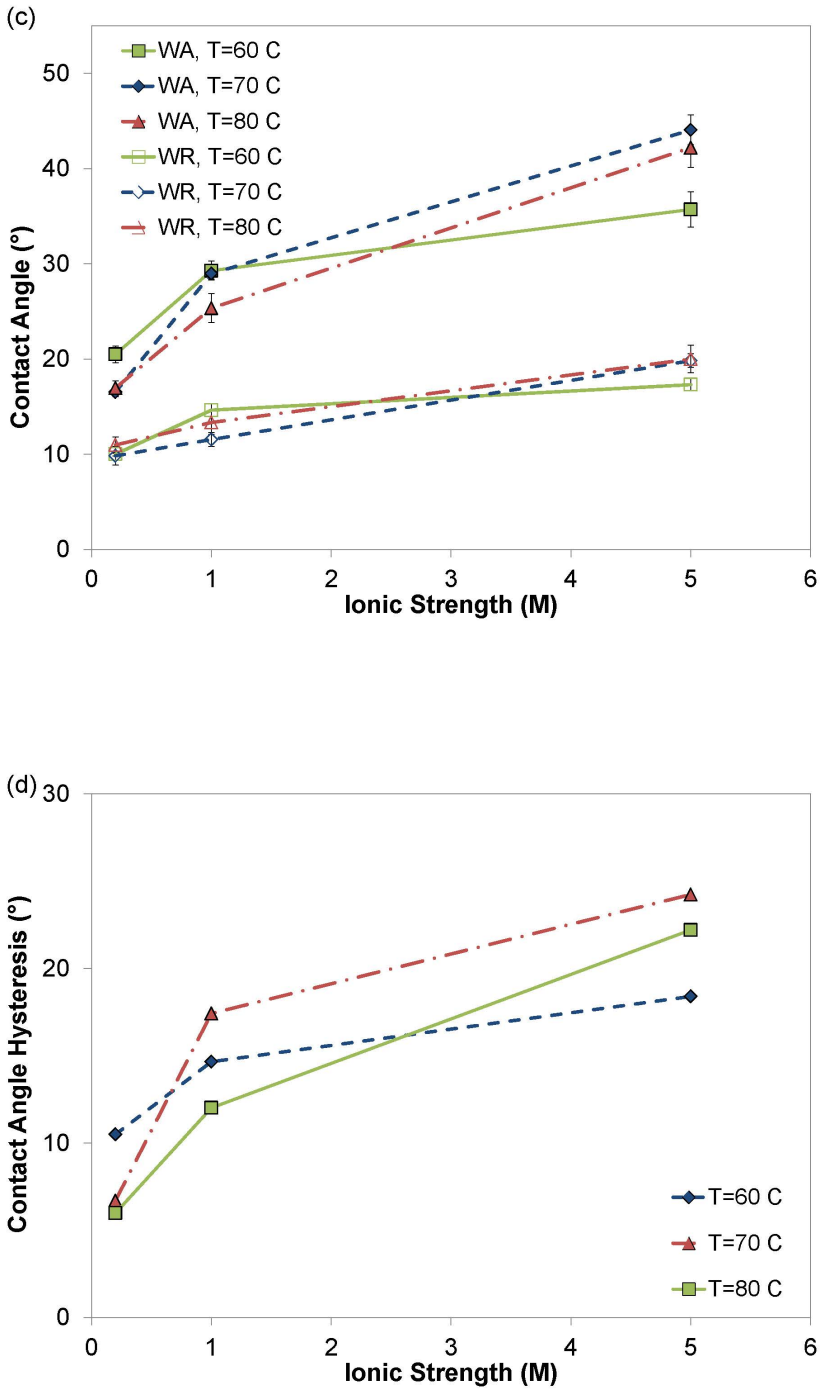

Figure 23: Continued.

4.5 Effect of SO_2 contaminant

Based on a report by Miller and Van Atten [76], the SO_2/CO_2 ratio in the emission stream of power plants varies between 0.02 to 8 wt.% with an average of 0.6 wt.%. Thus, to cover the reported SO_2 range, two CO_2 mixtures with 1 wt.% SO_2 (Test B16 in Table 3) and 6 wt.% SO_2 (Test B17 in Table 3) content were considered in this study. Pressure (3000 psig), temperature (60 °C), and brine salinity (1M) were kept constant for these experiments.

The densities of equilibrated CO_2-rich phase for SO_2+CO_2 mixtures were larger than those of equilibrated CO_2-rich phase in the absence of SO_2 (Figure 24a). This is because SO_2 has a higher density than CO_2. In spite of this, the densities of aqueous phases were slightly smaller in the presence of SO_2. This results in a decreasing trend of $\Delta\rho$ with increasing SO_2 concentration (Table 3). Figure 24b shows that the interfacial tension between equilibrated phases decreased linearly with increase in the SO_2 concentration. There was a significant decrease in IFT (i.e. 40%) from 29 mN/m in the case of pure CO_2 to 18 mN/m in the presence of 6 wt.% SO_2. A recent study [101] on the effect of SO_2 and CO_2 molecules on the gas/water interface was performed by comparing OH stretching intensities at the interfacial water spectrum. This study showed a clear difference between the interactions of these two molecules with water [101]. The authors observed that a weakly bounded surface complex was formed between SO_2 and interfacial water molecules, which affected the molecular structure at the interface. However, no specific surface-bound species were observed in the case of CO_2. The presence of this weakly bounded surface complex between SO_2 and water molecules at the supercritical fluid/liquid interface could be the main contributor for the considerable decrease in IFT values. Similar effects on the IFT of CO_2/brine in the presence of another acid gas (i.e. H_2S) have also been reported [75]. The IFT between H_2S+CO_2 mixtures and brine under conditions comparable to our experiments dropped from 32 mN/m for pure CO_2 to 26 mN/m with 30 mole% H_2S and 7.5 mN/m with pure H_2S. The dynamic contact angles and hysteresis for SO_2+CO_2/brine/quartz system are shown in Figures 24c and 24d. We have not observed any significant change in water receding/advancing contact angles and CA hysteresis by increasing SO_2 concentration. This is comparable with the work of Broseta et al. [66] who did not observe any major change in the wettability of quartz when switching from CO_2 to H_2S.

5 Conclusions

The safety and total storage capacity of carbon dioxide in deep saline aquifers are dependent on fluid-fluid and rock-fluids interactions. In this study, a novel apparatus for measuring interfacial tension and contact angle at high temperatures and pressures based on axisymmetric drop shape analysis with no-apex (ADSA-NA) method was developed and validated with a simple system. Densities, interfacial tensions, and dynamic contact angles of equilibrated CO_2 and brine on quartz surface were measured at pressure and temperature conditions relevant to deep saline aquifers. IFT values dropped sharply with increase in pressure at the subcritical region (gaseous CO_2) and then stabilized in the supercritical region. The CA data show that the quartz surface becomes less water-wet in the presence of supercritical CO_2. This wettability change occurs mostly in the phase transition zone and then remains unchanged. Furthermore, the results at the supercritical CO_2 region indicated that pressure and temperature variations, within the range studied, did not significantly affect IFT and CA. Also, contact angle hysteresis was only slightly changed by these parameters. On the other hand, an increase in brine salinity resulted in an increase in IFT, CA, and CA hysteresis. Furthermore, the effect of SO_2 as a co-contaminant on densities, IFT, and CA of the system was studied for the first time. While rock wettability was not affected by SO_2, the IFT between CO_2+SO_2 mixture and brine decreased linearly with increase in the amount of SO_2 in the CO_2-rich phase. Therefore, the co-injection of SO_2 at high concentrations in saline aquifers may increase the risk of gas leakage though the caprock.

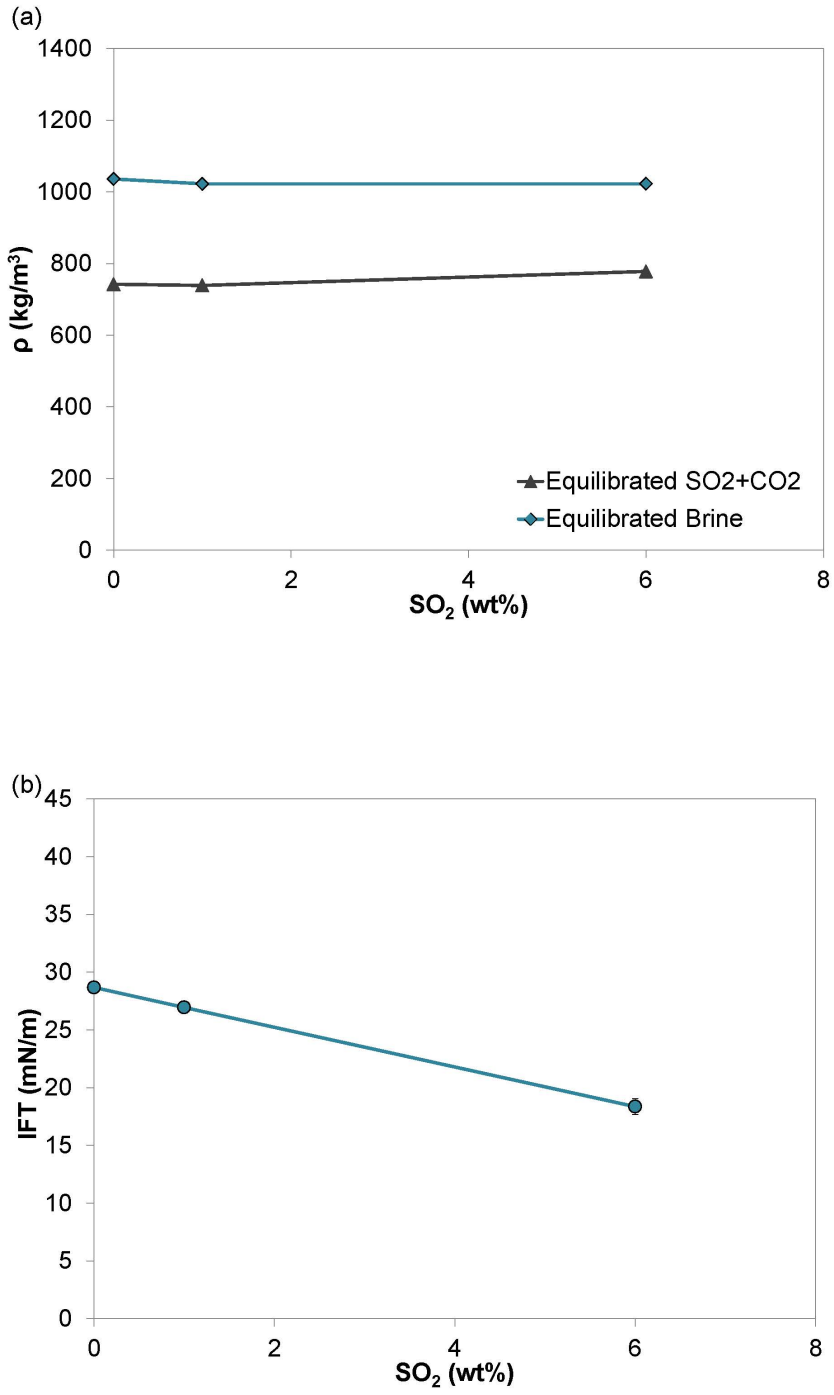

Figure 24: Effects of SO_2 concentration on (a) density, (b) interfacial tension, (c) dynamic contact angles (WR: water receding, WA: water advancing) and (d) contact angle hysteresis (Δθ) of SO_2+CO_2/brine/quartz system. (All the measurements were performed at 3000 psig, 60 °C, and 1M brine salinity)

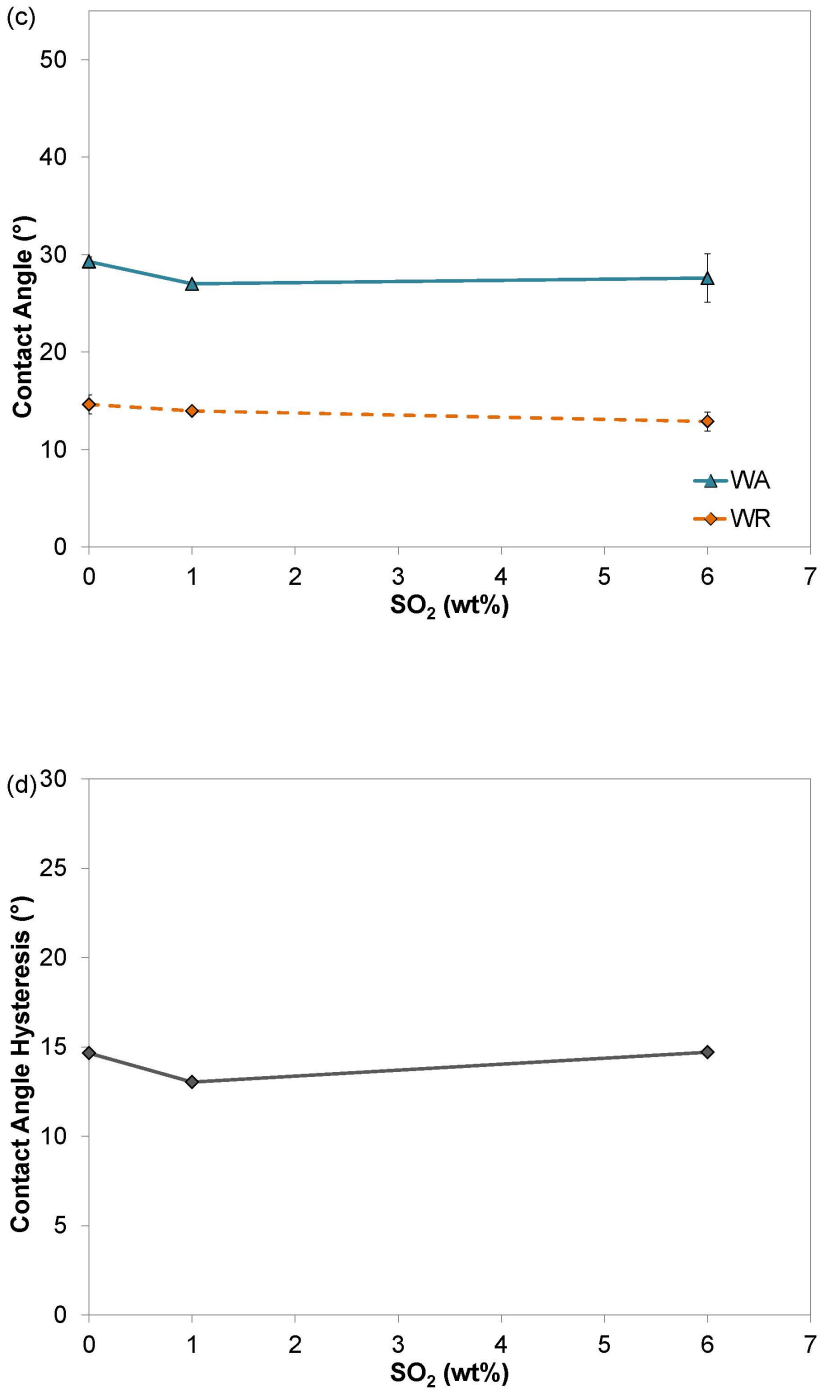

Figure 24: Continued.

Task 4: Development of physically-based dynamic parallel core-scale pore network model for samples from RSU

PI: Dr. Mohammad Piri

1 Intrdocution

Multiphase flow in porous media occurs in many natural and artificial processes such as subsurface flow of hydrocarbons and brine, geologic storage of CO_2, non-aqueous phase liquids (NAPL) migration in soil, reactive transport, and water removal in gas diffusion layer (GDL) of proton exchange membrane (PEM) fuel cells. Understanding the displacement and transport processes relevant to multiphase flow systems and predicting the associated macroscopic properties are crucial for design and prediction of performance of these processes [102,103].

In petroleum and environmental engineering contexts, multiphase flow in porous rocks has been studied extensively using experimental and numerical techniques at multiple scales. Pore-scale investigations are often used to develop improved understanding of fundamental phenomena relevant to a given process and predict the pertinent flow and transport properties. These physically-based properties are then used to inform larger-scale models. In this work, we establish a direct up-scaling technique in which we develop and use dynamic pore-scale network models to study core-scale processes. We perform miniature core-flooding experiments to rigorously validate this approach before using it to investigate processes of interest.

The pore-scale models can be categorized into direct and network models. In direct models, multiphase flow is simulated directly in the pore space structure that is mapped using an imaging technique or created by a process-based reconstruction method, e.g., sedimentation simulation. Direct models include Lagrangian particle-based (mesh-free) methods, such as moving particle semi-implicit (MPS) [104-107], smoothed particle hydrodynamics (SPH) [108-110], and Lattice Boltzmann [111,112], and mesh-based methods, e.g., finite element [113]. These models use accurate representation of the pore space. However, due to irregular fluid-solid boundaries and deformability of fluid-fluid interfaces, direct models are computationally expensive and may not be suitable for studying multiphase flow at the core scale. In the second group of pore-scale models, i.e., network models, the pore space is represented by a network of idealized pores and throats. Pore-scale displacements are carried out in the pore network to simulate multiphase flow [114-118].

Pore network modeling was first introduced in the 1950's by Fatt [119-121] who used a network of real resistors to calculate relative permeability and capillary pressure for a drainage process. Network modeling, since its introduction, has evolved enormously. Today, one can map the pore space of a rock sample with high-resolution imaging techniques and extract an equivalent pore network. Our knowledge of the pore-scale displacement physics has also improved dramatically due to micro-fluidics and other types of experiments. Pore network models can be divided into quasi-static and dynamic. The majority of the previously-developed network models are quasi-static in which the pore-scale displacements take place based on their threshold capillary pressure. These models have had significant success in modeling two- and three-phase flow in porous media under capillary-dominated conditions [114,115,117,118, 122,123]. However, quasi-static models do not include the effects of viscous and gravity forces, and therefore, cannot be used to study cases in which capillary-dominated assumptions do not apply. Viscous and gravity forces become significant during many subsurface flow processes, such as CO_2 sequestration, enhanced oil recovery (EOR) methods of polymer and surfactant flooding, and high

velocity flow regimes that are encountered in naturally and hydraulically induced fractures as well as near well-bore areas. In these cases, the combined effects of capillary, viscous, and gravity forces determine the flow behavior in porous media. In dynamic network models, on the other hand, viscous and in some cases gravity forces are taken into account. These models can be used to study the cases in which viscous or gravity forces are relevant. However, due to various reasons, such as difficulties in implementing the complex pore-scale physics and the computational costs associated with these models, the previously-developed dynamic models lack some of the critical capabilities to successfully simulate dynamic two-phase flow processes at the core scale.

We introduce an entirely new dynamic network model to perform physically-based up-scaling of displacement processes from pore to core scale. The model takes into account viscous, capillary, and gravity forces as well as wettability effects. It incorporates all types of relevant displacement mechanisms and allows for variations in the order by which they take place under different flow regimes in response to changes in the capillary and Bond numbers. The wetting-phase corner flow with variable corner interface location responsive to changes in local capillary pressure is included in the model. Simultaneous injection of wetting and non-wetting fluids with constant flow rates from the inlet has been incorporated in the model, and it has enabled us to study the steady-state two-phase flow processes. Constant pressure boundary condition is used at the outlet. This platform is developed to run on massively parallel computer clusters and to bridge the gap between pore-scale displacements and core-scale processes. In this report, first, we give a detailed description of the dynamic model and techniques used to model two-phase flow at the core scale. This is followed by a rigorous validation of the model by comparing the simulation results against their experimental data available in the literature. Finally, we include a set of conclusions and final remarks.

2 Model Description

2.1 Network Representation of the Porous Medium

We use three-dimensional random networks that are generated from high-resolution micro-CT images of rock samples. A pore network representing the pore space in the Berea rock sample was used in this work. A 17 mm long section at the middle of the Berea core sample was scanned at a resolution of 2.49 µm. A pore network with a length of 16.3 mm and a square cross section of 3.11x3.11 mm^2 was generated. Twenty replicates of the 16.3 mm long Berea network were connected to build a larger network. Average properties from the original network (e.g., coordination number and throat radii) were used at the connection site. A cylindrical pore network with a length of 76.4 mm and a diameter of 4.58 mm was cut from the larger network. We refer to this network as the Berea network in the rest of this work.

Table 1. Properties of the Pore Network Representative of the Berea Sandstone Core Sample

Item	Throats	Pores	Total
Number	3,913,222	1,891,260	5,804,482
Porosity excl. clay (%)	8.236	12.616	20.852
Porosity incl. clay (%)	8.458	12.892	21.350
Absolute Permeability (mD)	-	-	638
Length (mm)	-	-	76.4
Diameter (mm)	-	-	4.58
Minimum coordination number	-	0	-
Maximum coordination number	-	45	-
Average coordination number	-	4.017	-
Minimum radius (µm)	0.21	0.25	0.21
Maximum radius (µm)	63.50	101.0	101.0
Average radius (µm)	6.95	13.95	9.27
Average shape factor	0.039	0.047	0.042
Triangular cross sections (%)	78.522	57.667	71.592
Square cross sections (%)	20.954	41.594	27.813
Circular cross sections (%)	0.524	0.739	0.595
Connected to the inlet	1515	0	1515
Connected to the outlet	1507	0	1507
Isolated clusters	-	-	24
Isolated	7460	7791	15251

The dimensions and petrophysical properties of the Berea network are listed in Table 1. The pores and throats of our networks have rectangular, scalene triangular, and circular cross sections. Figure 1(a) shows a volume rendered gray scale image of the Berea sandstone core sample. This gray scale image is segmented using the histogram thresholding technique producing a pore-grain separated labeled image seen in Figure 1(b), where red and gray colors represent the pore and grain voxels, respectively. The gray-scale and pore-grain separated images are used to construct a pore network representative of the Berea core sample, as shown in Figure 1(c). In the pore network image, pores and throats are shown with red spheres and blue cylinders, respectively. Figure 1(d) shows a magnified image of a small section of the Berea pore network.

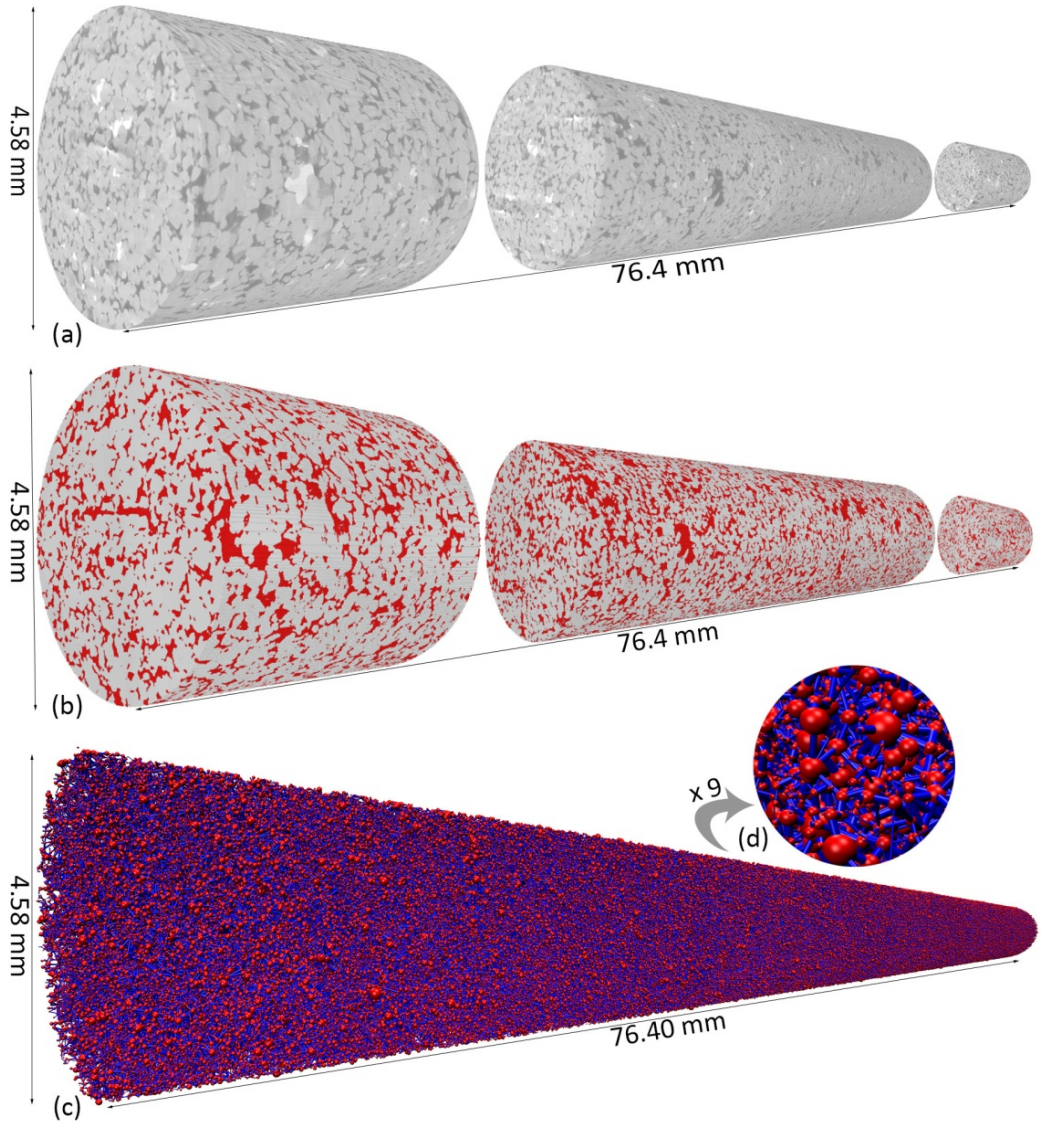

Figure 1: Pore network representation of the Berea sandstone core sample. (a) Volume rendered gray-scale images of the Berea core sample scanned with a micro-CT scanner at a resolution of 2.49 µm. (b) Volume rendered pore-grain separated images of the Berea core sample. Red and gray colors represent the pore and grain voxels, respectively. (c) Pore network generated from images (a) and (b). Red and blue colors represent the pores and throats in the network, respectively. For illustrative purposes pores and throats are shown with circular cross-section here. (d) A magnified image of a small section of the Berea pore network.

2.2 Pore-Scale Displacements

A series of pore-scale fluid displacements are carried out in the pore network to simulate two-phase flow displacements in porous media. Three fundamental types of pore-scale displacement mechanisms included in this dynamic model are piston-like, pore-body filling (cooperative filling), and snap-off.
The simulations start with fully water saturated pores and throats where all possible displacements from the inlet have been added to the system. Displacements occur in the order of highest-to-lowest

displacement potential that takes into account the effects of capillary, viscous, and gravitational pressure drops. After each displacement, new displacements are added to the system based on the access of fluid phases to each other.

2.3 Displacement Pressure Drop and Sequence

The multiphase flow behavior in porous media is determined by the interlinked effects of capillary, viscous, and gravity forces. Therefore, in order to capture the true physics of two-phase flow in porous media, it is essential to include the effects of these three basic forces in the model. In our dynamic pore network model, this is achieved by combining the capillary, viscous, and gravitational pressure drops of a displacement into a new parameter called the *displacement pressure drop* as given by equation (1). The displacement pressure drop is the total "cost" that the system must pay when a certain pore-scale displacement takes place. The contribution of each term in the displacement pressure drop to its total value depends on the capillary and Bond numbers (equations (2) and (3)). The capillary number refers to the ratio of viscous to capillary forces and is given by equation (2) where μ is the viscosity, v is the fluid velocity, and σ is the interfacial tension. The Bond number is defined as the ratio of gravity to capillary forces and is given by equation (3) where $\Delta\rho$ is the density difference of the fluid phases, g is the acceleration of gravity, L is the length scale, and σ is the interfacial tension. In the cases where the capillary and Bond numbers are both very low, capillary pressure dominates the flow behavior in porous media. However by increasing the capillary and Bond numbers the contributions of viscous and gravitational pressure drops, respectively, become more significant.

$$\Delta P_{disp} = \Delta P_{cap} + \Delta P_{visc} + \Delta P_{grav} \quad (1)$$

$$N_c = \frac{\mu v}{\sigma} \quad (2)$$

$$B_o = \frac{\Delta\rho g L^2}{\sigma} \quad (3)$$

The capillary pressure drop is the threshold pressure drop needed to perform the displacement. For piston-like displacements we use the Mayer-Stowe-Princen (MSP) method to calculate the capillary pressure drop of displacements [114,118, 124-126]. In this method, an energy balance equation is written for the fluid configuration changes associated with a pore-scale displacement. By assuming the equilibrium conditions at constant temperature and combining the resultant equation with the Young-Laplace equation, the capillary pressure drop during a fluid configuration change is obtained.

The viscous pressure drop occurs due to the friction between layers of fluid that move with different velocities. In our dynamic model, we calculate the viscous pressure drop for *both* the invading and defending fluid phases. For the invading fluid phase the viscous pressure drop is calculated from the inlet of the pore network to the displacement location, and for the defending fluid phase, it is calculated from the displacement location to the outlet of the pore network as written in equation (4). The summation of the invading and defending viscous pressure drops gives the total viscous pressure drop of a displacement. The pressure values for each fluid phase used in calculating the viscous pressure drop are obtained by solving the system of material balance equations. The fluid viscosities, inlet flow rates, connectivity of fluid phases in the network, and the displacement location are some of the parameters that affect the viscous pressure drop of a displacement.

$$\Delta P_{visc} = (P_{inlet}^{invd} - P_{elm}^{invd}) + (P_{elm}^{def} - P_{outlet}^{def}) \quad (4)$$

The gravitational pressure drop is the result of the hydrostatic pressure difference of the invading and defending fluid phases as given by equation (5), where ρ^{invd} and ρ^{def} are the densities of the invading and defending phases, respectively, g is the acceleration of gravity, and h_{elm} is the height of the pore or throat involved in the displacement measured from the injection face of the medium. The larger the network height and the greater the invading and defending fluid phase density difference are the more significant the effect of gravitational pressure drop becomes.

$$\Delta P_{grav} = (\rho^{invd} - \rho^{def}) g h_{elm} \quad (5)$$

Whether pore-scale displacements can take place and their sequence are determined by a parameter called the *displacement potential*. The displacement potential is defined as the difference of the *driving force* and the displacement pressure drop. The driving force is defined as the difference of the inlet pressure of the invading phase and the outlet pressure of the defending phase. The displacement potential for any given displacement is calculated by equation (6), where P^{invd}_{inlet} is the inlet pressure of the invading phase, P^{def}_{outlet} is the outlet pressure of the defending phase, and ΔP_{disp} is the displacement pressure drop. Displacements can take place only if they have a positive potential, and they take place in the order of highest-to-lowest displacement potential. The occurrence likelihood of any two displacements can be compared by comparing their displacement potentials.

$$\Phi_{disp} = P_{inlet}^{invd} - P_{outlet}^{def} - \Delta P_{disp} \quad (6)$$

2.4 Material Balance and Pressure Calculations

Fluid phase pressure field calculations are regarded as the backbone of this dynamic model. Fluid phase pressure values are used to calculate the viscous pressure drop of displacements, which affects the displacement sequence, and determine the corner interface locations, which have a strong impact on relative permeability values. The pressure fields are obtained by writing a material balance equation for each fluid phase at each pore and solving the resulting system of linear equations with the appropriate boundary conditions. Equation (7) gives the material balance for phase p at pore i where q^p_{ij} is the flow rate of the phase p between pores i and j, and n is the coordination number of pore i.

$$\sum_{j=1}^{n} q_{ij}^{p} = 0 \quad (7)$$

$$q_{ij}^{p} = g_{ij}^{p} (P_i^p - P_j^p) \quad (8)$$

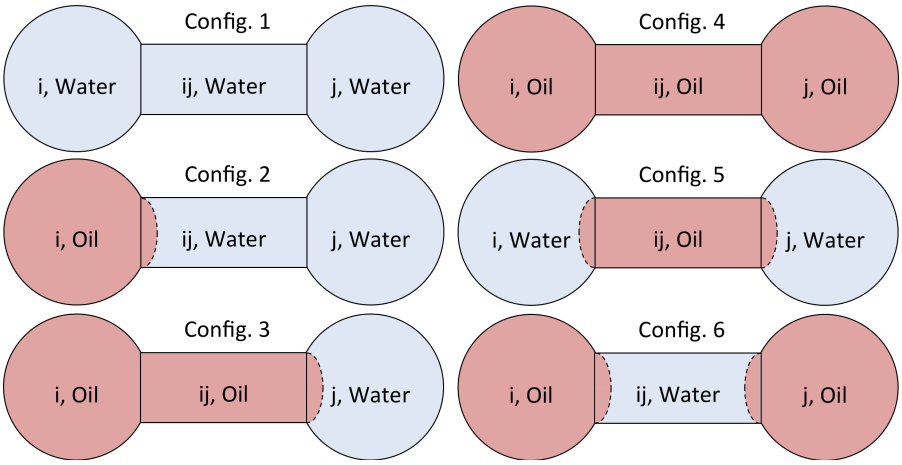

Figure 2: All possible fluid configurations in a combination of two pores and a throat. Pores and throats are shown with circles and rectangles for illustrative purposes only. They can have angular cross-sections and contain a center as well as a corner phase. Only the center phases are illustrated here. The corners will contain water if the elements are angular. The dotted curvatures show the Main Terminal Menisci (MTM's) present between the wetting and non-wetting phases.

There are six possible configurations of two fluid phases in an assembly of two pores and a throat as shown in Figure 2. Pores and throats are shown by circles and cylinders for illustrative purposes only. They can have angular cross sections and contain center and corner phase locations. In configurations 1 and 4, no *Main Terminal Meniscus* (MTM) exists between pores *i* and *j*, therefore the single phase flow equations are written for the center and corner phases of these configurations as given by equation (8), where g^{p}_{ij} is the conductance of fluid phase *p* between pores *i* and *j*, and P^{p}_{i} and P^{p}_{j} are pressures of fluid phase *p* in pores *i* and *j*, respectively. However, in other configurations, one or two MTM's exist between two pores. Flow equations for configuration 2 will be discussed here. As shown in Figure 2, in configuration 2, one oil-water MTM is located at the entrance of throat *ij*. The MTM can either move into throat *ij* and cause a drainage-type flow, or retreat into pore *i* and cause an imbibition-type flow depending on the local capillary pressure and threshold capillary pressures of pore *i* and throat *ij*. Local capillary pressure for configuration 2 is written as the difference of oil pressure in pore *i* and water pressure in pore *j* (equation (9)). The potentials for two possible types of the MTM movement in configuration 2 are given by equations (10) and (11), where $P^{dra}_{c,ij}$ is the drainage threshold capillary pressure of throat *ij* and $P^{imb}_{c,i}$ is the imbibition threshold capillary pressure of pore *i*. As written in equation (12), if the drainage potential of the MTM is positive and greater than its imbibition potential then a drainage-type flow will be considered for the MTM. However, if the imbibition potential is positive and greater than the drainage potential then an imbibition-type flow will be considered for the MTM. In cases where both potentials are negative there will be no two-phase flow taking place between pores *i* and *j*. For configuration 2, the single-phase corner flow is given by equation (8).

$$P_c^{config.2} = P_i^o - P_j^w \quad (9)$$

$$\Phi_{config.2}^{dra} = P_c^{config.2} - P_{c,ij}^{dra} \quad (10)$$

$$\Phi_{config.2}^{imb} = P_{c,i}^{imb} - P_c^{config.2} \quad (11)$$

$$q_{ij} = \begin{cases} g_{ij}(P_i^{nw} - P_j^{w} - P_{c,ij}^{dra}) & if \quad \Phi_{config.2}^{dra} > \Phi_{config.2}^{imb} \quad and \quad \Phi_{config.2}^{dra} > 0 \\ g_{ij}(P_i^{nw} - P_j^{w} - P_{c,ij}^{imb}) & if \quad \Phi_{config.2}^{imb} > \Phi_{config.2}^{dra} \quad and \quad \Phi_{config.2}^{imb} > 0 \\ 0 & if \quad \Phi_{config.2}^{dra} < 0 \quad and \quad \Phi_{config.2}^{imb} < 0 \end{cases} \quad (12)$$

The conductance values in equations (8) and (12) are functions of the area open to flow, element shape factor, length, and viscosity. The center flow conductances are calculated by using the equations proposed by *Patzek and Silin* [115] and *Øren et al.* [114]. The corner flow conductances are calculated by equations proposed by *Hui and Blunt* [127].

By writing the material balance equation for each fluid phase at each pore, a system of linear equations is obtained. These linear equations are solved using the MUMPS (MUltifrontal Massively Parallel sparse direct Solver) package, which is a massively parallel sparse matrix solver [128,129].

2.5 Boundary Conditions

An important feature of this dynamic model is the realistic boundary conditions used during simulations. In order to replicate the experimental conditions during simulations and to be able to study steady-state two-phase flow processes, wetting and non-wetting fluids are injected simultaneously at constant flow rates from the inlet of the medium. Drainage and imbibition processes are simulated by changing the inlet flow rates. The direction in which the inlet flow rates change determines the type of two-phase flow process we simulate.

The inlet of the medium is regarded as a big pore and single and two-phase flow equations are written for the inlet and the pores connected to it. Material balance is written for the inlet as shown in equation (13) where q^{p}_{inlet} is the flow rate of phase p at the inlet. Pressures of wetting and non-wetting phases at the inlet are obtained by solving the material balance equations.

$$\sum_{j=1}^{n} q_{ij}^{p} = q_{inlet}^{p} \quad (13)$$

At the outlet of the medium, constant pressure boundary conditions are enforced. Since the *local* capillary pressure at the pore scale cannot be zero, a non-zero capillary pressure is enforced at the outlet. The outlet capillary pressure has the value below which no network-spanning cluster of the non-wetting phase can exist in the system. During drainage, when the non-wetting phase reaches the outlet of the network, the pressures of the wetting and non-wetting fluids are averaged in a partition of the network adjacent to the outlet, and capillary pressure is determined in that partition. This capillary pressure is set as the outlet capillary pressure. However, if the capillary number is high, the outlet capillary pressure can be overestimated using this method. Therefore, the capillary pressure set at the outlet is reduced gradually in small increments to find the value below which the connection of the non-wetting phase to the outlet is lost completely. This critical value is set as the outlet capillary pressure. This procedure is performed automatically by the model as soon as the breakthrough of the non-wetting phase occurs. The outlet capillary pressure is kept constant during the simulations. One should note that the values set as the outlet capillary pressure are insignificant compared to the macroscopic pressure drops along the network.

2.6 Corner Interface Handling

The locations of *Arc Menisci* (AM's) determine the area open to corner and center flows and have a significant impact on pressure values and thereby relative permeabilities as well as other predicted properties. This dynamic model allows the location of AM's to be updated based on the local capillary pressure and receding and advancing contact angles. Corner interface hinging and movements are included in the model.

2.7 Parallelization

Dynamic pore network modeling is computationally expensive. The computational challenges in dynamic network models have limited the size of the mediums that were studied with previously developed models. They have also hindered studies of heterogeneous mediums at the pore scale. Calculating the fluid phase pressure field and updating the fluid-fluid interface locations and displacement potentials at each time step, and updating the continuity flags of neighboring fluid phase locations after each displacement are computationally the most demanding steps in our dynamic model. The main purpose of this research work has been the development and use of dynamic network modeling technology as a physically-based up-scaling tool to simulate two-phase flow processes at the core scale (millions of pores). To achieve this goal we take advantage of greater memory and computational resources available on massive computer clusters. Data parallelism through three-dimensional domain decomposition was employed in designing the parallel algorithms.

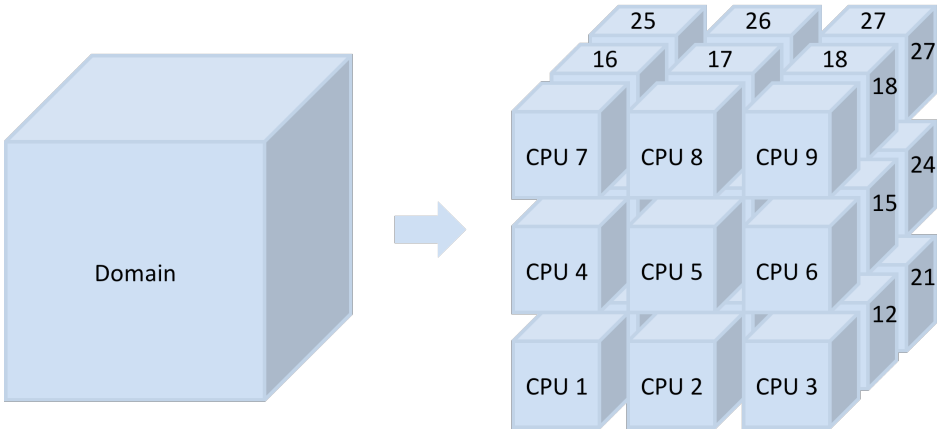

Figure 3: Domain decomposition. The domain of the problem, in this figure, is divided into 27 blocks and each block is assigned to a processor.

In Figure 3, a domain decomposition scheme is illustrated, in which the domain of the problem is divided into, in this case, 27 subdomains and each subdomain is assigned to one processor. In this work, the pore network is divided into multiple blocks based on the availability of the computational resources, and each block is assigned to one processor. The pores and throats whose center coordinates lie inside the boundaries of a block are considered as *local* elements to that block and their information is stored on the memory of the processor assigned to that block. The computations related to a pore or throat are done by the processor to which the element is local. Consider two neighboring blocks *A* and *B* as shown in Figure 4. Pore *i* and throat *ij* are local to block *A*, which is assigned to processor *a*, and pore *j* is local to block *B*, which is assigned to processor *b*. Processor *a* is responsible for computations related to pore *i*, and throat *ij* and processor *b* is responsible for computations related to pore *j*. However, during

some computations, processors *a* and *b* might also need the information related to pore *j* and throat *ij*, respectively. Therefore pore *j* and throat *ij* are considered as *inter-block* elements to blocks *A* and *B*, respectively, and part of their information needs to be stored in the memory of their respective processors as well. The information related to inter-block elements needs to be communicated during simulations between neighboring processors. MPI (Message Passing Interface) libraries are used to carry out communications between processors in this model.

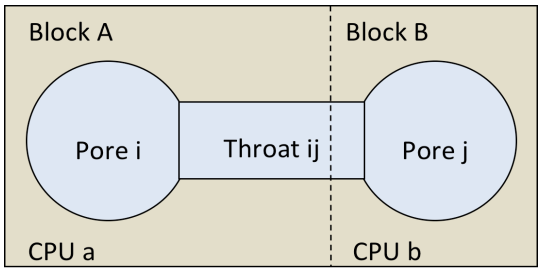

Figure 4: Local and inter-block elements. Pore *i* and throat *ij* are local to block *A*, which is assigned to processor *a*. Pore *j* is local to block *B*, which is assigned to processor *b*. Pore *j* and throat *ij* are inter-block elements to blocks *A* and *B*, respectively.

2.8 The Model Algorithm

The general outline of the model is explained in this section. Algorithm flow chart of the model is presented in Figure 5. The first step is reading the simulation parameters, which include the network decomposition scheme, fluid properties such as viscosities and densities, rock-fluid properties such as contact angles and the interfacial tension, inlet flow rates, and the outlet boundary condition.

The next step is reading the pore network data and decomposing it among the available processors. As explained earlier, the pore network is decomposed into multiple blocks based on a decomposition scheme given by the user. The decomposition scheme needs to be designed in a way that will result in approximately equal loads on every processor. Every processor calculates a range of *x*, *y*, and *z* coordinates and stores the information of the elements whose coordinates are in those ranges.

The simulations usually start with fully water saturated pores and throats. After setting the initial fluid phase occupancy in the pores and throats, the isolated elements are detected in the pore network. A parallel clustering algorithm is developed for the cluster detection in a decomposed domain. The clustering starts on the single processor to which the starting element belongs. The cluster starts growing and as soon as it reaches the boundaries of the starting block, new processors start the clustering process. The clustering continues until either an escape route is found to the inlet or outlet of the network or all the elements in the cluster have been detected. When the latter happens the elements in the cluster are given a trapped flag. This clustering module is also used when the connection of the non-wetting phase place to one or more of its neighbors is lost as a result of the displacement.

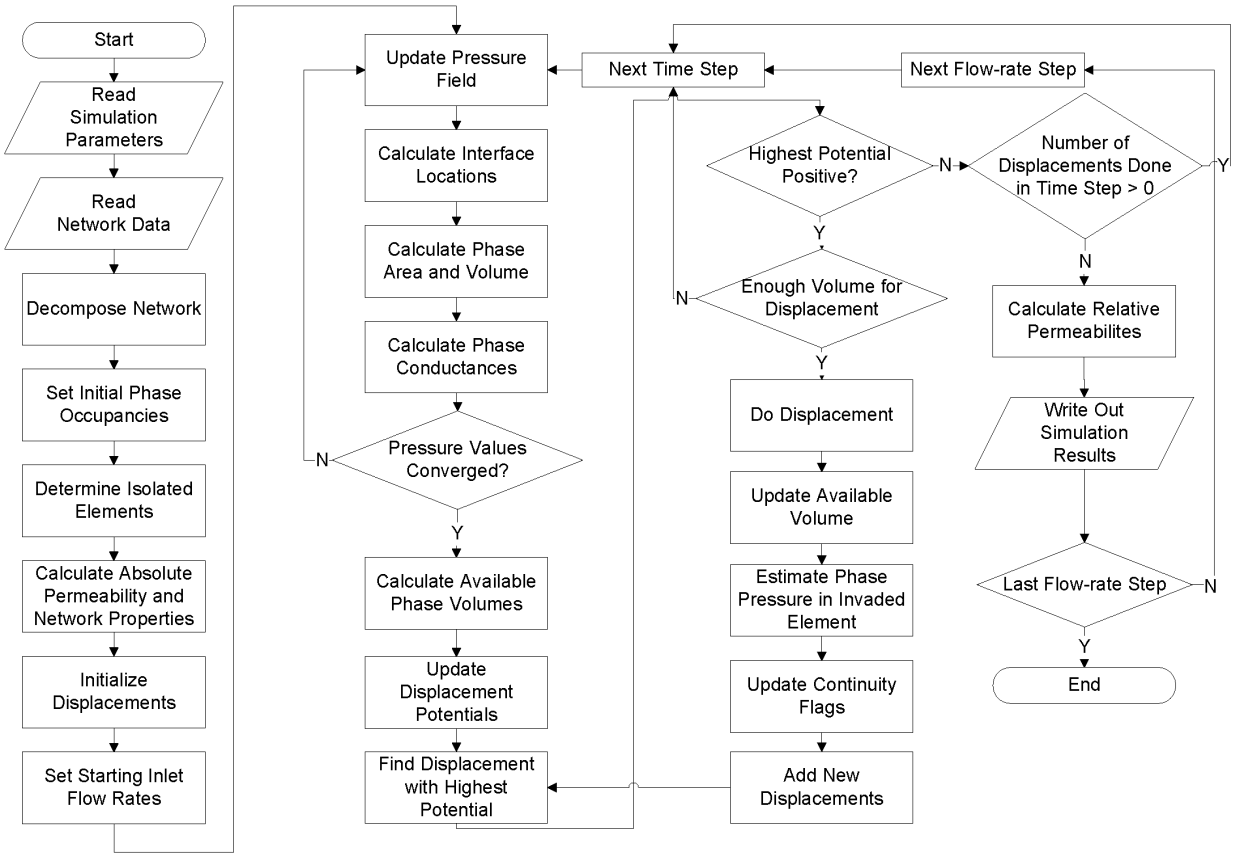

Figure 5: The algorithm flow chart of the dynamic pore network model presented in this work.

After the detection of the isolated elements in the pore network, the absolute permeability and porosity of the pore network is calculated. Single phase flow equations are written in the network that is full of water and by solving the resulting system of linear equations the pressure field in the network is obtained. Knowing the total pressure drop across the network for a given flow rate, the absolute permeability is calculated by using the Darcy's law:

$$K = \frac{\mu Q L}{A \Delta P} \quad (14)$$

where K is the absolute permeability, μ is the viscosity, Q is the inlet flow rate, L is the length of the network in the flow direction, A is the cross-sectional area, and ΔP is the pressure drop across the network. Next, the initial displacements from the inlet are detected and added to the system. The elements connected to the inlet of the network are examined and all possible displacements from the inlet to these elements are added to the displacement lists.

Now that the model has been initialized, the first flow-rate step is started by setting the first pair of wetting and non-wetting phase flow rates as the inlet boundary condition. The pressure field is computed with the new inlet flow rates as explained earlier. The new pressure values are used to update the corner interface locations. After the new corner interface locations are found, the cross-sectional area and volume of each phase in each pore and throat is calculated. Since the cross-sectional area open to flow might have changed due to corner interface movements, phase conductances are

updated in each pore and throat. Using an iterative procedure the pressure calculation, corner interface update, area-volume calculations, and phase conductance calculations are repeated until the pressure values converge.

After the pressure values converge the first time step is started. The available volume of each phase during a time step is calculated by multiplying the time step length by the inlet flow rate of that phase. The time step length is an input parameter that has different values for different flow-rate steps. Next, the displacement potentials are updated based on the current pressure field in the pore network. The displacement with the highest positive potential is identified as the most favorable displacement. If no displacement with a positive potential exists, the simulation goes to the next flow-rate step.
After detecting the most favorable displacement, the volume of the invading phase required to perform that displacement is determined. This volume is estimated by comparing the old and new configurations of fluids in the element in which the displacement will take place. If the volume required for carrying out the most favorable displacement is lower than or equal to the available volume during that time step, the displacement takes place. However, if the available volume is not sufficient for doing the displacement, the simulation goes to the next time step. After a displacement takes place, the amount of available volume is updated by subtracting the displacement volume from it. The pressure value of the invading phase in the invaded element is estimated based on the pressure gradient of the invading fluid phase and the coordinates of the invaded element.

When a pore-scale displacement takes place, the fluid configuration in the pertinent pore or throat changes. During some wetting to non-wetting phase, especially snap-off type, displacements, the non-wetting phase in the neighboring elements may become disconnected from the continuous non-wetting phase cluster, and trapped clusters of the non-wetting phase may form. This phenomenon is detected by sophisticated *chain connectivity* and clustering modules, which are explained in detail by *Piri and Blunt* [117]. These modules have been heavily parallelized. The continuity flags of fluid phases in neighboring elements are updated after a displacement takes place.

New pore-scale displacements are detected and added to the system. These displacements might be valid or invalid, i.e., involving a trapped phase place, when they are detected. The displacements continue to take place until no displacement with a positive potential is left. At that point, the system has reached a steady-state condition. The relative permeabilities, phase saturations, pressure distributions, and fluid occupancy data are reported at steady-state points. After reporting the simulation results, the simulation ends if it is at the final flow-rate step. Otherwise it goes to the next flow-rate step.

3 Results and Discussions

In this section, the dynamic pore network model described in Section 2 is used to perform a two-phase steady-state simulation in the Berea sandstone pore network. The results of core-flooding tests from Experiment 2 in *Aghaei and Piri* [130] were used for the validation of the simulation results in this report.

3.1 Simulation Procedures and Conditions

The simulation was performed in the Berea sandstone pore network that was constructed from high-resolution micro-CT images of the Berea core sample used Experiment 2 in *Aghaei and Piri* [130]. The

Berea pore network had the same dimensions as the Berea core sample used in the core-flooding tests (see Table 1). The properties of fluids that were measured during Experiment 2 [*130*] were given as inputs to the model to replicate the fluid systems of the experiment (see Table 2). The simulation was performed using the same wetting-phase and non-wetting-phase flow rates used in Experiment 2. These flow rates and their corresponding capillary numbers are presented in Table 3.

Table 2. The properties of fluids used in the simulation.

Fluid	Viscosity (cP)	Density (gr/cm^3)	IFT (mN/m)
Soltrol 170 (non-wetting)	2.851	0.774	41.33
Brine 7.5 wt % NaI (wetting)	1.240	1.055	

The simulation was started with a fully wetting phase saturated pore network. The wetting and non-wetting phases were injected from the inlet at constant flow rates. A predetermined constant pressure, similar to outlet pressures used in the experiment, was maintained at the outlet. The vertical orientation of the core sample was simulated by using the appropriate coordinates of pore elements as the height in gravity pressure drop calculations.

Table 3. The wetting-phase and non-wetting-phase flow rates and their corresponding capillary numbers used in the simulation.

	FF no.	$f_{wetting}$	$Q_{wetting}$ cm^3/min	$Q_{non\text{-}wetting}$ cm^3/min	N_c	Scanned spots[a]
Drainage	1	0.952	0.1	0.005	5.07×10^{-7}	1,2,3
	2	0.833	0.05	0.01	1.01×10^{-6}	2
	3	0.5	0.02	0.02	2.03×10^{-6}	2
	4	0.167	0.01	0.05	5.07×10^{-6}	2
	5	0.048	0.005	0.1	1.01×10^{-5}	2
	6	0.007	0.001	0.15	1.52×10^{-5}	1,2,3
Imbibition	1	0.038	0.002	0.05	2.40×10^{-7}	2
	2	0.167	0.004	0.02	4.80×10^{-7}	2
	3	0.444	0.008	0.01	9.60×10^{-7}	1,2,3
	4	0.667	0.01	0.005	1.20×10^{-6}	2
	5	0.909	0.02	0.002	2.40×10^{-6}	2
	6	1	0.05	0	6.00×10^{-6}	1,2,3

[a] Spots 1, 2, and 3 represent bottom, middle, and top sections of the core sample, respectively.

3.2 Steady-State Criteria for Simulations

In the simulation, the pore-scale displacements were carried out in the order of highest-to-lowest displacement potential. The displacements were carried out until no displacement with a positive potential was left in the system. At that point, the system had reached the steady-state condition for one set of inlet flow rates. The simulation and experimental results are compared against each other at steady-state points.

3.3 Contact Angles Used in Simulations

The in-situ contact angles measured during the experiments in the Berea sandstone core sample obtained from *Aghaei and Piri* [130] were used to design realistic contact angle distributions in the pore network. Table 4 lists the average, minimum, and maximum values of the random distributions of the receding and advancing contact angles used in the simulation in the Berea pore network.

Table 4. Contact angles used in the simulation.

Type	Average (°)	Minimum (°)	Maximum (°)
Receding	16	6	26
Advancing	50	40	60

3.4 Comparison with Experimental Results

As explained in *Aghaei and Piri* [130], in Experiment 2, the middle section of the Berea core sample was scanned in all fractional flows. The bottom and top parts of the core were scanned in selected fractional flows (see Table 3). The scanning resolution was 2.49 µm in all directions. For brine saturation profile measurements, the 2D micro-CT slices were divided into 60 groups of 30 slices. The thickness of each group was 74.7 µm. In the simulation, the pore network was divided into 60 partitions in the same middle, bottom, and top sections of the medium as Experiment 2, and the brine saturation was calculated in each partition. The brine saturation profiles in the middle section of the medium at the end of each fractional flow obtained from the simulation and experiment are presented in Figures 6 and 7. The brine saturation profiles in the bottom and top sections of the medium at the end of selected fractional flows are shown in Figures 8 and 9, respectively. The saturation profiles from the simulation compare well with those from Experiment 2 in *Aghaei and Piri* [130]. Since this experiment was performed under capillary-dominated displacement regime, the saturation profiles are uniform along the length of the sample, a condition that is critical for steady-state relative permeability measurements [*131*]. Therefore, there is almost no difference between the saturation values in the middle, bottom, and top sections of the medium.

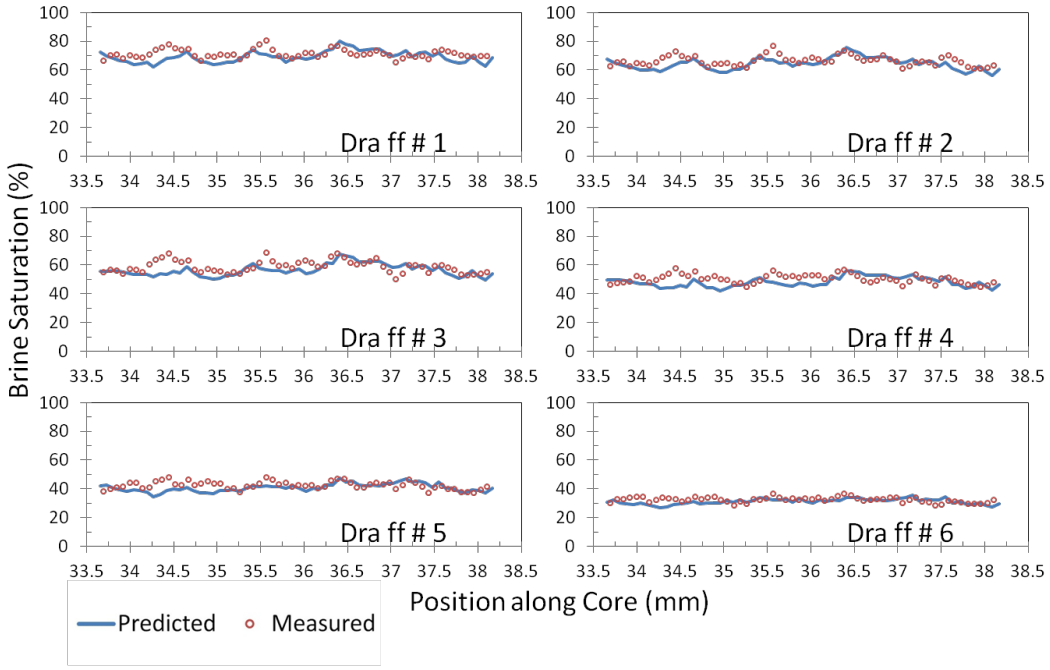

Figure 6: Predicted and measured brine saturation profiles in the middle of the medium at the end of drainage fractional flows.

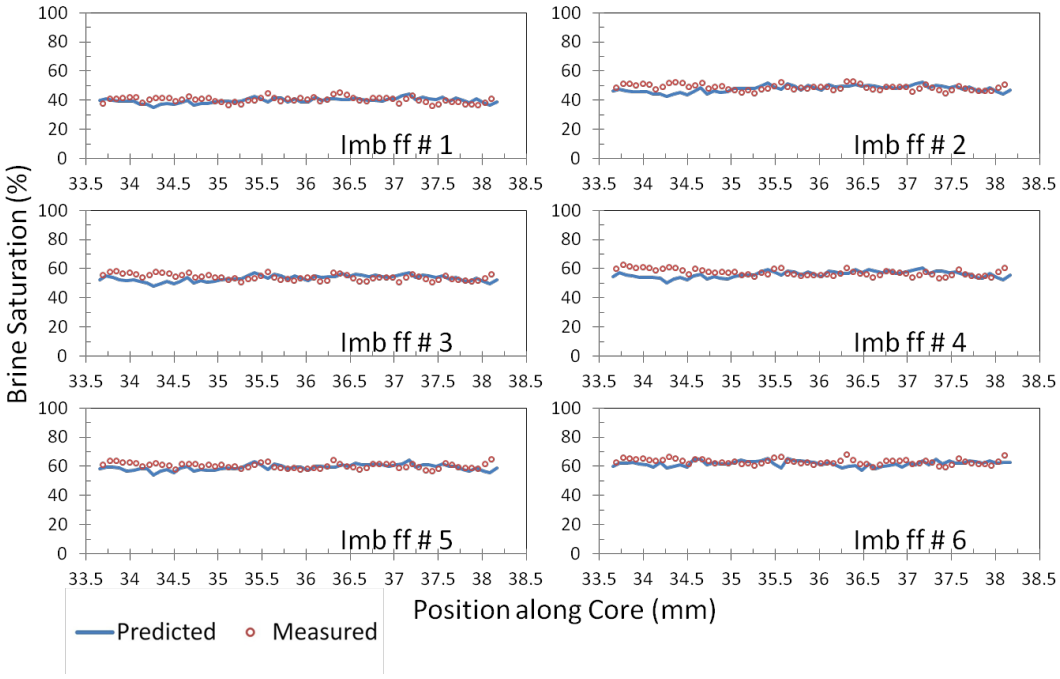

Figure 7: Predicted and measured brine saturation profiles in the middle of the medium at the end of imbibition fractional flows.

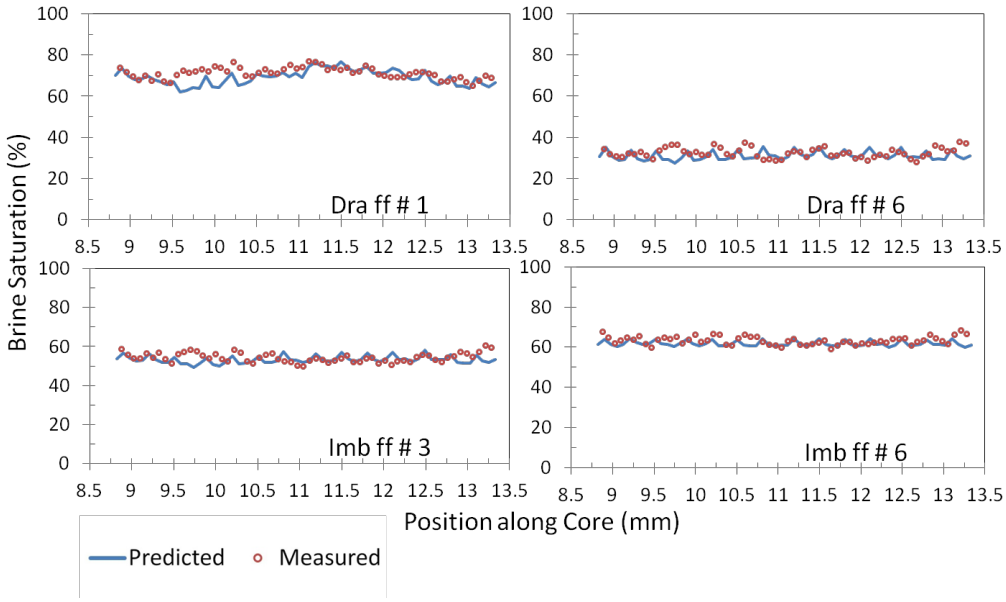

Figure 8: Predicted and measured brine saturation profiles in the bottom of the medium at the end of selected fractional flows.

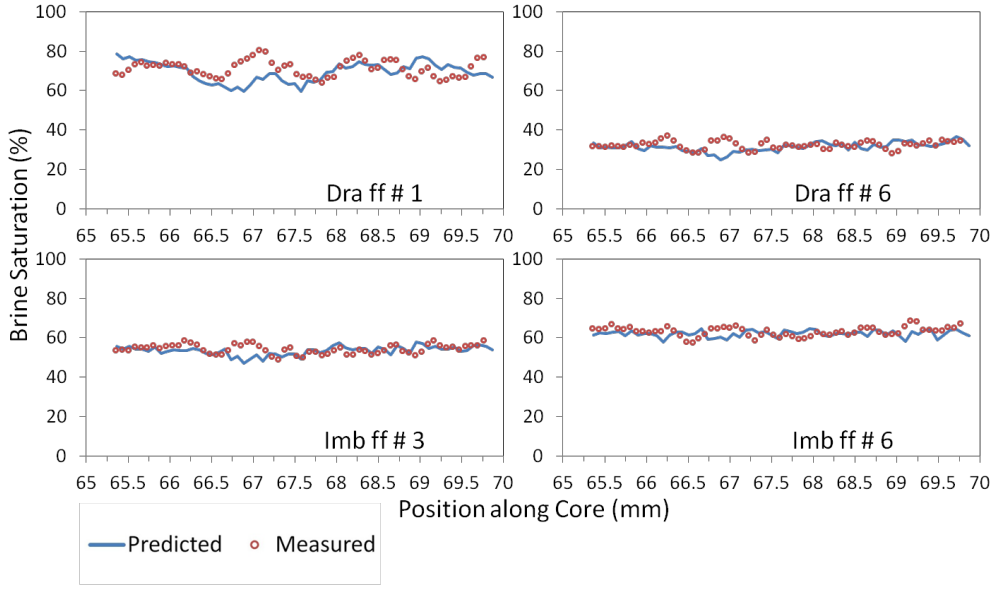

Figure 9: Predicted and measured brine saturation profiles in the top of the medium at the end of selected fractional flows.

Fractional flows of brine versus saturation obtained from the simulation and the experiment at each steady-state point are presented in Figure 10. The fractional flow curves show good agreement between the measured and predicted data.

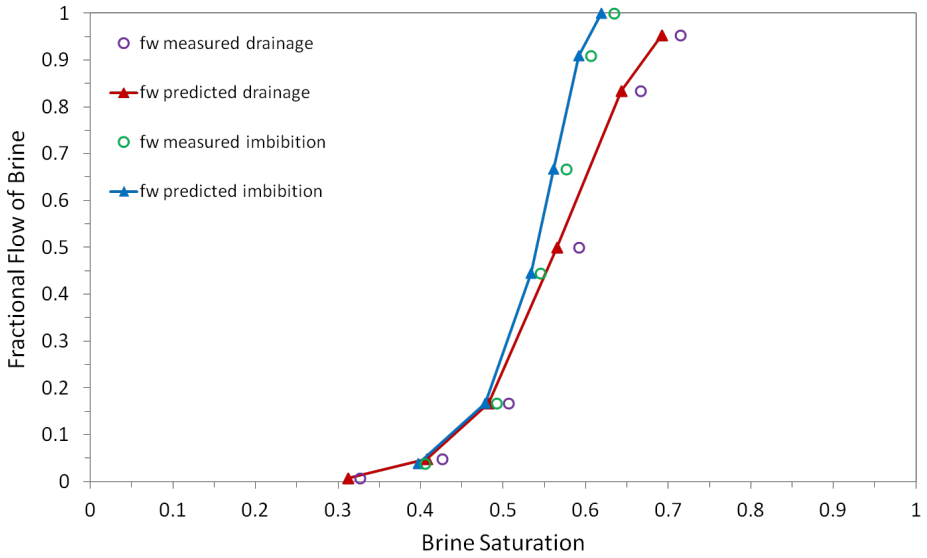

Figure 10: Fractional flow curves obtained from the simulation and Experiment 2 in *Aghaei and Piri* [130].

The predicted relative permeabilities are compared against relative permeabilities from Experiment 2 in *Aghaei and Piri* [130] and the data from *Oak* [132]. Figure 11 shows the relative permeabilities from the simulation, Experiment 2, and *Oak* [132]. As shown in this figure, the predicted and measured relative permeability and saturation values show good agreement. The data from the simulation and Experiment 2 in *Aghaei and Piri* [130] show a slight discrepancy with the data from *Oak* [132], which may be attributed to the differences in the samples used. For instance, the absolute permeabilities of the samples used by *Oak* [132] were 200 mD, 800 mD, and 1000 mD while our sample had an absolute permeability of 623 mD. Furthermore, the core samples used by *Oak* [132] were fired before performing the flow experiments. It is noteworthy that in the quasi-static pore network models that have been used to match the data from *Oak* [132], the pore networks have higher porosity and clay content than the Berea sandstone network used in this work (see, for instance, *Lerdahl et al.* [133]; *Piri and Blunt* [117,118]).

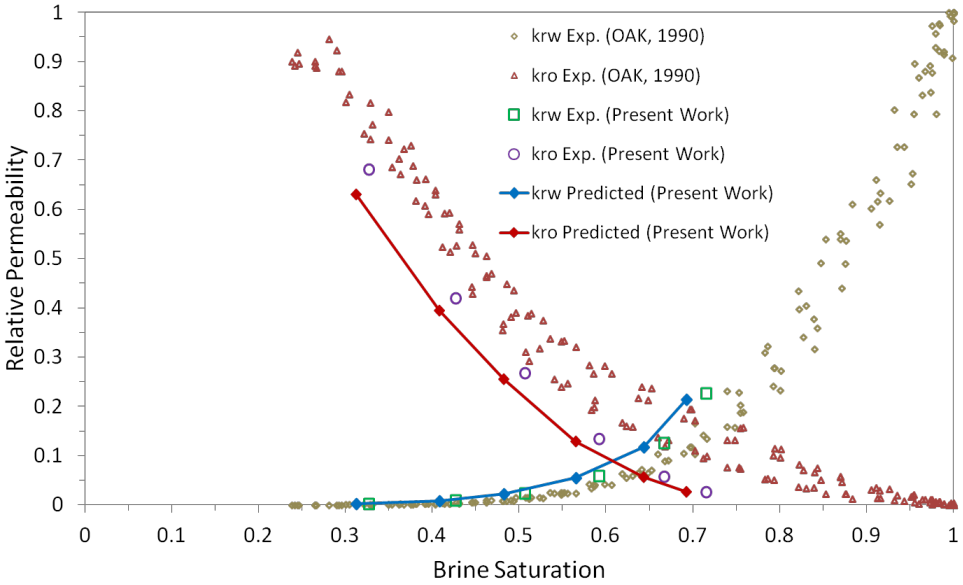

(a)

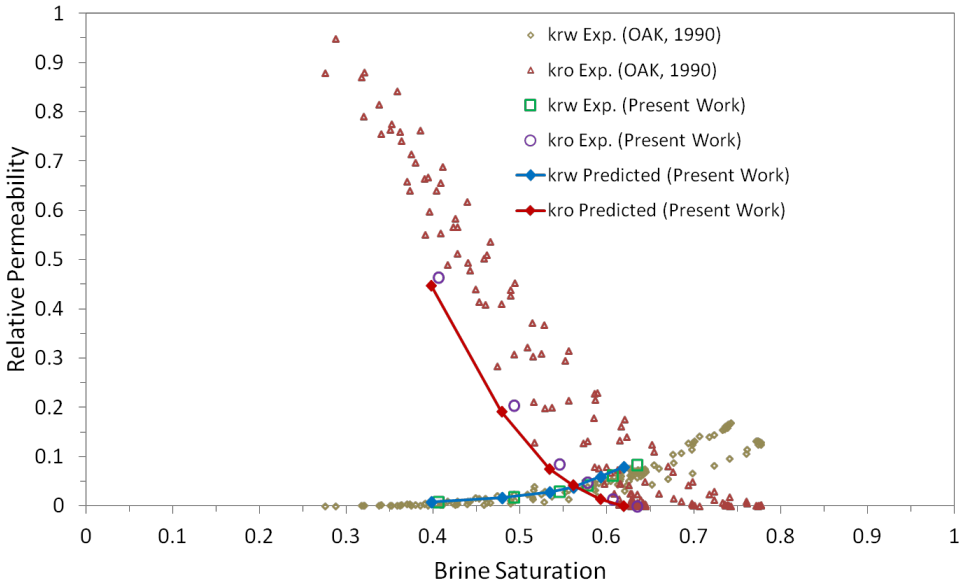

(b)

Figure 11: Berea sandstone relative permeabilities versus brine saturation. The predicted data from the simulation are compared against the measured data from Experiment 2 in *Aghaei and Piri* [2014] and the data by *Oak* [132]. (a) Drainage. (b) Imbibition.

4 Conclusions

A new dynamic pore network model that is capable of simulating flow at the core scale was developed. This dynamic pore network model can be used as a platform to study various two-phase flow processes in porous media. The dynamic model included five critical elements: (1) the pressure drops associated with capillary, viscous, and gravity forces, (2) wetting-phase corner flow, (3) corner interface adjustments based on changes in local capillary pressure, (4) simultaneous injection of wetting and non-

wetting phases from the inlet of the medium at constant flow rates, (5) parallelization based on a three-dimensional domain decomposition scheme that made simulations on large core-size samples possible, and (6) constant pressure boundary condition at the outlet. These features make the model, to the best of our knowledge, the first of its kind that can be used to bridge the gap between pore and core scales for a wide range of flow problems in different conventional rock types.

The model is validated by comparing the simulation results against the steady-state core-flooding experimental data available in *Aghaei and Piri* [130] and *Oak* [132]. The predicted saturation profiles, fractional flow curves, relative permeabilities, and residual non-wetting-phase saturations compared successfully against their experimental counterparts. The encouraging agreement between the measured results and the predicted results is the manifestation of the relevant two-phase flow physics along with the realistic boundary conditions and fluid and rock properties used in the model. This makes the pore network model introduced in this work a powerful platform for studying complex dynamic two-phase flow processes in porous media in core-size rock samples. Moreover, this dynamic model can be used for coupling with continuum-scale reservoir simulators.

Task 5: Reservoir modeling activities
PI: Frederico Furtado

A) Thermodynamic Models of Mixed $scCO_2$ Dissolution in Brine

Part 1 Model Description

1.1 Solubility Model of SO_2 + CO_2 Mixtures in Brine

We model the water molecule to consist of a single segment with two associating sites of proton-donor type and two associating sites of proton-acceptor type. The association between molecules, in this case also known as hydrogen bonding, occurs between two sites of different types. The proton-donor sites in water molecules belong to the hydrogen atoms, while the other type belongs to the electron lone-pairs in the oxygen atoms. Therefore, four electron lone-pairs that are also present in the oxygen atoms of SO_2 and CO_2 contribute four associating sites of proton-acceptor type in each molecule. These sites enable the gases to cross associate with water molecules, but do not associate among themselves. For SO_2, there is an extra electron lone-pair in sulfur atom, which makes the total of five sites of proton-acceptor type. The presence of this extra site is consistent with the fact that SO_2 is more soluble in water than CO_2. Figure 1 shows the associating sites in H_2O, SO_2, and CO_2 in our model.

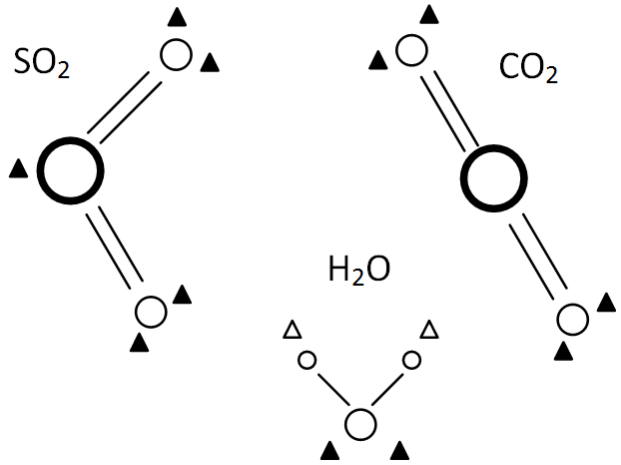

Figure 1: Association scheme of the molecules in our model; triangles are the associating sites (empty: proton-donor type; filled: proton-acceptor type)

The ions are modeled as single segments that interact with one another through the hard-core and long-range Coulombic interactions. They also interact with the electrically neutral molecules (water and the gases) through the hard-core and dispersion interactions. In this work, the brine is assumed to contain only NaCl, which is the major salt dissolved in aquifers. This approximation is justified through investigative calculations [134], from which it is known that the approximation introduces noticeable difference (at about 5%) only for the density at the highest salinity considered in this work.

In the following, we will briefly introduce the EOS that we use to apply the model for this particular system, i.e., PCSAFT/PMSA and eCPA. The details of both EOS can be found in Tan's work [135].

PCSAFT/PMSA. The EOS calculates the residual Helmholtz free energy of the chemical system, i.e., the gases + brine in our case, as follows.

$$\widetilde{A}^{\text{res}} = \widetilde{A}^{\text{hs}} + \widetilde{A}^{\text{chain}} + \widetilde{A}^{\text{disp}} + \widetilde{A}^{\text{assoc}} + \widetilde{A}^{\text{ion}} \quad (1)$$

where the superscripts of the free energy terms on the right-hand side of eq 1 are hard-sphere, chain, dispersion, association, and ion, respectively. These refer to the molecular interactions in the system: the hard-core repulsion, the chain-forming covalent bond, the van-der-Waals type of dispersive attraction, the highly directed associating interaction through hydrogen bonds, and the long-range electrostatic interactions between ions, respectively.

For each species in the system, the EOS has three parameters: the segment number m, the segment diameter σ, and the segment energy ε. For self-associating species, there are two additional parameters: the association volume κ and the association energy ε_A. For ions, we have another extra parameter, namely the hydrated diameter δ. The neutral species parameters are derived from the vapor-liquid equilibria (VLE) data, i.e., the vapor pressure and the saturated liquid density. The ionic parameters are derived from the mean activity coefficient ($\gamma_\pm$) data along with the density of the aqueous electrolytes (in our case, water + NaCl). Therefore, the ionic parameters are specific for aqueous solutions (water as the solvent). All PCSAFT/PMSA parameters are listed in Table 1. SO_2 and CO_2 do not self-associate, as indicated by their $\varepsilon_A = 0$, but cross associate with water molecules, as facilitated by their κ equal to that of water [136].

Table 1. PCSAFT/PMSA pure-component and ionic parameters[a]

	m	*σ* [Å]	ε/k_B [K][b]	Associating sites[c]	ε_A/k_B [K]	*κ*
Water	1.2190	eq 20[d]	213.5741	(2,2)	1851.9773	0.052246
CO_2	2.0729	2.78520	169.2100	(0,4)	0	0.052246
SO_2	2.7566	2.71150	210.0274	(0,5)	0	0.052246
Na^+	1.0000	2.25183	eq 21[d]	(0,0)	-	-
Cl^-	1.0000	2.34298	eq 22[d]	(0,0)	-	-

[a]The ionic hydrated diameters are given in eq 23 and eq 24.
[b]k_B: Boltzmann constant.
[c]First digit is the number of proton-donor type of associating sites; the second digit is the number of proton-acceptor type of associating sites.
[d]Temperature-dependent functions as given in the corresponding equations.

eCPA. This EOS is the electrolyte version of the Cubic Plus Association EOS [137,142], which adds the association free energy term to a cubic EOS (PR [138] or SRK [139,140]) to describe systems with associating molecules. Without the association term, the cubic EOS does not perform well for such systems. The residual Helmholtz energy for the eCPA version[29,37] used in this paper is:

$$\widetilde{A}^{\text{res}} = \widetilde{A}^{\text{SRK}} + \widetilde{A}^{\text{assoc}} + \widetilde{A}^{\text{PMSA}} + \widetilde{A}^{\text{Born}} \quad (2)$$

where the superscripts of the energy terms on the right-hand side are the SRK term from the original cubic EOS, the association term, PMSA ionic term that are principally the same as in eq 1, and Born term that accounts for the ion transfer from a gas phase to a liquid solvent. Details of this EOS may be found elsewhere[38] and in the supporting information of this paper.

Table 2. eCPA pure-component and ionic parameters

	a_0 [Pa.m^6/mol^2]	b [× 10^{-5} m^3/mol]	c_1	Associating sites	ε_A/k_B [K][c]	κ	σ [× 10^{-10} m]
Water[a]	0.12277	1.45	0.6736	(2,2)	2003.248	0.0692	-
CO_2[b]	0.35079	2.72	0.7602	(0,4)	0	0.0692	-
SO_2	0.64621	3.52	0.8113	(0,5)	0	0.0692	-
Na^+ [d]	3.01600	1.04	0	(0,0)	-	-	3.21
Cl^- [d]	0.31500	1.99	0	(0,0)	-	-	3.98

[a]Ref [195]; [b]Ref [196];[c] k_B: Boltzmann constant.
[d] Ref [141], in which b is calculated from σ.[2]

For each species, the eCPA has three parameters for the cubic SRK term: a_0, b, and c_1, in addition to the critical temperature (T_C is 647.1 K, 304.2 K, and 430.8 K for water, CO_2, and SO_2, respectively). For self-associating species, there are two additional parameters: the association volume κ and the association energy ε_A. For ions, additional information about their diameter σ is needed. The eCPA parameters for the species in our systems are listed in Table 2.

1.2 Solubility Model of NO_2 + CO_2 Mixtures in Water

NOx is probably the most complex case of absorption due to the large number of species and reactions that involve in the process. NO_x is in fact a mixture of all nitrogen oxides (N_2O, NO, NO_2, N_2O_3, N_2O_4, and N_2O_5), most of which react immediately with water upon dissolution resulting in HNO_3 (nitric acid) and HNO_2 (nitrous acid). Only N_2O (nitrous oxide) and NO (nitric oxide) do not react with water and hardly dissolve in water. Dozens of chemical equilibria, both in liquid and vapor phases, exist in the absorption and desorption processes that occur simultaneously [143]. Therefore, the knowledge of the process's physicochemical data such as the solubility of those gases in water is still incomplete [144].
Among the species that react with water, N_2O_3 (nitrogen trioxide) and N_2O_5 (nitrogen petoxide) are the anhydrate forms of nitrous and nitric acids, respectively, while NO_2 (nitrogen dioxide) and its dimer N_2O_4 (nitrogen peroxide or nitrogen tetroxide) coexist in equilibrium up to about 150 °C [145]:

$$2NO_2 \leftrightarrow N_2O_4 \quad (3)$$

Generally speaking, the term nitrogen dioxide is meant to include both NO_2 and N_2O_4. In this work we denote them with an asterisk to remind us of these duo species, i.e., NO_2*.
It is customary to summarize the overall chemical equilibrium in the absorption of NO_2* in water as [146-149]:

$$3\ NO_2^* + H_2O \leftrightarrow 2\ HNO_3 + NO \quad (4)$$

The high reactivity of NO_2* in water precludes direct measurement of physical properties such as the Henry's coefficient, the magnitude of which is customarily used in the interpretation of kinetic processes [143]. In this case, the coefficient must be indirectly inferred from kinetic studies, the results of which have large uncertainties [144].

The buildup of the products in eq 4 complicates the situation. At high concentration, HNO_3 will tend to dissociate according to [150]:

$$4\ HNO_3 \leftrightarrow 4\ NO_2 + 2\ H_2O + O_2 \quad (5)$$

which is dominant, for example, in the work series of Sage and coworkers [151-156].
The resulting oxygen may involve in another reaction with NO and NO_2 following [146]:

$$2\ NO + O_2 \leftrightarrow 2\ NO_2 \quad (6)$$

According to this reaction, the availability of O_2 is therefore required in the production of pure HNO_3 using the absorption process eq 4, i.e., to prevent the buildup of NO from halting the formation of HNO_3.

At moderate temperatures, the resulting NO or O_2 from eq 4 or eq 5, respectively, build the system pressure to levels much higher than that it would have been if the reactions did not occur [151] Still to worsen the situation, the resulting NO in eq 4 may associate with NO_2 to form N_2O_3 [143,144]:

$$NO + NO_2 \leftrightarrow N_2O_3 \quad (7)$$

N_2O_3 is unstable and reacts with water to form nitrous acid [149], HNO_2, which is often considered to involve in intermediate reactions for the overall reaction of eq 4. Both acids, HNO_2 and HNO_3, in turn also dissociate into their constituting ions in water [143,149].

Furthermore, the overall reaction eq 3 is in fact a heterogeneous equilibrium, in which the aqueous liquid phase is in equilibrium with the vapor phase above it [144]. Therefore, the system has the physical equilibrium of the phases and simultaneously the chemical reaction equilibrium in eq 4.

In summary, the complexity makes the modeling of this reacting system more difficult. In this work, we attempt to derive a model for the physical and chemical equilibria of NO_2 in water, which is needed to describe the absorption of NO_2 into aqueous solutions. This study will also be the initial step for a later application of the model in flue gas sequestration into aquifers. We also apply PCSAFT EOS [157] for this system. The details of PCSAFT/PMSA are explained in Section 1.1. The kinetics is not considered, as we

are only concerned with the equilibrium state of the system. To the best of our knowledge, it is the first attempt to model the physicochemical equilibria of this reacting system using a statistical-mechanics based EOS such as PCSAFT.

Chemical Equilibrium. The most widely-used property of the reacting system of NO_2 in water or in aqueous nitric acid solutions is the partial equilibrium constant of reaction eq 4 defined as [146,147],

$$K_1 = \frac{\left(P_{\mathrm{NO}}\right)}{\left(P_{\mathrm{NO2}}\right)^3} = \frac{\left(y_{\mathrm{NO}}\right)}{\left(y_{\mathrm{NO2}}\right)^3}\frac{1}{P^2} \tag{8}$$

which is actually a factor of the reaction equilibrium constant:

$$K = \frac{\left(\hat{f}_{\mathrm{NO}} / f^0_{\mathrm{NO}}\right)\left(\hat{f}_{\mathrm{HNO3}} / f^0_{\mathrm{HNO3}}\right)^2}{\left(\hat{f}_{\mathrm{NO2}} / f^0_{\mathrm{NO2}}\right)^3\left(\hat{f}_{\mathrm{H2O}} / f^0_{\mathrm{H2O}}\right)} \tag{9}$$

In eq 8, *y* and *P* are the gas mole fractions and the total pressure, respectively, while *f* 's with hats in eq 9 are the fugacities in mixtures and those with superscripts 0 are the fugacities at standard states, which are the ideal gas at 1 bar in vapor phase, or the pure-component fugacities at 1 bar and the system temperature in the liquid phase. The fugacity and the mole fraction of component *i* are related through:

$$\hat{f}_i = y_i \hat{\phi}_i P \tag{10}$$

where ϕ is the fugacity coefficient, which is calculated using an EOS, in our case the PCSAFT. The fugacities in mixtures in eq 9 may be calculated in either phase because the vapor and liquid phases are in equilibrium, where the fugacities are equal in both phases. However, as indicated in eq 9, the value of *K* still depends on the standard states of the phases. In this work, the vapor phase is chosen for convenience because the reaction equilibrium constant has been determined in the vapor phase [159], which can be expressed in temperature in the range of interest 293 K < *T* < 400 K as:

$$\log K = -8.84785 + 2045.88356\, T^{-1} \tag{11}$$

The value of *K* in eq 11 was determined using the experimental entropy of nitric acid gas and the known thermodynamic properties of the other reactants [159] but it has never been verified in applications due to the lack of reliable EOS in calculating the fugacity coefficients. Instead, K_1 is often used to represent this system and estimated through eq 8, i.e., the partial pressures of NO_2 and NO in the vapor phase, which may be derived from experimental measurements [146,147]. Some models for K_1 were proposed using empirical equations [160,161] and nomograms [161,162].

Whereas *K* is thermodynamically a function of temperature only [163] as evident in eq 11, it is not the case with K_1. Upon substituting the fugacities given by eq 10 into eq 9, K_1 in the vapor phase may be calculated as:

$$K_1 = \frac{\left(\hat{\phi}_{NO2}\right)^3}{\left(\hat{\phi}_{NO}\right)} \frac{\left(\hat{\phi}_{H2O}\right)}{\left(\hat{\phi}_{HNO3}\right)^2} \frac{y_{H2O}}{y_{HNO3}^2} \frac{K}{P} \tag{12}$$

Therefore, without a reliable EOS, it is not possible to connect the experimentally derived value of K_1 with the equilibrium constant K. In this work, we couple eq 11 for K with PCSAFT to calculate K_1 and match it with the literature data, thus establish the EOS validity before making predictions on the solubility of NO_2 in water at various conditions relevant to flue gas geologic sequestration.

Physical Equilibrium. The heterogeneous nature of the reaction eq 3 also requires the system to be in vapor-liquid phase equilibrium (VLE), where the fugacity of component i in the mixture is the same throughout all phases, in this case vapor (V) and liquid (L) phases:

$$\hat{f}_i^{V} = \hat{f}_i^{L} \tag{13}$$

The equality of the fugacities in eq 13 must be solved simultaneously with mass-balance equations to find the equilibrium compositions in both vapor and liquid phases:

$$\ell\, x_i + (1-\ell)\, y_i = z_i \tag{14}$$

where ℓ is the mole fraction of the liquid phase, and z_i is the overall mole fraction of component i. It is also important to realize that all mole fractions must sum up to unity:

$$\Sigma\, x_i = \Sigma\, y_i = 1 \tag{15}$$

Physicochemical Equilibrium. The VLE of the overall reaction eq 4 has 4 chemical components: H_2O, HNO_3, NO_2*, and NO. As we will show in the model, NO_2* may be treated as a component instead of two in SAFT framework. Therefore, upon bookkeeping we have 9 independent equations to solve for 9 variables: $\{x_i\}$, $\{y_i\}$, and ℓ. However, the compositions must also satisfy the chemical equilibrium represented by the reaction constant K, eq 9, consequently the mass balance of the chemical reaction, where the overall mole fractions $\{z_i\}$ in fact result from the chemical reaction and are calculated through:

$$z_i = \frac{n_{0,i} + \varepsilon \nu_i}{\sum \left(n_{0,i} + \varepsilon \nu_i\right)} \tag{16}$$

In eq 16, $\{n_{0,i}\}$ is the initial moles before the reaction occurs, v_i is the stoichiometric coefficient of species i in the reaction, and ε is the extent of reaction. An effective algorithm for this physicochemical equilibrium was adopted from Sanderson and Chien [164].

To know what inputs are needed for the equilibrium calculations, we must first determine the degree of freedom of the reacting system, which follows the Gibbs rule [154]:

$$F = N - \pi + 2 - r \tag{17}$$

where N, π, and r are the number of components, phases, and chemical reactions, respectively; in our case they are 4, 2, and 1, leading to a degree of freedom of 3. This means that beside the temperature (T) and pressure (P), we still need another entity as a known variable in order to have the information of the system complete. We may choose, for example, the loading of NO_2 in water, which can be defined as moles of NO_2 injected per 1,000 moles of water. We will use this entity to calculate the solubility of NO_2 in water.

In some previous studies, this additional entity was chosen to be the amount of nitric acid in the liquid phase that is in equilibrium with the gases in the vapor phase [146,147]. However, the experiments were carried out using an inert background gas, i.e., nitrogen, to dilute NO_2 before passing it through the aqueous liquid phase. Though this gas does not participate in the chemical reaction, its presence affects the concentrations in the equilibria in two ways: first, its mole must be added to the denominator of eq 16, and second, it participates in the physical phase equilibria, i.e., eqs 13 and 14. Therefore, instead of 4 components, in this case we have 5 components, thus 12 variables ($\{x_i\}$, $\{y_i\}$, ε, and ℓ) to solve for from 12 equations, i.e., eqs 13 – 15 and eq 9 with K from eq 11, after applying eq 16 to find $\{z_i\}$ as described elsewhere [164]. Such usage of a background gas increases the system degree of freedom by one, so that the reacting system of NO_2 in water now has a degree of freedom of 4, which means we need two known entities in addition to T and P to have the system information fixed. In reproducing their data, we choose the concentration of HNO_3 in liquid phase (x_{HNO3}) and the mole fraction of NO in vapor phase (y_{NO}) to accompany the pressure and temperature as the inputs of the calculations.

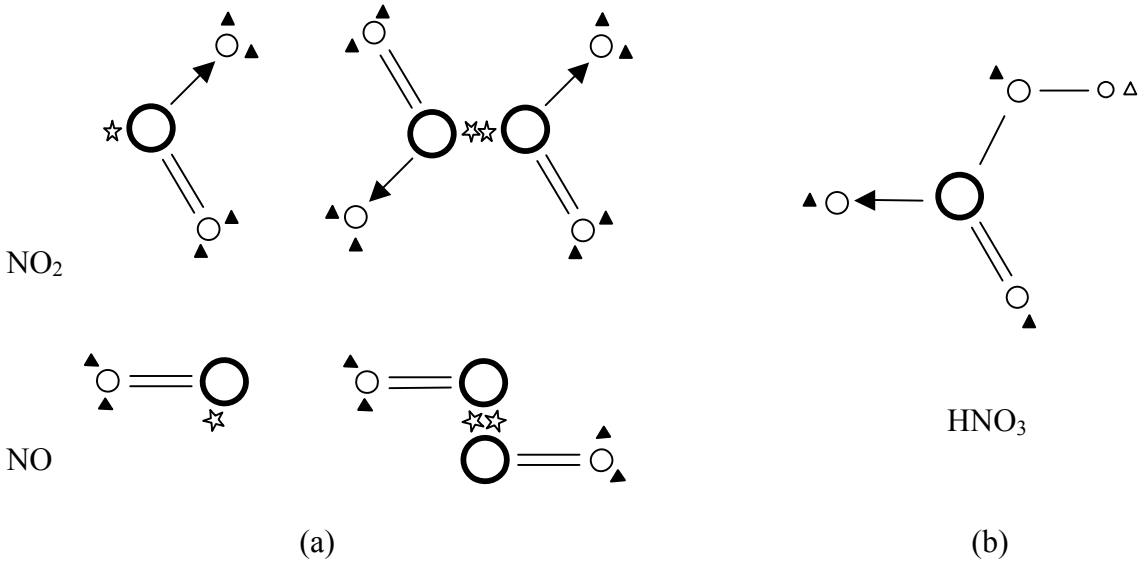

Figure 2: Association schemes used in the model: (a) NO_2 and NO molecules – stars and triangles are the associating sites (stars: dimer type; triangle: proton-acceptor type). The dimer forms are shown on the right next to them; (b) HNO_3 molecule – open triangle is the associating site of proton-donor type (hydrogen atom)

Molecular Association. To make all calculations in the previous section, we apply an EOS, the input of which needs some modeling for the molecules in the system. Because NO_2, H_2O, NO, and HNO_3 are associating molecules, the model for the molecular association is pivotal in this work.

As commonly done, we model the water molecule to consist of a single segment with two associating sites of proton-donor type and two associating sites of proton-acceptor type. The association between molecules, in this case also known as hydrogen bonding, occurs between two sites of different types. The proton-donor sites in water molecules belong to the hydrogen atoms, while the other type belongs to the electron lone-pairs in the oxygen atoms. Such association scheme is known as type 4C [165].

Four electron lone-pairs that are also present in the oxygen atoms of NO_2 contribute four associating sites of proton-acceptor type in the molecule. These sites enable NO_2 to cross associate with water molecules, but do not associate among themselves. However, NO_2 molecules are capable to form dimers N_2O_4 through eq 3, which is in fact dominant at low temperatures particularly in liquid phase [166]. In SAFT framework, the dimerization is modeled as an association bonding through a site, in this case on the nitrogen atom, that is neither proton-donor nor proton-acceptor type, known as type 1A [165], which can associate between themselves but not with other types of associating sites. This approach provides us with an advantage that we do not need to consider N_2O_4 as an independent species, so that NO_2 is actually NO_2* in SAFT framework exactly as in the overall reaction eq 4. This treatment has been proven effective [167]. Dimerization also occurs for NO molecules [168], but they do not cross associate with water molecules as inferred from molecular simulations [169]. The monomer and dimer structures of NO_2 and NO in our model are depicted in Figure 2a.

For nitric acid molecules, the presence of a proton-donor site on the hydrogen atom and some proton-acceptor sites at the oxygen atoms makes both the self-association and cross-association with water molecules possible. There are six electron lone-pairs at three oxygen atoms in the molecule, but only some of them are effective as proton-acceptor sites due to the steric effects arising from crowded configuration of the oxygen atoms. Similar situation has been found in alcohols, in which the presence of the alkyl group allows only one effective site on the oxygen atom [170]. Therefore, one associating site may be assigned on each oxygen atom in HNO_3 as shown in Figure 2b. However, this assignment does not give adequate representation of binary phase equilibria data, particularly that of H_2O/HNO_3, which is dominant in the investigated chemical systems. It may be caused by the presence of the proton-donor site on the hydrogen atom that introduces steric shielding to the neighboring proton-acceptor site. The fact that HNO_3 undergoes ionic dissociation in water provides an estimate of the number of proton-acceptor sites to be between 2 and 3, corresponding to molecular and ionic structures, respectively. We choose the average value of 2.5 for this number, which is quite unusual being a non-integer, but justifiable as it turns out to represent the binary H_2O/HNO_3 very well as discussed later in the paper. The direct benefit of this assignment is that there is no need to explicitly treat the ionic dissociation of the acid in the SAFT framework, which makes the calculation tasks much simpler.

Cross associations occur between HNO_3 and H_2O, HNO_3 and NO_2, as well as NO_2 and H_2O. The association between HNO_3 and H_2O is made asymmetric, in which the site on the hydrogen atom of HNO_3 does not cross associate with oxygen atoms of water. Cross association occurs only between hydrogen atoms of H_2O and sites on oxygen atoms of HNO_3. This asymmetric assignment is needed to make the model work in representing the azeotropic binary mixture of HNO_3/H_2O. In addition to the aforementioned cross associations, the NO_2 and NO molecules are also allowed to cross associate each

other through their type-1A associating sites to account for the fact that the molecules may combine as N_2O_3 through eq 7 [143,144].

To validate the model against the experimental K_1, where nitrogen is used as the background gas, the nitrogen molecule is to be included. But because nitrogen is a non-associating molecule, it does not have any association sites.

Part 2 Results and Discussions

2.1 Results and Disscussions of SO_2+CO_2+Brine Solubility Model

In mixtures, where interactions between unlike species occur, binary interaction parameters k_{ij} are needed and derived from binary VLE data for interactions between neutral species, and solubility data of the gases in brine for interactions involving ions. They are generally functions of temperature, i.e.,

$$k_{ij}(T) = \mathrm{p} + \mathrm{q} \times 10^{-4}\, T + \mathrm{r} \times 10^{-6}\, T^2 \qquad (18)$$

where the coefficients p, q, and r are listed in Table 3 for PCSAFT/PMSA and eCPA. The experimental data used to fit these parameters are listed in Table 4. The binary interaction parameters are used to correct the molecular interactions and implemented in the combining rule of the energy parameters:

$$\varepsilon_{ij} = \sqrt{\varepsilon_i \varepsilon_j}\left(1 - k_{ij}\right) \qquad \text{for PCSAFT/PMSA} \qquad (19a)$$

$$\alpha_{ij} = \sqrt{\alpha_i \alpha_j}\left(1 - k_{ij}\right) \qquad \text{for eCPA} \qquad (19b)$$

where the eCPA energy parameter α in eq 19b is related to the EOS parameters a_0 and c_1 [135].

Table 3. Coefficients of binary interaction parameters in eq 18

Binary	PCSAFT/PMSA			eCPA		
	p	*q*	*r*	*p*	*q*	*r*
H_2O-CO_2	-0.41727	25.48	-3.2	-1.1996	70.624	-8.0
H_2O-SO_2	-0.00700	-	-	-0.3309	19.6727	-2.0629
H_2O-Na^+	-	-	-	0.5067	-74.695	13.494
H_2O-Cl^-	-	-	-	-0.3107	22.785	-4.3264
CO_2-SO_2	0.18204	-4.2143	-	0.1894	-3.33	-
CO_2-Na^+	2.00721	-87.22	12.17	0.7123	-81.132	13.636
CO_2-Cl^-	2.00721	-87.22	12.17	0.7123	-81.132	13.636
SO_2-Na^+	-0.01272	6.25	-	1.6308	-134.34	21.25
SO_2-Cl^-	-0.01272	6.25	-	1.6308	-134.34	21.25
$k_{D\text{-}CO2}$[a]	-	-	-	8.4260	–530.66	68.182
$k_{D\text{-}SO2}$[a]	-	-	-	–3.9650	175.97	–31.250

[a] k_D is a fitted parameter in the expression of water dielectric constant to account for the presence of the gases [135].

Table 4. The experimental data used to fit the binary interaction parameters

Binary	Reference	Temperature range	Salt molality
H_2O-CO_2	Wiebe & Gaddy [175]	25 - 75ºC	-
H_2O-SO_2	Rumpf & Maurer [172]	20 - 120ºC	-
H_2O-NaCl	Pitzer et al. [192]	25 - 120ºC	-
CO_2-SO_2	Cumming [180]	40 - 130ºC	-
CO_2-NaCl in H_2O	Rumpf et al. [176] Yan et al. [194]	40 - 120ºC 50ºC	4 & 6 1 & 5
SO_2-NaCl in H_2O	Xia et al. [193]	40 - 120ºC	3

To improve the performance of PCSAFT/PMSA in aqueous electrolytes, the segment-diameter parameter of water was made temperature-dependent in representing the coexistence curve [171]. In this work, we refitted the parameter using a polynomial in reciprocal of temperature ($1/T$) to get fewer coefficients but still obtain an equal performance. As the temperature changes from 25°C to 120°C, the water segment diameter varies from 2.8158 Å to 2.8247 Å. The temperature-dependent parameters, mostly of the ions, are listed in the following equations:

$$\sigma_1 = 2.798384 + 120.733275\ T^{-1} - 71515.85\ T^{-2} + 11052303\ T^{-3}\ [\text{Å}] \quad (20)$$

$$\varepsilon^{+}/k_B = 798.7893\ [1 - 628.9294\ (T^{-1} - 298.15^{-1})]\ [\text{K}] \quad (21)$$

$$\varepsilon^{-}/k_B = 112.2339\ [1 + 0.3644\ (T^{-1} - 298.15^{-1})]\ [\text{K}] \quad (22)$$

$$\delta^{+} = 1.6470\ [1 - 1475.5590\ (T^{-1} - 298.15^{-1})]\ [\text{Å}] \quad (23)$$

$$\delta^{-} = 8.2552\ [1 + 565.6977\ (T^{-1} - 298.15^{-1})]\ [\text{Å}] \quad (24)$$

where the subscript 1 refers to water and the superscripts + and – refer to the positively- and negatively-charged ions, respectively (k_B is the Boltzmann constant).

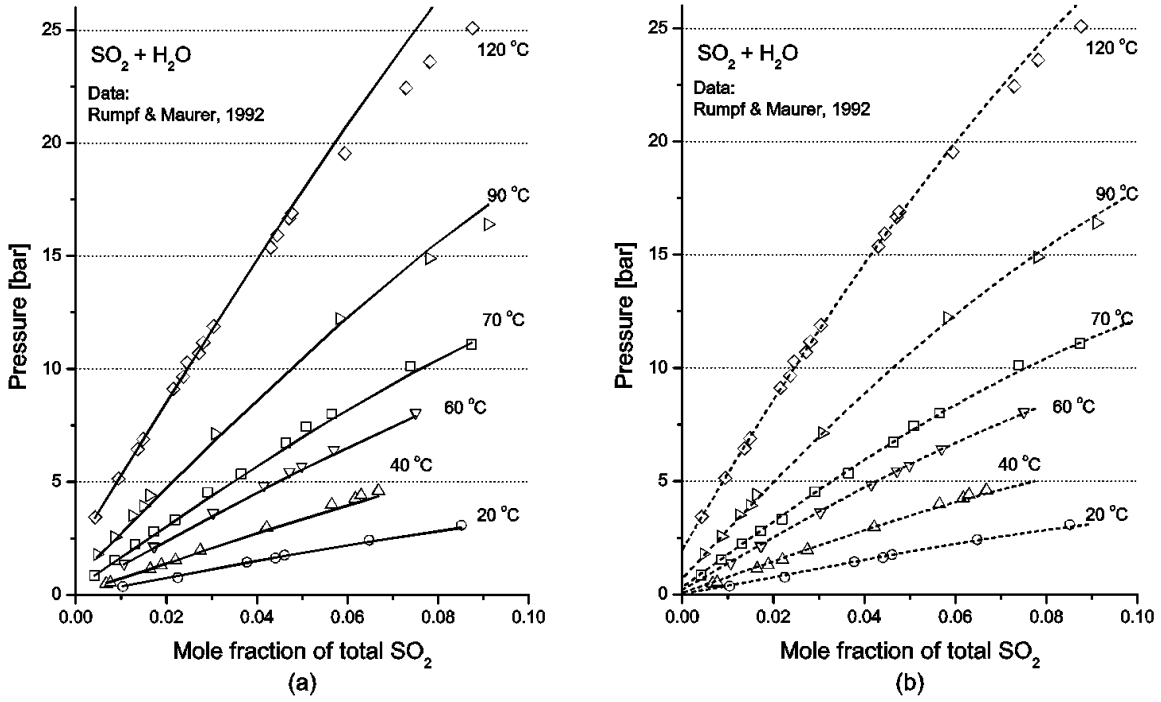

Figure 3: Fitted EOS for SO_2 dissolution in water: (a) PCSAFT (b) CPA; symbols are experimental data [172].

On the other hand, as shown in Table 3, the eCPA applies binary parameters of ions with water to facilitate the temperature dependence, thus also relaxing the hard-sphere assumption of the ions. The binary parameters, however, are not unique, because the parameters of the individual ions are derived

from the aqueous solution of the salt; not from pure ions. Therefore, in a strict sense, such derived ionic parameters have already contained some effects from water as the solvent. In this work, the binary parameters are still to appear in CPA to allow us to use the ionic parameters from the original eCPA work [141]. With this approach, we just extend the EOS application range to include higher temperatures and pressures using proper binary parameters.

To absorb the non-ideality, the dielectric constant of water in eCPA is made a function of temperature and concentrations of both salt and the gas present in the brines; the latter is represented by gas-specific parameters, k_D, which are also included in Table 3. In contrast, the dielectric constant is just a function of temperature in PCSAFT/PMSA following its true values at different temperatures. See the supporting information that accompanies this paper for details.

Figures 3 and 4 show the EOS performance in SO_2+water systems. The binary parameter was fitted to the VLE data [172] in Figure 3. This parameter was then used to calculate the phase diagrams in Figure 4 and then compared with experimental data [173,174], which confirm that the model works with any concentrations of SO_2. It is worth noting that in Figure 3 eCPA applies a quadratic temperature-dependent binary parameter instead of a constant as PCSAFT does.

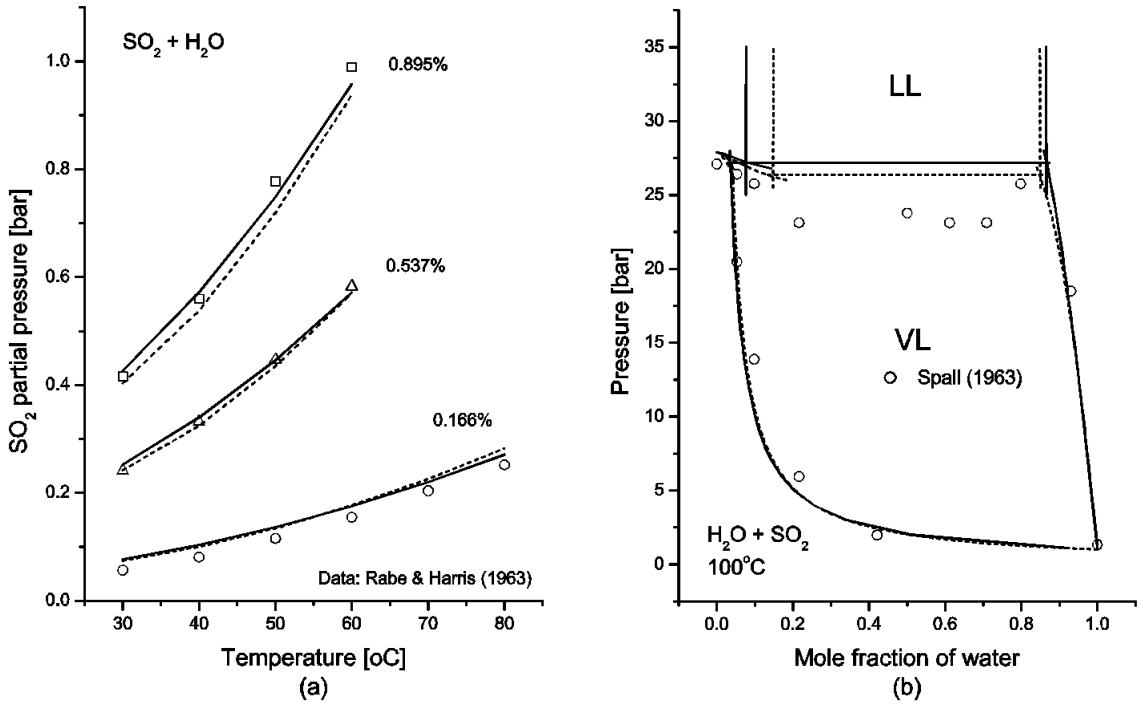

Figure 4: EOS predictions compared with other experimental data [173,174] for SO_2 dissolution in water: PCSAFT (solid curves) and CPA (dotted curves); percentages in figure (a) are mole fractions of SO_2; figure (b) also shows the existence of the second liquid phase.

Figures 5 and 6 show the EOS performance for CO_2+water systems, where the binary interaction parameter between CO_2 and water was derived from the VLE data [175,176] in Figure 5, where both EOS work equally well. However, the prediction using eCPA is slightly inaccurate at high pressures for the water content in the light phase, which is vapor at low pressures and CO_2-rich supercritical fluid phase at

high temperatures. Using this binary interaction both EOS successfully predict the solubility curves in Figure 6 when compared with experimental data [175,177-179]. This also confirms that they work at high temperatures. The solubility curves in the figures are the maximum amount of the gases at a particular pressure, temperature, and salinity, below which the gases can completely dissolve in the liquid phase.

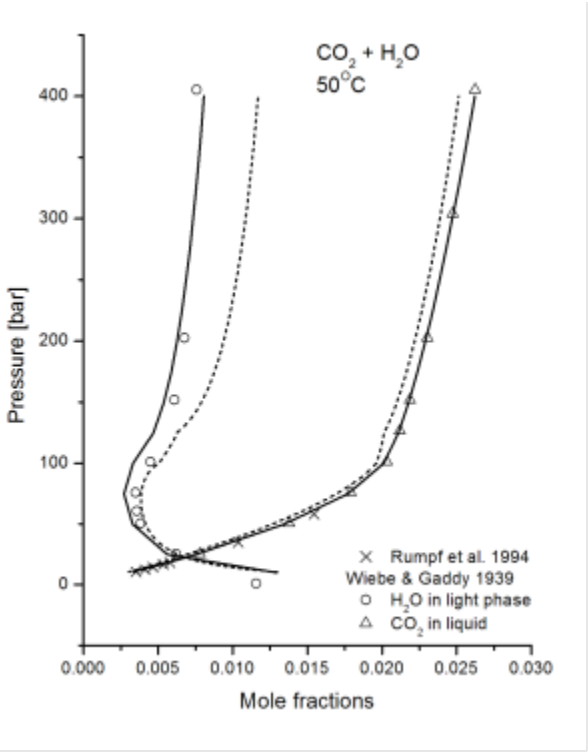

Figure 5: Fitted EOS for CO_2 dissolution in water: PCSAFT (solid curves) and CPA (dotted curve); symbols are experimental data [175,176]. The curves for mole fraction of water in the light phase are predictions (see text).

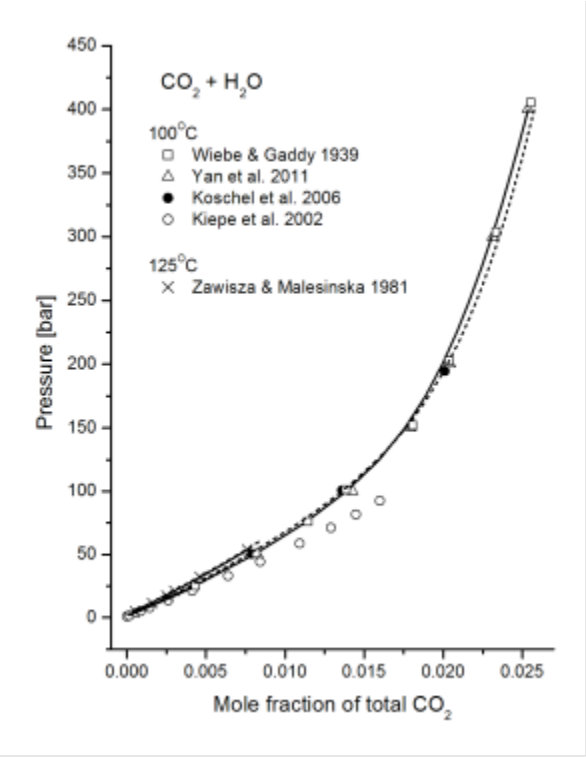

Figure 6: EOS predictions compared with other experimental data for CO_2 dissolution in water [175,177,180,192]: PCSAFT (solid curve) and CPA (dotted curve).

Another important interaction parameter belongs to the mixture of CO_2+SO_2, which was derived from the VLE data [180] of the binary system. The result is shown in Figure 7.

Based on the good performance that we obtained for all binary systems above, both EOS were employed, using all parameters in Tables 1 and 2, to describe the phase behavior of SO_2 in brine and CO_2 in brine; see Figures 8 and 9, respectively. The EOS performance in describing saline water, i.e., NaCl+water in this work, is provided in the supporting information.

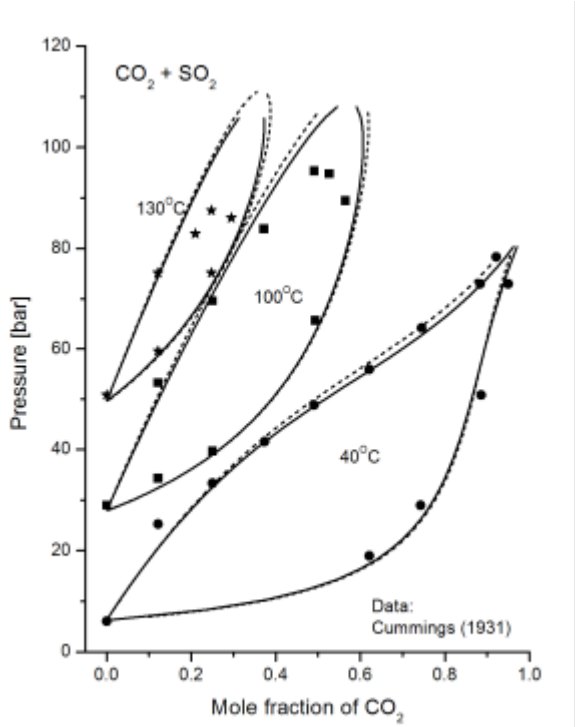

Figure 7: Fitted EOS calculation for the vapor-liquid equilibrium of CO_2+SO_2 mixtures: PCSAFT (solid curves) and CPA (dotted curves); symbols are experimental data [180].

We have a second liquid phase other than aqueous phase for SO_2 in brine at the high-pressure end of the solubility curves as shown in Figure 8. Because salt dissociations only occur in solvents with large dielectric constant such as water, the salt is also assumed to stay in the aqueous phase when we have two liquids in equilibrium, as it is in the VLE case. Though both EOS overestimate the liquid-liquid regions at high temperatures, the deviation will not affect the EOS overall performance because the liquid-liquid region of this system lies at high SO_2 concentration, while our concern for SO_2 co-sequestration is always at lower concentration side.

In this work, we use solubility pressures to measure the degree of gas solubility. The solubility pressure is the total pressure, above which the whole amount of the gas dissolves in the solvent. Therefore, higher solubility pressure indicates lower solubility, such as that shown in Figure 8b, where the presence of salt increases the solubility pressure, which means it reduces the gas solubility. This phenomenon is known as the salting-out effect, which is also present in CO_2+brine systems as shown in Figure 9.
For systems of CO_2 in brines shown in Figure 9, the supercritical phase is quite dominant at high pressures and at temperatures beyond the CO_2 critical temperature (31.1 ºC). At a moderate temperature, for example, 50 °C, the supercritical phase appears above the points where the solubility pressure changes dramatically with the CO_2 concentration. At high temperatures, e.g., 100 °C, the curves are entirely in the supercritical region.

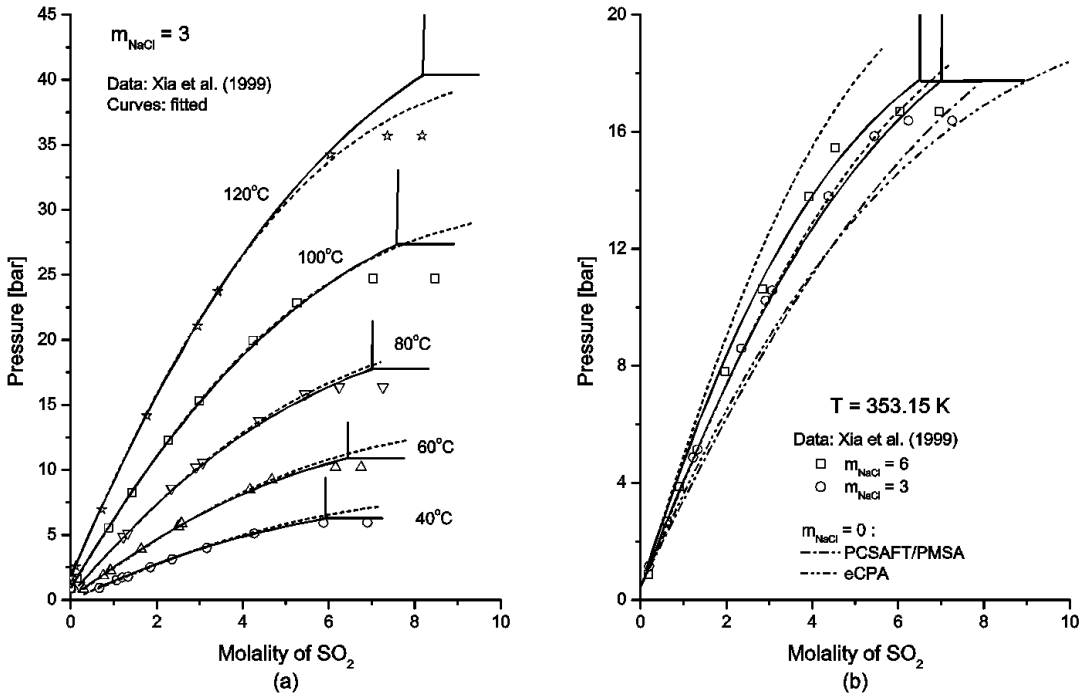

Figure 8: Solubility curves of SO_2 in brines: symbols are experimental data [193]; curves are calculated; the nearly vertical lines are calculated liquid-liquid equilibria (using PCSAFT/PMSA). The curves at the salt molality of 6 in (b) are predictions.

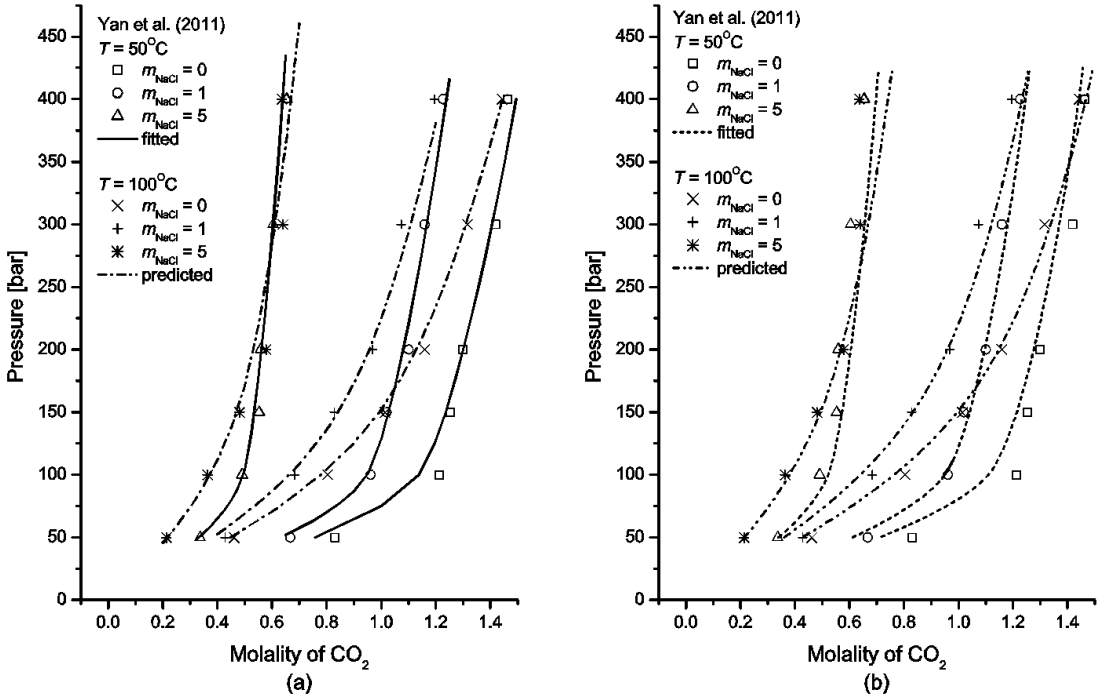

Figure 9: Solubility curves of CO_2 in brines: symbols are experimental data [194]; curves are calculated: (a) PCSAFT/PMSA (b) eCPA.

Evaluations on all of the results above, as evident from Figures 8 and 9, reveal that both EOS can be alternatives to each other except for high-salinity range at high pressures, where PCSAFT/PMSA substantially outperforms eCPA. This may be caused by the poorer performance of eCPA in describing the brines (see the supporting information). This fact in turn justifies the use of PCSAFT/PMSA to evaluate the phase behavior of SO_2+CO_2 mixtures in brines in the whole range of temperature, pressure, and salinity of interest, for which do not have experimental data are not available in the literature. This is the very idea of this work, i.e., using a reliable EOS to perform analyses on chemical systems that lack experimental data.

In sequestration schemes where the SO_2-to-CO_2 mole ratio is very small (in the order of 10^{-2}), the solubility curves will nearly coincide with those for CO_2 in Figure 9. Therefore, we calculate the phase diagrams at a much higher SO_2-to-CO_2 mole ratio (e.g., 2) in Figure 10 to discern the discrepancies. We use pressure-temperature phase diagrams, instead of pressure-concentration ones in Figures 8 and 9, to make the diagrams more useful for sequestration purposes as they can be superimposed with the underground pressure-temperature profiles of the geological sites.

In Figure 10a, the solubility curves of the gas mixture in brine are compared with those without SO_2. The solubility of CO_2 increases if the presence of SO_2 lowers the solubility pressure at a fixed temperature and gas composition. The solubility-pressure drop, or equivalently the solubility increase, is plotted against the temperature in Figure 10b to show the phase behavior more clearly. The pressure drop is the difference between the solubility pressure of the case with the presence of SO_2 and that with CO_2 only, i.e., the filled circles and the open circles in Figure 10a, respectively. The horizontal dotted line in the figure gives the reference, i.e., the cases without SO_2, to which all pressure drops are calculated and

referred to. A positive pressure drop in Figure 10b means an increase in solubility, relative to that of the corresponding case without SO_2, at the same temperature and gas composition. Therefore, the presence of SO_2 increases the solubility of CO_2 in brines with salinities $m_{NaCl} > 1$ only in the temperature range of 40 °C < T < 120 °C; at lower and higher temperatures the presence of SO_2 decreases CO_2 solubility.

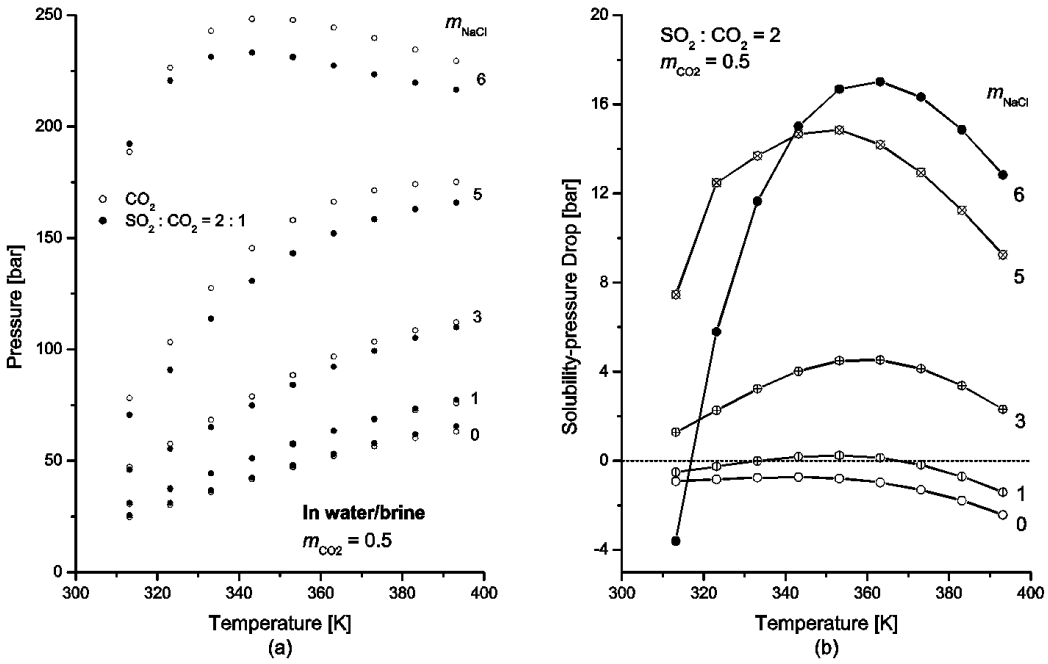

Figure 10: Phase behavior of SO_2+CO_2 in brine at a SO_2-to-CO_2 mole ratio of 2 and a CO_2 molality of 0.5; lines are for visual guidance. The dotted line in (b) is when no SO_2 is present.

Similar to the plot on Figure 10b, Figure 11 shows the solubility-pressure drop if the SO_2-to-CO_2 mole ratio is reduced to 0.05, thus approaching the values in geologic co-sequestration scenarios. Comparing the two figures, which only differ in the amount of SO_2 impurity, concludes that the phase behaviors are qualitatively very similar to each other.

It is also evident from Figure 11 that in high-salinity brines, where the solubility of CO_2 (without SO_2) decreases due to the salting-out effect as was shown in Figure 9, the presence of SO_2 improves the solubility of CO_2 significantly. However, considering that the curve for $m_{NaCl} = 1$ lies in negative region at all temperatures, the SO_2 impurity makes CO_2 less soluble if the brine is of low salinity ($m_{NaCl} < 1$). Lower solubility can also be interpreted as higher total pressure that is required to get the whole gas mixture dissolved in the brine, which immediately translates to higher operating costs.

For the reservoir simulation studies of SO_2+CO_2 co-sequestration, one will need to note that at temperature range between the critical temperature of CO_2 (31.1 °C) and that of SO_2 (157.5 °C), where the relative solubility of the gas mixture increases, the higher solubility of the gases would enhance the chemical reactions that may occur between the generated ions and the geological minerals. This will indirectly affect the permanent storage of carbon.

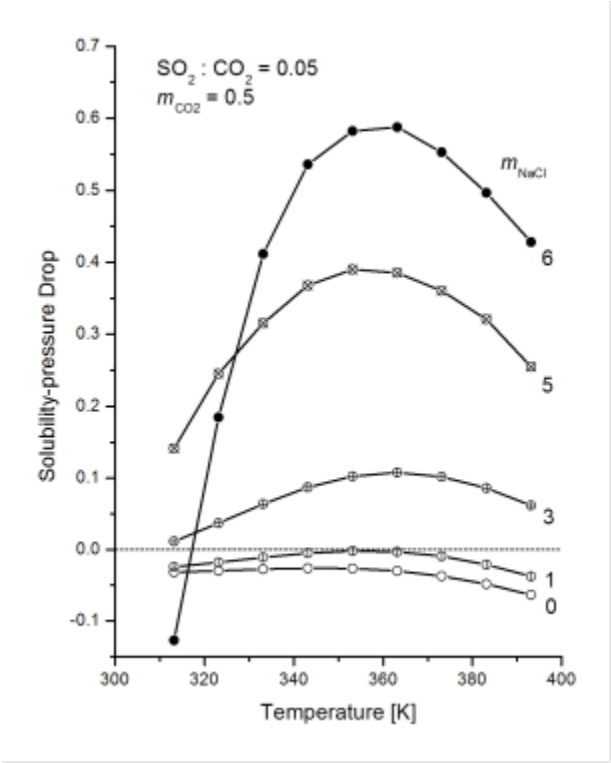

Figure 11: The phase behavior of SO_2/CO_2 in brine at a SO_2-to-CO_2 mole ratio of 0.05 and a CO_2 molality of 0.5; lines are for visual guidance.

2.2 Results and Discussions for Solubility Model of NO_2+CO_2+Water

The pure-component parameters of all species in the system are tabulated in Table 5. They are derived from fitting the literature vapor pressure and saturated-liquid specific volume data [181]. The fitting properties, references, and the quality of fit are tabulated in Table 6. As defined before, NO_2* is in fact a mixture of NO_2 and its dimer N_2O_4. The parameters of H_2O and N_2 are directly taken from previous studies [182,183].

In mixtures, where interactions between unlike species occur, binary interaction parameters k_{ij} are needed and derived from binary VLE data for interactions between species. The binary interaction parameters are used to correct the molecular interactions and implemented in the combining rule of the energy parameters:

$$\varepsilon_{ij} = \sqrt{\varepsilon_i \varepsilon_j}\left(1 - k_{ij}\right) \tag{25}$$

Table 5. Pure-component parameters

	m	σ [Å]	ε/k_B [K][a]	Associating sites[b]	ε_A/k_B [K]	κ	Ref.
H_2O	1.2190	[c]	213.5741	(2,2,0)	1851.9773	0.052246	[164]
NO_2*	1.7202	2.79341	203.6308	(0,4,1)	6596.2014	4.335×10^{-6}	This work
HNO_3	2.5859	2.81749	287.8668	(1,2.5,0)	652.6610	0.049890	This work
NO	1.4388	2.76806	112.0302	(0,2,1)	1504.8371	0.000185	This work
N_2	1.2414	3.29920	89.2230	(0,0,0)	-	-	[165]

[a] k_B: Boltzmann constant

[b] First digit is the number of proton-donor type of associating sites; the second digit is the number of proton-acceptor type of associating sites; third digit is the number of type-1A associating sites.

[c] $\sigma_{H2O} = 2.798384 + 120.733275\ T^{-1} - 71515.85\ T^{-2} + 11052303\ T^{-3}$ [Å]

Table 6. Fitting of the pure-component parameters

	Fitting range		Ref	AAD[a] P^{sat}	AAD $v^{L,sat}$
	T [K]	P^{sat} [bar]			
NO_2*	294-388	1 - 31.28	DIPPR [181]	0.09%	0.07%
HNO_3	233-373	0.0007 – 1.783	DIPPR [181]	1.23%	0.24%
NO	110-172	0.24 - 43.93	DIPPR [181]	0.47%	0.53%

[a] Average Absolute Deviation = $(\beta_{exp} - \beta_{calc})/\beta_{exp} \times 100\%$ (exp = experimental; calc = calculated); β is the vapor pressure P^{sat} or the saturated liquid volume $v^{L,sat}$.

The binary interactions are generally functions of temperature, which are in the form of polynomials:

$$k_{ij}(T) = a + b \times 10^{-4}\ T + c \times 10^{-6}\ T^2 + d \times 10^{-6}\ T^3 \quad (26)$$

where the coefficients a, b, c, and d are listed in Table 7. The exception is for H_2O-NO_2, which is also given in the last row of the table. The use of a high-order polynomial in the parameter correlation is necessary in our case to obtain acceptable accuracies for several binary mixtures due to the limited availability of their experimental data as described later. Moreover, as our applications fall within the correlation temperature range, the use of eq 26 is safe and justified for our model. Greater data availability in the future will definitely improve the correlation quality and extend the applicability to a wider temperature range.

Among the binary parameters, the k_{ij} between H_2O and NO_2* is the only one that was derived from the experimental physical VLE of ternary mixture, which is in this case $H_2O/HNO_3/NO_2$* [184], because the data of physical VLE of the binary H_2O/NO_2* do not exist due to the high reactivity of the system. There are three binary mixtures that do not have experimental data, i.e., NO/HNO_3, N_2/HNO_3, and NO_2/N_2, the

binary parameters of which could fortunately be set to zero. This fortunate fact is justified in parameter sensitivity tests of the quinary mixture of $N_2/H_2O/HNO_3/NO_2*/NO$ discussed later in this paper.

The cross-association parameters, which are commonly derived from mixing rules, have to be directly fitted from the experimental data due to the high complexity of the reacting system. The parameters are listed in Table 8. No cross association occurs between NO and H_2O or HNO_3.

Table 7. Coefficients of binary interaction parameters in eq 26 and the references of the experimental data used to derive them

Binary	*a*	*b*	*c*	*d*	Data Ref	Temperature range [°C]
H_2O-HNO_3	-0.26416	5.097	0	0	[167]	24.6–120.6
H_2O-NO	-1.1144	64.235	-8.5220	0	[170]	0-100
H_2O- N_2	-0.89215	40.205	-4.316	0	[168]	5-89.8
HNO_3-NO_2*	75.48675	-6911.96194	2114.65923	-2.1614	[171]	21.5-76.6
HNO_3-NO	0	0	0	0	-	
HNO_3-N_2	0	0	0	0	-	
NO_2*-NO	2.345	-141.6	20.57	0	[173]	37.7-104.4
NO_2*-N_2	0	0	0	0	-	
NO-N_2	0.04	0	0	0	[172]	(-159.4)–(-153.6)
H_2O-NO_2*	$k_{ij} = 0.33743 - 4.827\times10^{7}\times \exp(-0.06092\ T)$				[166]	20-80

Table 8. Cross association parameters[a]

	H_2O	NO_2*	HNO_3	NO
H_2O	-	900.00	2340.00[b]	-
NO_2*	0.05	-	881.0923	5450.437[c]
HNO_3	0.05[b]	0.04989	-	-
NO	-	0.00015[c]	-	-

[a] The diagonally upper-right entries are the cross-association energy ε_{Aij}/k_B [K] and the lower-left entries are the cross-association volume κ_{ij}.
[b] Only between proton-donor sites in H_2O and proton-acceptor sites in HNO_3 (see text).
[c] Type 1A cross association

The EOS performance is presented here for both the correlations in deriving the parameters and their extrapolations to independent data, not included in the correlations, using the derived parameters without additional adjustments.

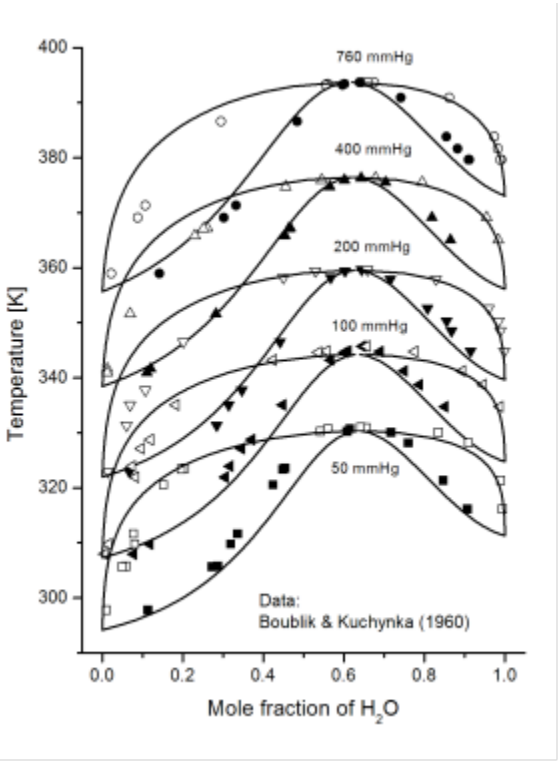

Figure 12: The VLE of H_2O/HNO_3: experimental data [185] – open symbols are the dew points; filled symbols are the bubble points. Curves are PCSAFT correlations.

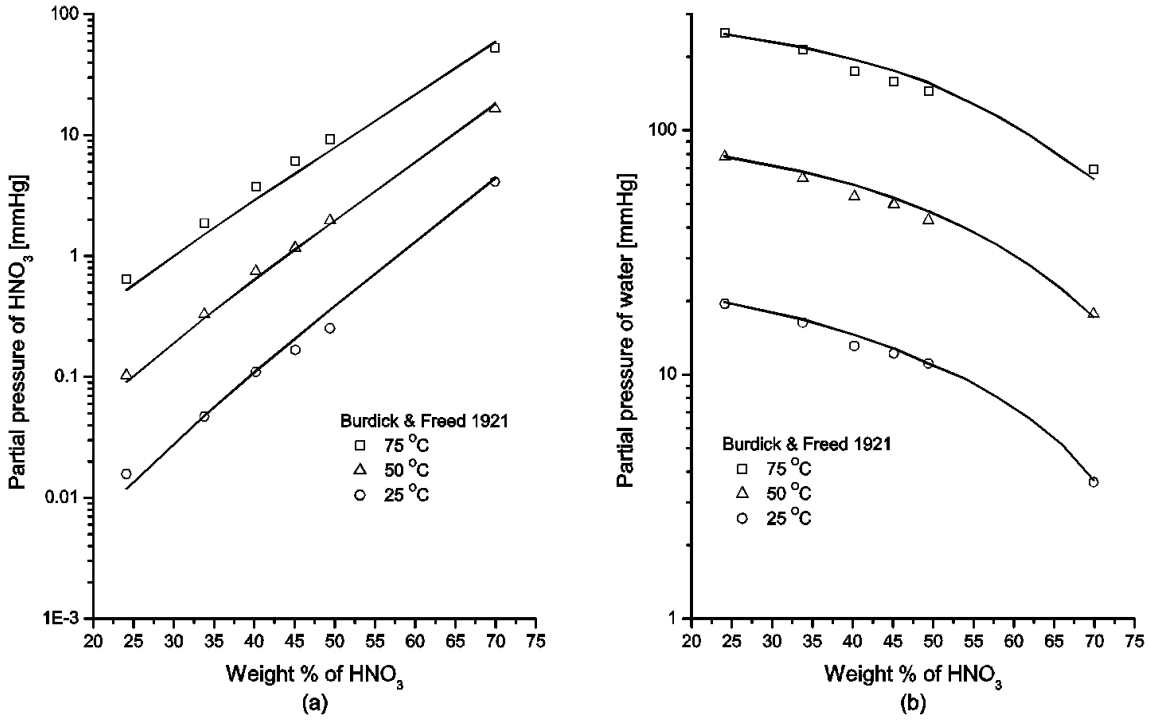

Figure 13: EOS extrapolation on the behavior of dilute HNO_3 aqueous solutions: symbols are experimental data [146]; curves are PCSAFT calculation.

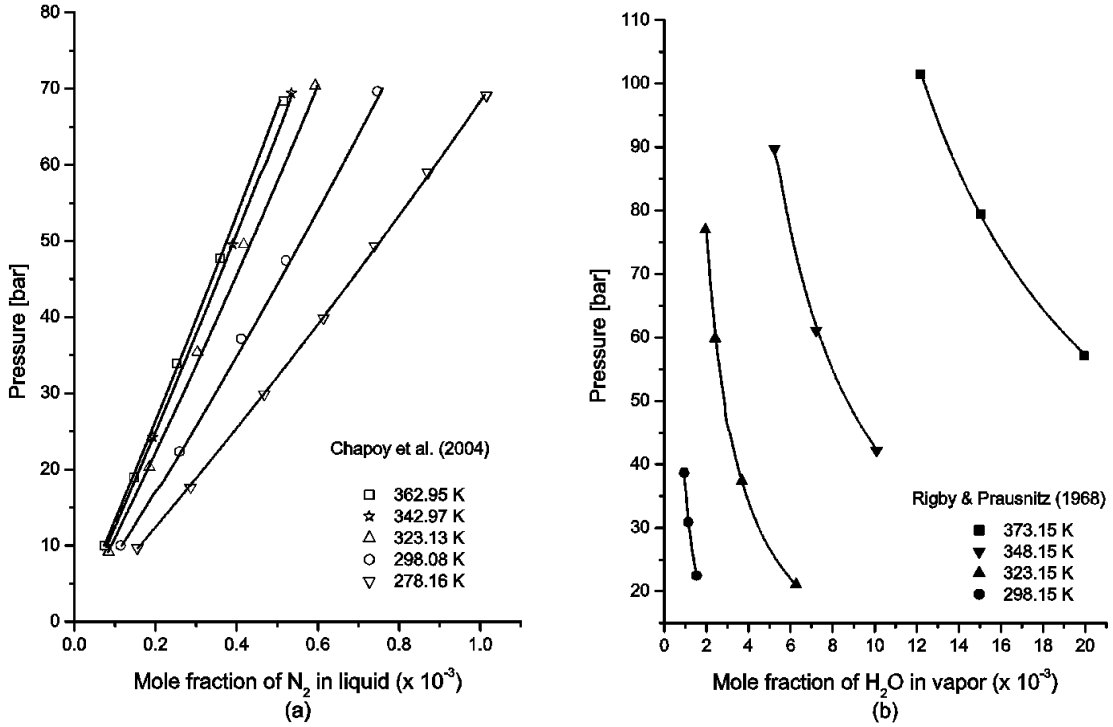

Figure 14: The VLE of N_2/H_2O: (a) Solubility of N_2 in liquid phase, curves are PCSAFT correlation; (b) Mole fraction of water in vapor phase, curves are PCSAFT extrapolation. Symbols are experimental data [186,187].

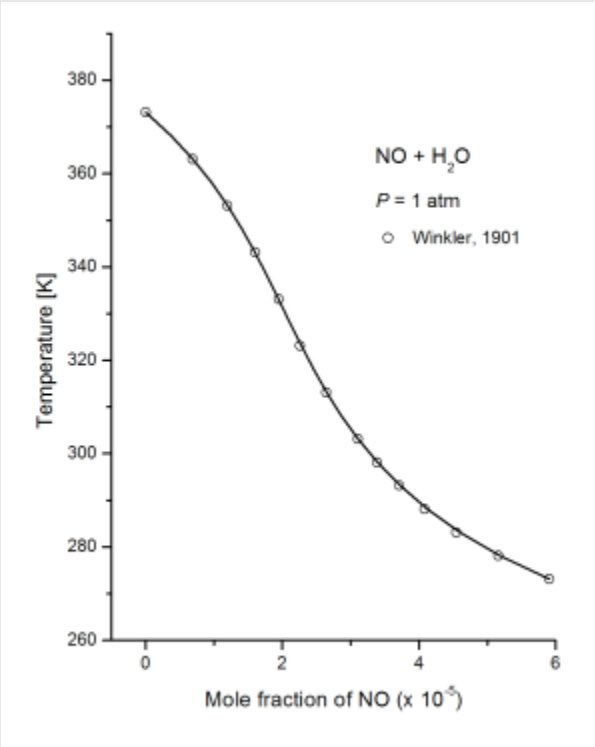

Figure 15: The solubility of NO in H_2O: symbols are experimental data [188]; curves are PCSAFT correlation.

The most important binary mixture is H_2O/HNO_3, which contains the dominant species in the liquid phase. Although many authors have discussed this particular system [151-153], most of them did not provide the physical equilibria data that we need to derive the binary interaction parameter. The performance of PCSAFT correlation for this binary, which has an azeotropic behavior, is shown in Figure 12 at various *T* and *P* along with the experimental data [185]. The performance is then extrapolated to the dilute HNO_3 aqueous solutions at atmospheric pressure and compared with the data of Burdick and Freed [146] in Figure 13.

Figures 14 and 15 show the EOS performance in N_2/H_2O and NO/H_2O systems, respectively, both of which have small gas solubility in the aqueous phase. While the experimental data for N_2/H_2O are abundantly available in the literature, for example those shown in Figure 14 [186,187], there is only one set of data available for NO/H_2O [188]. It is also the case for HNO_3/NO_2*, for which only one set of physical equilibrium data is available [189], while many others are physicochemical data at high concentration of HNO_3 [153-156] that follow the dissociation reaction of eq 5 irrelevant to flue gas geologic sequestration. The EOS performance for HNO_3/NO_2* is shown in Figure 16, where it exhibits liquid-liquid equilibrium (LLE) at low temperatures.

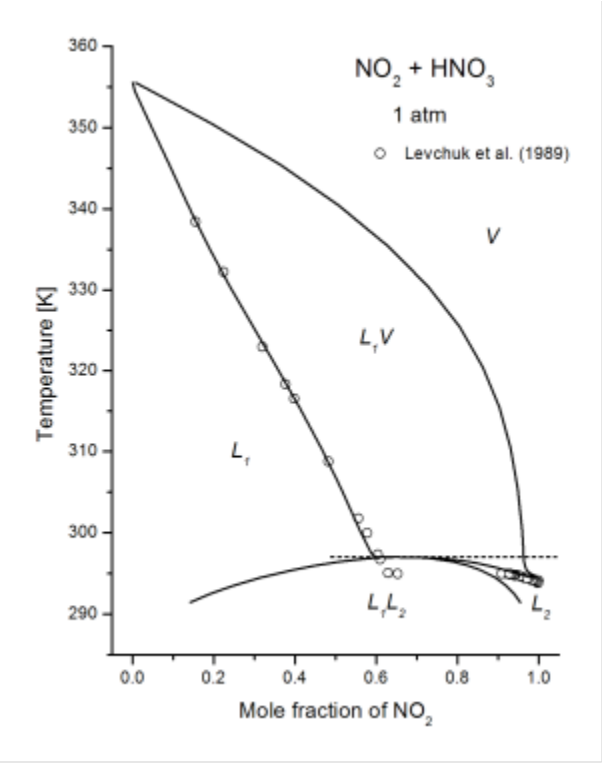

Figure 16: The phase equilibria of HNO_3/NO_2*: symbols are experimental data [189]; curves are PCSAFT correlation.

The VLE of the gases, N_2/NO and NO_2*/NO, are well represented along with the experimental data [190,191] in Figures 17a,b, respectively.

Due to the unavailability of physical VLE data as mentioned before, the binary parameter of NO_2 in water was derived from the NO_2*/H_2O/HNO_3 ternary. Since we already have the binary parameters for NO_2*/HNO_3 and H_2O/HNO_3, the derivation of that of NO_2*/H_2O from the ternary data is straightforward. Caution must be taken for this ternary, however, because most of the data in the literature are physicochemical rather than physical VLE. The physical VLE data [184] are shown in Figure 18 together with the EOS representation.

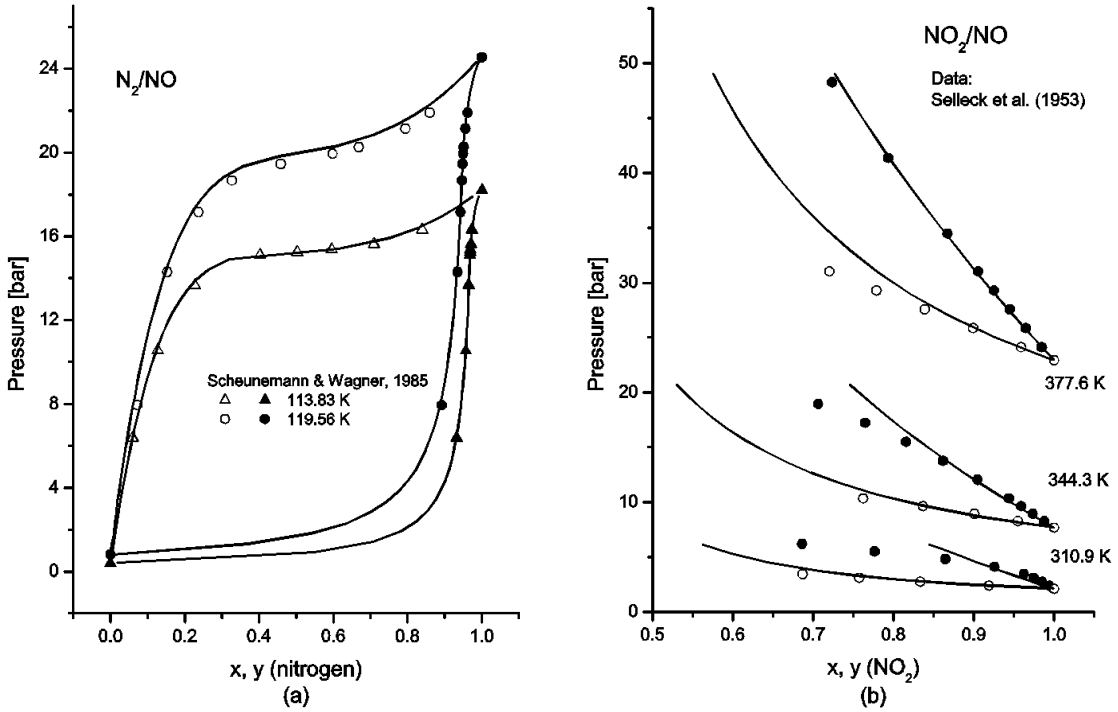

Figure 17: The binary VLE: (a) N_2/NO; (b) NO_2*/NO; Symbols are experimental data [190,191]; curves are PCSAFT correlation.

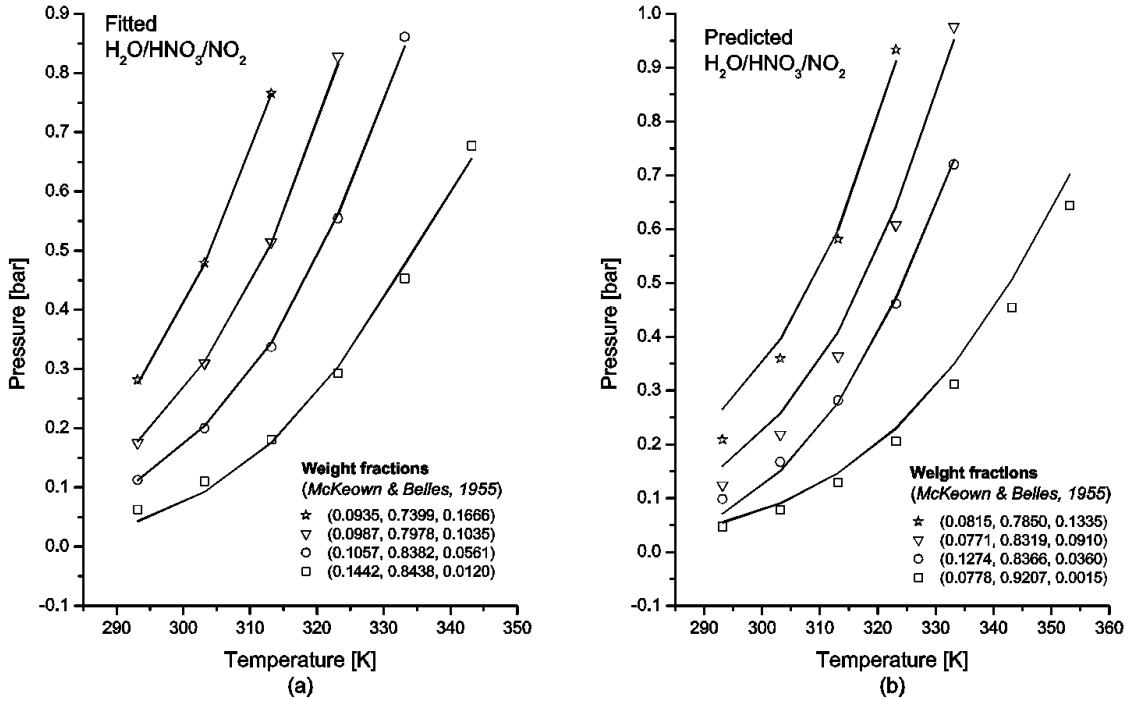

Figure 18: The VLE of $H_2O/HNO_3/NO_2$*: (a) Data used to derive the binary parameter of NO_2*/H_2O; Symbols are experimental data [184]; curves are PCSAFT correlation. (b) EOS extrapolation examples at other compositions compared with experimental data [184].

Up to this point, all parameters have been derived, except for the binary parameters of N_2/HNO_3, NO/HNO_3, and N_2/NO_2*, the experimental data of which are not available in the literature. We ran parameter sensitivity tests over the quinary mixtures $N_2/H_2O/HNO_3/NO_2$*/NO, from which we conclude that those remaining three binary parameters have very small effects on the phase equilibria calculations. Therefore, we safely set them to zero for simplicity.

Now, using the parameters listed in Tables 4, 6, and 7, along with the equilibrium constant *K* in eq 11, the logarithm of K_1 can be calculated and matched with the experimental data. The available data were all obtained by varying the temperature and liquid concentration of HNO_3 (x_{HNO3}) at atmospheric pressures. Due to the use of N_2 as the background gas, as discussed before, the degree of freedom of the chemical system is in fact 4, not 3, so that the data were not measured systematically as they should have been if another property was fixed in the experiments in addition to the system *P*, *T*, and x_{HNO3}. The researchers assumed that the presence of the background gas could safely be neglected due to the small N_2 solubility in water as well as the inert nature of the N_2 in the chemical reaction eq 4.

Unfortunately, this assumption produced experimental data with obvious scattered distribution, as can be seen in the original paper [146], in which experiments at the same condition (*P*, *T*, x_{HNO3}) give very different concentrations in the vapor phase. Even worse, the determination of gas concentration in the vapor phase is inaccurate in some cases, particularly when the gas exists in small quantities, i.e., at low concentration of HNO_3 (< 10 wt%) for NO_2* and at high concentration of HNO_3 (> 55 wt%) for NO [146].

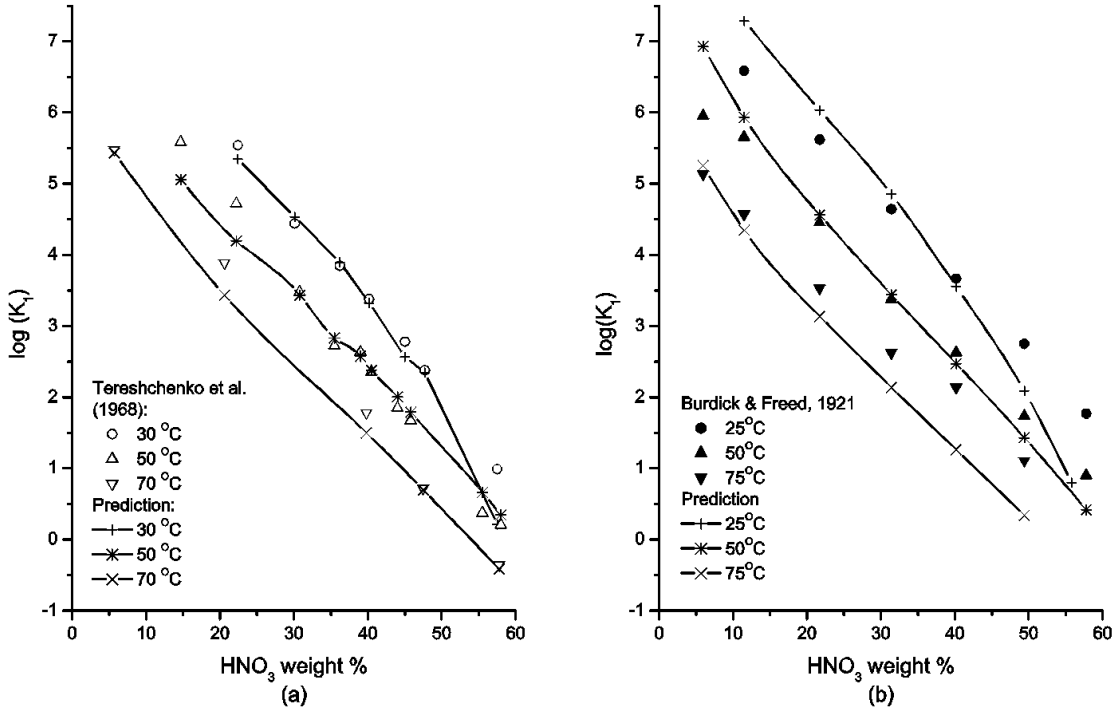

Figure 19: The logarithm of partial equilibrium constant K_1 versus nitric acid concentration at P = 1 atm: (a) Tereshchenko et al. [147]; (b) Burdick & Freed [146]. Symbols with connecting curves are calculated using the EOS.

Figure 19 shows the comparison between the EOS-calculated log K_1 with that of Burdick and Freed [146], as well as that of Tereshchenko et al. [147]. We calculated log K_1 at the original experimental conditions (P, T, x_{HNO3}) and one of the mole fractions of NO that was experimentally derived in the vapor phase (y_{NO}) to satisfy the system degree of freedom of 4. In Figure 19a, the data of Tereshchenko et al. [147] are well reproduced except at low temperature (20 °C) and high acid concentration, where the resulting NO in the vapor phase is so small that may be buried in the uncertainty of the measurements.

As shown in Figure 19b for the data of Burdick and Freed [146], similar symptom occurs at 25 °C and high HNO_3 concentration, as well as at 75 °C, the very reason why no data was measured at 57.8 wt% of HNO_3. Considering the omission of some data before averaging the values of log K_1, the apparent order of the logarithm of K_1 data in Figure 19b may be deceptive.

Regarding the deviation observed above at high acid concentrations, particularly at low temperatures, we recalculated the log K_1 at 25 °C at the same conditions (P, T, x_{HNO3}) as that in Burdick and Freed, but now with a systematic choice of y_{NO}. In addition, we also calculated log K_1 at the conditions for quaternary $H_2O/HNO_3/NO_2/NO$, in which we have a degree of freedom of 3, so that the input (P, T, x_{HNO3}) is sufficient to fix the system properties; in this case log K_1 does not depend on y_{NO}. The results are shown in Figure 20a with the corresponding y_{NO} used in the calculations in Figure 20b. The y_{NO} curve for the quaternary in Figure 20b is not by choice, but fixed by the conditions (P, T, x_{HNO3}).

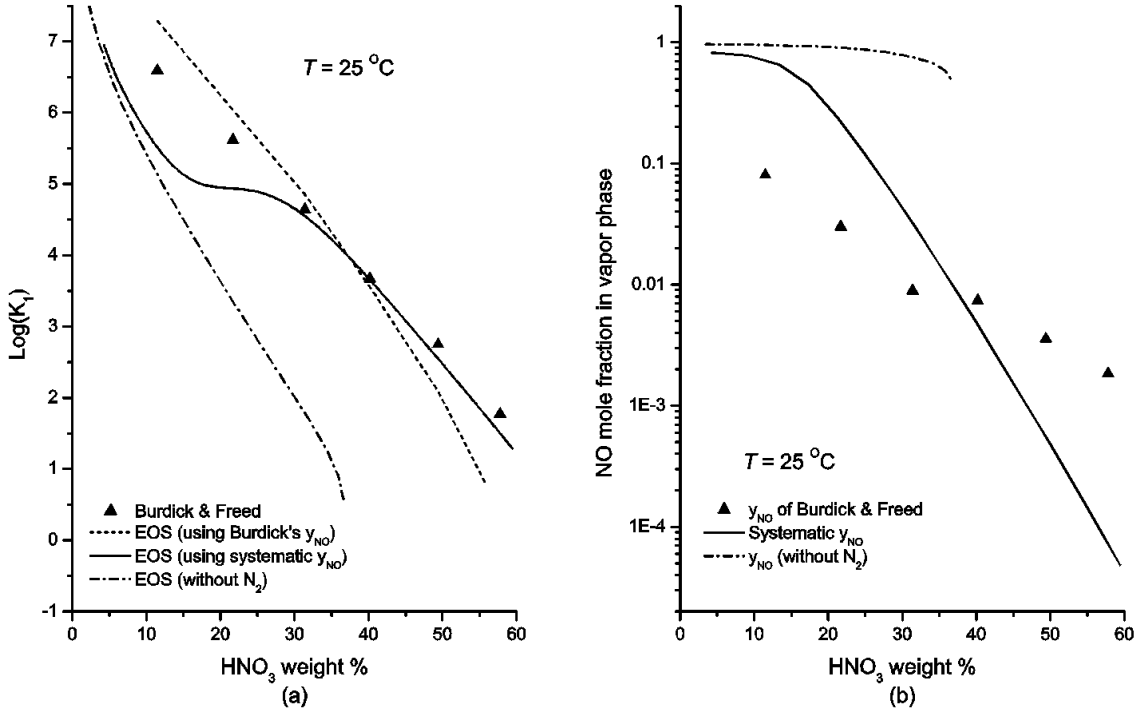

Figure 20: The calculated values of log K_1 at 25°C based on the choice of y_{NO}: a. Comparison with Burdick and Freed [146]–dotted curve from Figure 19b, dash-dotted curve for quaternary $H_2O/HNO_3/NO_2$*/NO, solid curve for quinary with y_{NO} from Figure 20b; b. The corresponding choices of y_{NO} (for the quaternary, y_{NO} is fixed by the experimental conditions, not by choice).

As seen in Figure 20a, the values of Burdick and Freed at high acid concentration can be reproduced (solid curve) only if we use much smaller y_{NO} (solid curve) as shown in Figure 20b. In other words, the experimentally derived y_{NO} is inaccurate due to the diminishing amount of NO in the gas phase. The dependency of log K_1 on y_{NO} can be clearly observed if the acid concentration is lowered while y_{NO} is increased as we track the solid curves upward in Figure 20a,b. When y_{NO} is larger than that of Burdick and Freed, log K_1 gets lower approaching the fixed value given by the quaternary system, where NO is the dominant gas in the vapor phase replacing N_2. From this discussion, we learn that the presence of N_2 cannot be neglected in calculating K_1, particularly at low and high acid concentrations.

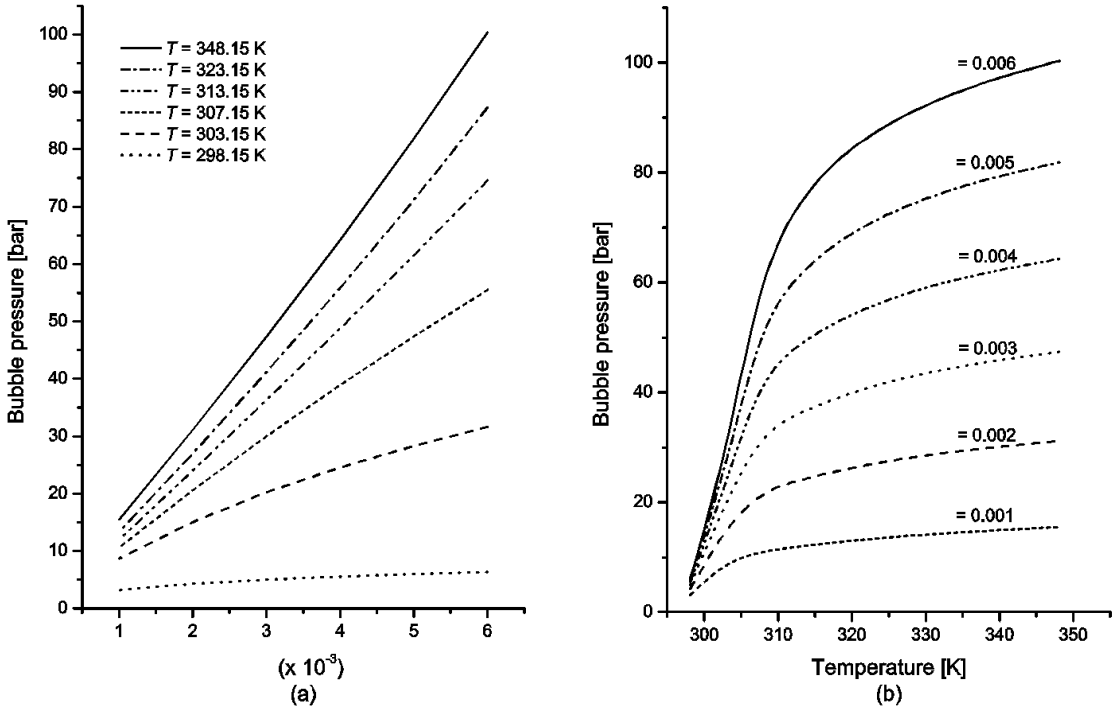

Figure 21: The prediction of solubility curves of NO_2* in water: (a) Bubble pressure vs. NO_2* loading at different temperatures; (b) Bubble pressure vs. temperature at different NO_2* loadings.

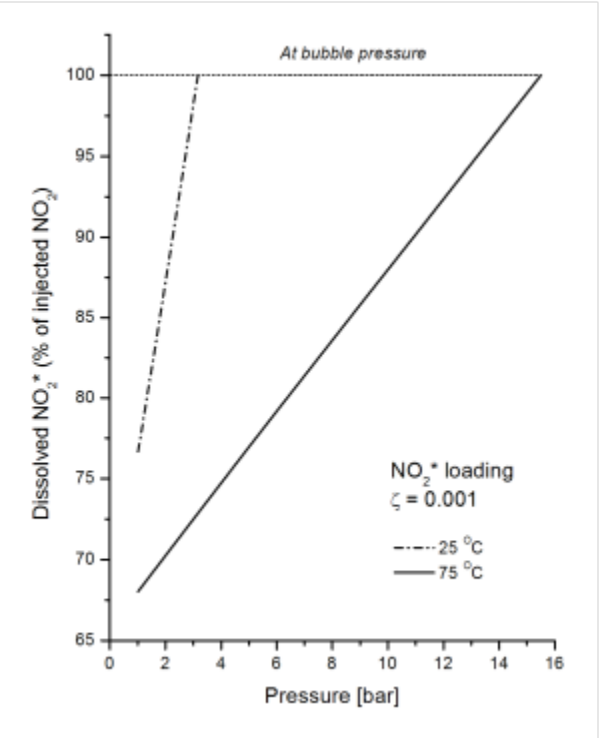

Figure 22: The predicted portion of injected NO_2* that dissolves in water at 25 °C and 75 °C for ζ = 0.001.

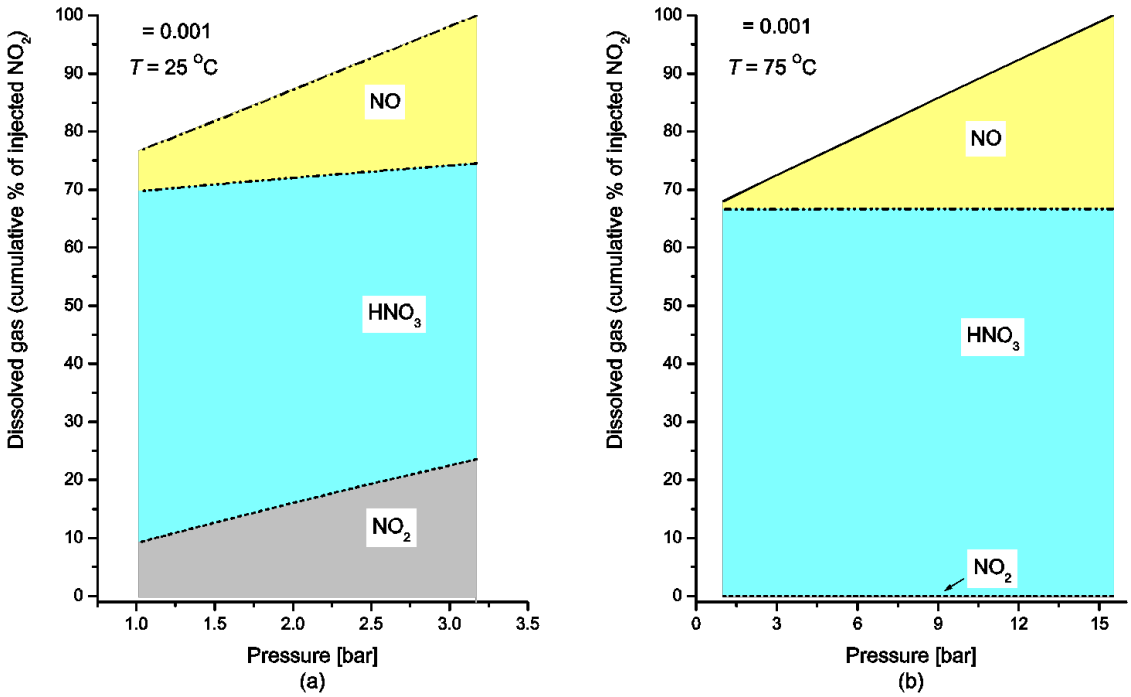

Figure 23: The predicted composition of the dissolved portion of NO_2* in water: (a) at 25 °C; (b) at 75 °C for ζ = 0.001.

The matching calculated K_1 values with that derived from experiments provide us with two pieces of information. First, the literature values of K in eq 11 are verified for use in the main reaction of eq 4. Second, the EOS is validated that allows us to proceed with calculations predicting the solubility of NO2* in water.

The total NO_2* that dissolves in water also includes the reaction products (HNO_3 and NO), and can be calculated through the mole balance:

$$\text{Total } NO_2\text{* mole dissolved} = n_{NO2*}\text{ (liquid)} + n_{HNO3}\text{ (liquid)} + n_{NO}\text{ (liquid)} \quad (27a)$$

$$= \left(x_{NO2*} + x_{HNO3} + x_{NO}\right)\frac{\ell \sum\left(n_{0,i} + \varepsilon\nu_i\right)}{n_{0,NO2*}} \quad (27b)$$

The solubility of NO_2* in water is calculated from the quaternary system of $H_2O/HNO_3/NO_2$*/NO with P, T, and the NO_2* loading as the input, which makes more sense for absorption purposes rather than x_{HNO3}. The NO_2* loading ζ is defined here as moles of NO_2* injected into every 1000 moles of water:

$$\zeta = \frac{n_{0,NO2*}}{1000\ \text{mol}\ H_2O} \quad (28)$$

We assume that there is no product species (HNO_3 and NO) in the system before the chemical reaction eq 4 as it should be in the absorption of NO_2 in water. The results are presented as solubility curves in bubble-point diagrams in Figures 21a,b. The bubble-point pressure is the pressure above which all the gas dissolves in water. In Figure 21a the solubility curve can also be interpreted as the maximum loading below which all injected NO_2* dissolves in water. In Figure 21b, it can be understood as the maximum temperature above which some of the gas escapes to the vapor phase.

It is clear from Figure 21b that the bubble pressure dramatically increases at temperatures between 25 °C and 40 °C. Consequently, the solubility of NO_2* hugely drops from 25 °C to 40 °C.

The percentage of dissolved NO_2* relative to the injected amount, i.e., the dissolved species on the right-hand side of eq 27a for every 1000 molecules of H_2O divided by 1000 × ζ, is presented in Figure 22 as a function of pressure for loading ζ = 0.001. The percentage reaches 100% at the bubble pressures. The corresponding composition of the dissolved portion of NO_2* is presented in Figures 23a,b. The top lines in these figures are the same as those in Figure 22.

It can be seen in Figures 23a,b that most of the dissolved NO_2* is in the form of HNO_3. The acid concentration decreases with pressure as the amount of unreacted NO_2* increases, which doubles from atmospheric pressure to the bubble pressure at 25 °C. At 75 °C, this behavior is not obvious in Figure 23b due to the minute amount of NO_2*. The percentage of the resulting HNO_3 at 75 °C approaches 66.67% at all pressures, which means the reaction of NO_2* with H_2O is practically complete according to eq 4 even at atmospheric pressure. It also confirms that the reaction in eq 4 does occur in the liquid phase. The completion of the reaction is the cause of the dramatic increase of the bubble pressure at 25-40 °C in Figure 21, as demonstrated in Figure 24 where the acid concentration quickly approaches 66.67% (x_{HNO3} = 0.004 for ζ = 0.006, and x_{HNO3} = 0.00067 for ζ = 0.001) in this range of temperature. The corresponding maximum weight fraction of the resulting HNO_3 is 1.38% and 0.23%, respectively. The curves in Figure 24 were calculated at their bubble pressures; the behavior at other pressures is very similar to that at bubble pressures.

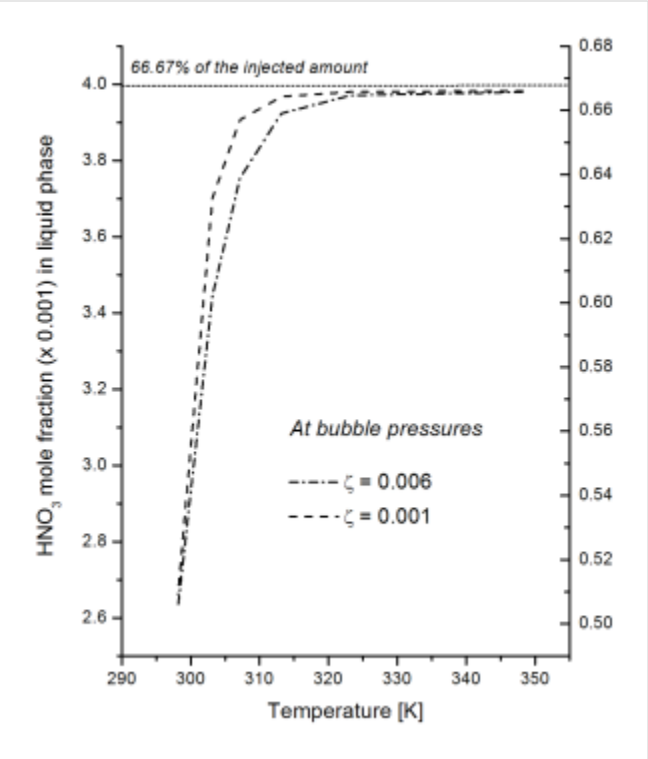

Figure 24: The predicted concentration of HNO_3 in liquid phase at bubble pressures: ζ = 0.001 (right vertical axis) and ζ = 0.006 (left vertical axis).

The compositions of vapor and liquid phases at different pressures corresponding to the conditions in Figure 22 are given in Figure 25a,b, respectively. The calculations start at atmospheric pressure up to the bubble pressure at each temperature. Since the aqueous liquid phase consists of mostly water (more than 99.9 mole %) at both temperatures, water mole fraction in liquid is not included in Figure 25b for clarity.

The order of abundances is NO, H_2O, NO_2*, and HNO_3 in the vapor phase and, H_2O (not shown in Figure 25b), HNO_3, NO, and NO_2* in the liquid phase. At 25 °C and lower pressure region, however, NO_2* is more than NO in the liquid phase. As the pressure increases, the concentrations of NO and NO_2* increase in both phases; the increase is not so obvious at 75 °C in the vapor phase due to the scale of Figure 25a. On the contrary, the concentrations of water and HNO_3 in the vapor phase decrease with pressure, while they are relatively constant in the liquid phase.

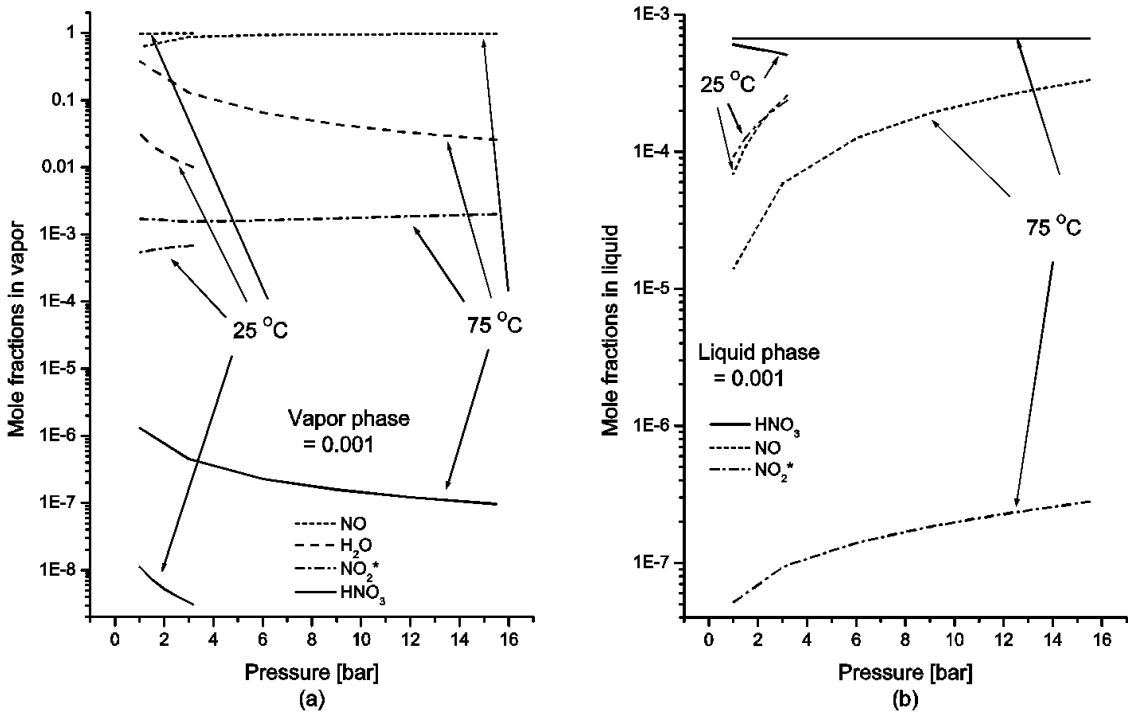

Figure 25: The predicted compositions of NO_2*/H_2O system at 25 °C and 75 °C for ζ = 0.001: (a) Vapor phase; (b) Liquid phase.

Part 3 Conclusions

The first model in this work can describe the important chemical system of SO2+CO2+brine, the experimental data of which are absent in the literature, for flue gas sequestration. It can be used as a stand-alone solubility evaluator or as a module of a larger geologic sequestration simulation platform. For the EOS to apply the model, PCSAFT/PMSA and eCPA may be alternatives to each other except for the high-salinity range at high pressures, where PCSAFT/PMSA substantially outperforms eCPA.
The second model using PCSAFT is found capable of describing the physicochemical equilibria of an important reacting chemical system of NO_2 in water, which involves the reaction products HNO_3 and NO. Several important findings are as follow:

1. In this model, the total reaction eq 4 is effective to represent the reacting system of NO_2* in water in the dilute region of the resulting HNO_3. The reaction is confirmed to occur in the liquid phase.

2. The literature value of the reaction constant *K* in eq 11 is verified for applications.

3. The use of an inert background gas introduces an additional degree of freedom. Despite the inert nature of the gas with respect to the chemical reaction and the low solubility of the gas in the aqueous liquid phase, the presence of the gas has substantial effects that cannot be neglected.

Therefore, the use of partial reaction constant K_1 is not recommended. With the availability of the new model, K_1 is no longer needed, and should be replaced by the total constant K.

4. Without an inert background gas, the solubility of NO_2* in water dramatically drops in the temperature range of 25-40 °C due to the completion of reaction eq 4 at higher temperatures.

5. In equilibrium without an inert background gas, NO dominates the vapor phase, while HNO_3 trails water in dominating the liquid phase.

B) Hysteresis & Computational Modeling

1 Introduction

We analyze a strategy of injecting supercritical $\mathbf{CO}_2$ in aquifers that leaves it immobilized within the porous rock, due to hydrodynamic effects. This strategy has been proposed in works such as [209, 226, 231, 233], which are based on approximations of these effects. We utilize recent high pressure, high temperature measurements of permeability hysteresis in water and supercritical $\mathbf{CO}_2$, the non-wetting phase. Furthermore, we focus on one-dimensional flow, which often can be solved analytically by the method of characteristics, or by numerical methods with well controlled accuracy. This focus allows us to quantify the mechanism underlying permeability hysteresis trapping.

This trapping strategy consists of two stages: $\mathbf{CO}_2$ injection and $\mathbf{CO}_2$ immobilization. In the first stage we inject supercritical carbon dioxide at a significant volumetric rate; in the second one we inject a much smaller volume of chase brine. The immobilization was actually observed in laboratory experiments [197]; the present study fully explains the laboratory observations. As verified by our analysis, the mechanism for immobilization is capillary trapping during secondary water imbibition, enhanced by the unusually strong $\mathbf{CO}_2$ permeability hysteresis discovered in this physical system. A very rapidly moving discontinuity is generated that quickly brings the $\mathbf{CO}_2$ saturation to residual values, halting its movement.

In this work we explain this mechanism by means of the method of characteristics and double-check its results utilizing a one-dimensional simulator that is especially accurate for calculating permeability hysteresis effects. In one spatial dimension we provide the total amount and the distribution of the immobilized $\mathbf{CO}_2$; this distribution turns out to be essentially a standard Buckley-Leverett profile. In more dimensions we expect the chase brine to follow the paths of least resistence in the porous rock already taken by the injected $\mathbf{CO}_2$, which is then immobilized.

If $\mathbf{CO}_2$ is reinjected soon after the second stage, the previously immobilized $\mathbf{CO}_2$ will become mobile. Thus WAG injection must be very carefully planned [209, 226, 230, 233], or it will be counterproductive.

Concern about the evolution of buoyant plume in a porous medium is not recent [199, 201, 208]. The two latter books present analytic solutions describing certain aspects of the flow. The idea of immobilizing supercritical $\mathbf{CO}_2$ in a deep aquifer as a residual phase by the mechanism of relative permeability hysteresis is not new. Numerous studies have been made, especially in the last decade [205, 209, 212, 220-222, 226, 230-233]. The main features of these studies are: (i) the hysteresis models

used ad-hoc rather than experimental parameters; (ii) the main features revealed in recent experimental data, namely, high scanning-permeability slopes, responsible for the rapidly growing trapping shock speed were missing from the models employed (Killough [211], Land [215]); (iii) the studies were performed through multidimensional simulations to study the effect of various parameters, including permeability, the ratio of vertical to horizontal permeability, $\mathbf{CO}_2$ injection rate, residual $\mathbf{CO}_2$ saturation, salinity, temperature, aquifer dip angle, and rock heterogeneity. Of course, in our genuinely one-dimensional flow gravity segregation cannot be taken into account, while the models [207, 210, 216, 217] are designed for this purpose. In other words, the lack of gravity segregation is an assumption in our model.

Alternative mechanisms for $\mathbf{CO}_2$ sequestration, many of which would be active at long time scales, were studied in the following non-exhaustive list: [198, 204, 219, 227]. Other relevant studies at long time scales are [203, 218, 224, 228].

2 Measurement of permeabilities with hysteresis

In this section, we explain very briefly, for the sake of completeness, the experiments performed by Akbarabadi and Piri, fully presented in [197]. We compile their experimental data as used in the present study. The fluids involved are "brine" and "supercritical CO_2," somewhat improperly called "water" and "CO_2" in the rest of the paper.

A 15.4 cm long and 3.79 cm in diameter Berea sandstone core sample was cut from a block obtained from a quarry in Ohio. The porosity ϕ and absolute permeability K of the core were measured as 0.212 and 612 mD.

Pure CO_2 and brine with 10 wt % NaI, 5 wt % NaCl, and 0.5 wt % $CaCl_2$ composition were used. The temperature and pressure of the experiments were 55°C and 11 MPa, at which CO_2 is at its supercritical state [229].

They performed seven steady state relative permeability drainage and imbibition experiments in closed-loop procedures, meaning that all the fluids were recirculated throughout each experiment. With this method, a better equilibrium between the two phases (aqueous and CO_2-rich phases) was obtained, which dramatically reduced the amount of mass transfer between the phases. This is very important since CO_2 is soluble in brine and without stable equilibrium the dissolution of CO_2 in brine would introduce inaccuracies in the values of the measured residual saturations.

The experiments comprised two full and two half drain-age-imbibition cycles, as well as the following partial cycles: a one quarter, a one-eighth and a one-sixteenth drain-age-imbibition cycles. The initial condition was the same in each drainage experiment, namely, $s = 1$. The difference among these cycles was the brine saturation at which the imbibition step was started. For instance, for full cycle tests, at the end of drainage the brine saturation was 0.525 (s_h, the initial condition for the subsequent imbibition, see Fig. 4), whereas for half cycle tests s_h was 0.68. We remark that such a high value for water saturation, 0.525, at which it is considered immobile has already been mentioned in another experimental paper [200] for supercritical CO_2 and water.

The cycles of drainage and imbibition processes were performed using the steady-state method, during which both phases were injected with monotone increasing or decreasing fractional flows. In the seven steady-state experiments the supercritical CO_2 flow rate in cm^3/min varied in the range 0–5.0 during drainage and imbibition. On the other hand, the brine flow rate varied in the range 0–0.45 during drainage and 0–0.2 during imbibition. Thus CO_2 fractional flows of 0.18–1.0 were attained during drainage and 1.0–0.33 during imbibition.

The authors performed the experiments under the capillary-dominated displacement regime and kept constant flow rate at the (bottom) inlet and constant pressure boundary conditions at the (top) outlet of the vertical core sample. They used fully equilibrated fluids in the flow tests and employed a medical CT scanner to obtain in-situ saturations and verify that steady state was reached at the end of each measurement. The CT saturation measurements supplemented the pressure measurements. Additional details of the experimental procedure are explained elsewhere [197, 223]. Capillary end effects were reduced by placing the pressure transducers far away from the ends of the cylinder.

Fig. 1 shows the relative permeability data obtained from different cycles to exhibit hysteresis. As illustrated, the initial CO_2 saturation $1 - s_h$ and its corresponding residual value $1 - s_r$ vary from 0.475 to 0.102 and from 0.34 to 0.081, respectively; incidentaly, this means that almost 80% of the in-place CO_2 was trapped permanently through imbibition processes. The quantities s_h, s_r are marked in Fig. 4.

The trapping efficiency of each imbibition process is given by $(1 - s_r)/(1 - s_h)$. Figures 1 and 2 also show that a lower initial brine saturation leads to a higher residual CO_2 saturation, while a higher initial brine saturation causes better trapping efficiency. High trapping efficiency is attained because more pores and throats are filled with brine, which, in turn, leads to higher trapping of CO_2 by various pore-scale displacement mechanisms. It is also noticed that, at the beginning of the drainage process, the brine relative permeability drastically reduces with relatively small increase in CO_2 saturation. This event might be attributed to large, well-connected pores immediately becoming occupied by CO_2 significantly reducing brine connectivity.

Fig. 2 demonstrates the variation of $1 - s_r$ with $1 - s_h$ for many more cycles than those shown in Fig. 1. The results are compared with the empirical model of Spiteri et al. [232]. The model provides a relationship between the initial wetting phase saturation and residual non-wetting saturation. As it is seen, the results generated by the model agree well with our results. The parameters utilized in the Spiteri et al. empirical correlation are given and employed in Eq. (8).

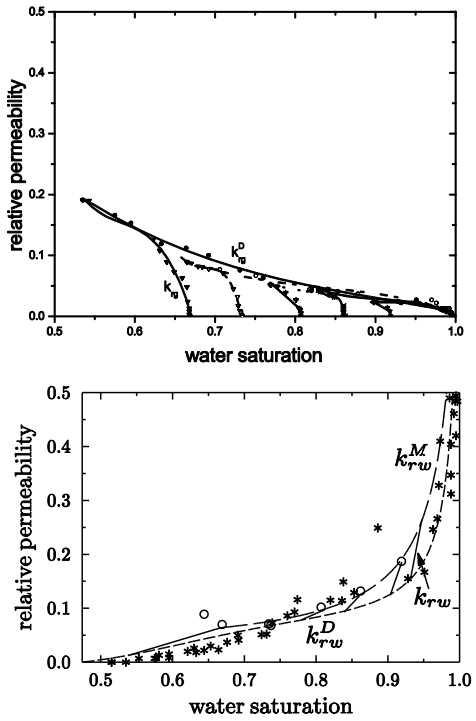

Figure 1: (Above) The results of all steady-state drainage-imbibition relative permeability cycles obtained in [197].

All imbibition tests are complete, and the end is attained when the $\mathbf{CO}_2$ saturation becomes so small that the $\mathbf{CO}_2$ permeability is negligible in the scales relevant for the experiments. Drainage tests are either incomplete or complete; in the latter case the water saturation becomes small enough that now the water permeability is negligible. Of course this does not mean that connate water saturation has been attained, as the aquifer rock is bound to be water wet.

Top: the points depicted by several symbols in the figure represent individual measurements of supercritical CO_2 relative permeabilities. Fits of the drainage k_{rg}^D and several scannings k_{rg} were drawn in [197] to facilitate the visualization of the data in the figure. These fits are not used in our analysis. Bottom: the stars represent measurements of water drainage relative permeabilities k_{rw}^D. The circles represent measurements of water relative permeabilities k_{rw}^M when the supercritical $\mathbf{CO}_2$ saturations are at residual values. The two curves represent our fits to k_{rw}^M and k_{rw}^D from top to bottom. We also show the water permeability scannings utilized in our model that correspond to the $\mathbf{CO}_2$ scannings from the top figure. The water scannings are straight line segments because only the endpoints originate from experimental data. The endpoints are calculated using the map in Fig. 2, as well as k_{rw}^M and k_{rw}^D, as explained in the caption of Fig. 4.

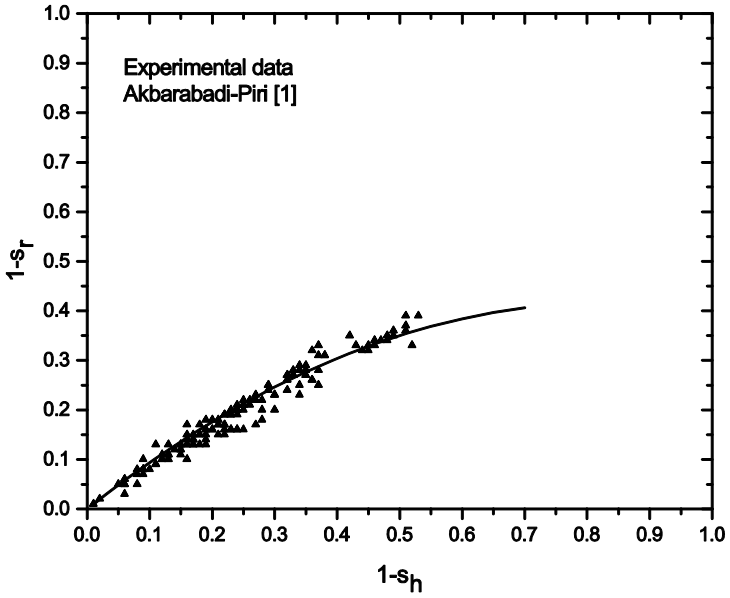

Figure 2: (Above) Each point represents the $\mathbf{CO}_2$ saturations at the end points of a $\mathbf{CO}_2$ scanning curve in Fig. 1 top.

The abscissa of each point is the $\mathbf{CO}_2$ saturation $1-s_h$ at the top of the scanning curve in question, i.e., of the intersection of the scanning curve with the $\mathbf{CO}_2$ drainage permeability curve. The ordinate of the same point is the $\mathbf{CO}_2$ saturation $1-s_r$ at the bottom of the scanning curve in question, i.e., of the intersection of the scanning curve with the horizontal axis. This is how the parabola in Eq. (8) arises.

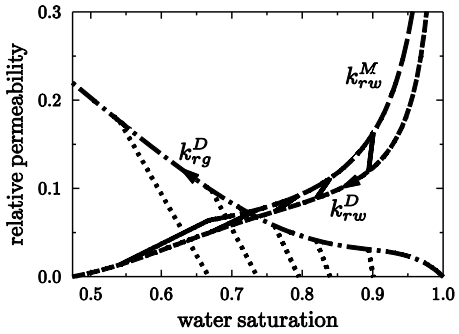

Figure 3: Our reprocessed experimental data from Fig. 1.

The short-dashed k_{rw}^D and dotted-dashed k_{rg}^D curves are the permeability of water and supercritical $\mathbf{CO}_2$ during drainage, i.e., when the water saturation s decreases. The long-dashed curve k_{rw}^M is the permeability of water when the supercritical $\mathbf{CO}_2$ saturation is at its residual value $1-s$. The two water permeability curves, drainage and imbibition, on the top right, meet at water saturation 1 with

permeability value 1. There are associated scanning straight lines joining each pair of curves. The first pair is k_{rg}^{D} and the horizontal axis; the second pair is k_{rw}^{D} and k_{rw}^{M}. The scanning lines in the first pair represent reversible variation of the $\mathbf{CO}_2$ permeability. The scanning lines in the second pair represent reversible variation of the water permeability. For each associated pair of scanning lines the corresponding end points have the same saturation value, as depicted in Fig. 4.

3 From measurements to rock and fluid properties

Fitting full drainage and imbibition relative permeability curves to the experimental data in Fig. 1 gives rise to the following expressions, to appear in Sect. 4 and used in Sect. 6:

$$k_{rw}^{D}(s) = \sum_{n=0}^{3} a_{2n} s^{2n} / \sum_{n=0}^{4} b_{2n} s^{2n}, \quad \text{with coefficients}$$

$$\begin{aligned} &a_0 = -0.0063170828,\ a_2 = -0.019746546,\\ &a_4 = 0.25217257,\ a_6 = -0.17420798,\\ &b_0 = 0.94645017,\ b_2 = -4.123325727,\ b_4 = 9.49068429,\\ &b_6 = -7.211207805,\ b_8 = 0.94930002, \end{aligned}$$

$$\begin{aligned} k_{rg}^{D}(s) = \quad & 0.4320773 - 1.3020969 s^2 + 2.2058758 s^4 \\ & - 3.5647535 s^6 + 3.9501271 s^8 - 1.7212298 s^{10}, \end{aligned}$$

$$k_{rw}^{M}(s) = \frac{0.03774691 - 0.0029555237 s^2}{1.0 - 0.96526242 s^2}.$$

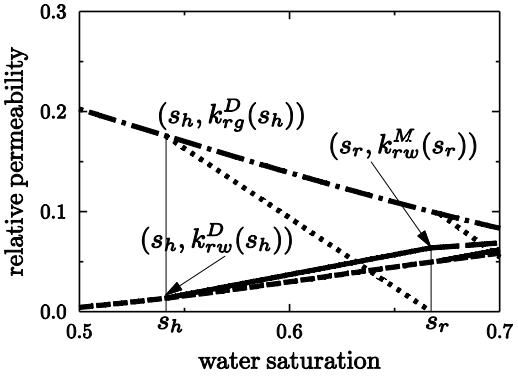

Figure 4: Expanded view of left portion of Fig. 3.

The short-dashed $k_{rw}^{D}(s)$ and dotted-dashed k_{rg}^{D} curves are the permeability of water and supercritical $\mathbf{CO}_2$ during drainage, i.e., when the water saturation s decreases. The long-dashed curve on the right

of $(s_r, k_{rw}^M(s_r))$ is k_{rw}^M, see Fig. 3. There are associated scanning lines joining the two pairs of curves. The first pair is k_{rg}^D with the horizontal axis; the second pair is k_{rw}^D with k_{rw}^M. The scanning lines in the first pair represent reversible variation of the $\mathbf{CO}_2$ permeability, while those in the second pair represent reversible variation of the water permeability. Each associated pair of scanning lines arises from a complete drainage-to-imbibition cycle. In such a cycle the imbibition defines a mapping from its initial water saturation s_h to its final water saturation s_r, Fig. 2. We recall that there is a hysteretic reversion from drainage to imbibition at water saturation s_h, while at water saturation s_r the $\mathbf{CO}_2$ phase ceases to move. The description is complete.

4 Permeability hysteresis in two-phase buoyant flow

Buckley-Leverett equation with gravity. We consider the flow of two immiscible fluid phases that do not exchange mass; for simplicity we assume they are incompressible. We indicate them by the subscripts w and g, even though we have in mind brine saturated with $\mathbf{CO}_2$ and supercritical $\mathbf{CO}_2$ saturated with water. Since the densities of the two phases are constant, for each phase conservation of mass is equivalent to conservation of volume. For one-dimensional upward sloped flow and homogeneous rock porosity ϕ we have:

$$\phi \frac{\partial s_w}{\partial t} + \frac{\partial u_w}{\partial x} = Q_w, \qquad \phi \frac{\partial s_g}{\partial t} + \frac{\partial u_g}{\partial x} = Q_g, \tag{1}$$

where Q_w, Q_g are the volumetric injection rates of water and $\mathbf{CO}_2$. According to Darcy's law, the volumetric flow rates u_w, u_g, phase densities ρ_w, ρ_g, viscosities μ_w, μ_g, and pressures p_w, p_g satisfy:

$$\begin{aligned} u_w &= -K \frac{k_{rw}}{\mu_w} \left(\frac{\partial p_w}{\partial x} - \rho_w g \cos\theta \right), \\ u_g &= -K \frac{k_{rg}}{\mu_g} \left(\frac{\partial p_g}{\partial x} - \rho_g g \cos\theta \right). \end{aligned} \tag{2}$$

Here, K is the rock absolute permeability and k_{rw}, k_{rg} are the relative permeabilities of water and $\mathbf{CO}_2$. Also, g is gravity acceleration (9.81 m/s^2) and θ is the angle between $\vec{x}$ and $\vec{g}$.

We will ignore capillary effects on the pressures in (2) and set $p_w = p_g = p$. We define the total Darcy velocity $u = u_w + u_g$ by adding the equations in (2). Taking into account that in our case $\cos\theta = -1$, as our flow is vertically upward, we obtain:

$$u = -K \left[\frac{k_{rw}}{\mu_w} + \frac{k_{rg}}{\mu_g} \right] \frac{\partial p}{\partial x} - K \left(\frac{k_{rw}}{\mu_w} \rho_w + \frac{k_{rg}}{\mu_g} \rho_g \right) g. \tag{3}$$

Extracting the pressure gradient from (3) and substituting into the first equation in (2) we obtain:

$$u_w = \left(u\frac{k_{rw}}{\mu_w} - K(\rho_w - \rho_g)g\frac{k_{rw}}{\mu_w}\frac{k_{rg}}{\mu_g} \right)\left[\frac{k_{rw}}{\mu_w} + \frac{k_{rg}}{\mu_g} \right]^{-1}. \tag{4}$$

Last but not least, adding the two equations in (1) and taking into account that $s_w + s_g = 1$ we obtain $\partial u/\partial x = Q$, where $Q = Q_w + Q_g$, which says that u is homogeneous in regions where there are no source terms.

Substituting (4) into the first equation in (1), introducing the viscosity ratio $\mu = \mu_w/\mu_g$ and dividing by ϕ, the final equation is

$$\frac{\partial s_w}{\partial t} + \frac{\partial F_w}{\partial x} = \frac{Q_w}{\phi}, \textbf{ with } F_w = \left(\nu + \varepsilon k_{rg}\right) f_w, \textbf{ where} \tag{5}$$

$$f_w = \frac{k_{rw}}{k_{rw} + \mu k_{rg}}, \quad \varepsilon = \frac{-K(\rho_w - \rho_g)g}{\phi\mu_g}, \quad \nu = \frac{u}{\phi}. \tag{6}$$

Equivalently one can write

$$\begin{aligned} &\frac{\partial s_g}{\partial t} + \frac{\partial F_g}{\partial x} = \frac{Q_g}{\phi}, \quad \textbf{where} \\ &F_g = \left(\nu - \varepsilon\frac{k_{rw}}{\mu} \right) f_g, \quad f_g = \frac{\mu k_{rg}}{k_{rw} + \mu k_{rg}}. \end{aligned} \tag{7}$$

Notice that $f_w + f_g = 1$ and $F_w + F_g = \nu$.

When it does not lead to confusion we will drop the subscript w from s_w, F_w and other water related quantities.

Including hysteresis in the permeabilities. The water saturations at beginning and end of an imbibition cycle, s_h and s_r, are obtained as follows. Water is drained, i.e., its saturation s decreases and the permeability k_{rw}^D decreases whereas k_{rg}^D increases, following the corresponding curves in Fig. 3. This is done until water is injected back; thus a minimum water saturation value s_h is attained. The $\mathbf{CO}_2$ permeability decreases, following down one of the dotted curves in Fig. 3, until zero $\mathbf{CO}_2$ permeability is reached for a water saturation value that we call $s_r(s_h)$. At saturation reversal the water permeability increases, following up one of the solid scanning curves in Fig. 3, until the saturation value $s_r(s_h)$ is reached; this value corresponds to maximum water permeability $k_{rw}^M(s_r(s_h))$.

For simplicity, all scanning curves are approximated by straight lines through the end points, as shown in Fig. 3.

The data in Fig. 2 was fit to a parabola following [232], with $\alpha = 1$ and $\beta = 0.6$, obtaining

$$s_r(s_h) = s_h + 0.6(1 - s_h)^2. \tag{8}$$

Fitting the experimental data described in Sect. 2 by the expressions in Sect. 3, we obtain k_{rw}^D and k_{rg}^D during water drainage. When the permeabilities are governed by the straight scanning lines, k_{rw} and k_{rg} are obtained by linear interpolation of the end point values. The resulting permeability model is:

$$k_{rw}^D(s),\ k_{rg}^D(s),\ \text{when } s = s_h \text{ and } \frac{\partial s}{\partial t} < 0, \tag{9}$$

i.e., in drainage flow; and

$$\begin{aligned} k_{rw}(s, s_h) &= \left(\frac{s_r - s}{s_r - s_h}\right) k_{rw}^D(s_h) + \left(\frac{s - s_h}{s_r - s_h}\right) k_{rw}^M(s_r), \\ k_{rg}(s, s_h) &= \left(\frac{s_r - s}{s_r - s_h}\right) k_{rg}^D(s_h),\ \text{when } s_h \le s \le s_r(s_h), \end{aligned} \tag{10}$$

i.e., in scanning flow.

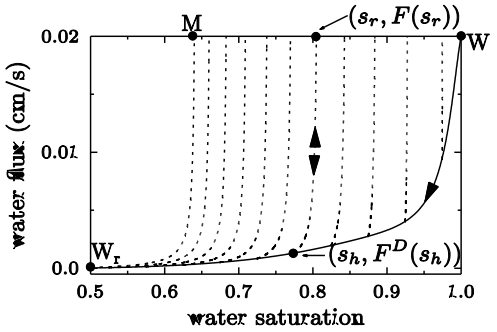

Figure 5: Water flux function.

Lower solid curve: irreversible drainage F^D in (11). There is an almost invisible inflection point in the drainage flux function very near W. Steep dashed curves: reversible scanning curves F in (12); reversibility is indicated by the two opposing arrowheads. Horizontal solid line M - W at 0.02: end points of imbibition process along each scanning curve. On such a curve maximum water relative permeability k_{rw}^M is attained at M - W. The $\mathbf{CO}_2$ is immobile on each point of M - W, so we name the latter the $\mathbf{CO}_2$ immobilization locus (IL). Notice that the solution path lies in the keel MWW_r the shape of these fluxes does take into account the buoyancy coefficient and background flow values.

The hysteresis model is obtained by inserting (9) in (5)–(6), in the drainage regime, and (10a,b) in (5)–(6), in the scanning regime. The corresponding drainage flux function and family of scanning flux functions can be seen in Fig. 5; they are

$$F^D = \frac{k_{rw}^D(s)\left[\nu + \varepsilon k_{rg}^D(s)\right]}{k_{rw}^D(s) + \mu k_{rg}^D(s)}, \text{ if } s = s_h \text{ and } \frac{\partial s}{\partial t} < 0, \tag{11}$$

(drainage case) and

$$F = \frac{k_{rw}(s,s_h)\left[\nu + \varepsilon k_{rg}(s,s_h)\right]}{k_{rw}(s,s_h) + \mu k_{rg}(s,s_h)}, \frac{\partial s_h}{\partial t} = 0, s \in [s_h, s_r], \tag{12}$$

(scanning case).

5 Numerical method for hysteretic two-phase flow

In this section, we describe a modification of the high resolution finite difference scheme [213] that numerically approximates the hysteresis model defined by Eqs. (5)–(6), (11), (12). This Godunov-type central scheme is based on the use of more precise information about the speeds of propagation and can be viewed as a generalization of the Kurganov-Tadmor central schemes [214]. The main advantages of this central scheme are high resolution, due to the smaller amount of numerical dissipation, and simplicity. There are no Riemann solvers or characteristic decomposition involved. At the same time, the central-upwind scheme has an upwind nature, since it respects the directions of wave propagation by measuring the one-sided speeds.

We consider only uniform grids and use the notation: $x_j = j\Delta x$, $x_{j\pm\frac{1}{2}} = x_j \pm \Delta x/2$, $t^n = n\Delta t$. The modified scheme proceeds in two stages: Advance-s and Advance-s_h. Assume that we have already computed an approximation to the solution at time $t = t^n$ of the form,

$$\widetilde{s}(x,t^n) = \sum_j s^{j,n}\chi_j(x), \quad \widetilde{s}_h(x,t^n) = \sum_i s_h^{j,n}\chi_j(x). \tag{13}$$

Here χ_j is the characteristic function of the cell $(x_{j-\frac{1}{2}}, x_{j+\frac{1}{2}})$ and $s^{j,n}$, $s_h^{j,n}$ are cell averages computed at time $t = t^n$. We compute the maximum and minimum possible speeds of propagation, for $(s,s_h) \in S$,

$$a^+ = *max\left\{\frac{\partial F}{\partial s}(s,s_h;\nu),0\right\}, a^- = *min\left\{\frac{\partial F}{\partial s}(s,s_h;\nu),0\right\},$$

where $S = \left\{(s,s_h) \in [0,1]\times[0,1] : s_h \le s \le s_r(s_h)\right\}$ is the keel in state space, depicted in Fig. 13, and we use the maximum value of ν, namely, $\nu = \nu_+$.

Advance-s. In the first stage, s_h is kept frozen in time. We compute predictor cell averages (s^j, s_h^j) at time $t = t^{n+1}$ using the central-upwind scheme

$$\frac{s^j - s^{j,n}}{\Delta t} + \frac{H^n_{j+\frac{1}{2}}(\nu) - H^n_{j-\frac{1}{2}}(\nu)}{\Delta x} = 0, \quad s_h^j = s_h^{j,n}, \tag{14}$$

with the numerical flux

$$H^{n}_{j+\frac{1}{2}}(\nu) = \frac{a^{+}F(s^{j,n}, s_h^{j,n}; \nu) - a^{-}F(s^{j+1,n}, s_h^{j+1,n}; \nu)}{a^{+} - a^{-}} + \frac{a^{+}a^{-}(s^{j+1,n} - s^{j,n})}{a^{+} - a^{-}}. \quad (15)$$

Injection at the inlet, which occurs in cell j_0 and corresponds to the term Q_w/ϕ in Eq. (5), requires changing (14a) into

$$\frac{s^{j_0} - s^{j_0,n}}{\Delta t} + \frac{H^{n}_{j_0+\frac{1}{2}}(\nu_{+}) - H^{n}_{j_0-\frac{1}{2}}(\nu_{-})}{\Delta x} = \frac{q}{\Delta x}, \quad (16)$$

where $\nu_{+} = \nu_{-} + q$, ν_{-} is the background flow velocity and q is the volumetric injection rate.

Advance-s_h. In the second stage, we compute $(s^{j,n+1}, s_h^{j,n+1})$ from (s^{j}, s_h^{j}) as follows. If (s^{j}, s_h^{j}) represents a point in the domain S, we set $(s^{j,n+1}, s_h^{j,n+1}) = (s^{j}, s_h^{j})$. On the other hand, if (s^{j}, s_h^{j}) represents a point outside the domain S, $(s^{j,n+1}, s_h^{j,n+1})$ is obtained by projecting (s^{j}, s_h^{j}) back onto the boundary of S, maintaining s constant, as proposed in [224]. In more details, if $s_h^{j} > s^{j}$, we set $(s^{j,n+1}, s_h^{j,n+1}) = (s^{j}, s^{j})$; on the other hand, in the case $s_h^{j} < s_r^{-1}(s^{j})$, we set $(s^{j,n+1}, s_h^{j,n+1}) = (s^{j}, s_r^{-1}(s^{j}))$. See Fig. 13.

Boundary conditions are implemented using the method of ghost cells. Both at the left and right boundaries an artificial cell is used, where the variables s and s_h are set to their values in the proper adjacent cell at every time step.

Results and Discussion

6 Quantification of hysteretic trapping

In this section, we utilize numerical and analytical techniques to quantify hysteretic trapping. We do so in the context of two gedanken trapping experiments for two typical regimes, corresponding to low and significant injection rates. The experiments are explained in terms of solutions for one-dimensional, vertically-upward flow, modeled by the Buckley-Leverett equation (5), which takes into account the effects of gravity and of a possible background flow in the aquifer, but neglects the diffusive effect due to capillary pressure [209, 230]. Compressibilities of both phases are neglected: this is a good approximation if the $\mathbf{CO}_2$ plume size is not too large; furthermore, incompressibility allows the usage of fractional flow theory and of the method of characteristics. In this initial study there is no mass exchange between the $\mathbf{CO}_2$-rich and water-rich phases, exactly as in the laboratory experiments [197], in which fluids had been thoroughly equilibrated before entering the rock sample. The essential feature of the model is permeability hysteresis of the two phases, measured experimentally in the capillary dominated regime. Expressions for permeabilities with hysteresis are defined in (8)–(10) and given in Sect. 3.

Let us imagine a vertical porous rock cylinder with impermeable surface, except at top and bottom. The cylinder has length 10 cm (4 inches in the figures); there is an inlet located 2.5 cm above the bottom at $x = 1$ *in*, which by convention corresponds to $x = x_1$.

The vertical cylinder is drawn horizontally in Figs. 6, 7, and 8. At the top of the figure, white arrowheads indicate $\mathbf{CO}_2$ injection at the inlet; black arrowheads indicate water injection. The position of the arrowhead indicates the section of the cylinder where injection takes place. At the left side, black arrowheads indicate the background flow, entering uniformly upward through the bottom of the cylinder. We do not mark the obvious outflow on the right.

Let us describe hysteresis by means of a gedanken standard experiment on the water flux function, because the latter is customarily used to describe two-phase flow. The laboratory experiments described in Sections 2–3 lead to a drainage flux function F^D and scanning flux functions F that include the effect of gravity, such as those represented in Fig. 5. The points along the solid drainage curve are obtained by starting at the upper right corner, where the water saturation is $s_w = 1$, and reducing the proportion of water in the injected fluid slowly enough so that hysteretic effects have time to act. This is done until the saturation $s_w = s_h$ is reached. During this process, we traverse the portion of the drainage curve between the upper right corner and the point with saturation $s_w = s_h$. Now a reversal takes place and the proportion of water in the injected fluid is slowly increased: the dashed curve based at $(s_h, F^D(s_h))$ is traversed up to the top, where the carbon dioxide becomes immobile because its saturation is reduced to its history-dependent residual value $1 - s_r$, corresponding to water saturation s_r. The dashed curve is called a scanning curve, rather than imbibition curve, because once a point of this curve is reached by increasing water saturation, reversal to decreasing water saturation generates points that lie on the same curve. In practice this reversibility is approximate, but we will assume it to be exact in our model.

In the results of the experiments for supercritical $\mathbf{CO}_2$ and water [197] an unexpected feature is the very large slope of the scanning curves, which can be observed in Fig. 5; these slopes are orders of magnitude larger than those appearing in hysteresis models for oil and water, such as Killough's [211] and Land's [215]. Simulations based on explicit schemes will be impaired by very large CFL numbers resulting from such slopes. Our simulations are accurate because they employ sufficiently small time steps dictated by these CFL numbers.

6.1 The two stages in hysteretic trapping

Initially the porous cylinder is saturated with water, which perpetually enters the bottom of the cylinder at a constant rate ν_-, mimicking background flow of water in the aquifer. We used an unrealistically large rate $\nu_- = 0.02 \mathbf{cm}^3/(\mathbf{cm}^2\mathbf{s})$, which tends to drag the $\mathbf{CO}_2$ upward, in order to show that the method works to immobilize $\mathbf{CO}_2$, nevertheless. At time zero, injection of supercritical $\mathbf{CO}_2$ at a constant rate q starts at the inlet; the buoyancy coefficient ε, defined in (6), used in (5), (7), (11), (12), has value -4.62×10^{-5} [cm/s], according to the experiments in [197]. The injection continues for time T^{inj}; during this stage, in which water is drained, typical Buckley-Leverett profiles are formed. These profiles are governed by the drainage fractional flow function for water, which is similar to the solid curve in Fig. 5.

At the end of this stage we replace $\mathbf{CO}_2$ injection by water injection at the inlet, but preserve the same volumetric flow rate q for simplicity. In this second stage we have imbibition of water, so the flow is governed by scanning fractional flow functions, the dotted curves in Fig. 5. According to an argument to be presented in Sect. 6.3, which is based on the method of characteristics, along these scanning curves a saturation discontinuity is formed. It moves upward and separates a $\mathbf{CO}_2$/water mixture above from a similar mixture below in which the $\mathbf{CO}_2$ saturations have been brought down to their residual values. Therefore the $\mathbf{CO}_2$ below the discontinuity becomes immobile. Hence the name *trapping shock* for this discontinuity. This trapping shock moves upward at a very fast speed because the slopes of the scanning fractional flow functions are large, as indicated in the same figure. This shock rapidly reaches the top of the $\mathbf{CO}_2$ plume at a time that we call T^{top}, leaving it immobile and completing stage two. From this time on the $\mathbf{CO}_2$ profile remains immobile and unchanged irrespective of further water injection at the inlet or even of changes in the background flow.

Hysteretic trapping may occur in two different regimes, according to the presence of a Welge shock formed in the initial drainage stage $t \le T^{inj}$. We analyze first the regime without this shock because the solution has a simpler structure, as can be seen in Fig. 6.

6.2 Very low $\mathbf{CO}_2$ injection regime

Typically, in this regime the $\mathbf{CO}_2$ saturation is small, as can be seen in Fig. 6 and deduced from Eq. (18). In Fig. 6 we use the value $q = 0.00237 \mathbf{cm}^3/(\mathbf{cm}^2\mathbf{s})$. In the first stage ($\mathbf{CO}_2$ injection at the inlet) a widening square wave profile of $\mathbf{CO}_2$ is formed, viz., a constant state bounded by an upward moving shock and by a discontinuity standing at the inlet, see Figs. 6(a)–(c). To facilitate the visualization of motion in the flow, we also plot $\mathbf{CO}_2$ flux profiles. Since no water is injected at the inlet in the first stage $t \le T^{inj}$, the amplitude $1 - s_+$ of the carbon dioxide square wave is computed through conservation of water mass, enforced by equating the water drainage fluxes F^D from Eq. (11) evaluated immediately below and above the inlet, in which $\mathbf{CO}_2$ is injected at a rate q, where the states are defined by water saturations s_-, s_+ and flow rates ν_-, ν_+, yielding

$$F^D(s_- = 1; \nu_-) = F^D(s_+; \nu_+ = \nu_- + q). \tag{17}$$

The usage of the water drainage flux F^D on the R.H.S. of (17) is justified by the $\mathbf{CO}_2$ injection, in which water saturation above the inlet decreases. The same usage on the L.H.S. is not so clearly justified, except that for $s = 1$ the values of the drainage and scanning fluxes F^D and F coincide (so the end result is independent of the choice). Equation (17) leads to a nonlinear equation for s_+ in terms of μ and ε from Eq. (5) and drainage permeabilities k^D_{rw}, k^D_{rg} from Sect. 3. The resulting equation, which has a unique solution s_+, easily found by a numerical procedure, is:

$$q = \frac{\mu \nu_- - \varepsilon k^D_{rw}(s_+)}{k^D_{rw}(s_+)} k^D_{rg}(s_+). \tag{18}$$

Here it turns out that $1-s_+ = 0.005$, a small $\mathbf{CO}_2$ saturation, as predicted, which entails that the storage of significant amounts of $\mathbf{CO}_2$ can only be achieved at longer times and spread over larger aquifer volumes. The speed σ^{W} of the upward moving shock that is the front of the square wave is obtained from fractional flow theory as

$$\sigma^{\mathrm{W}} = \frac{F^D(s=1) - F^D(s_+)}{1-s_+}, \tag{19}$$

where $\nu = \nu_- + q$ is used to evaluate both F^D.

After time T^{inj}, the injection of $\mathbf{CO}_2$ at the inlet is replaced by water injection, leading to water imbibition, and the trapping shock forms; its amplitude is tiny, so saturation changes can only be observed after a blow-up, as in Fig. 6(e1). It is located at the upstream side of the $\mathbf{CO}_2$-flux wave, given by F_g (see (7b,c)), which is clearly displayed in all of Figs. 6 and 7. We argue that, if the saturation above the trapping shock is s_+, then below it the saturation is $s_r(s_+)$ (see Eq. (8) for the expression of s_r). Indeed, $\mathbf{CO}_2$ mass conservation determines the saturation just above the inlet, dubbed s_*, through the requirement (see (7b,c) and (10) for the definition of the $\mathbf{CO}_2$ flux F_g)

$$F_g(s=1, s_h=1; \nu_-) = F_g(s_*, s_h = s_+; \nu = \nu_- + q). \tag{20}$$

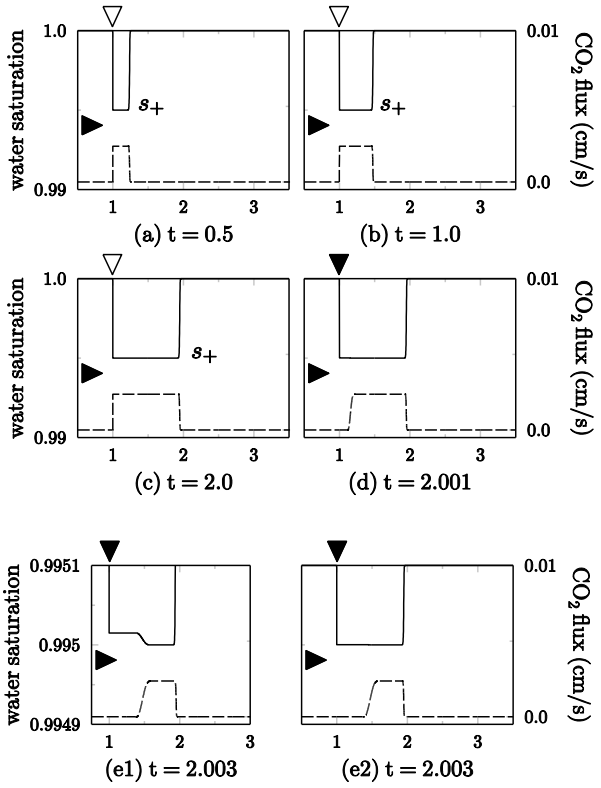

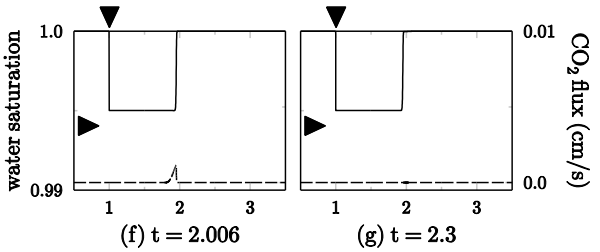

Figure 6: Simulation of gedanken low CO_2 injection rate into a 4 inch long core, at seven distinct times, Sect. 6.2.

Solid lines are brine saturations, with values on the left vertical axis in each figure. Dashed lines are CO_2 fluxes, F_g in (7b,c), drawn to aid locating mobile and immobile CO_2, with values on the right vertical axis of each figure. The horizontal axis in x represents vertical position, measured in inches, in the gedanken vertical cylinder. Background flow enters from the left, as indicated by the black arrowhead at the left side of the figures. The arrowheads at the top of the figures indicate the location where injection of CO_2 (white arrowheads) or water (black arrowheads) takes place. The CO_2 injection from the inlet at $x=1$ *in* occurs between $t=0$ and $t=T^{inj}=2.0$ s, figures (a)–(c). The chase brine injection stage ends at $t=T^{top}\approx 2.006$ s. To facilitate understanding (e2), a plot at the same time is shown in (e1) with a vertical scale expanded for the saturation only. This scale results from a blow-up by a factor of 10^4 around the saturation value $s_+=0.995$. The scale for the flux is left unchanged. One sees clearly the trapping shock location at the upstream side of the dashed square CO_2 flux wave in figures (d)–(f). Moreover, there is no CO_2 downstream of the dashed square flux wave, while upstream the CO_2 is immobile. For more details on this caption, see text in Sect. 6.2.

The usage above of the imbibition flux at the L.H.S. (which has the same expression as the scanning flux) is justified by the fact that there was never any $\mathbf{CO}_2$ below the inlet; we use $s_h=1$ for the same reason. On the R.H.S. the injected chase brine is trying to displace $\mathbf{CO}_2$, leading to an imbibition process with $s_h=s_+$. In the absence of $\mathbf{CO}_2$ the L.H.S. vanishes. According to the discussion in Sect. 4, this implies that $s_*=s_r(s_+)$, a residual $\mathbf{CO}_2$ saturation. In other words, there is a transition along the scanning curve corresponding to $s_h=s_+$ between its two extreme points, $s_r(s_+)$ to s_+. Inspecting the curvature of the scanning curves in Fig. 10(b) we see that a single shock is formed between B (with $s=s_*$) and C (with $s=s_+$). It turns out that this is the trapping shock; its speed is

$$\sigma^{\mathbf{Tr}}=\frac{F(s_+)-F(s_r(s_+))}{s_+-s_r(s_+)}, \tag{21}$$

where $s_h=s_+$ and $\nu=\nu_-+q$ are used to evaluate the values of F, given in Eq. (12); we see that the numerator of (21) is the jump of the water flux between top and bottom of the scanning curve with $s_h=s_+$ while the denominator is the corresponding jump of water saturation.

The states immediately above and below the trapping shock as well as its speed remain constant for $T^{inj}<t<T^{top}$ during the second stage (i.e., water injection). Inspecting the scanning curves in Fig. 10 one sees that the saturation at the top $s_r(s_+)$ does not differ much from the saturation at the bottom

s_+. Thus it makes sense to apply the Mean Value Theorem to (21) in order to conclude that $\sigma^{\mathbf{Tr}}$ approximates $\partial F/\partial s$ along scanning curves. The slopes of these curves are large, according to Fig. 10, and so are the trapping shock speeds. We conclude that the trapping shock sweeps and immobilizes the carbon dioxide very quickly, i.e., T^{top} is only slightly larger than T^{inj}. Moreover, because s_* and s_+ are very close, the original CO_2 square wave at $t = T^{inj}$ and the immobilized square wave for $t > T^{top}$ are almost identical in shape.

6.3 Significant supercritical $\mathbf{CO_2}$ injection regime

Typically, the $\mathbf{CO_2}$ injection rate q is not low. In Fig. 7 we use the value $q = 1.917\mathbf{cm}^3/(\mathbf{cm}^2\mathbf{s})$. This value was chosen to generate clear figures in the gedanken experiments; for lower more realistic values the figures would be qualitatively similar. If this rate were used in the laboratory experiments to measure permeabilities, a correction to Darcy's law, such as Forchheimer's, would have to be used in the calculation of permeabilities. This usage is unnecessary in the synthetic experiments for our purposes.

In the first stage the profile is a small shock at D trailed by a rarefaction wave until C and a thin constant state region above the inlet, see Figs. 7(a)–(b), 8. Here, the water saturation s_+ for this constant state turns out to be 0.6, according to Eq. (18). The profile can be constructed by fractional flow theory; the first stage is illustrated in Figs. 7(a)–(b), 8 and 10(a). The thin constant state region is clearly visible in Fig. 8, obtained numerically. The region originates from the fact that the characteristic speed at the inlet state is positive (at point C in Fig. 10).

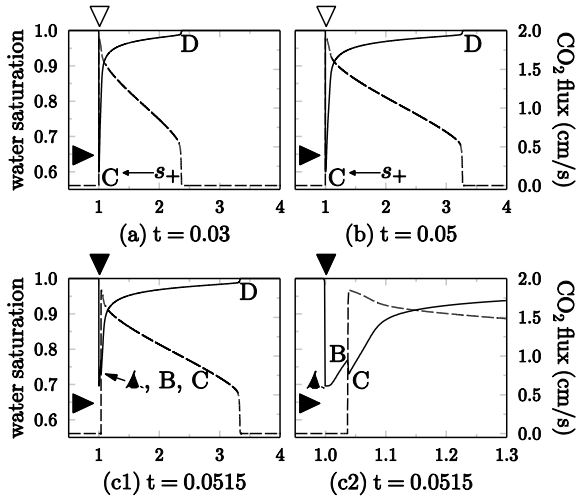

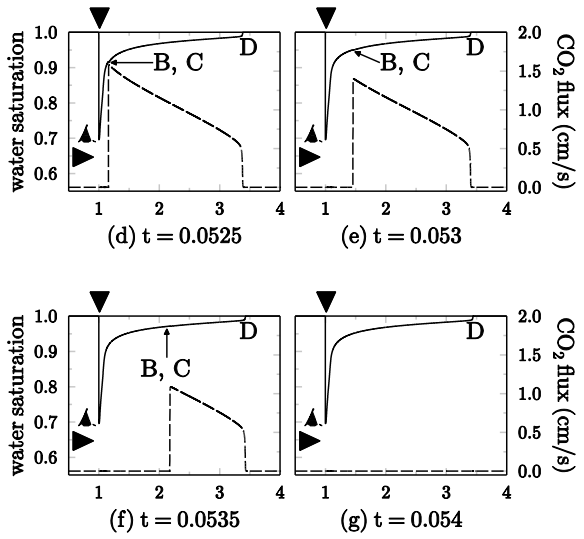

Figure 7: Simulation of gedanken significant CO_2 injection rate into a 4 inch long core, at seven distinct times, Sect. 6.3.

The CO_2 injection occurs at $x=1$ *in* from $t=0$ to $t=T^{inj}=0.05$ s. The chase brine injection stage starts at $t=T^{inj}$ and ends at $t=T^{top}\approx 0.0536$ s. Solid lines are brine saturations, with values on the left vertical axis in each figure. Dashed lines are CO_2 fluxes, with values on the right vertical axis in each figure. To facilitate understanding (c1), a plot at the same time is shown in (c2), with horizontal scale resulting from a blow-up by a factor of 10 around the inlet at $x=1$ *in*. The tiny trapping shock is located at the upstream side of the trapezoidal CO_2 flux pulse in figures (c1)–(f). Again, there is no CO_2 downstream of the dashed trapezoidal flux wave, while upstream the CO_2 is immobile. The states A–D correspond to saturation-flux points in Fig. 10. The white and black arrowheads have the same meaning as in Fig. 6. Taking into account the tiny range of saturations in the vertical axis of Fig. 6, compared to the saturation range in Fig. 7, as well as the difference in time scales between the two simulations, one sees that CO_2 is stored much closer to the injection point in the higher injection rate regime. For more details on this caption, see text in Sect. 6.3.

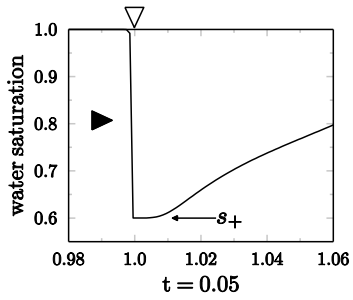

Figure 8: Figure 8: Gedanken significant CO_2 injection rate.

The black arrowhead indicates direction of homogeneous background flow. The white arrowhead indicates the location where injection of CO_2 takes place. Horizontal blow up of saturation in Fig. 7(b)

around $x=1$ *in* by a factor of 100. Starting at $x=1$ *in*, note constant state corresponding to C at $t=0.05$ s, which has saturation $s_+=0.6$ defined by (21) and calculated by (18).

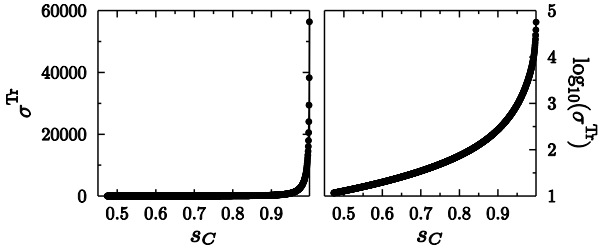

Figure 9: Speed (cm/s) of trapping shock $\sigma^{\mathbf{Tr}}$ in terms of variable s_C in Eq. (19), for background and $\mathbf{CO}_2$ rates from Fig. 7.

There is a dramatic increase in $\sigma^{\mathbf{Tr}}$ near $s_C=1$ to almost half a mile per second. Notice that the scale of the vertical axis for σ^{Tr} is linear in the left figure and logarithmic in the right one.

When at $t=T^{inj}$ the injection of $\mathbf{CO}_2$ is replaced by injection of water in the inlet, the trapping shock is formed at the inlet position in Fig 7(b). The saturation immediately above the trapping shock is s_+, and the one immediately below it is $s_r(s_+)$, according to Eq. (20) and its explanation. The speed of the trapping shock $\sigma^{\mathbf{Tr}}$ is given by (21), which is the same as the slope of B-C in Fig. 10(b). The trapping shock quickly traverses the thin constant state region (in which $s=s_+$) with constant speed $\sigma^{\mathbf{Tr}}$ and starts interacting with the rarefaction wave at time t_2 and position x_2, given by the expressions (with $\nu_+=\nu_-+q$ as before)

$$t_2=\frac{\sigma^{\mathbf{Tr}}T^{inj}}{\sigma^{\mathbf{Tr}}-\dfrac{dF^D}{ds}(s_+;\nu_+)},\quad x_2=x_1+\sigma^{\mathbf{Tr}}\left(t_2-T^{inj}\right) \tag{22}$$

Fig 7(c1) shows the profile shortly after $t=t_2$. Since the figure is not clear, we redraw it in Fig 7(c2) around the inlet position at $x=1$, expanding the horizontal scale by a factor of ten. Of course the location of the trapping shock is the same as that of the back of the trapezoidal $\mathbf{CO}_2$ flux pulse. The pulse shows that below the trapping shock the $\mathbf{CO}_2$ is immobile; Fig 7(c2) confirms that water saturation increases when the trapping shock crosses the porous medium (i.e., we have imbibition).

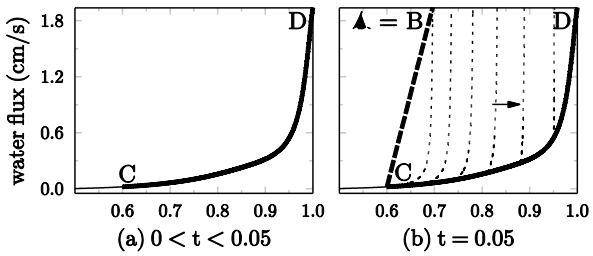

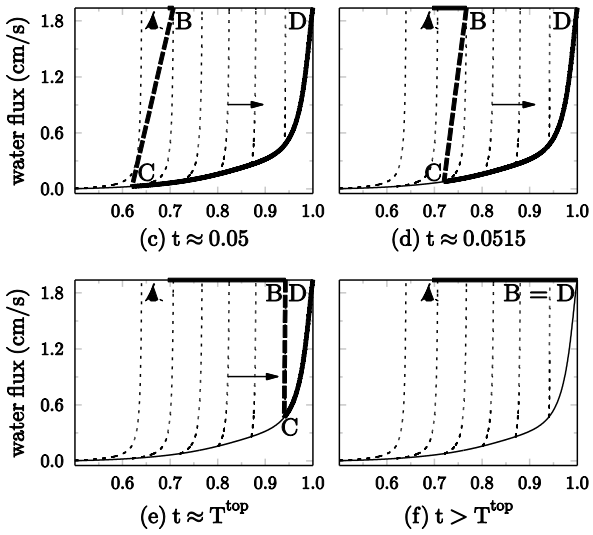

Figure 10: Solution paths for the gedanken flow in Fig. 7 drawn in saturation-flux plane.

The horizontal axis is water saturation. The curve C - D generates a typical Buckley-Leverett profile, namely, a rarefaction until the Welge point preceded by a small shock to D. The dashed line B - C represents the trapping shock; only the states B and C appear in physical space. The increasing arrows indicate the growth of the trapping shock speed until it disappears when it reaches D. In this sequence, A remains fixed but B begins to move at $t = t_2$ (see Eq. (22a)) rightward and disappears at $t = T^{top}$, as discussed in Sect. 6.1. The immobilized portion of the original $\mathbf{CO}_2$ profile is represented by A - B (or A - D in (f)). The saturation-flux points $A - D$ correspond to states $A - D$ in Fig. 7. Notice that the solution path lies in a keel-like region. This region is covered by the dashed scanning curves, including the drainage curve underneath and the horizontal segment M - W above appearing in Fig. 5.

The figures also show that above the trapping shock we still have the Buckley-Leverett solution generated in the first stage. In the saturation-flux plane the solution path evolves from the one in Fig. 10(b) to that in Fig. 10(c). The curve D - C is the water drainage flux along the Buckley-Leverett profile. The segment C - B represents the trapping shock as a dashed line along a dotted scanning curve, corresponding to water imbibition. Notice that the trapping shock satisfies the requirements for shock admissibility dictated by the method of characteristics. The segment B - A corresponds to the immobile $\mathbf{CO}_2$ profile between the inlet and the trapping shock positions.

In both the sequences in Figs. 7(c1)–(f) and Figs. 10(b)–(e) the trapping shock moves upward. Its speed $\sigma^{\mathbf{Tr}}$ increases because it is given by the slope of B - C, namely,

$$\sigma^{\mathbf{Tr}} = \frac{F(s_{\mathbf{C}}) - F(s_r(s_{\mathbf{C}}))}{s_{\mathbf{C}} - s_r(s_{\mathbf{C}})}, \tag{23}$$

where s_C is the saturation at C along the drainage curve, and $s_h = s_C$, $\nu = \nu_- + q$ are used to evaluate the values of F. Meanwhile the amplitude of the trapping shock decreases because it is the difference

between the saturations at B and C. The trapping shock disappears when it reaches the Welge shock at the top of the Buckley-Leverett plume, leaving the $\mathbf{CO}_2$ immobile from time T^{top} on, see Fig. 10(f).

Let us describe analytically the immobile profile; to do so we need to calculate also the trapping shock path $x = X(t)$ in the (x,t) plane. This path is a straight line between the points (x_1, T^{inj}) and (x_2, t_2), the latter given by (22). Before interacting with the trapping shock, the rarefaction part of the Buckley-Leverett profile above this shock has saturation given by an expression of the standard form

$$s = s(x,t) = S\left(\frac{x - x_1}{t}\right), \mathbf{for} t \geq 0, \frac{x - x_1}{t} \geq \frac{x_2 - x_1}{t_2}, \tag{24}$$

determined implicitly by the standard rarefaction equation

$$\frac{x - x_1}{t} = \frac{d}{ds} F^D(s; \nu_+ = \nu_- + q). \tag{25}$$

The saturation just above the shock is $s^> = s(X(t),t)$ and just below the shock is $s^< = s_r\left(s(X(t),t)\right)$ (the saturations $s^>$ and $s^<$ correspond to C and B in Figs. 7, 10). Thus the shock speed $dX(t)/dt$ satisfies

$$\frac{d}{dt} X(t) = \frac{F(s^>) - F(s^<)}{s^> - s^<}, \tag{26}$$

where $s_h = s_h(t) = s(X(t),t)$ and $\nu = \nu_- + q$ are used to evaluate the values of F for water imbibition, given in equation (12). Equation (26) is an ordinary differential equation with independent variable t, dependent variable X, and initial condition $X(t_2) = x_2$, which can be solved and is valid until the trapping shock reaches the Welge shock.

As to the saturation profile, we find t as a function of x along the trapping path, i.e., by inverting $x = X(t)$, determining $t = T(x)$. The profile is

$$s = s(x) = s_r\left(s(x, T(x))\right). \tag{27}$$

Because usually $s_{s_h}(s)$ is very close to s, the immobile profile is very close to the Buckley-Leverett profile at the end of the first stage, the period of $\mathbf{CO}_2$ injection.

As long as the $\mathbf{CO}_2$ in the Buckley-Leverett profile does not reach the top of the reservoir, the amount of trapped $\mathbf{CO}_2$ is just the time duration of injection multiplied by the injection rate. Moreover, faster injection rates of $\mathbf{CO}_2$ lead to trapping of $\mathbf{CO}_2$ closer to the injection inlet.

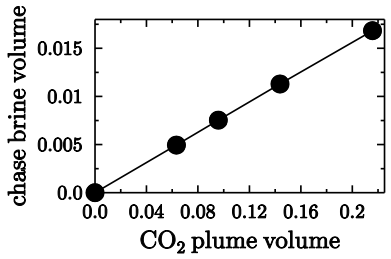

Figure 11: Volume of chase brine vs. volume of injected $\mathbf{CO}_2$ for gedanken simulation in Fig. 7.

Notice that the volume of chase brine necessary to immobilize $\mathbf{CO}_2$ is exactly proportional to the volume of the latter. To immobilize ten volumes of $\mathbf{CO}_2$ one volume of chase brine is needed, i.e., the volumetric overhead is $\mathbf{VO} = 0.1$. The filled circles were obtained numerically, while the line was obtained analytically.

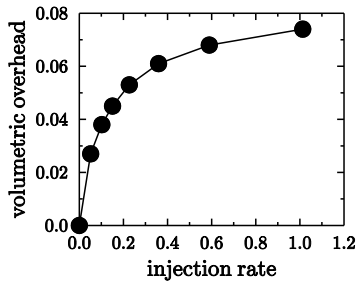

Figure 12: On the cost of $\mathbf{CO}_2$ trapping by chase brine: volumetric overhead vs. injection rate q.

The volumetric overhead is VO defined in Fig. 11. The injection rate at the inlet has the same value for $\mathbf{CO}_2$ and chase brine. Notice that chase brine volumetric overhead is favorable for very high injection rates. The filled circles were obtained numerically, while the lines were obtained by interpolation.

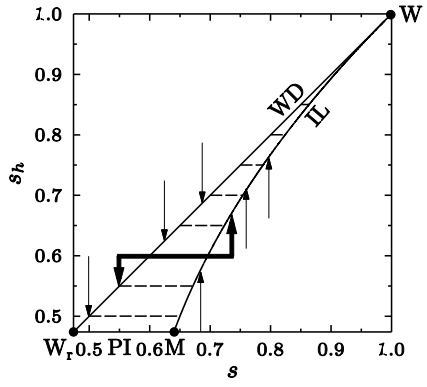

Figure 13: *The saturation state space "keel" from Fig. 5.*

The water drainage (WD) line W - W_r and the scanning curve W_r - M are part of the keel boundary. (Primary) imbibition (PI) occurs along the latter curve. The curve M - W is the locus of $\mathbf{CO}_2$ immobilization (IL).

Advancing the solution profile from t^n to t^{n+1}. The solution path lies initially in the keel MWW_r. When performing the Advance-s stage the points in the solution path are displaced horizontally, preserving the value of s_h, but quite possibly exiting the keel. Then the Advance-s_h stage is applied to the points of the solution path outside the keel. These points move to the boundary of the keel in the vertical direction indicated in the figure; thus the solution returns to the keel.

Conclusions

7 Discussion

We do not discuss the important issue of practicality of $\mathbf{CO}_2$ capture and storage in deep saline aquifers; see, e.g., [202]. Once $\mathbf{CO}_2$ is injected, its buoyancy has to be counteracted to prevent it from leaking to the atmosphere in the long run. Dissolution into the water, descending natural convection flow and reactions with the rock are essential to long time trapping, but they are not very effective in the short term [198, 204, 209, 212, 219, 233].

In this work we analyze supercritical $\mathbf{CO}_2$ retention enhanced by permeability hysteresis, a technique proposed elsewhere. This retention is predicted to occur in the capillary dominated regime, which predominates in large regions of the aquifer. Here we use recent steady state measurements of supercritical $\mathbf{CO}_2$ and water relative permeabilities at high pressure and temperature. The usage of a CT scanner, constant flow rate and pressure boundary conditions contribute to the high quality of these measurements.

The analysis is performed by a combination of exact analytic solutions based on fractional flow theory and the method of characteristics, as well as highly accurate modern simulation techniques adapted to take hysteresis into account. This combination is used to analyze the one dimensional upward flow of fluids, first the injected $\mathbf{CO}_2$, then the injected water that takes advantage of permeability hysteresis to immobilize the $\mathbf{CO}_2$.

We find it advantageous to inject $\mathbf{CO}_2$ at substantial rates before the injection of water, as summarized in Fig. 12. This water immobilizes the $\mathbf{CO}_2$ by means of a hysteretic shock that propagates very quickly, a peculiarity of supercritical $\mathbf{CO}_2$ revealed in these experiments, which has no counterpart in oil and is not contemplated in existing commercial simulators.

Our model considers genuinely one-dimensional flow, such as the one occurring when $\mathbf{CO}_2$ is injected at one end of a thin, long cylinder containing a homogeneous porous medium with pores initially filled by water. Of course we assume that the injected $\mathbf{CO}_2$ and water have different densities. The saturation is assumed to be uniform in each cross section of the cylinder. This assumption is valid in a variety of circumstances: very small aspect ratio, large flow rates or homogenizing effects due to capillarity. The flow in our model is governed by the Buckley-Leverett conservation law, reflecting the

balance between gravity and viscous forces. As motion in this model is genuinely one dimensional, it cannot capture any gravitational segregation transversal to the flow.

This model is very different from a family of models for the evolution of $\mathbf{CO}_2$ injected in an aquifer initially filled with water [207, 210, 216, 217]. Such models rely on the assumption of vertical equilibrium between gravity and capillary forces. Most of the time, the evolution is primarily driven by buoyancy and restricted by geometry. The injected $\mathbf{CO}_2$ forms a plume whose motion is to be predicted. A number of works study this plume under the assumption that its motion is two dimensional; the fluids do not interpenetrate but a sharp interface between them is formed. These models use the depth of the interface as dependent variable rather than the saturation we employ; this depth satisfies a nonlinear convection-diffusion equation that can be solved numerically. In certain limits the convection-diffusion equation reduces to a hyperbolic equation, which can be solved by the method of characteristics [207, 210, 216, 217]. It is interesting to notice that in the latter work a shock is formed that interacts with a rarefaction wave leaving behind immobile $\mathbf{CO}_2$. There are two analytic confirmations for the existence of the trapping shock, in two models that are rather different. Indeed, in our model there is no gravitational segregation, while in the other one gravitational segregation is exaggerated by the assumption that the two fluids are separated by an interface.

In the present work the practicality of capillary trapping can only be mentioned superficially. We are led to define the rough cost of the process as the volumetric amount of injected brine needed to immobilize one volume of injected supercritical $\mathbf{CO}_2$. This provides an estimate of the process *volumetric overhead* VO. The VO is the slope of the plot in Fig. 11; it depends on the injection rate of the fluids.

A natural question is to determine the injection rate that minimizes the VO cost. This issue is partially addressed in Fig. 12. Notice that high injection rates are more efficient because the slope of the plot decreases.

This work can be improved by taking into account supercritical $\mathbf{CO}_2$ compressibility, which could conceivably slow down the hysteretic shock and reduce its immobilizing efficiency.

We believe that considering radial flow away from a well would lead to analogous results through the use of the similarity variable $x/\sqrt{t}$, but this remains to be verified.

Task 6: Development of the UW-team simulator
PI: Dr. Felipe Pereira

Mathematical/Computational methods

1 Introduction

In this work we present a three-dimensional discretization of a compositional model for the injection of CO_2 in saline aquifers. The model considers the flow of aqueous (aq) and supercritical CO_2 (g) rich phases in a heterogeneous rigid porous media accounting for gravity, capillary pressure and compressibility of the supercritical CO_2. The exchange of mass between the phases is incorporated in the model through flash computations under the assumption of thermodynamic equilibrium through all the reservoir. Such flash computations have been discussed in the report of Task 5 (see also [251]) and take into account evaporation of water into the CO_2 rich phase and the influence of the brine's salinity upon the dissolution of CO_2 in water [255].

In this work the discretization proposed to solve the compositional model is based on a operator splitting in time technique where the system of equations is divided into subsystems as suggested by [256] and evolved separately for each time step. Following the Implicit Pressure Explicit Saturation (IMPES) scheme [234], the pressure equation is numerically solved by a implicit in time conservative method while the transport equations subsystem is approximated by a finite volume method with CFL restrictions, that can display hysteresis, as discussed in the report of Task 5. The accuracy of the discretization has been demonstrated with numerical experiments.

This report is organized as follows. We first discuss in detail the development of the UW-team simulator in approximating a classical compositional model. Next, we describe the Bayesian framework that we have developed. It is used to validate the classical compositional model against exprimental results.

2 Governing equations

The mass conservation equations are given in terms of the total moles per pore volume of each component in the model: CO_2 (m^c), water (m^w) and salt (m^s).

$$\frac{\phi\partial m^c}{\partial t} + \nabla\cdot\left(\frac{m_g^c}{S_g}\mathbf{v_g} + \frac{m_{\mathbf{aq}}^c}{S_{\mathbf{aq}}}\mathbf{v_{aq}}\right) = 0 \tag{1}$$

$$\frac{\phi\partial m^w}{\partial t} + \nabla\cdot\left(\frac{m_g^w}{S_g}\mathbf{v_g} + \frac{m_{\mathbf{aq}}^w}{S_{\mathbf{aq}}}\mathbf{v_{aq}}\right) = 0. \tag{2}$$

$$\frac{\phi\partial m^s}{\partial t} + \nabla\cdot\left(\frac{m_{aq}^s}{S_{aq}}\mathbf{v_{aq}}\right) = 0. \tag{3}$$

where $\mathbf{v_{aq}}$ and $\mathbf{v_g}$ are the percolation velocities of the aqueous and CO_2 rich phase while $S_{\mathbf{aq}}$ and S_g represent the saturations of the phases. The variables $m_{\mathbf{aq}}^s$, $m_{\mathbf{aq}}^c$, $m_{\mathbf{aq}}^w$, m_g^c, m_g^w are the total

moles per pore volume of each component in each phase. The superscripts c, w, s refer to the components CO_2, water and salt, respectively, while the subscripts aq and g denote the aqueous and CO_2 rich phase. By mass conservation, the following relations hold:

$$m^i = m^i_{aq} + m^i_g, \quad i = c, w, s. \tag{4}$$

The phase velocities $\mathbf{v_{aq}}, \mathbf{v_g}$, are functions of the corresponding phase saturation and pressure, and given by Darcy's law for multiphase flows [235]:

$$\mathbf{v_{aq}} = -\mathbf{K}\lambda_{\mathbf{aq}}(S_{\mathbf{aq}})(\nabla p_{\mathbf{aq}} - \rho_{\mathbf{aq}}\mathbf{g}), \tag{5}$$

$$\mathbf{v_g} = -\mathbf{K}\lambda_g(S_g)(\nabla p_g - \rho_g\mathbf{g}), \tag{6}$$

where ρ_g, $\rho_{\mathbf{aq}}$ are the phases densities, K absolute permeability of the rock and $\mathbf{g}$ is the gravity. The functions $\lambda_{\mathbf{aq}}$, λ_g stands for the relative phase mobilities which are defined as

$$\lambda_\alpha(S_\alpha) = \frac{k_{r\alpha}}{\mu_\alpha} \quad \alpha = \mathrm{aq}, g. \tag{7}$$

where $k_{r\alpha}$ denotes the relative permeability of the α phase. They are given by empirical correlations and usually are functions of the phase saturations $S_{\mathbf{aq}}$ and S_g. We assume that the pore volume of the porous medium is fully filled with fluid, resulting in the constraint

$$S_g + S_{aq} = 1. \tag{8}$$

The constants μ_α, $\alpha = \mathrm{aq}, g$ in equation (7) are the phase viscosities. In this work we assume that the viscosities are constants but in principle they are functions of pressure and phase compositions and can be computed through empirical correlations [247].

In addition to the above equations, a constitutive relation between the capillary pressure and saturation must be specified in order to describe the dynamic of the hole fluid mixture as function of the saturation and pressure of one of the phases. This relation is given by

$$p_c(S_{\mathbf{aq}}) \equiv p_g - p_{\mathbf{aq}} \tag{9}$$

3 Phase package

The equations in the previous section describe the transport of the components inside the porous media. The components interact among themselves, forming phases whose dynamic is governed by the Darcy's law. Such dynamic by its turn depends on the properties of the phases such as viscosity and density that are functions of the pressure, temperature and concentrations of each component in each phase.

Assuming thermodynamic equilibrium it is possible to calculate the phases composition given the pressure, temperature and the total moles of each component (m^c, m^w, m^s) using a procedure called flash calculation that has been discussed in details in the report for Task 5. Here we review some aspects of it that are relevant to the coupling of the flash calculations with our flow and tranport codes. The flash calculation can be characterized as a constrained minimization problem stated as follows:

$$\begin{array}{rc} \text{Given} & m^w, m^c, m^s, \geq 0 \\ \text{find} & m^w_{\mathbf{aq}}, m^c_{\mathbf{aq}}, m^s_{\mathbf{aq}}\ ,\ m^w_g \text{ and } m^c_g \end{array}$$

$$\begin{array}{rc} \text{inorder to minimize} & G = G_{\mathbf{aq}} + G_g, \\ \text{subject to} & m^c_{\mathbf{aq}} + m^c_g = m^c, \\ & m^w_{\mathbf{aq}} + m^w_g = m^w, \text{ and} \\ & m^w_{\mathbf{aq}}, m^c_{\mathbf{aq}}, m_{\mathbf{aq}}, m^w_g, m^c_g \geq 0 \end{array} \tag{10}$$

where G denotes the Gibbs free energy of the system, G_w and G_g denotes the total Gibbs free energy of the aqueous and CO_2 phases, respectively. The minimization problem (10) leads to the equality of chemical potentials of each component i in the different phases (Kuhn-Tucker conditions). They are given as follows:

$$g^i_{aq} = g^i_g, \quad i = w, c, s, \tag{11}$$

where g^i_α, $\alpha = w, g$, stand for the chemical potential of component i in the α phase; They are defined by:

$$g^i_\alpha = \left(\frac{\partial G_\alpha}{\partial m^i_\alpha} \right)_{(p, T, m^{j, j \neq i}_\alpha)}, \quad i = c, w, s, \quad \alpha = \text{aq}, g. \tag{12}$$

Since the phases composition is a solution of a minimization problem with restriction, it must obey the Kuhn-Tucker conditions. This implies that [254],

$$\frac{\partial S_{\mathbf{aq}}}{\partial m^c} m^c_{\mathbf{aq}} + \frac{\partial S_{\mathbf{aq}}}{\partial m^w} m^w_{\mathbf{aq}} + \frac{\partial S_{\mathbf{aq}}}{\partial m^s} m^s_{\mathbf{aq}} = S_{\mathbf{aq}} \tag{13}$$

$$\frac{\partial S_{\mathbf{aq}}}{\partial m^c} m^c_g + \frac{\partial S_{\mathbf{aq}}}{\partial m^w} m^w_g = 0 \tag{14}$$

$$\frac{\partial S_g}{\partial m^c} m^c_g + \frac{\partial S_g}{\partial m^w} m^w_g = S_g \tag{15}$$

$$\frac{\partial S_g}{\partial m^c} m^c_{\mathbf{aq}} + \frac{\partial S_g}{\partial m^w} m^w_{\mathbf{aq}} = 0 \tag{16}$$

4 Saturation and Molar Volume calculations

The saturations S_g, $S_{\mathbf{aq}}$ are crucial to determine the dynamic of the fluids inside the porous media. These saturations are calculated from the phases compositions using equations of state that must be consistent with the flash computations adopted in this work.

For the CO_2 rich phase, we assume that the water vapor absorbed by the supercritical CO_2 does not alter the molar volume of the phase. Therefore, the saturation S_g is given by

$$S_g = V_g(p,T)(m_g^c + m_g^w) \tag{17}$$

where V_g is the molar volume of pure supercritical CO_2 defined by the Redlich-Kwong equation as a function of temperature and pressure.

$$V_g^3 - V_g^2\left(\frac{RT}{p}\right) - V_g\left(\frac{RTb}{p} - \frac{a}{p\sqrt{T}} + b^2\right) - \frac{ab}{p\sqrt{T}} = 0. \tag{18}$$

Equation (18) can be solved using the Newton-Raphson root-finding algorithm where the initial value v_0 for the iterative solution will depend on the CO_2 physical state [251]. For the gaseous or supercritical state, we use $v_0 = RT/p$, which is an approximation to the molar volume of the ideal gas at the same conditions, and for the liquid state, which we will not consider in this work, we use $v_0 = 59.22\ \mathrm{cm}^3/\mathrm{mol}$, that corresponds to the molar volume of liquid CO_2 at $25\,^{\circ}\mathrm{C}$ and $80\mathrm{bar}$. The parameters of the above equation are given below

Parameter	Value	Units
a	$7.54\times10^7 - 4.13\times10^4 T$	$\mathrm{bar}\cdot\mathrm{cm}^6\cdot\mathrm{K}^{0.5}\cdot\mathrm{mol}^{-2}$
b	27.80	$\mathrm{cm}^3/\mathrm{mol}$

Considering the incompressibility of brine, the saturation of the aqueous phase composed of brine and dissolved CO_2 is given given by

$$S_{\mathbf{aq}} = V_{\mathbf{aq}}^w m_{\mathbf{aq}}^w + V_{\mathbf{aq}}^c(p,T) m_{\mathbf{aq}}^c + V_{\mathbf{aq}}^s m_{\mathbf{aq}}^s, \tag{19}$$

where $V_{\mathbf{aq}}^w = 18.1\ \mathrm{cm}^3/\mathrm{mol}$ is the apparent molar volume of liquid water, $V_{aq}^s = 18\ \mathrm{cm}^3/\mathrm{mol}$ is the apparent molar volume of the salt component and $V_{\mathbf{aq}}^c$ is the apparent molar volume of the dissolved CO_2 in the aqueous phase. The later is computed using the formula [241]:

$$V_{\mathbf{aq}}^c = V_{\mathbf{aq}}^w\left(1 + A(T) + p_{\mathbf{aq}}B(T)\right), \tag{20}$$

where A, B are functions of temperature defined by the power series

$$A(T) = a_1 T^2 + a_2 T + a_3 + a_4 T^{-1} + a_5 T^{-2}$$
$$B(T) = b_1 T^2 + b_2 T + b_3 + b_4 T^{-1} + b_5 T^{-2}.$$

with coefficients a_i, b_i ($i = 1, \ldots, 5$) defined in Table 1.

Table 1: Coefficients a_i, b_i for the calculation of the apparent molar volume V_{aq}^c.

i	a_i	b_i
1	$0.38384020 \cdot 10^{-3}$	$-0.57709332 \cdot 10^{-5}$
2	$-0.55953850 \cdot 10^{0}$	$0.82764653 \cdot 10^{-2}$
3	$0.30429268 \cdot 10^{3}$	$-0.43813556 \cdot 10^{1}$
4	$-0.72044305 \cdot 10^{5}$	$0.10144907 \cdot 10^{4}$
5	$0.63003388 \cdot 10^{7}$	$-0.86777045 \cdot 10^{5}$

5 Primary variables of the model

We choose the following set of independent variables to describe the compositional model: $m^c, m^w, m^s, p_{\mathbf{aq}}$. The phases composition can be calculated from these primary variables through flash computations and then used to calculate the saturations and densities of the phases. Note that the CO_2 rich phase pressure p_g can be derived from $p_{\mathbf{aq}}$ using the capillary pressure function. Since the entire dynamic of the mixture is described in terms of the aqueous phase, the choice of $p_{\mathbf{aq}}$ as the pressure primary variable implies that the aqueous phase exists in all the reservoir.

6 Pressure equation

In this work we adopt the “volume balance" (VB) method to obtain a partial differential equation for the aqueous phase pressure denoted by p.

Define $S^0 = S_{\mathbf{aq}} + S_g$, the total saturation given by the ratio between the total volume occupied by the reservoir fluid and the pore volume. Due to the compressibility of the fluid mixture and the fact that the transport equations, the pressure equation and the flash calculation are iterated separately in each time step, the simulation may produce values of S^0 which are not exactly 1. The VB technique takes this possibility into account, and introduces a mechanism to recover $S^0 = 1$ at the new time level [256].

For a given pressure and fluid composition at the current time level, t_n, the pressure diferential equation attempts to predict the value of the pressure at the advanced level, $t_{n+1} = t_n + \Delta t$, so that the volumetric constraint $S_{\mathbf{aq}} + S_g = 1$ is satisfied.

In order to derive this equation consider $S^0 = S^0(p, \overline{\mathbf{m}})$ where $\overline{\mathbf{m}} = (m^c, m^w, m^s)$ is the vector of total moles per pore volume for each component. We use the Taylor series to expand the term ϕS^0 in time to get

$$\phi S^0(p(t_{n+1}), \overline{\mathbf{m}}(t_{n+1})) = \phi S^0(p(t_n), \overline{\mathbf{m}}(t_n)) + \phi \Delta t \frac{dS^0}{dt}$$
$$\phi \frac{1 - S^0(p(t_n), \overline{\mathbf{m}}(t_n))}{\Delta t} = \phi \frac{dS^0}{dt}, \tag{21}$$

where the right hand side of the equation (21) is the correction of volumetric discrepancy error introduced at previous time level from a phase package. This correction is necessary to avoid the accumulation of errors. By the chain rule we have

$$\phi \frac{S^0(t_n) - 1}{\Delta t} = -\phi \left(\frac{\partial S_g}{\partial p} + \frac{\partial S_{\mathbf{aq}}}{\partial p} \right) \frac{\partial p}{\partial t} - \phi \left(\frac{\partial S_g}{\partial \overline{\mathbf{m}}} + \frac{\partial S_{\mathbf{aq}}}{\partial \overline{\mathbf{m}}} \right) \frac{\partial \overline{\mathbf{m}}}{\partial t}, \tag{22}$$

using the equations (1), (2), (3) and defining

$$\beta_T(p, \overline{\mathbf{m}}) = -\phi \left(\frac{\partial S_g}{\partial p} + \frac{\partial S_{aq}}{\partial p} \right) \tag{23}$$

as the total fluid compressibility, we can rewrite equation (22) as

$$\begin{aligned} \phi \frac{S^0(t_n) - 1}{\Delta t} &= \beta_T \frac{\partial p}{\partial t} + \\ \frac{\partial S^0}{\partial m^w} \operatorname{div} &\left(\frac{m_g^w}{S_g} \mathbf{v_g} + \frac{m_{\mathbf{aq}}^w}{S_{\mathbf{aq}}} \mathbf{v_{aq}} \right) + \\ \frac{\partial S^0}{\partial m^c} \operatorname{div} &\left(\frac{m_g^c}{S_g} \mathbf{v_g} + \frac{m_{aq}^c}{S_{aq}} \mathbf{v_{aq}} \right) + \\ \frac{\partial S^0}{\partial m^s} \operatorname{div} &\left(\frac{m_{\mathbf{aq}}^s}{S_{\mathbf{aq}}} \mathbf{v_{aq}} \right), \end{aligned} \tag{24}$$

using the product rule for derivatives, we get

$$\begin{aligned} \phi \frac{S^0(t_n) - 1}{\Delta t} &= \beta_T \frac{\partial p}{\partial t} + \\ \operatorname{div} &\left(\frac{\partial S^0}{\partial m^w} \frac{m_g^w}{S_g} \mathbf{v_g} + \frac{\partial S^0}{\partial m^w} \frac{m_{\mathbf{aq}}^w}{S_{\mathbf{aq}}} \mathbf{v_{aq}} \right) + \end{aligned}$$

$$\begin{aligned}
&\mathrm{div}\left(\frac{m_g^c}{S_g}\frac{\partial S^0}{\partial m^c}\mathbf{v_g}+\frac{m_{\mathbf{aq}}^c}{S_{\mathbf{aq}}}\frac{\partial S^0}{\partial m^c}\mathbf{v_{aq}}\right)+\\
&\mathrm{div}\left(\frac{\partial S^0}{\partial m^s}\frac{m_{\mathbf{aq}}^s}{S_{\mathbf{aq}}}\mathbf{v_{aq}}\right)+\\
&\nabla\frac{\partial S^0}{\partial m^w}\left(\frac{m_g^w}{S_g}\mathbf{v_g}+\frac{m_{\mathbf{aq}}^w}{S_{\mathbf{aq}}}\mathbf{v_{aq}}\right)+\\
&\nabla\frac{\partial S^0}{\partial m^c}\left(\frac{m_g^c}{S_g}\mathbf{v_g}+\frac{m_{\mathbf{aq}}^c}{S_{\mathbf{aq}}}\mathbf{v_{aq}}\right)+\\
&\nabla\frac{\partial S^0}{\partial m^s}\left(\frac{m_{\mathbf{aq}}^s}{S_{\mathbf{aq}}}\mathbf{v_{aq}}\right)
\end{aligned} \tag{25}$$

Computational results of the flash model demonstrate that the second derivatives of S^0 with respect to m^c, m^w, m^s are significant small so we can neglect the terms involving $\nabla(\partial S^0/\partial m^i)$, $i = c, w, s$ in equation (25).

Combining the above equation with equations (13-16) finally results in

$$\phi\frac{S^0(t_n)-1}{\Delta t}=\beta_T\frac{\partial p}{\partial t}+\mathrm{div}(\mathbf{v_t}), \tag{26}$$

where $\mathbf{v_t}$ is the total Darcy velocity defined as

$$\mathbf{v_t}=\mathbf{v_g}+\mathbf{v_{aq}} \tag{27}$$

Note that equations (26) and (27) can be easily solved by a mixed finite element method. These equations together with the transport system equations and the flash minimization problem constitute the three subsystems that must be evolved consistently in time.

7 Discretization strategy

The discretization is based on a operator splitting scheme approach where we advance each subsystem independently for each time step in a way very similar to the Implicit Pressure Implicit Saturation (IMPES) approach used in [248] and [234]. In what follows we describe the discretization of the pressure and transport subsystems presented initially as separate problems that are then evolved sequentially in time according to a syncronization alghorithm presented at the end of the section.

7.1 Pressure Subsystem Discretization

The discretized mathematical formulation to evolve the pressure equation from time t_n to t_{n+1} can be stated as follows:

Formulation 1 *Let* Ω *and* Γ *denotes the reservoir region and its boundary. Given the pressure* $p(\mathbf{x},t_n)$ *, the saturations* $S^0(\mathbf{x},t_n)$*,* $S_{\mathbf{aq}}(\mathbf{x},t_n)$*, the compressibility* $\beta_T(\mathbf{x},t_n)$ *and the phases densities* $\rho_{\mathbf{aq}}(\mathbf{x},t_n)$*,* $\rho_g(\mathbf{x},t_n)$ *for* $\mathbf{x}\in\Omega$*, find the pair* $p(\mathbf{x},t_{n+1})$*,* $\mathbf{v_t}(\mathbf{x},t_{n+1})$ *such that*

$$\phi\frac{S^0(\mathbf{x},t_n)-1}{\Delta t}=\beta_T(\mathbf{x},t_n)\frac{p(\mathbf{x},t_{n+1})-p(\mathbf{x},t_n)}{\Delta t}+\mathrm{div}(\mathbf{v_t}) \tag{28}$$

$$\mathbf{v_t}=-\mathbf{K}(\lambda_t\nabla p(\mathbf{x},t_{n+1})+\lambda_g\nabla p_c-(\lambda_{\mathbf{aq}}\rho_{\mathbf{aq}}+\lambda_g\rho_g)g_c) \tag{29}$$

considering Neumann and Dirichlet boundary conditions given by

$$\mathbf{v_t}\cdot\mathbf{n}=g(x),\ x\in\Gamma_N$$
$$p(x,t_{n+1})=d(x),\ x\in\Gamma_D$$
$$\Gamma_N\cup\Gamma_D=\Gamma,\Gamma_N\cap\Gamma_D=\varnothing$$

To discretize formulation 1 in space, we use the mixed hybrid finite element [236] where the resulting linear system is solved by the conjugate gradient method with algebraic multigrid preconditioner [252]. Once the total Darcy's velocity $\mathbf{v_t}$ is obtained one can obtain the phases velocities needed to evolve the transport equations through the expressions

$$\mathbf{v_{aq}}=\frac{\lambda_{\mathbf{aq}}}{\lambda_t}\mathbf{v_t}+\mathbf{K}\frac{\lambda_{\mathbf{aq}}\lambda_g}{\lambda_t}(\rho_{\mathbf{aq}}-\rho_g)\mathbf{g}+K\frac{\lambda_g\lambda_{\mathbf{aq}}}{\lambda_t}\nabla p_c, \tag{30}$$

$$\mathbf{v_g}=\frac{\lambda_g}{\lambda_t}\mathbf{v_t}-\mathbf{K}\frac{\lambda_{\mathbf{aq}}\lambda_g}{\lambda_t}(\rho_{\mathbf{aq}}-\rho_g)\mathbf{g}-K\frac{\lambda_g\lambda_{\mathbf{aq}}}{\lambda_t}\nabla p_c. \tag{31}$$

7.2 Transport Equations Discretization

Combining equations (1), (2), (3), (30) and (31), the system of transport equations can be written as

$$\frac{\phi\partial m^c}{\partial t}+\nabla\cdot\left((\frac{m_g^c}{S_g}\frac{\lambda_g}{\lambda_t}+\frac{m_{\mathbf{aq}}^c}{S_{\mathbf{aq}}}\frac{\lambda_{\mathbf{aq}}}{\lambda_t})\mathbf{v_t}\right)+ \tag{32}$$
$$\nabla\cdot\left((\frac{m_{\mathbf{aq}}^c}{S_{\mathbf{aq}}}-\frac{m_g^c}{S_g})\mathbf{G_f}\right)+\nabla\cdot\left((\frac{m_{\mathbf{aq}}^c}{S_{\mathbf{aq}}}-\frac{m_g^c}{S_g})\mathbf{F_{p_c}}\right)=0,$$

$$\frac{\phi\partial m^w}{\partial t}+\nabla\cdot\left((\frac{m_g^w}{S_g}\frac{\lambda_g}{\lambda_t}+\frac{m_{\mathbf{aq}}^w}{S_{\mathbf{aq}}}\frac{\lambda_{\mathbf{aq}}}{\lambda_t})\mathbf{v_t}\right)+ \tag{33}$$
$$\nabla\cdot\left((\frac{m_{\mathbf{aq}}^w}{S_{\mathbf{aq}}}-\frac{m_g^w}{S_g})\mathbf{G_f}\right)+\nabla\cdot\left((\frac{m_{\mathbf{aq}}^w}{S_{\mathbf{aq}}}-\frac{m_g^w}{S_g})\mathbf{F_{p_c}}\right)=0,$$

$$\frac{\phi\partial m^s}{\partial t} + \nabla\cdot\left(\frac{m^s_{\mathbf{aq}}}{S_{\mathbf{aq}}}\left(\frac{\lambda_{aq}}{\lambda_g}\mathbf{v_t} + \mathbf{G_f} + \mathbf{F_{p_c}}\right)\right) = 0, \tag{34}$$

where $\mathbf{G_f}$ and $\mathbf{F_{p_c}}$ are the fluxes terms related to gravity and capillary pressure

$$\mathbf{G_f} = \mathbf{K}\frac{\lambda_{\mathbf{aq}}\lambda_g}{\lambda_t}(\rho_{\mathbf{aq}} - \rho_g)\mathbf{g}, \tag{35}$$

$$\mathbf{F_{p_c}} = \mathbf{K}\frac{\lambda_{\mathbf{aq}}\lambda_g}{\lambda_t}\frac{dp_c}{dS_{\mathbf{aq}}}\nabla S_{\mathbf{aq}}. \tag{36}$$

To discretize the system above we use the operator splitting technique to compute the convection and diffusion parts separately in time. For each time step we first solve the convection part neglecting the divergence term related to $\mathbf{F_{p_c}}$ in equations (32), (33) and (34). The numerical solution obtained is then used as initial condition for the second iteration of the transport system of equations where we don't compute the convective term of the flux. For each time step $\Delta t = t_{n+1} - t_n$ the operator splitting technique can be described as a numerical approximation of two formulations presented bellow

Formulation 2 *Given the total moles per pore volume of each component* $\overline{\mathbf{m}}(\mathbf{x}, t_n)$*, the pressures and velocity fields* $p(\mathbf{x}, t_n)$*,* $p(\mathbf{x}, t_{n+1})$*,* $\mathbf{v_t}(\mathbf{x}, t_n)$*,* $\mathbf{v_t}(\mathbf{x}, t_{n+1})$ *the saturation* $S_{aq}(\mathbf{x}, t_n)$*, the phases densities* $\rho_{\mathbf{aq}}(\mathbf{x}, t_n)$*,* $\rho_g(\mathbf{x}, t_n)$ *the distribution of the components among the phases* $m^w_{\mathbf{aq}}(\mathbf{x}, t_n)$*,* $m^c_{\mathbf{aq}}(\mathbf{x}, t_n)$*,* $m^s_{\mathbf{aq}}(\mathbf{x}, t_n)$*,* $m^w_g(\mathbf{x}, t_n)$*,* $m^c_g(\mathbf{x}, t_n)$ *obtained from* $\overline{\mathbf{m}}(\mathbf{x}, t_n)$ *and* $p(\mathbf{x}, t_n)$ *by flash calculations, find* $\overline{\mathbf{m}}^*(\mathbf{x}, t_{n+1}) =< m^c, m^w, m^s >$ *such that for* $t \in [t_n, t_{n+1}]$*,* $\mathbf{x} \in \Omega$*,*

$$\frac{\phi\partial m^c}{\partial t} + \nabla\cdot\left(\left(\frac{m^c_g}{S_g}\frac{\lambda_g}{\lambda_t} + \frac{m^c_{\mathbf{aq}}}{S_{\mathbf{aq}}}\frac{\lambda_{\mathbf{aq}}}{\lambda_t}\right)\mathbf{v_t}\right) + \tag{37}$$

$$\nabla\cdot\left(\left(\frac{m^c_{aq}}{S_{aq}} - \frac{m^c_g}{S_g}\right)\mathbf{G_f}\right) = 0,$$

$$\frac{\phi\partial m^w}{\partial t} + \nabla\cdot\left(\left(\frac{m^w_g}{S_g}\frac{\lambda_g}{\lambda_t} + \frac{m^w_{\mathbf{aq}}}{S_{\mathbf{aq}}}\frac{\lambda_{\mathbf{aq}}}{\lambda_t}\right)\mathbf{v_t}\right) + \tag{38}$$

$$\nabla\cdot\left(\left(\frac{m^w_{\mathbf{aq}}}{S_{\mathbf{aq}}} - \frac{m^w_g}{S_g}\right)\mathbf{G_f}\right) = 0,$$

$$\frac{\phi\partial m^s}{\partial t} + \nabla\cdot\left(\frac{m^s_{\mathbf{aq}}}{S_{\mathbf{aq}}}\left(\frac{\lambda_{\mathbf{aq}}}{\lambda_g}\mathbf{v_t} + \mathbf{G_f}\right)\right) = 0, \tag{39}$$

with Dirichlet boundary conditions

$$\overline{\mathbf{m}}(x,t) = \overline{\mathbf{m}}_{\mathbf{d}}(x),\ \forall \mathbf{x} \in \Gamma_I,\ \forall t \in [t_n, t_{n+1}] \tag{40}$$

where Γ_I is the part of the boundary of the reservoir domain Ω with inward flux.
Note that there are no source terms in the formulation 2 to account for the presence of wells inside the domain since they are interpreted as holes in the domain with boundary conditions imposed in their boundaries.

We discretize this nonlinear hyperbolic system using the high resolution finite volume Kurganov-Tadmor (KT) method [250]. Such method is explicit in time and its stability depends on the CFL condition which imposes a restriction on the maximum time step this method can have. Therefore the time step of the KT method Δt_t is generally less than the time interval Δt being necessary many iterations of the KT method in order to obtain the solution $\overline{\mathbf{m}}^*(\mathbf{x}, t_{n+1})$. Each iteration of the KT method must be preceded by Flash Computations to update the values of saturation, phases densities and the distribution of the components among phases necessary to compute the fluxes terms. Also for each microstep of the KT method the values of the pressure p and velocity $\mathbf{v_t}$ are always updated using linear interpolation in time with their values at time t_n in t_{n+1}. For instance, $\mathbf{v_t}$ would be defined as

$$\mathbf{v_t}(t) = \frac{t - t_n}{\Delta t_t}\mathbf{v_t}(t_n) + \left(1 - \frac{t - t_n}{\Delta t_t}\right)\mathbf{v_t}(t_{n+1}). \tag{41}$$

The numerical solution $\overline{\mathbf{m}}^*(\mathbf{x}, t_{n+1})$ obtained with the KT method is then used as initial condition for the following formulation:

Formulation 3 *Given the pressure* $p(\mathbf{x}, t_n)$*, the initial condition* $\overline{\mathbf{m}}^*(\mathbf{x}, t_{n+1})$ *and the values* $S_{\mathbf{aq}}(\mathbf{x}, t_n)$, $m_{aq}^w(\mathbf{x}, t_n)$, $m_{aq}^c(\mathbf{x}, t_n)$, $m_{aq}^s(\mathbf{x}, t_n)$, $m_g^w(\mathbf{x}, t_n)$, $m_g^c(\mathbf{x}, t_n)$ *obtained from* $\overline{\mathbf{m}}^*(\mathbf{x}, t_{n+1})$ *and* $p(\mathbf{x}, t_n)$ *through flash calculations, find* $\overline{\mathbf{m}}(\mathbf{x}, t_{n+1}) =< m^c, m^w, m^s >$ *such that for* $t \in [t_n, t_{n+1}]$, $\mathbf{x} \in \Omega$,

$$\frac{\phi \partial m^c}{\partial t} = \nabla \cdot \left((\frac{m_g^c}{S_g} - \frac{m_{\mathbf{aq}}^c}{S_{\mathbf{aq}}})\mathbf{F}_{\mathbf{p_c}} \right), \tag{42}$$

$$\frac{\phi \partial m^w}{\partial t} = \nabla \cdot \left((\frac{m_g^w}{S_g} - \frac{m_{\mathbf{aq}}^w}{S_{\mathbf{aq}}})\mathbf{F}_{\mathbf{p_c}} \right), \tag{43}$$

$$\frac{\phi \partial m^s}{\partial t} = -\nabla \cdot \left(\frac{m_{\mathbf{aq}}^s}{S_{\mathbf{aq}}}\mathbf{F}_{\mathbf{p_c}} \right), \tag{44}$$

where

$$\mathbf{F}_{\mathbf{p_c}} = \mathbf{K}\frac{\lambda_{\mathbf{aq}}\lambda_g}{\lambda_t}\frac{dp_c}{dS_{\mathbf{aq}}}\nabla S_{\mathbf{aq}}(m^w, m^c, m^s) \Leftrightarrow \tag{45}$$

$$\mathbf{F}_{\mathbf{p_c}} = \mathbf{K}\frac{\lambda_{\mathbf{aq}}\lambda_g}{\lambda_t}\frac{dp_c}{dS_{\mathbf{aq}}}\left(\frac{\partial S_{\mathbf{aq}}}{\partial m^c}\nabla m^c + \frac{\partial S_{\mathbf{aq}}}{\partial m^w}\nabla m^w + \frac{\partial S_{\mathbf{aq}}}{\partial m^s}\nabla m^s\right), \tag{46}$$

with Dirichlet boundary conditions

$$\overline{\mathbf{m}}(x,t) = \overline{\mathbf{m}}_{\mathbf{d}}(x),\ \forall \mathbf{x}\in\Gamma_I,\ \forall t\in[t_n, t_{n+1}]. \tag{47}$$

Formulation 3 consists of a parabolic system of equations in three variables to be solved preferable by an implicit in time method. However, the computational cost can be dramatically decreased by evolving the system implicitly in time in just one variable. This is done using the mass conservation equation of the aqueous phase written in terms of the saturation $S_{\mathbf{aq}}$ as

$$\phi\frac{\partial(\xi_{aq}S_{\mathbf{aq}})}{\partial t} = \nabla\cdot\left(\xi_{\mathbf{aq}}\left(\frac{\lambda_{\mathbf{aq}}}{\lambda_t}\mathbf{v}_{\mathbf{t}} + \mathbf{G}_{\mathbf{f}}\right)\right) - \nabla\cdot\left(\xi^n_{\mathbf{aq}}K\frac{\lambda_g\lambda_{\mathbf{aq}}}{\lambda_t}\frac{dp_c}{dS_{\mathbf{aq}}}\nabla S_{\mathbf{aq}}\right) \tag{48}$$

where the convective term in equation (50) related to $\mathbf{v}_{\mathbf{t}}$ and $\mathbf{G}_{\mathbf{f}}$ is neglected since it is already being computed by the numerical scheme of the formulation 2. The $\xi_{\mathbf{aq}}$ is the molar density of the aqueous phase being a function of pressure and molar composition. Therefore, the following equality applies

$$S_{\mathbf{aq}}\xi_{\mathbf{aq}} = m^w_{\mathbf{aq}} + m^c_{\mathbf{aq}} + m^s_{\mathbf{aq}} \tag{49}$$

The semi discrete formulation related to equation (32) is given by

Formulation 4 *Given the initial value* $S^n_{\mathbf{aq}} = S_{\mathbf{aq}}(\mathbf{x}, t_n)$ *and the aqueous phase's molar density* $\xi^n_{\mathbf{aq}} = \xi_{\mathbf{aq}}(\mathbf{x}, t_n)$. *Find* $S^{n+1}_{\mathbf{aq}}$ *satisfying the following partial discretized differential equation*

$$\phi\xi^n_{\mathbf{aq}}\frac{S^{n+1}_{\mathbf{aq}} - S^n_{\mathbf{aq}}}{\Delta t} = -\nabla\cdot\left(\xi^n_{\mathbf{aq}}K\frac{\lambda_g\lambda_{\mathbf{aq}}}{\lambda_t}\frac{dp_c}{dS_{\mathbf{aq}}}\nabla S^{n+1}_{\mathbf{aq}}\right) \tag{50}$$

with boundary conditions

$$S_{\mathbf{aq}}(\mathbf{x},t) = S_d(x), \qquad \forall x\in\Gamma, \forall t\in[t_n, t_{n+1}]$$

The initial condition $S^n_{\mathbf{aq}}(\mathbf{x})$ and the boundary condition $S_d(x)$ are obtained from $p(\mathbf{x}, t_n)$ and $\overline{\mathbf{m}}^*(\mathbf{x}, t_{n+1})$. In the semi discrete formulation 3 the molar density $\xi_{\mathbf{aq}}$ is considered constant in time for each diffusion iteration. Important to note that such assumption does not cause any additional error because according to the staggered approach the diffusive step advances in time without considering flash computations or change in pressure with time.

Equation (50) is numerically solved in a similar way as the pressure equation, using the lower order mixed hybrid method with backward Euler discretization in time [248]. The resulting linear system is then solver by the conjugate gradient method with algebraic multigrid preconditioner.

Once we obtain the numerical solution $S_{\mathbf{aq}}^{n+1}$ with the value of the saturation constant by parts in each cell of the discretized domain, we then calculate m^c, m^w, m^s at the cells. This is accomplished by discretizing equations (42), (43) and (44) using the same stencil that would result in the case we apply the mixed hybrid finite element to discretize formulation 3. Considering equation (42) for a 1D problem as an example we would have the following stencil

$$\phi \frac{m^c(x_i, t_{n+1}) - m^c(x_i, t_n)}{\Delta t} = \tag{51}$$
$$-\left(\frac{2D_i^n D_{i+1}^n}{D_i^n + D_{i+i}^n} \frac{S_{\mathbf{aq}}^{n+1}(x_{i+1}) - S_{\mathbf{aq}}^n(x_i)}{\Delta x} - \frac{2D_{i-1}^n D_i^n}{D_{i-1}^n + D_i^n} \frac{S_{\mathbf{aq}}^{n+1}(x_i) - S_{\mathbf{aq}}^n(x_{i-1})}{\Delta x} \right)$$

where

$$D_i^n = \left(\frac{m_g^c(x_i, t_n)}{S_g^n(x_i, t_n)} - \frac{m_{\mathbf{aq}}^c(x_i, t_n)}{S_{\mathbf{aq}}^n(x_i)} \right) \mathbf{K} \frac{\lambda_{\mathbf{aq}} \lambda_g}{\lambda_t} \frac{dp_c}{dS_{\mathbf{aq}}}(S_{\mathbf{aq}}^n(x_i)) \tag{52}$$

and the values $m_g^c(\mathbf{x}_i, t_n)$, $m_{\mathbf{aq}}^c(\mathbf{x}_i, t_n)$, $S_{\mathbf{aq}}^n(\mathbf{x}_i)$, are obtained from $\overline{\mathbf{m}}^*(\mathbf{x}_i)$, $p(\mathbf{x}_i, t_n)$ via flash calculation for each cell with center x_i of the discretized domain.

7.3 Staggered algorithm

Each subsystem is formulated in terms of a subset of the primary variables of the model assuming other variables constant in time. Now we present the Operator Splitting algorithm used to exchange information among the subsystem while they evolved in time.

Assuming that in time t_n the aqueous pressure $p(t_n)$ and the vector of total moles of each component per pore volume $\overline{\mathbf{m}}(t_n) = < m^c, m^w, m^s >$ is known for each cell in the discretized domain. To obtain the values of these fields for the next time step t_{n+1}, the following algorithm is executed:

• Compute the flash calculations as described in Task 5 to obtain the distribution of components among phases, the phases saturations $S_{\mathbf{aq}}(t_n)$, $S^0(t_n)$ the densities $\rho_{\mathbf{aq}}(t_n)$, $\rho_g(t_n)$ and the compressibility β_T for each cell based on the values $p(t_n)$, $\overline{\mathbf{m}}(t_n)$.

• Solve Formulation 1 to obtain the pressure for the next time step $p_{aq}(t_{n+1})$ and the total Darcy velocity field $\mathbf{v_t}(t_{n+1})$.

• Use $\mathbf{v_t}(t_{n+1})$ to calculate a suitable time step $\Delta t_t = (t_{n+1} - t_n)/N$ for the KT method that obeys the CFL condition. N corresponds to the number of iterations in time that will be done by the KT method.

• Evolve the convection part of the transport system using the Kurganov-Tadmor method with time step Δt_t in order to obtain a predictor solution $\overline{\mathbf{m}}^*(t_{n+1})$, given the values $\overline{\mathbf{m}}(t_n)$, $S_{\mathbf{aq}}(t_n)$, $p(t_n)$, $\mathbf{v_t}(t_n)$, $p(t_{n+1})$, $\mathbf{v_t}(t_{n+1})$. Each microstep of the KT is followed by a flash computation in order to obtain the fluxes of the next microstep. Also for each microstep the values $\mathbf{v_t}$ and p are update using a linear interpolation of the values of p and $\mathbf{v_t}$ at times t_n and t_{n+1}.

• Compute the flash to obtain $S^*_{\mathbf{aq}}(t_{n+1})$ from $\overline{\mathbf{m}}^*(t_{n+1})$ and $p(\mathbf{x}, t_{n+1})$.

• Solve Formulation 4 considering $S^*_{aq}(t_{n+1})$ as the initial value obtaining the corrected saturation value $S_{aq}(\mathbf{x}, t_{n+1})$.

• Discretize equations (42), (43) and (44) using the scheme exemplified in equation (51) in order to obtain the corrected value $\overline{\mathbf{m}}(t_{n+1})$ given the initial condition $\overline{\mathbf{m}}^*(t_{n+1})$ and the values $S_{aq}(t_{n+1})$.

7.4 Initial Conditions

The initial conditions for the pressure $p_{\mathbf{aq}}(x,0)$ and the vector $\overline{\mathbf{m}}(x,0)$ must obey the volume restriction $S_{\mathbf{aq}} + S_g = 1$. To ensure this property, the $\overline{\mathbf{m}}$ vector is multiplied by a constant n for each cell such that

$$S_{\mathbf{aq}}(p_{\mathbf{aq}}, n\ \overline{\mathbf{m}}) + S_g(p_{\mathbf{aq}}, n\ \overline{\mathbf{m}}) = 1. \tag{53}$$

Since the phases molar volumes are functions of the relative concentrations of each component and not the total amount of moles of each component, the saturations are linear functions of n, and then

$$n = \frac{1}{S_{\mathbf{aq}}(p_{\mathbf{aq}}, \overline{\mathbf{m}}) + S_g(p_{\mathbf{aq}}, \overline{\mathbf{m}})} \tag{54}$$

So in the initialization step, given $p_{\mathbf{aq}}(x,0)$ and the vector $\overline{\mathbf{m}}(x,0)$ the simulator calculates the n constant according to equation (72) and correct the value $\overline{\mathbf{m}}(x,0)$ multiplying it by n for each cell.

8 Code Validation

8.1 A Bayesian Framework using MCMC

In the study of uncertainty quantification, a Bayesian approach combines prior information about the unknown parameters of interest and information obtained by solving a forward model. Here we have considered a mathematical model describing compositional fluid flow (discussed in earlier sections) to be the forward model which allows for mass transfer between the two phases. Bayesian methods have two essential components, the prior distribution and the likelihood. The prior distribution is absolutely independent of the measured data and contains only information about the unknown quantities that we want to quantify the uncertainty in, while the likelihood describes the distribution of the observed data conditioned on the unknown parameters that we have in the prior. The likelihood function requires solution of the forward model for each permeability field and, as a consequence, increases the

computational complexity of computational methods based on Bayesian statistics. The problem of interest here is to generate permeability fields that are consistent with measured data in lab experiemnts, and at the same time allow us do make reliable predictions of future fluid flow. As this study is conducted on the laboratory scale, the measured data refers to the CO_2 saturation at a finite number of slices of the core (we denote them by d_m).

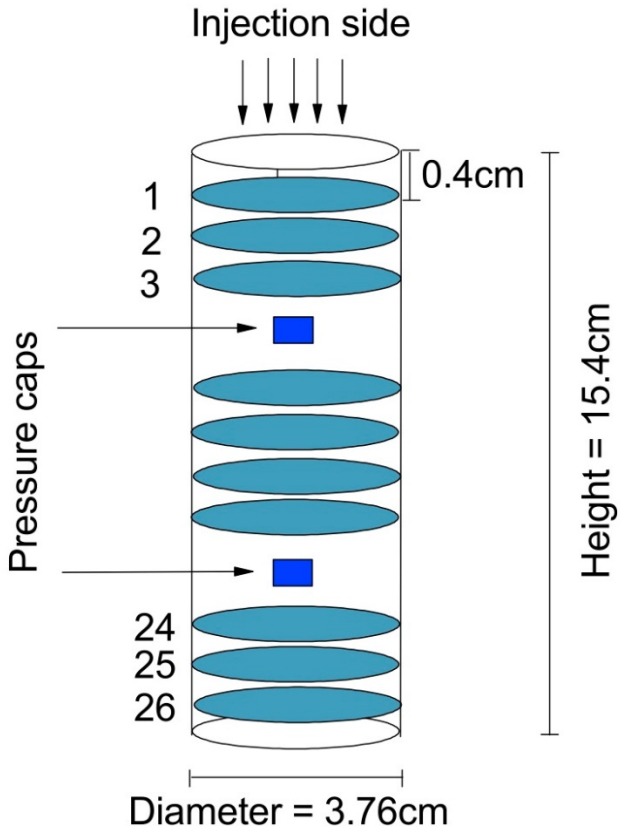

Figure 1: Core description: Height 15.4cm, diameter 3.76cm, two pressure caps (in blue), 26 slices (in light blue) for monitoring saturation of CO_2 and injection in the direction of gravity.

The description of the core is given in Fig. 1. The slices are positioned 4mm apart from each other. However, the experimentalists put two pressure caps inside the core to monitor the pressure and one can not take reliable measurements close to the pressure caps. That is why we will ignore some slices at each side of the two pressure caps.

When the likelihood and the prior distribution are given the posterior distribution can be updated according to the Bayes' theorem as follows,

$$\pi(k) = P(k \mid d_m) \propto P(d_m \mid k)P(k), \tag{55}$$

where $P(d_m \mid k)$ denotes the likelihood and $P(k)$ denotes the prior distribution of a candidate permeability field. The likelihood represents the conditional probability of the permeability field k after observing data d_m. We assume the likelihood function follows Gaussian distribution as given below,

$$P(d_m \mid k) \propto \exp\left(- \frac{\left\| d_m - d_{\mathbf{obs}} \right\|_{L^2}^2}{\sigma^2} \right), \tag{56}$$

where d_{obs} is the observed data when the permeability is k, and σ^2 is the precision parameter associated with measured and observed data, and the error norm is given by

$$\begin{aligned} \left\| d_m - d_{\mathbf{obs}} \right\|_{L^2}^2 &= \sum_{i=1}^{N_s} \left(d_m(\mathbf{z_i}) - d_{\mathbf{obs}}(\mathbf{z_i}) \right)^2 \\ &= \sum_{i=1}^{N_s} \left(\sum_{m,n=1}^{N_c} \left(d_m(x_m, y_n, z_i) - d_{\mathbf{obs}}(x_m, y_n, z_i) \right) \right), \end{aligned} \tag{57}$$

where $\mathbf{z_i}$ denotes the position of a 2D slice in the 3D core, N_s is the number of slices and N_c is the number of cells in a slice. It is important to mention that in the prior it is not practical to use the permeability field k directly due to the heterogeneity and large dimensionality of the field. Instead, we use $\xi_n(\omega)$ given in equation (70) (discussed in detail later).

In the Bayesian approach the posterior distribution summarizes the current state of knowledge about all the uncertainties, that is, all the possible errors e.g. error generated by the mathematical model, error coming from the numerical methods and error in the measurements, are all combined in the likelihood function [244], and error in the unknown quantities are combined in the prior. Therefore, we sample the permeability field based on the measured data from the posterior distribution $P(k \mid d_m)$. There exists many different permeability fields for one simulated data i.e. the map from permeability field to saturation data is not one-to-one. This is also known as ill-posed inverse problem.

We will use Metropolis-Hastings MCMC method to sample from the posterior distribution $P(k \mid d_m)$. The description of the basic working principle of the Metropolis-Hastings MCMC method is quite straight-forward. The main idea of the MCMC is to generate a Markov chain with limiting distribution $\pi(k)$ which is equal to the target distribution, i.e., $\pi(k)$ is invariant. The Metropolis-Hastings MCMC algorithm is given in Algorithm 1.

Algorithm 1. Metropolis-Hastings MCMC [249]

Step 1. At state k_n generate a proposal $k : q(k \mid k_n)$

Step 2. Take

$$k_{n+1} = \begin{cases} k & \text{with probability } \rho(k_n, k), \\ k_n & \text{with probability } 1 - \rho(k_n, k), \end{cases}$$

where

$$\rho(k_n,k)=\min\left\{1,\frac{q(k_n\,|\,k)P(k\,|\,d_m)}{q(k\,|\,k_n)P(k_n\,|\,d_m)}\right\}, \tag{58}$$

where $q(k_n\,|\,k)$ is called proposal (or instrumental) distribution, k is the current proposal, and k_n is the previously accept proposal.

To move the chain from the current state to the next state each proposal is tested in the fine-grid for the solution of the forward model to get the probability $\rho(k_n,k)$ for the jump in the chain. In general MCMC algorithms test thousands of proposals in fine-grid numerical solutions before it converges to the steady-state. This has a huge computational cost and most of the time is spent in determining proposals to be rejected, i.e., one has to face a low acceptance rate of the algorithm, due to the large dimensionality of the permeability field. Algorithm 1 is also known as a single-stage MCMC method. To quantify the uncertainty of the permeability field using less computational resources the idea is to run the forward problem, based on upscaled permeability, on a coarse-grid first, before running it on the fine-grid. This is called a two-stage MCMC method with upscaling, and was proposed in [4, 11]. The first stage is the screening stage where we run an inexpensive forward problem on coarse-grid, if the proposal passes the screening test it will be tested on the fine-grid otherwise generate a new proposal. The computations become less expensive since we avoid running the proposals on the fine-grid which are highly unlikely to be accepted. To test a proposal on the coarse-grid we need to upscale the permeability proposal.

To compute the effective permeability on the coarse-grid we solve the following pressure equation

$$\nabla\cdot v_j=0,\;\; v=-\frac{k(\mathbf{x})}{\mu}\nabla p_j, \tag{59}$$

where the subscript $j=1,2,3$, corresponds to the x-, y- and z-directions, respectively, μ is fluid viscosity, v and p are velocity and pressure, respectively. We impose the unit gradient pressure boundary condition at both sides in the direction of vector e_j and no flow boundary condition on the remaining four orthogonal sides to e_j on each coarse block B, where e_j is the standard Euclidean basis in 3D. Once we have the velocities for each block B we compute the effective permeability anisotropic tensor denoted by K_T as,

$$(K_T(\mathbf{x})e_i,e_j)=|\,B\,|^{-1}\int_B(k(\mathbf{x})\nabla p_i(\mathbf{x}),e_j)\mathbf{dx} \tag{60}$$

When the tensor K_T is in hand we solve our forward model on coarse-grid. As pointed out earlier the coarse-grid models are inexpensive, but not necessarily very accurate. However, strong correlation between coarse and fine-grid simulations will reasonably increase the acceptance rate. The two-stage MCMC algorithm is given below.

Algorithm 2. Two-Stage MCMC [237]

Step 1. At state k_n generate a proposal $k:q(k\,|\,k_n)$ and a random number ζ from a uniform distribution [0,1].

Step 2. Solve the forward model on the coarse-grid with anisotropic tensor K_T. Compute the saturation at cells denoted by $\bar{d}_m$.

Step 3. Choose

$$\begin{cases} k & \text{accept with probability } \bar{\rho}(k_n,k) \text{ if } \bar{\rho}(k_n,k) > \xi, \\ k_n & \text{otherwise reject with probability } 1-\bar{\rho}(k_n,k), \end{cases}$$

where

$$\bar{\rho}(k_n,k) = \min\left\{1, \frac{q(k_n \mid k)\bar{P}(k \mid \bar{d}_m)}{q(k \mid k_n)\bar{P}(k_n \mid \bar{d}_m)}\right\}, \tag{61}$$

Step 4. If accepted, test the proposal on the find grid to get d_m, and go to the next step, otherwise go to step 1.

Step 5. Take the proposal as

$$k_{n+1} = \begin{cases} k & \text{accept with probability } \rho(k_n,k) \text{ if } \rho(k_n,k) > \xi, \\ k_n & \text{otherwise reject with probability } 1-\rho(k_n,k), \end{cases}$$

where

$$\rho(k_n,k) = \min\left\{1, \frac{P(k \mid d_m)\bar{P}(k_n \mid \bar{d}_m)}{P(k_n \mid d_m)\bar{P}(k \mid \bar{d}_m)}\right\}. \tag{62}$$

Repeat the steps until the chain stabilizes. Note that for coarse-grid simulations we use a different precision parameter than σ^2, denoted by $\bar{\sigma}^2$. The choice of these parameters depend on the correlation between coarse and fine grid simulations.

8.2 Parameterization of geological properties

Permeability and porosity fields are subject to exceptionally large uncertainties due to the heterogeneities of porous media in the subsurface. In this work we only concentrate in quantifying the uncertainty in the permearbility field, since the porosity field of the core is known from laboratory measurements. In general, the number of degrees of freedom of the permeability field could be of $O(10^6)$. Thus, reduction of the space dimensions is necessary for the convergence of the MCMC and computationally feasible simulations. We use the Karhunen-Loéve expansion (KLE) [253, 242] for the parametrizaiton of the permeability filed. The KLE may allow us to significantly reduce the dimensions of the permeability field by truncating the series. Analogous to generalized Fourier series, if the basis functions are chosen such that the coefficients in the series expansion are uncorrelated then the series expansion is known as Karhunen-Loéve expansion. Several authors have used the same reduction technique, i.e., spatial fields with fewer degree of freedom, for the description of these fields in [239, 243, 244, 246, 257] .

It is often assumed that in most reservoirs the permeability field exhibit a log normal distribution. Therefore, a standard practice in geostatistics for the stochastic description of the permeability field is based on the two-point correlation function of log-normal permeability field [245]. Suppose $Y^k(\mathbf{x},\omega) \in L^2(\Omega)$, i.e. a second-order stochastic process, where $\Omega \subseteq \mathbf{R}^3$, $\mathbf{x} = (x,y,z) \in \Omega$, ω is a random variable, and the superscript k associates the stochastic process for permeability. Then we

denote the stochstic process by $Y^k(\mathbf{x},\omega)=\frac{1}{s}\mathbf{log}\left[k(\mathbf{x},\omega)\right]$, where s is the strength of the permeability field and in our work it is a stochastic parameter.

To work with the permeability field with fewer degree of freedom, we express the stochastic process $Y^k(\mathbf{x},\omega)$ as an infinite series of two functions. To construct this infinite sum we assume that there is an arbitrary orthonormal basis $\{\psi(\mathbf{x})\}$ in $L^2(\Omega)$ and a function $Y^k(\omega)$ such that

$$Y^k(\mathbf{x},\omega)=\sum_{j=1}^{\infty}Y_j^k(\omega)\psi_j(\mathbf{x}) \tag{63}$$

where the coefficients $Y_j^k(\omega)$ are given by the integral

$$Y_j^k(\omega)=\int_{\Omega}Y^k(\mathbf{x},\omega)\psi_j(\mathbf{x})\mathrm{d}x$$

We assume that the mean of the stochastic process is zero that is $E[Y^k(\mathbf{x},\omega)]=0$. This assumption is due to the fact that $E[Y^k(\omega)]=0$. In general, the random coefficients $Y^k(\omega)$ are correlated. It would be a consequence of a special basis in $L^2(\Omega)$ to have the random coefficients $Y^k(\omega)$ uncorrelated, that is, $E[Y_iY_j]=0$ for all $i\neq j$. Also, we assume that the two-point correlation function $R(\mathbf{x_1},\mathbf{x_2})$, which we need for the description of the permeability field, is known. For $N\times N$ discrete grid the correlation function $R(\mathbf{x_1},\mathbf{x_2})$ is a square matrix of size $N^2\times N^2$. In this study, we consider a covariance function called squared-exponential covariance function which is given by

$$R(\mathbf{x_1},\mathbf{x_2})=\sigma_Y^2\exp\left(-\frac{|x_1-x_2|^2}{2l_x^2}-\frac{|y_1-y_2|^2}{2l_y^2}-\frac{|z_1-z_2|^2}{2l_z^2}\right), \tag{64}$$

where σ_Y^2 is the variance of the stochastic field given by $\sigma_Y^2=E[Y^kY^k]$ and l_x,l_y and l_z are the correlation lengths in x-, y- and z-direction, respectively. The squared-exponential covariance function is one of the possible choices. The other frequently used covariance function is known as exponential covariance function given by

$$R(\mathbf{x_1},\mathbf{x_2})=\sigma_Y^2\exp\left(-\frac{|x_1-x_2|}{l_x}-\frac{|y_1-y_2|}{l_y}-\frac{|z_1-z_2|}{l_z}\right), \tag{65}$$

The squared-exponential has a slight advantage over the exponential covariance function. The former require less terms in the KLE because the ordered-dominant eigenvalues in the KLE decay much faster than the latter. In other words, more degree of freedom more complicated the problem would be.
By definition $R(\mathbf{x_1},\mathbf{x_2})=E[Y(\mathbf{x_1},\omega)Y(\mathbf{x_2},\omega)]$ and the orthonormal basis functions $\{\psi_j(\mathbf{x})\}$ satisfy

$$E[Y_i^k Y_j^k] = \int_\Omega \psi_i(\mathbf{x_1})\mathrm{d}\mathbf{x_1} \int_\Omega R(\mathbf{x_1},\mathbf{x_2})\psi_j(\mathbf{x_2})\mathrm{d}\mathbf{x_2} = 0, \text{ whenever } i \neq j. \tag{66}$$

Using the completeness of $L^2(\Omega)$ the orthonormal functions $\{\psi_j(\mathbf{x})\}$ turned out to be the eigenfunctions of the covariance function $R(\mathbf{x_1},\mathbf{x_2})$. We solve Fredholm integral equation to find these eigenfunctions i.e. the orthonormal basis functions $\{\psi_j(\mathbf{x})\}$ are found via the integral equation

$$\int_\Omega R(\mathbf{x}_1,\mathbf{x}_2)\psi_i(\mathbf{x}_2)\mathrm{d}\mathbf{x}_2 = \lambda_i\psi_i(\mathbf{x}_1),\ i = 1,2,..., \tag{67}$$

where the eigenvalues λ_i are $\lambda_i = E[Y_i^k(\omega)Y_i^k(\omega)] > 0$. The reason these eigenvalues are positive is due to the positive kernel of the integral equation. The basis functions which make the random coefficients uncorrelated must satisfy the integral equation given in equation (67). The covariance function can be decomposed in terms of the basis as follow

$$R(\mathbf{x}_1,\mathbf{x}_2) = \sum_{i=0}^{\infty}\lambda_i\psi_i(\mathbf{x}_1)\psi_i(\mathbf{x}_2), \tag{68}$$

Let us denote $\xi_j(\omega) = Y_j^k(\omega)/\lambda_j$, and utilizing the eigenfunctions of the covariance function the series expansion of the stochastic process gets the form

$$Y^k(\mathbf{x},\omega) = \sum_{j=1}^{\infty}\lambda_j\xi_j(\omega)\psi_j(\mathbf{x}). \tag{69}$$

This expansion is known as Karhune-Loéve expansion (KLE). The KLE of a stochastic process consists of a deterministic set $\{\lambda_j,\psi_j(\mathbf{x})\}$ which is a set of eigenvalues and the corresponding eigenvectors of equation (67), and uncorrelated random coefficients $\{\xi_j(\omega)\}$ with zero mean and unit variance. Practically, the infinite KLE is not applicable. In applications, the approximation of the permeability field is performed by truncated the KLE after finite many terms. The eigenvalues determine the proper truncation i.e. how many terms to be considered in the KLE to capture most of the energy of the stochastic process. Since the eigenvalues λ_j are positive it is possible to order them in a decreasing manner tending to zero which would help us with proper truncation. Suppose N_k eigenvalues dominate the KLE then the truncated KLE is given by

$$Y^k(\mathbf{x},\omega) = \sum_{j=1}^{N_k}\lambda_j\xi_j(\omega)\psi_j(\mathbf{x}), \tag{70}$$

Suppose $N(0,1)$ is a Gaussian distribution with mean zero and variance one. We sample $\xi_j(\omega)$ using the random-walk sampler [238] given by

$$\xi_j^{(n+1)}(\omega) = \beta\xi_j^{(n)}(\omega) + \sqrt{1-\beta^2}\ \varepsilon_n, \tag{71}$$

where β is called the tuning parameter such that $0 \le \beta \le 1$, and ε_n is $\mathsf{N}(0,1)$, i.e., a small perturbation to the previously accepted proposal. This kind of random-walk sampler preserves the mean zero and the variance one of the Gaussian distribution provided $\xi_j^0(\omega) \in \mathsf{N}(0,1)$. Using a random-walk sampler implies that the instrumental (or proposal) distribution is symmetric i.e. $q(k \mid k_n) = q(k_n \mid k)$, and hence the probabilities in Algorithm 1 and Algorithm 2 are independent of the proposal distribution. The tuning parameter β plays a significant role in the acceptance of the proposals and it's optimal value is somehow problem dependent. For smaller values of β the chain will eventually hit the target distribution with hundreds of thousands of MCMC realizations. However, it is quite possible that it gets stuck in the neighborhood of the local maximum of the target distribution and probably will stabilize in that neighborhood, and will never converge to the target distribution in the reasonable amount of time. In general, the Markov Chain will converge to the target distribution no matter what value we choose for β but it takes long time for the chain to go from one local maxima to another local maxima (or global maxima). Consequently, the method will accept large number of realizations that are not very different from each other. On the other hand for large values of β the chain will move faster towards the target with low acceptance rate, again it is mostly likely to totally miss the target distribution. Also, the convergence of the stochastic parameter s is β sensitive.

Results and discussions

We divide this section into two parts. In the first part, we present numerical experiments to illustrate the properties of the discretization proposed for the compositional model. In the second part we present results with synthetic permeability fields to indicated that our Bayesian framework for code validation gives correct results. Finally, we present validation results.

9 Numerical Experiments

9.1 Study-I: The Compositional Simulator

In this part we show some numerical results for the illustration the properties of the discretization presented in the earlier sections. Unless stated otherwise, the parameters of the simulations are as described in Table 2.

Table 2: Parameter values used for simulations

Temperature:	$80C$
Aqueous viscosity:	$5 \cdot 10^{-4} Pa \cdot s$
Supercritical CO_2 viscosity:	$6 \cdot 10^{-5} Pa \cdot s$
Porosity:	0.3
Initial Pressure:	$80 \cdot 10^5 Pa$
Pressure at left boundary:	$180 \cdot 10^5 Pa$
Pressure at right boundary:	$80 \cdot 10^5 Pa$
Intrinsic Permeability:	$1.06 \cdot 10^{-14} m^2$
Relative Permeabilities:	$k_{rg}(S_{aq}) = \{1-(1-S_{rg})^{-1} S_{aq}\}^2$
	$k_{raq}(S_{aq}) = (1-S_{raq})^{-2}(S_{aq}-S_{raq})^2$
Gravity:	$9.8 m/s^2$

The staggered discretization allows us to choose appropriate methods for each subsystem assuring numerical stability in time. The other approach would be to solve the pressure, transport and flash equations simultaneously in each time step using a nonlinear solver like Newton-Raphson iterations. This strategy increases dramatically the time of the simulation and it does not guarantee convergence of the solution specially for convective predominant nonlinear transport equations (i.e low capillary pressure).

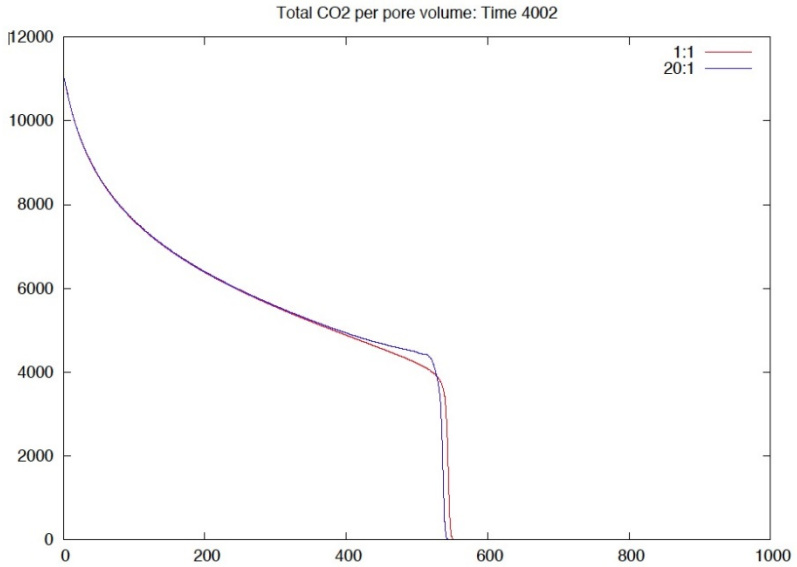

Figure 2: 1D simulation of supercritical CO2 injection in pure water. Case 1: Proportion of 20 transport time step per one pressure iteration. Case 2: Proportion of one to one.

Also, using the staggered discretization we can take advantage of the weak coupling between subsystems allowing different time steps for the discretizations of the pressure equation, and the convective and diffusive part of the transport subsystems. This fact was largely exploited in the case of incompressible multiphase flow where it is common practice to use large values for the ratio between

the time step of the pressure and transport equations ($\Delta t/\Delta t_t$) [248]. However, for compressible flow the coupling between the subsystems is much more severe. This fact is illustrated in Fig. 2 where we present a comparison of two numerical solutions using time steps ratio 1:20 between the pressure and transport equations, respectively. The simulation is a 1D injection of CO_2 considering no capillary pressure, no gravity and no residual saturations. We can see that excessively large time steps can result in bad estimation of the front position. This error is caused mainly because of the staggered approach. When the transport subsystem is advanced in time followed by a flash calculation, the constraint $S^0 = 1$ is not true anymore due to the compressibility of the mixture and the fact that the flash calculation does not assume ideal mixing behavour. The pressure equation was constructed using a first order approximation in time of the equation $S^0 = 1$ in order to assure that such constraint is true in the next time step considering that the moles componentes will not change in time. Therefore, large values for $\Delta t/\Delta t_t$ results in bad approximations for the saturations values causing errors in the estimation of the flux mainly in the front region. Fig. 3 illustrates the values of S^0 for the same simulation and time slice. In Fig. 4 we show the convergence of a heterogeneous problem as the mesh is refined.

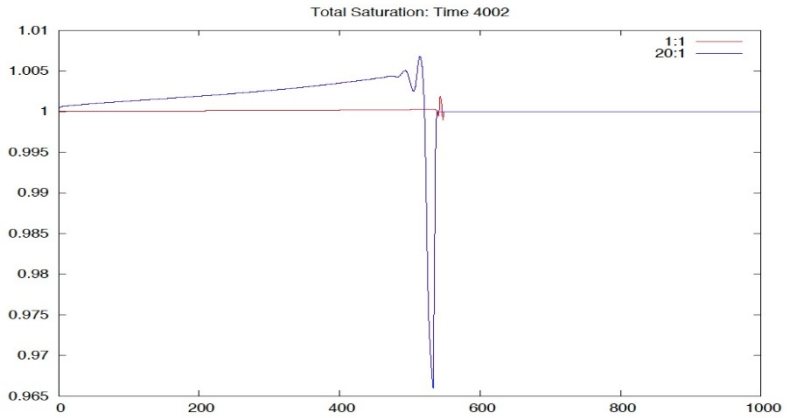

Figure 3: Values of S^0 illustrating the errors of the saturation values caused by the staggered approach. Case 1: Proportion of 20 transport time steps per one pressure iteration. Case 2: Proportion of one to one.

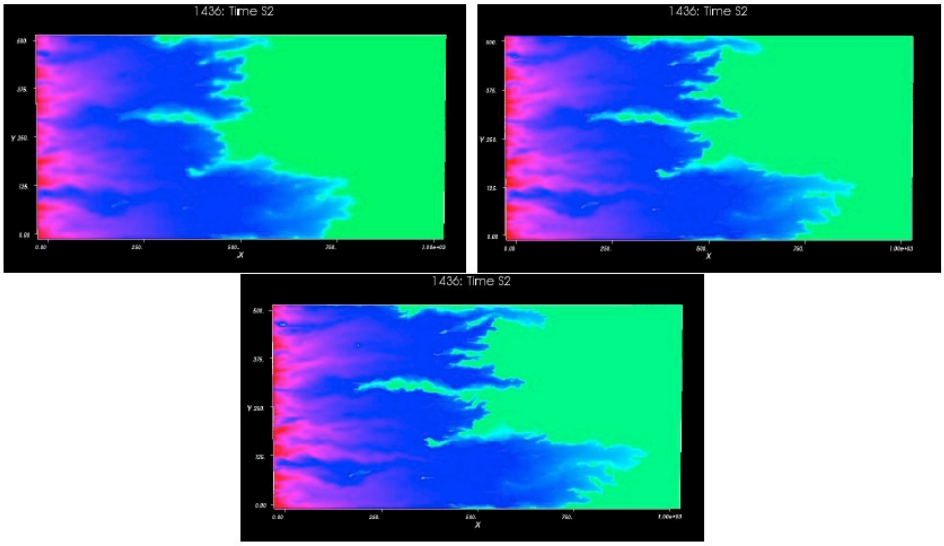

Figure 4: Convergence for the supercritical CO_2 moles density using meshes of size 256x128, 512x256, 1024x512 and assuming a permeability field of 256x128 geological blocks with coefficient of variation (CV) equal to 2.

9.2 Study-II: Synthetic and Validation results

In this section we first present some synthetic case studies to test the efficiency and feasibility of the proposed framework. The synthetic case is divided into two steps. The first step is the characterization step, where we obtain the reference data by running a forward simulation with a randomly generated permeability field K_{ref} and total injected volume of 14cc. Then we use the Bayesian MCMC method to find a family F of permeability fields that matches the reference data. The second step is the prediction step. In the prediction step we run a forward simulation with K_{ref} and 66cc the total injected volume to obtain the reference data $S_{\text{ref}}^{\text{p}}$ at the prediction step. We run Monte Carlo simulations on F to get the ensemble average and compare the ensemble average with $S_{\text{ref}}^{\text{p}}$. If the ensemble average and the $S_{\text{ref}}^{\text{pred}}$ matches then we can confidently apply the framework to the measured data from experiment. After the synthetic study, we use the same methodology for the validation of a standard compositional model for CO_2 sequestration in saline aquifers at the laboratory scale.

We consider a core initially fully saturated with brine, positioned vertically, of height $15.4\,\text{cm}$ and diameter $3.76\,\text{cm}$. The supercritical CO_2 is injected from the top of the core with a constant injection rate of 0.15cc. Here, we present two studies: (i) the influence of the mass transfer between phases and (ii) the influence of the diffusion on the proposed framework. Once change in pressure boundary conditions affects the mass transfer of CO_2 to the aqueous phase, we have considered three different pressures, i.e. 110, 150 and 300 bars (for these values the mass transfer always increases as the pressure increases [240]). The core is under constant temperate of 50° C. Note that the measurements of the core, thermodynamical conditions, injection rate and relative permeability curves are totally consistent with the real experimental setup.

We assume that the porosity of the core is known at all the spatial locations and call it static data because it doesn't change with time. We also assume that the log of the permeability field is Gaussian, and the covariance function $R(\mathbf{x},\mathbf{y})$ is given by equation (64) with $l_x = l_y = l_z = 0.5$ cm. We are taking into account the possible correlation between porosity and permeability, i.e., assuming they share the same spatial structure, however, they are statistically independent. In general, the variance s of the permeability field is not known, and in our study it is treated as a stochastic parameter. The variance s is also known as the strength of the heterogeneity of the permeability field, for simplicity we will call it strength of the permeability field. Typically one needs many eigenvalues in the KLE expansion to capture all of the energy, but it would lead to huge dimensionality of the stochastic field. We truncate the KLE expansion by considering 600 dominant eigenvalues that capture 92% of the total energy of the stochastic field. The energy ratio is obtained by summing the dominant eigenvalues of the truncated series over summation of all the eigenvalues. Fig. 5 shows the decay of the dominant eigenvalues for the squared-exponential covariance function.

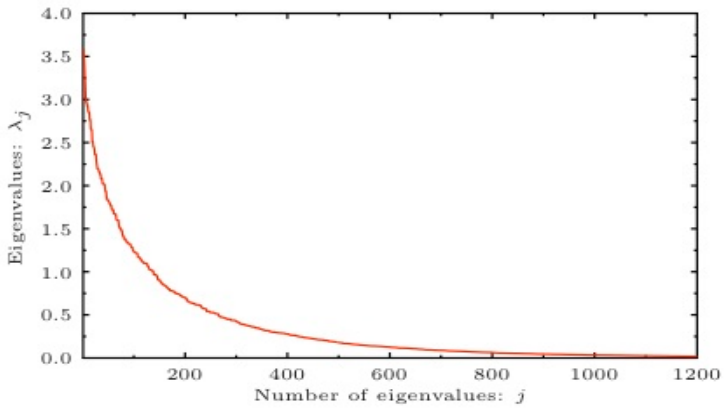

Figure 5: Eigenvalues of the KLE using squared-normal covariance function

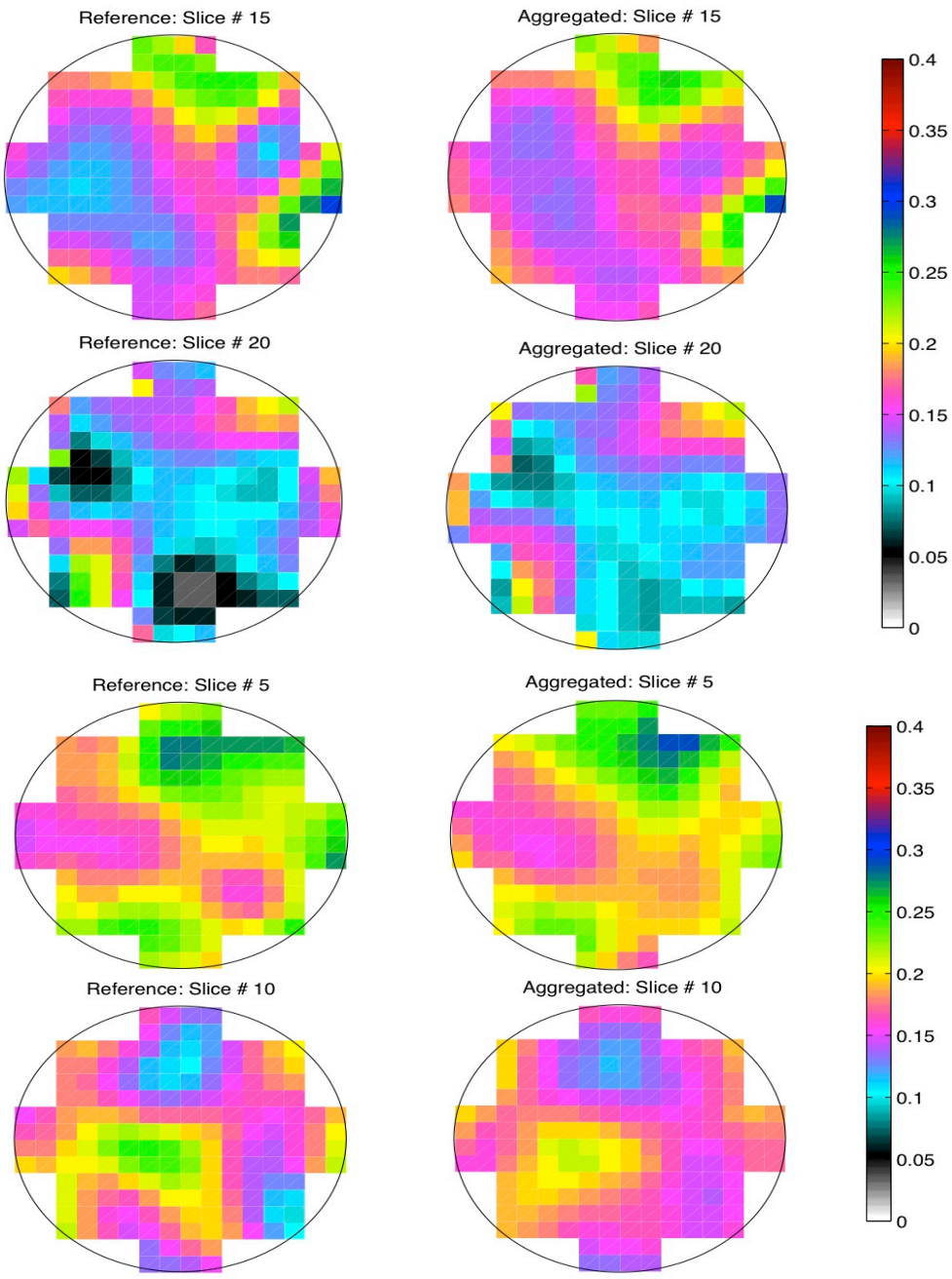

Figure 6: Characterization stage: Comparison of the reference and simulated data: Left: Reference data slices. Right: Ensemble average of the simulations for pressure 110 bars for the family F. First, second, third and fourth row correspond to slice # 5, 10, 15 and 20, respectively.

We run our coarse and fine-grid models on grids with $8\times8\times32$ and $16\times16\times64$ cells, respectively. We take our fine grid larger than the representative elementary volume (REV) for the permeability field. One can use a finer grid to overcome the numerical error but we have to ensure that the grid elements are large enough for the continuum model to be applicable. In other words, if we use a finer grid we

might get closer to the pore scale and the Darcy's law will not be applicable anymore. In all the studies reported here, we have used $\sigma^2 = 0.001$, $\bar{\sigma}^2 = 0.05$ and $\beta = 0.05$.

As stated earlier, for the characterization of the core we inject 14cc volume of supercritical CO_2, generate reference data and select a family of the permeability fields that matches the reference data. There are 38 slices in the core, but as pointed earlier, data close to the pressure caps is not reliable. Hence, we ignore three slices at each side of each pressure cap. For comparison with the reference data, we take the ensemble average of the saturation values at slices for the family F. Now we show some plots to see the accuracy of the proposed framework. In Fig. 6, we show the reference data at slices # 5, 10, 15 and 20 (left column), and the corresponding data slices of the ensemble average (right column) with pressure 110 bars. Where slice # 5 is close to the injection boundary, slice # 10, 15 are in the middle, and slice # 20 is close to the bottom boundary of the core. For the simulations with pressure 150 and 300 bars we get comparable results as well. Next we show the average saturation at the slices along the core. In Fig. 7, 8, 9 the average saturation at slices for all the three sets of simulations i.e. with pressure 110, 150 and 300 bars, respectively, are shown. We have plotted the initial realization, one before the burning period and the ensemble average of the simulations for the family F. We see very good agreement between average saturation curves corresponding to the reference run and the runs with accepted permeability realizations.

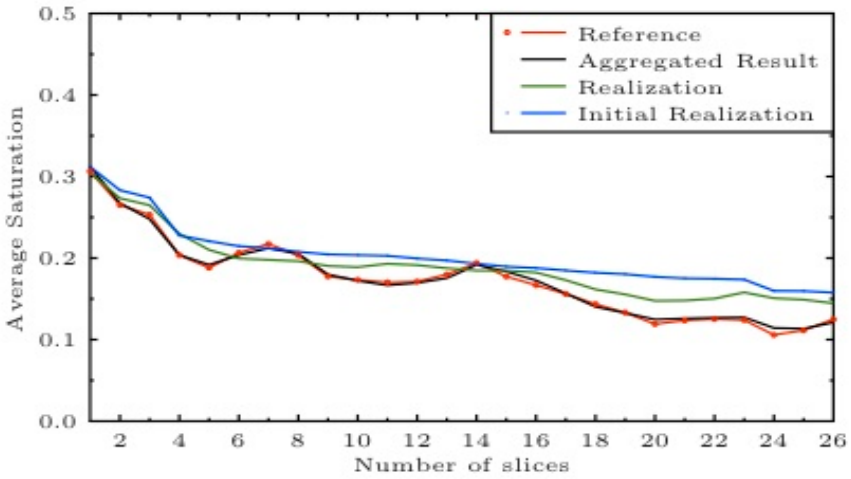

Figure 7: Characterization stage: Average saturation at slices along the core for the reference data, the initial realization, a realizations before the burning period, and the ensemble average of the simulations for *pressure 110 bars* for the family F.

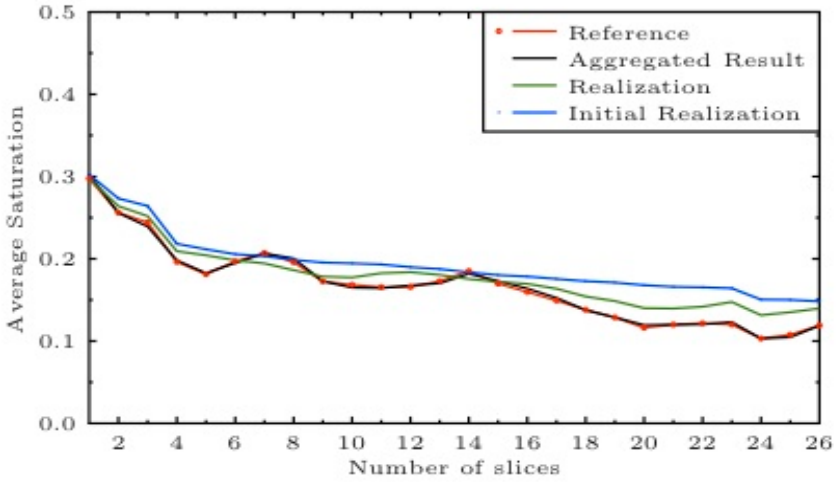

Figure 8: Characterization stage: Average saturation at slices along the core for the reference data, the initial realization, a realizations before the burning period, and the ensemble average of the simulations for *pressure 150* bars for the family F.

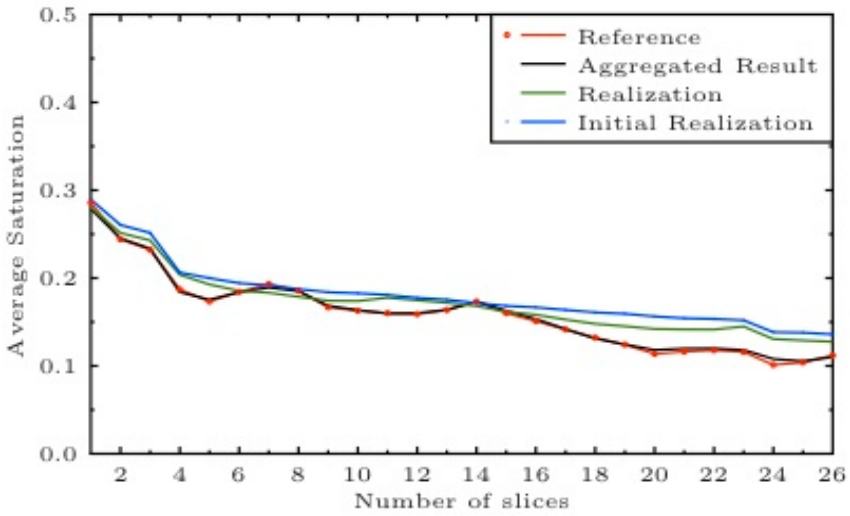

Figure 9: Characterization stage: Average saturation at slices along the core for the reference data, the initial realization, a realizations before the burning period, and the ensemble average of the simulations for *pressure 300 bars* for the family F.

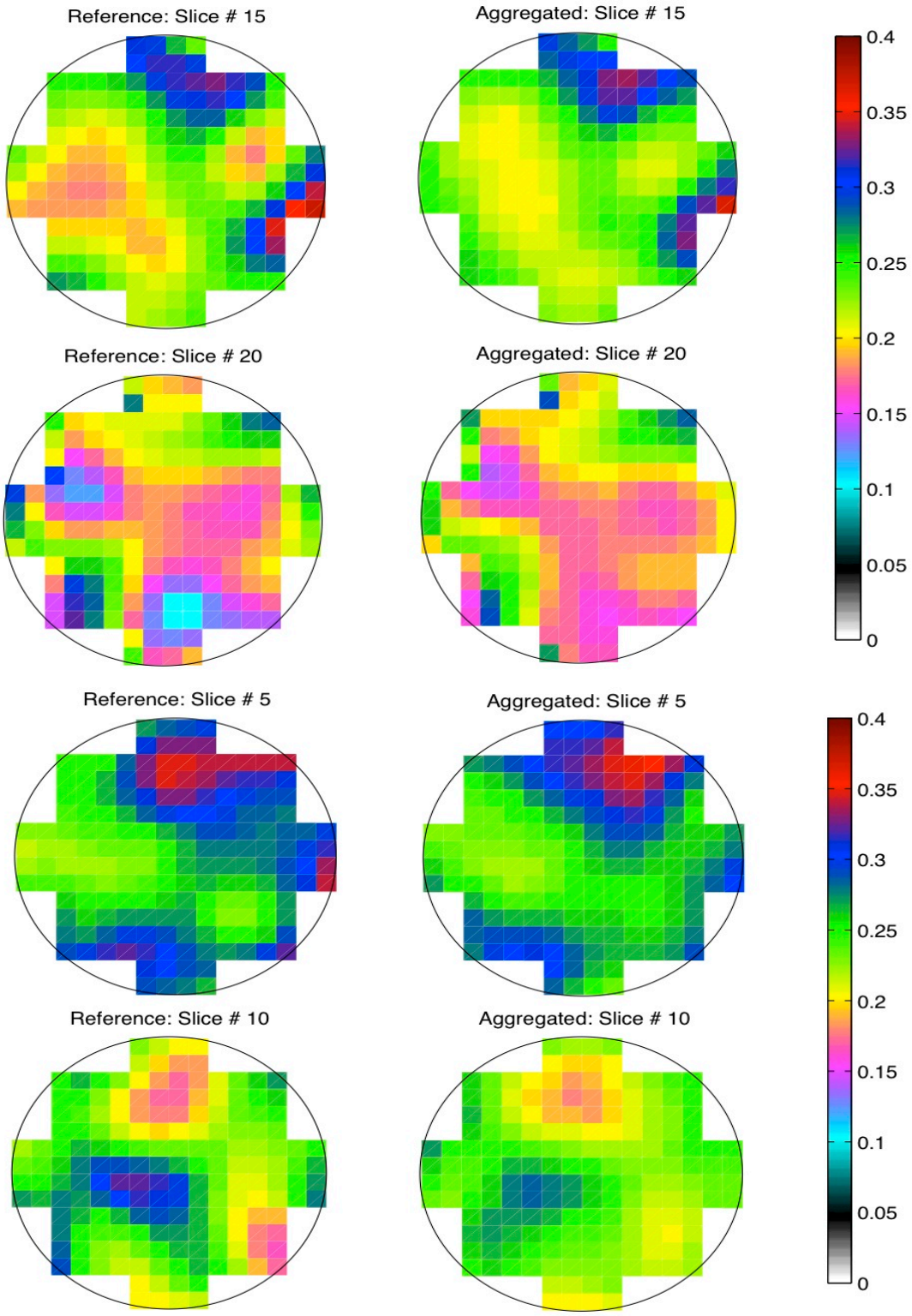

Figure 10: Prediction stage: Comparison of the reference and simulated data: Left: Reference data slices. Right: Ensemble average of the simulations for *pressure 110* bars for the family F. First, second, third and fourth row correspond to slice # 5, 10, 15 and 20, respectively.

Now we focus our attention on the prediction stage. The prediction stage refers to running the forward problem until 66cc of total injected volume, for the reference permeability field and for the family F of the permeability fields. We take the weighted average of the CO_2 saturation of all the simulations. The ensemble average of the CO_2 saturation is called the predicted result. In Fig. 10, we plot the reference, the ensemble average at the prediction stage for the simulations with pressure 110 bars. The left column corresponds to the reference data, the right column shows the ensemble average. We also show in Fig. 11, 12 and 13 the ensemble average of the saturation at slices along the core at the prediction stage. We can clearly see in all the plots that we have captured all the dominant regions of the reference data. Moreover, the accepted realizations resemble the reference data very closely. In conclusion, all these results show the effectiveness of the proposed framework.

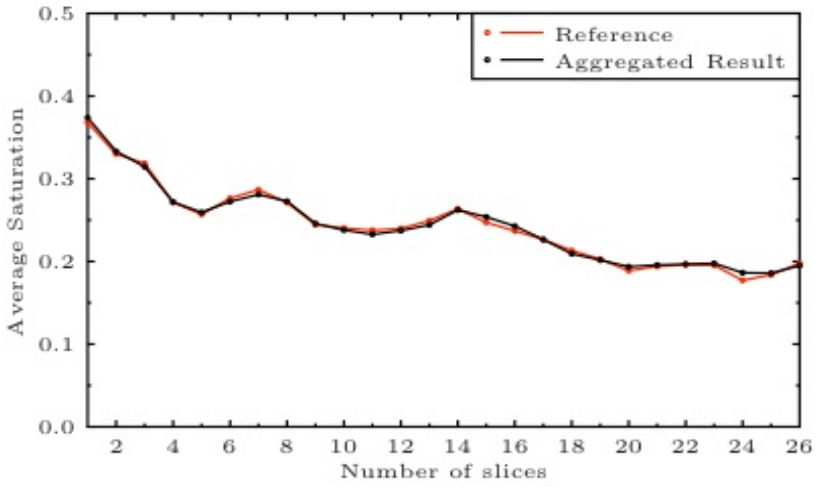

Figure 11: Prediction stage: Average saturation at slices for reference data and the ensemble average of the simulations for *pressure 110* bars for the family F.

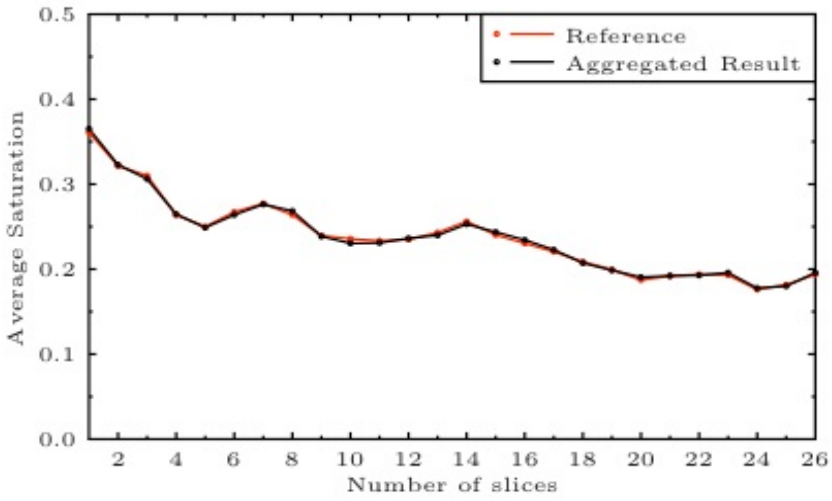

Figure 12: Prediction stage: Average saturation at slices for reference data and the ensemble average of the simulations for *pressure 150 bars* for the family F.

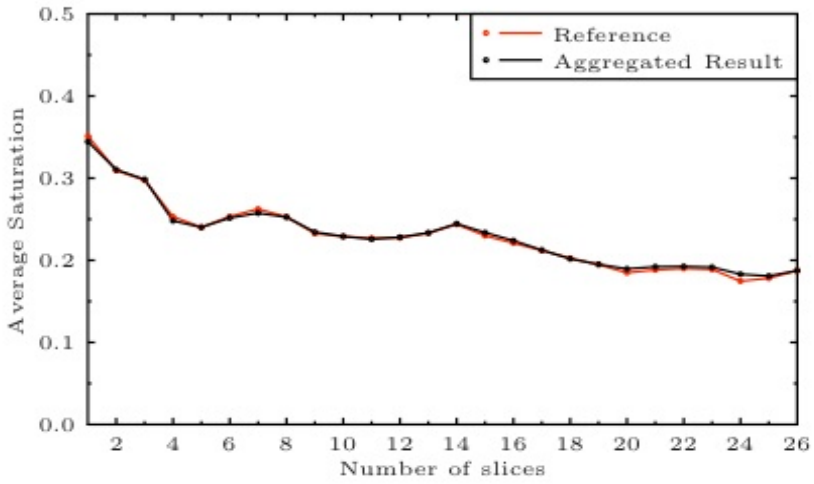

Figure 13: Prediction stage: Average saturation at slices for reference data and ensemble average of the simulations for *pressure 300 bars* for the family F.

We have indicated that we consider the strength of the permeability field to be a stochastic parameter. So it is interesting to see the convergence of the variance of the permeability field within the MCMC procedure to the variance of the reference permeability field. The strength of the reference permeability field is 0.5 and we call it the reference strength. The convergence of the variance s has been shown in Fig. 14 for the simulations with pressure 110 bars. It has shown that no matter where we start (different values for the initial strength) the strength will converge to the reference strength. It is worth to point out, that the strength is log-normally distributed and is given by $s = \exp(\theta)$, where θ

samples from equation (71), and we run the Markov chain for θ not for s explicitly. We observed the convergence of the strength even if we increase the mass transfer from one phase to another.
Our second study considers the effect of diffusion on the framework. We stop the mass transfer between phases and consider only diffusion in the simulations. We got promising results and in Fig. 15 we show the error between the reference and the simulated data, and the convergence of the strength for different diffusion strength.

Until this point, we have shown that the proposed Bayesian framework works well for synthetic data study. Next we incorporate the real experimental data (measured data) into the framework to validate a standard compositional model for the simulation of CO_2 sequestration in saline formation. In characterizaiton step, we have found a family of the permeability fields that matches the experimental data as shown in Fig. 16. For the predictions, we have injected 22.25, 38.45, 55.55 and 66.2 cc CO_2 volume, and the corresponding predicted results are shown in Fig. 17 against experimental results. The convergence of the stochastic strength of the permeabiluty field and the errorr between numerical and experimental data are shown in Fig. 18. Our results show that we have been successfully predicted the future fluid flow and validated the compositional model.

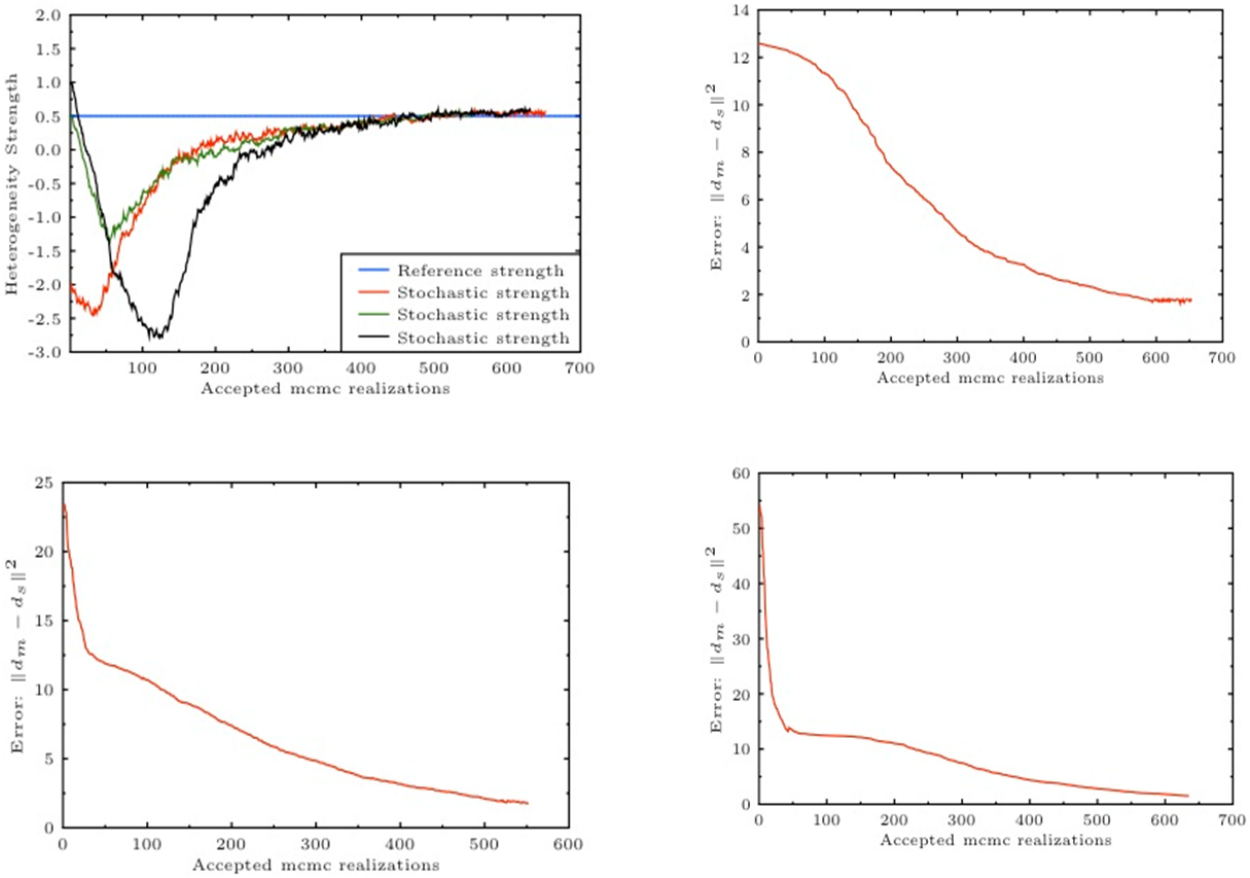

Figure 14: Top left: Markov chain for the variance of the permeability field vs. accepted MCMC realizations of the simulations for *pressure 110 bars*. Top right and bottom row: Error between reference and simulated data for initial permeability strength -2, 0.5 and 1, respectively.

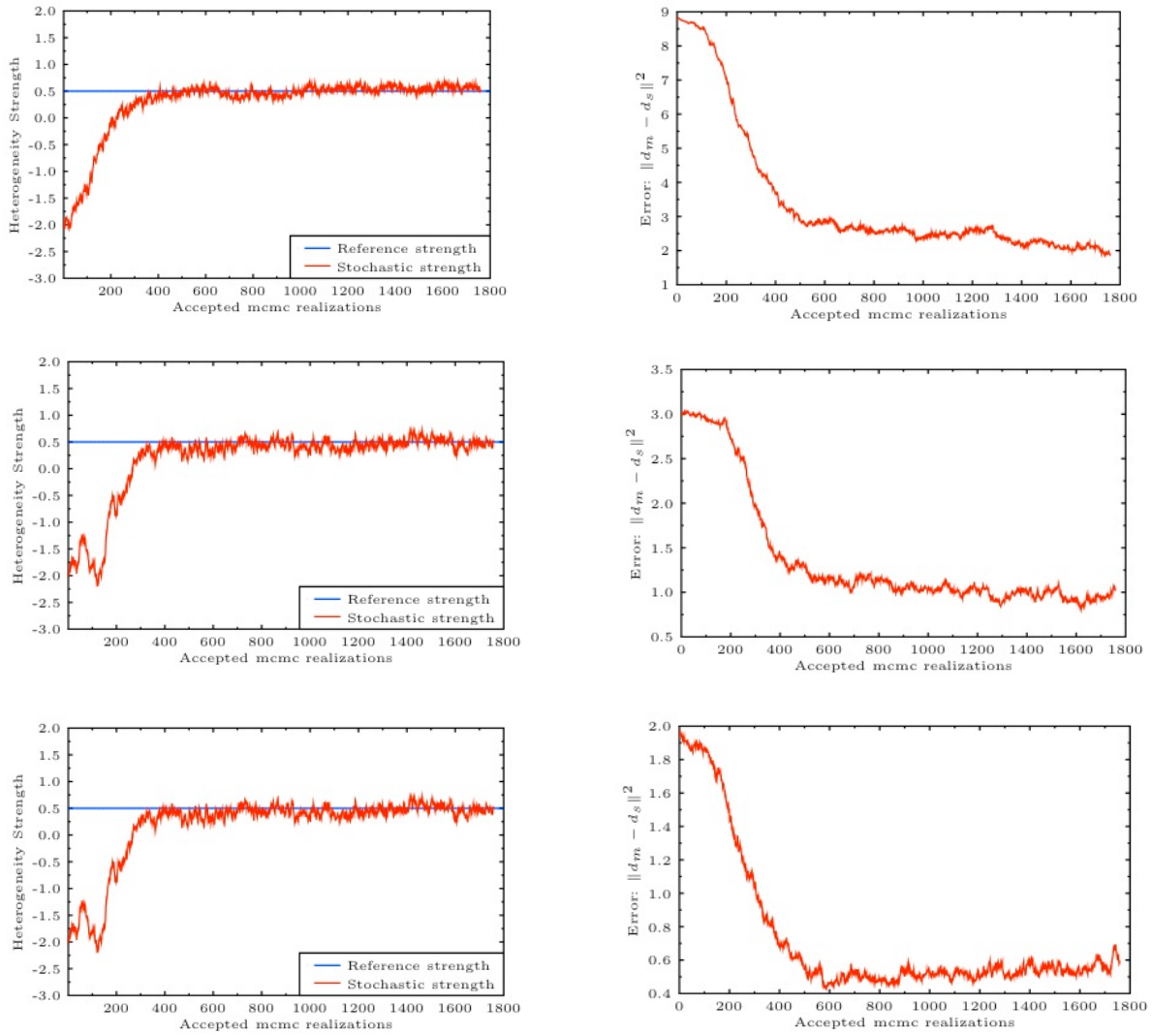

Figure 15: Simulations with different diffusion strengths: Left (top to bottom): strength 0.005, 0.01 and 0.1. Right: Error between reference and simulated data for the corresponding simulations on the left side.

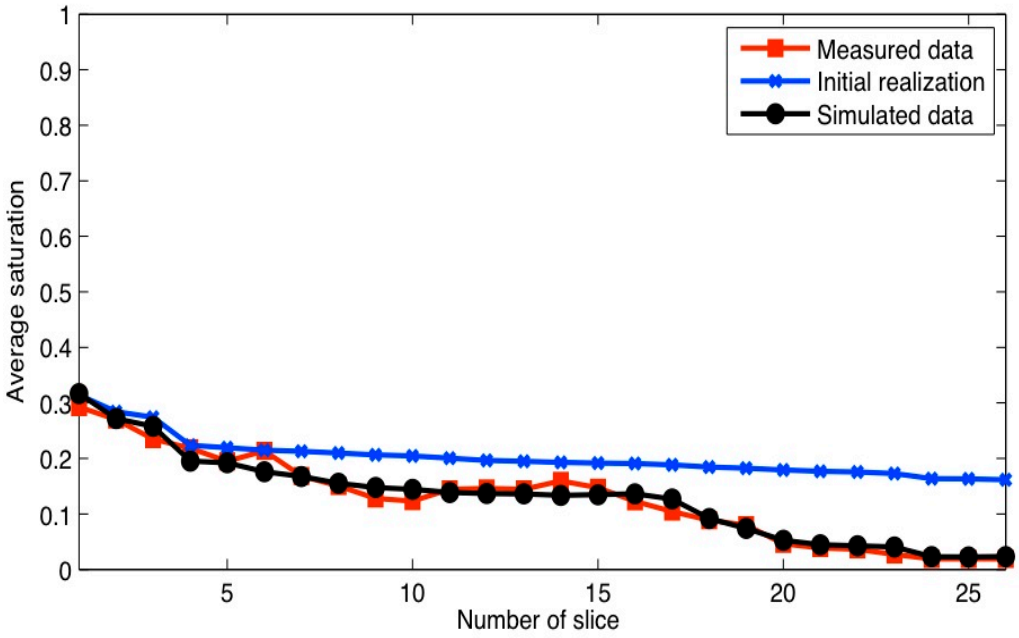

Figure 16: Experimental data and simulated data (ensemble average of CO_2 saturation at slices) at characterization stage.

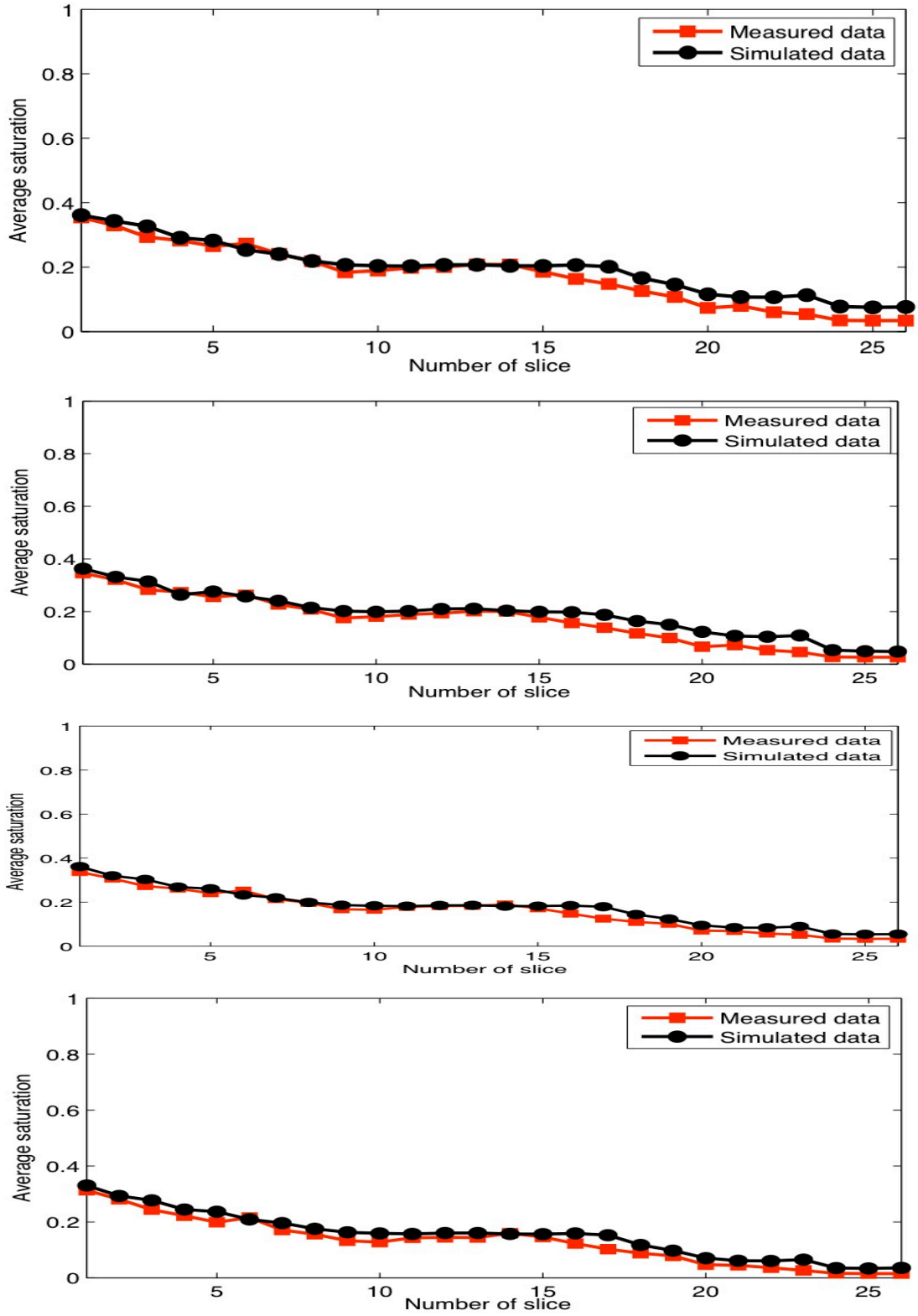

Figure 17: Experimental data vs. simulated data (ensemble average of CO_2 saturation at slices) at prediction stage. Total CO_2 volume injected (top to bottom): 22.25, 38.45, 55.55 and 66.2 cc

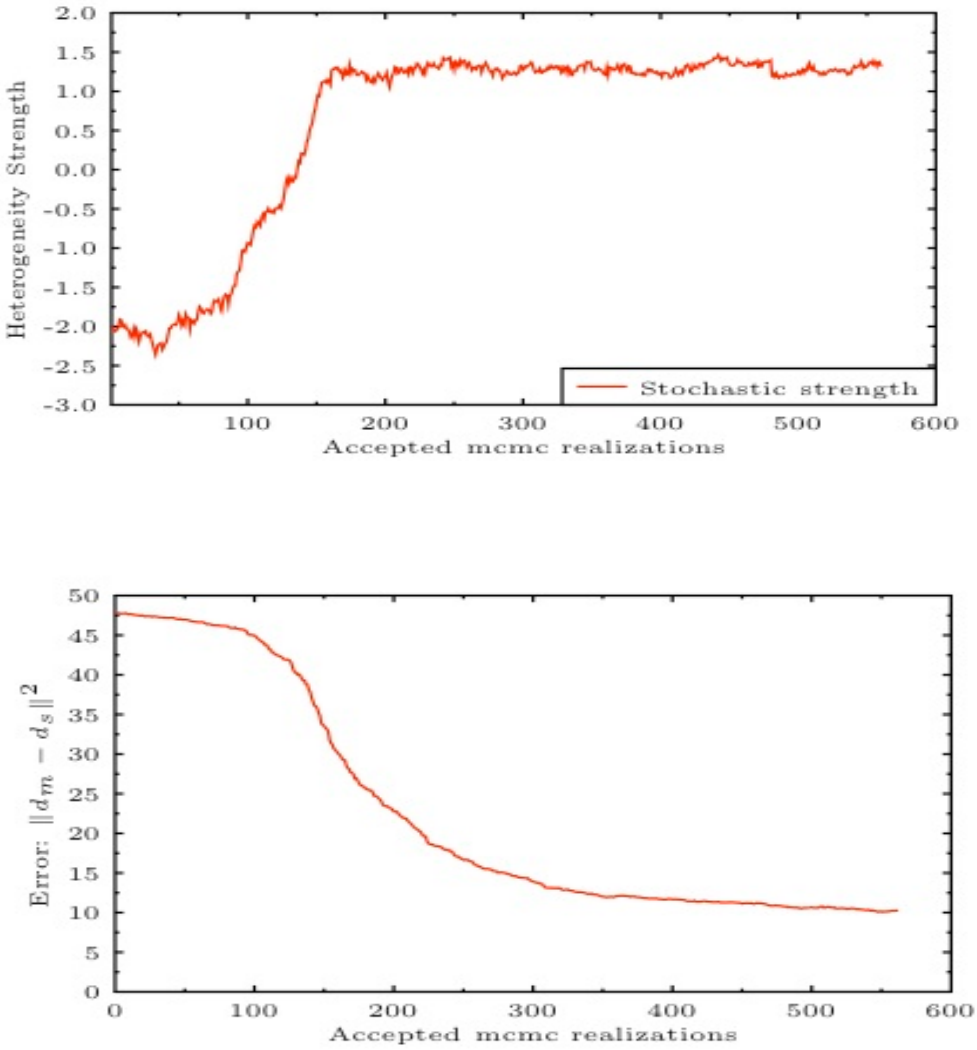

Figure 18: Top: Markov chain for the strength of the permeability field.
Bottom: Error between measured and simulated data

10 Conclusions

We have described an accurate and efficient operator splitting technique that has been tested for the numerical solution of a compositional two-phase model and then applied to validate numerical results against the experimental measurements of CO_2 injection in brine saturated cores. The numerical results obtained indicate that the delicate ballance between the focusing effects of nonlinear convection, which lead to the formation of shocks, and the smoothing effect of diffusion are captured by our method.

Futher, we focused on the development of a Bayesian framework for the validation of a compositional model to simulate CO_2 storage in saline aquifers. To test our framework for the validation study, first we presented a synthetic case study that is different from the validation in the sense that the measured data is not the real experimental data. Once the framework has been tested we can confidently apply to

the validation study. We consider a core initially fully saturated with brine at the laboratory scale and perform a drainage experiment at aquifer conditions. We assume that the porosity field of the entire core is known and taken as static data. The CO_2 saturation values at core slices measured with CT-scanner that are known for several values of time is treated as dynamic data. The problem at hand consists of finding permeability fields that are consistent with the measurements and, at the same time, allow one to predict future fluid flow. In other words, the static and dynamic data are used to characterize the posterior distribution of the permeability field of the core, and then, using the selected realizations of the permeability field, we predict the saturation at core slices for future times using Monte Carlo simulations.

The simulations have been done with high performance computing and a two-stage Markov Chain Monte Carlo (MCMC) method to minimize the computational time and increase the acceptance rate of the Metropolis-Hastings algorithm. In the characterization step we solve a compositional two-phase flow model for each permeability proposal and compare the solution of the model with the measured data.

The results reported in the numerical section show high agreement between the CO_2 saturation slices of the selected realizations and the reference data, at both the characterization and the prediction stage. The close resemblance between the reference and the accepted realizations guarantee that the proposed Bayesian framework will captured all the major features of the permeability field of the core if applied with the real experimental data. In general, the variance of the permeability field is not known and in our study it is taken to be a stochastic parameter. The numerical examples show that we have achieved convergence of the variance within the MCMC procedure to the variance of the reference permeability field. Moreover, the results presented in the numerical section show that we have recovered high dimensional posterior distribution of the permeability field.

After successfully testing the framework, we presented validation results in the numerical section. We obtained promising results in comparision with real experimental data.

At last, the recovery of the posterior distribution is needed to quantify the uncertainty in the geologic parameters of the reservoir. The novel uncertainty quantification framework presented here is fully consistent with the setup of real experiments. We remark that a new, parallelizable multiscale method (for pressure-velocity calculation) has also been developed within activities of Task 6. We refer the reader to the recent publication [258] for additional information.

Task 7: Development of a computational module for geomechanical deformation
PI: Dr. Shunde Yin

Computational Modeling Methods

1 Introduction

In this task we are concerned with the understanding of a coupled nonlinear model that describes the injection of CO_2 in deformable brine aquifers. We describe the development a high-performance, high resolution simulation tool for the solution of a comprehensive, 3D geomechanical model coupled to multi-phase flow in highly heterogenous, deformable porous media. This development is the first step aiming at the modeling of uncertainty in the poromechanical parameters. In a future project we intend to make predictions through high-resolution Monte Carlo studies using the computational framework developed here (some of the proposers and their collaborators have submitted a research proposal in response to a FOA from NSF's CMMI Division, in the area of Geomechanics & Geomaterials (GGS) in October/2013).

Here we describe the development of a new module to the compositional (multiphase, multi-component) simulator developed for the injection of CO_2 in rigid, multiscale heterogeneous porous media described in Task 6. The new module takes into account the coupling of flow with geomechanical deformation. In recent years the emphasis that has been placed on the development of computational models for CO_2 storage has mainly focused on the hydrodynamical and geochemical aspects of the problem (see [259-261] and references therein). In spite of their recent popularity, extended versions of these models to incorporate coupled flow and geomechanical processes in deformable heterogeneous media have achieved modest accomplishments [262-267].

Several poro-mechanical issues naturally arise during the injection of CO_2 in the subsurface and need to be properly addressed, otherwise they may compromise the safety of a storage project. For instance, in addition to well-known changes in permeability induced by the rock matrix deformation, CO_2 injection gives rise to anomalously high pore pressure which decreases effective stress and may potentially trigger slip on pre-existing reservoir-bounding faults. Initially impermeable before injection, such sealing faults may be activated due to shear or tensile failure modes giving rise to flow pathways for CO_2, thereby reducing sequestration effectiveness. Such misbehavior may also occur in the vicinity of injection wells where the appearance of local plastic deformations in the rock skeleton may mechanically damage the wells, thus affecting seal integrity. Avoiding the generation of fractures in the cap-rock by hydro-fracturing is another relevant issue. Since cap-rock acts as a geological barrier against $ CO_2 leakage its integrity is essential for the preservation of the sealing capacity.

The role of geomechanics in subsurface reservoirs is becoming increasingly important as deeper formations are detected and explored [268, 269]. Accurate predictions of fluid injection in weak rocks require a detailed coupled flow simulation and mechanical deformation modeling and demand precise understanding of the geomechanical factors affecting the hydrodynamics. The interaction between the geomechanical response and multiphase flow involves highly complex physics including several couplings mechanisms [270].

Since the seminal works of Terzaghi and Biot on single-phase flow in linear poroelastic media several extensions with varying degree of sophistication have been proposed to describe multiphase flows in geomaterials [271-273]. Thermodynamic consistent Darcy-scale models have been rigorously constructed using modern tools of mixture theories giving rise to a large system of nonlinear governing partial differential equations with the poromechanical coefficients properly interpreted [270].

The wide range of applications of multiphase flow in deformable media has produced distinct versions of the stress partition mechanisms along with different degree of hydro-mechanical couplings [270]. The former gave rise to several extensions of Terzaghi's decomposition starting from those derived from the efforts to identify a single effective stress concept [274] passing through the more general constitutive response of strain in terms of two independent stress variables [270] and finally through the characterizationof a thermodynamically consistent generalized effective stress [272]. We remark that the terminology of effective stress is still quite misleading (see the excellent reviews in [275]).

Several algorithms have been developed for the coupling between hydrodynamics and poromechanics and are known as one or two-way coupling (loose or full coupling) [276]. The former decomposes the systems into equations solved independently over the same total time interval with periodic one-way transfer. The two-way coupling geomechanics-reservoir models mainly fall into two categories: iteratively coupled and tightly coupled schemes [277]. Despite its higher computational burden the two-way coupling has produced more realistic results as it aims at solving simultaneously the system of the fully-coupled formulation of poromechanics [278-280].We refer the reader also to [281] for more references and a very good discussion about the stability of some of these schemes.

2 Geomechanical Coupling: Extension of the Compositional Model

We now describe the extension of the compositional model discussed in Task 6 to include coupling of fluid flow and rock deformation.

By neglecting the stress induced by the capillary pressure (we assume that in a two-phase system both phases have the same pressure) and using Terzaghi's principle, the total stress (T_t) applied on the solid-fluid system can be decomposed into

$$T_t = \mathbf{T}_{\mathit{e}\mathbf{ff}} - p_{\mathbf{avg}} I, \tag{1}$$

where $\mathbf{T}_{\mathbf{eff}}$ is the effective tension responsible for the deformation of the porous eskeleton and $p_{\mathbf{avg}}$ is an average pressure given by

$$p_{\mathbf{avg}} = S_{\mathbf{g}} p_{\mathbf{g}} + S_{\mathbf{aq}} p_{\mathbf{aq}}. \tag{2}$$

Applying the conservation of momentum law on the whole system we have

$$\mathrm{div}(T_t) + \phi(S_{\mathbf{aq}}\rho_{\mathbf{aq}} + S_g\rho_g)\mathbf{g} + (1-\phi)\rho_s\mathbf{g} = (\phi(S_{\mathbf{aq}}\rho_{\mathbf{aq}} + S_g\rho_g) + (1-\phi)\rho_s)\mathbf{a_t} \tag{3}$$

where $\mathbf{a}_t$ is the total acceleration vector. Considering that the overburden on the reservoir far surpasses its own weigth and assuming a very slow and gradual deformation we can disregard the gravity and inertia terms on equation (3) resulting in

$$\text{div}(\mathbf{T}_{\text{eff}} - p_{\text{avg}} I) = 0 \tag{4}$$

Here the porous media is assumed to be an isotropic linear elastic material and therefore

$$\mathbf{T}_{\text{eff}} = \lambda \text{div}(\mathbf{u}_s) I + 2\mu \nabla^s \mathbf{u}_s = 0 \tag{5}$$

where $\mathbf{u}_s$ is the solid displacement vector and λ, μ are the Lame constants.

Due to the solid deformation, the porosity will change in time according to the the porous media mass conservation equation given by

$$\frac{\partial(1-\phi)}{\partial t} = \text{div}((1-\phi)\mathbf{v}_s) \tag{6}$$

where $\mathbf{v}_s = \partial \mathbf{u}_s / \partial t$ is the solid velocity. Also, the percolation velocities are now defined as relatives velocities with respect to the porous media. Taking into account these two facts, the mass conservation equations for the total moles components are rewritten as

$$\frac{\partial \phi m^c}{\partial t} + \nabla \cdot \left(\frac{m_g^c}{S_g} (\mathbf{v}_g + S_g \phi \mathbf{v}_s) + \frac{m_{\text{aq}}^c}{S_{\text{aq}}} (\mathbf{v}_{\text{aq}} + S_{\text{aq}} \phi \mathbf{v}_s) \right) = 0 \tag{7}$$

$$\frac{\partial \phi m^w}{\partial t} + \nabla \cdot \left(\frac{m_g^w}{S_g} (\mathbf{v}_g + S_g \phi \mathbf{v}_s) + \frac{m_{\text{aq}}^w}{S_{\text{aq}}} (\mathbf{v}_{\text{aq}} + S_{\text{aq}} \phi \mathbf{v}_s) \right) = 0 \tag{8}$$

$$\frac{\partial \phi m^s}{\partial t} + \nabla \cdot \left(\frac{m_{\text{aq}}^s}{S_{\text{aq}}} (\mathbf{v}_{\text{aq}} + S_{\text{aq}} \phi \mathbf{v}_s) \right) = 0 \tag{9}$$

The pressure equation follows from the volume restriction $S^0 = 1$ which implies that

$$-\phi \frac{dS^0}{dt} = 0 \tag{10}$$

Since the total saturation is a function of pressure and total moles components per pore volume, we can use the chain rule to obtain

$$-\phi \frac{dS^0}{dt} = \beta_T \frac{\partial p}{\partial t} - \frac{\partial S^0}{\partial \overline{\mathbf{m}}} \phi \frac{\partial \overline{\mathbf{m}}}{\partial t}. \tag{11}$$

Using the mass conservation equations (7),(8) and (9), we get

$$-\frac{\partial S^0}{\partial \overline{\mathbf{m}}}\phi\frac{\partial \overline{\mathbf{m}}}{\partial t}=\frac{\partial S^0}{\partial m^w}\mathrm{div}\left(\frac{m_g^w}{S_g}(\mathbf{v_g}+S_g\phi\mathbf{v}_s)+\frac{m_{\mathbf{aq}}^w}{S_{\mathbf{aq}}}(\mathbf{v_{aq}}+S_{\mathbf{aq}}\phi\mathbf{v}_s)\right)+$$
$$\frac{\partial S^0}{\partial m^c}\mathrm{div}\left(\frac{m_g^c}{S_g}(\mathbf{v_g}+\phi\mathbf{v}_s)+\frac{m_{\mathbf{aq}}^c}{S_{\mathbf{aq}}}(\mathbf{v_{aq}}+S_{\mathbf{aq}}\phi\mathbf{v}_s)\right)+$$
$$\frac{\partial S^0}{\partial m^s}\mathrm{div}\left(\frac{m_{\mathbf{aq}}^s}{S_{\mathbf{aq}}}(\mathbf{v_{aq}}+S_{\mathbf{aq}}\phi\mathbf{v}_s)\right)$$
$$+\left(\frac{\partial S^0}{\partial m^w}m^w+\frac{\partial S^0}{\partial m^c}m^c+\frac{\partial S^0}{\partial m^s}m^s\right)\frac{\partial\phi}{\partial t}$$

Next, applying the product rule for derivatives and using the solid mass conservation equation (6) we have

$$-\phi\frac{dS^0}{dt}=\beta_T\frac{\partial p}{\partial t}+\mathrm{div}\left(\frac{\partial S^0}{\partial m^w}\frac{m_g^w}{S_g}(\mathbf{v_g}+S_g\phi\,\mathbf{v}_s)+\frac{\partial S^0}{\partial m^w}\frac{m_{\mathbf{aq}}^w}{S_{\mathbf{aq}}}(\mathbf{v_{aq}}+S_{\mathbf{aq}}\phi\,\mathbf{v}_s)\right)+$$
$$\mathrm{div}\left(\frac{\partial S^0}{\partial m^c}\frac{m_g^c}{S_g}(\mathbf{v_g}+S_g\phi\,\mathbf{v}_s)+\frac{\partial S^0}{\partial m^c}\frac{m_{\mathbf{aq}}^c}{S_{\mathbf{aq}}}(\mathbf{v_{aq}}+S_{\mathbf{aq}}\phi\,\mathbf{v}_s)\right)+$$
$$\mathrm{div}\left(\frac{\partial S^0}{\partial m^s}\frac{m_{\mathbf{aq}}^s}{S_{\mathbf{aq}}}(\mathbf{v_{aq}}+S_{\mathbf{aq}}\phi\,\mathbf{v}_s)\right)+$$
$$\nabla\frac{\partial S^0}{\partial m^w}\left(\frac{m_g^w}{S_g}(\mathbf{v_g}+S_g\phi\,\mathbf{v}_s)+\frac{m_{\mathbf{aq}}^w}{S_{\mathbf{aq}}}(\mathbf{v_{aq}}+S_{\mathbf{aq}}\phi\,\mathbf{v}_s)\right)+$$
$$\nabla\frac{\partial S^0}{\partial m^c}\left(\frac{m_g^c}{S_g}(\mathbf{v_g}+S_g\phi\,\mathbf{v}_s)+\frac{m_{\mathbf{aq}}^c}{S_{\mathbf{aq}}}(\mathbf{v_{aq}}+S_{\mathbf{aq}}\phi\,\mathbf{v}_s)\right)+$$
$$\nabla\frac{\partial S^0}{\partial m^s}\left(\frac{m_{\mathbf{aq}}^s}{S_{\mathbf{aq}}}(\mathbf{v_{aq}}+S_{\mathbf{aq}}\phi\,\mathbf{v}_s)\right)$$

$$-\phi\frac{dS^0}{dt}=\beta_T\frac{\partial p}{\partial t}+\mathrm{div}\left(\left(\frac{\partial S^0}{\partial m^w}\frac{m_g^w}{S_g}+\frac{\partial S^0}{\partial m^c}\frac{m_g^c}{S_g}\right)(\mathbf{v_g}+S_g\phi\,\mathbf{v}_s)+\right.$$
$$\left.\left(\frac{\partial S^0}{\partial m^w}\frac{m_{aq}^w}{S_{aq}}+\frac{\partial S^0}{\partial m^c}\frac{m_{aq}^c}{S_{aq}}+\frac{\partial S^0}{\partial m^s}\frac{m_{aq}^s}{S_{aq}}\right)(\mathbf{v_{aq}}+S_{\mathbf{aq}}\phi\,\mathbf{v}_s)\right)$$

$$\nabla \frac{\partial S^0}{\partial m^w}\left(\frac{m_g^w}{S_g}(\mathbf{v_g} + S_g\phi\,\mathbf{v}_s) + \frac{m_{aq}^w}{S_{aq}}(\mathbf{v_{aq}} + S_{\mathbf{aq}}\phi\,\mathbf{v}_s)\right) +$$
$$\nabla \frac{\partial S^0}{\partial m^c}\left(\frac{m_g^c}{S_g}(\mathbf{v_g} + S_g\phi\,\mathbf{v}_s) + \frac{m_{aq}^c}{S_{aq}}(\mathbf{v_{aq}} + S_{\mathbf{aq}}\phi\,\mathbf{v}_s)\right) +$$
$$\nabla \frac{\partial S^0}{\partial m^s}\left(\frac{m_{aq}^s}{S_{aq}}(\mathbf{v_{aq}} + S_{aq}\phi\,\mathbf{v}_s)\right) +$$
$$+\left(\frac{\partial S^0}{\partial m^w}m^w + \frac{\partial S^0}{\partial m^c}m^c + \frac{\partial S^0}{\partial m^s}m^s\right)\text{div}((1-\phi)\mathbf{v}_s)$$

For small compressibility we can ignore the terms $\nabla(\partial S^0/\partial m_\alpha)$. With these hypothesis and using the Kuhn-Tucker conditions, the above equation can be furthfer simplified to give

$$-\phi\frac{dS^0}{dt} = \beta_T\frac{\partial p}{\partial t} + \text{div}\left((\mathbf{v_g} + S_g\phi\,\mathbf{v}_s) + (\mathbf{v_{aq}} + S_{\mathbf{aq}}\phi\,\mathbf{v}_s) + (1-\phi)\mathbf{v}_s\right)$$
$$-\phi\frac{dS^0}{dt} = \beta_T\frac{\partial p}{\partial t} + \text{div}(\mathbf{v_t}) + \text{div}(\mathbf{v}_s) \tag{12}$$

Using equation (12) we finally obtain

$$\beta_T\frac{\partial p}{\partial t} + \text{div}(\mathbf{v_t}) + \text{div}(\mathbf{v}_s) = \phi\frac{S^0(t_n) - 1}{\Delta t} \tag{13}$$

The compositional model coupled with geomechanical deformation is given by the flash calculations and the following system of equations

$$\text{div}\left(\lambda\,\text{div}(\mathbf{u}_s)I + 2\mu\nabla^s\mathbf{u}_s\right) - \nabla\left(p_{\mathbf{aq}} + (1-S_{\mathbf{aq}})p_c\right) = 0 \tag{14}$$

$$\beta_T\frac{\partial p}{\partial t} + \text{div}(\mathbf{v_t}) + \text{div}(\mathbf{v}_s) = 0 \tag{15}$$

$$\frac{\partial\phi m^c}{\partial t} + \nabla\cdot\left(\frac{m_g^c}{S_g}(\mathbf{v_g} + S_g\phi\mathbf{v}_s) + \frac{m_{\mathbf{aq}}^c}{S_{\mathbf{aq}}}(\mathbf{v_{aq}} + S_{\mathbf{aq}}\phi\mathbf{v}_s)\right) = 0 \tag{16}$$

$$\frac{\partial\phi m^w}{\partial t} + \nabla\cdot\left(\frac{m_g^w}{S_g}(\mathbf{v_g} + S_g\phi\mathbf{v}_s) + \frac{m_{\mathbf{aq}}^w}{S_{\mathbf{aq}}}(\mathbf{v_{aq}} + S_{\mathbf{aq}}\phi\mathbf{v}_s)\right) = 0 \tag{17}$$

$$\frac{\partial\phi m^s}{\partial t} + \nabla\cdot\left(\frac{m_{\mathbf{aq}}^s}{S_{\mathbf{aq}}}(\mathbf{v_{aq}} + S_{\mathbf{aq}}\phi\mathbf{v}_s)\right) = 0 \tag{18}$$

Where p_c is the capillary pressure, $\beta_T = -\phi\partial S^0/p_{\mathbf{aq}}$ is a funtion of pressure.

Results and Discussion

The numerical solution of compositional model dicussed in detail in Task 6 has been further developed to handle deformable rocks in Task 7. We have approximated numerically the large coupled system within the framework of a loose staggered algorithm wherein the system of equations is decomposed into subsystems solved sequentially by numerical schemes properly designed to handle the particular features of each subsystem. We solve for the poromechanics and for the post-processing procedure in a staggered fashion with the nonlinear hyperbolic problem for the saturation. For the discretization of the poromechanics system we apply the finite element methodology in line with the procedure developed in [282]. For the discretization of the saturation equation rather than pursuing schemes based on upwind differentiating we adopt high-resolution non-oscillatory central schemes. To evolve consistently in time we have developed an accurate coupling algorithm between each subsystem and determined through numerical tests a good ratio between macro (used to update the poromechanics) and micro (used for transport calculations) time steps.

Within this project the simulation code has been tested for incompressible fluids, that can be a good approximation for the carbon dioxide-brine problem in the case of weak rock formations. Figure 1 shows the result of a simulation study where we compare the case of a rigid formation with a deformable one. Clearly the deformable rock can have a strong impact on the fluid flow problem.

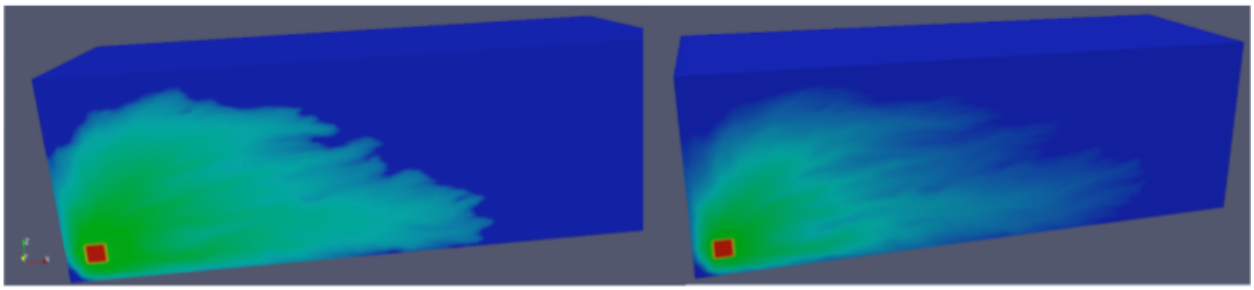

Figure 1: The impact of geomechanical coupling. Left: Rigid formation. Right: Deformable rock. The pictures show the saturation of injected CO_2 in an injection well located at bottom left of a heterogeneous aquifer.

Conclusions

Since the seminal works of Terzaghi and Biot on single-phase flow in linear poroelastic media several extensions with varying degree of sophistication have been proposed to describe multiphase flows in geomaterials. Our development contributes to extend the applicability of these models to make predictions for field scale, heterogeneous problems. The computational framework can be used for the assessment of uncertainty in CO_2 sequestration projects taking into account rock heterogeneity and geomechanical deformation. The work that has been carried out consists of the integration of recent developments of the proposers in the following areas:

- Modeling and numerical approximation of the hydrodynamics of CO_2 injection in saline (brine) aquifers;
- Modeling and numerical approximation of geomechanical deformation of aquifer rocks.

Task 8: Field-scale numerical experiment
PI: Dr. Victor Ginting

Computational Modeling Methods

1 Introduction

Here we focus on the development of a Bayesian-type framework for uncertainty quantification in CO_2 injection projects. Our new procedure that has been developed with funding from this project is an extension of the 2-stage MCMC method that was used in Task 6 in our validation of the compositional for the injection of CO_2 in brine saturated subsurface formations. It provides a very flexible framework for subsurface characterization and predictive simulation for CO_2 injection projects.

In CO_2 sequestration in deep saline aquifers, contaminant transport in subsurface, or oil or gas recovery, we often need to forecast flow patterns. In the flow forecasting, subsurface characterization is an important step. To characterize subsurface properties we establish a statistical description of the subsurface properties that are conditioned to existing dynamic (and static) data. We use a Markov Chain Monte Carlo (MCMC) algorithm in a Bayesian statistical description to reconstruct the spatial distribution of two important subsurface properties: rock permeability and porosity. The MCMC algorithm requires repeatedly solving a set of nonlinear partial differential equations describing displacement of fluids in porous media for different values of permeability and porosity. The time needed for the generation of a reliable MCMC chain using the algorithm can be too long to be practical for flow forecasting. In this paper we develop computationally fast and effective methods of generating MCMC chains in the Bayesian framework for the subsurface characterization. Our strategy consists of constructing a family of computationally inexpensive preconditioners based on simpler physics as well as on surrogate models such that the number of fine-grid simulations is drastically reduced in the generation MCMC chains. We assess the quality of the proposed multi-physics MCMC methods by considering Monte Carlo simulations for forecasting oil production in an oil reservoir.

Scientifically correct models based on first principles, accurate numerical simulators and state-of-the-art computers are of utmost importance in producing reliable predictions of multiphase flows in the subsurface. These aspects of predictive simulations have been properly addressed in Tasks 5, 6 and 7 of this project. However, uncertainty in the determination of subsurface properties, such as permeability and porosity, remains the main challenge that one has to overcome to produce accurate predictions.

The typical situation encountered in the investigation of problems such as CO_2 sequestration in saline aquifers is that there is very little data available to characterize subsurface properties. Only sparse data is available: at well locations permeability and porosity (static data) can be measured as well as well pressure values, production curves, and saturation or concentration values at monitoring wells (dynamic data) are usually available. Thus, the problem of determining permeability and porosity fields from available data is not well posed and a stochastic prediction methodology must be considered [301].

We are concerned with the development of a computationally fast and effective Bayesian framework for the characterization of porous media. To characterize subsurface properties we establish a statistical description of the subsurface properties that are conditioned to existing dynamic (and static) data. We

use a Markov Chain Monte Carlo (MCMC) algorithm in a Bayesian statistical description to reconstruct the spatial distribution of rock permeability and porosity. In this context however, acceptance or rejection criterion in the MCMC algorithm requires calculation of likelihood function that involves repeatedly solving a set of nonlinear partial differential equations describing displacement of fluids in porous media for different values of permeability and porosity. For each proposal in the MCMC algorithm, we compare measured data with its simulated counterpart [288,292,305]. The time needed for the generation of a reliable MCMC chain using the algorithm can be too long to be practical for the subsurface characterization.

The search of computationally efficient MCMC methods has been attracting the attention of several research groups. Fox and Nicholls [294] employed a perturbation technique to identify proposals that are most likely rejected in the posterior probability exploration. Oliver et al. [307] were perhaps among the first to apply MCMC in the petroleum reservoir simulations to characterize uncertainty in the permeability fields conditioned to the pressure data. The authors in [295] improved the algorithm in [307] by proposing a blocking MCMC approach in which each proposed member of the chain is different from the previous one over an entire, relatively large, block of cells. This blocking scheme accelerates the creation of the chain of realizations. Higdon et al. [302] presented a methodology for improving the speed and efficiency of an MCMC by combining runs on different scales. They introduced a coarse-scale to make the MCMC chain run faster and better explore the posterior, and linked the coarse chain back to the original fine-scale chain of interest. In [287] a two-stage MCMC algorithm was presented for generating samples from an unnormalized posterior distribution in which the evaluation of the posterior distribution is very difficult or computationally demanding. The algorithm was applied to recovering resistor values in a network from electrical measurements made at the boundary. Later in [292, 293], the two-stage MCMC algorithm, which utilizes inexpensive coarse-scale models to screen out detailed flow and transport simulations, was used to explore the posterior distribution of the permeability field. In the first stage, a new proposal is tested at the coarse-scale model. If the proposal passes the testing at the coarse-scale model, then at the second stage the fine-scale simulation will be run and this fine-scale run is computationally very expensive when compared to the coarse-scale run. Vrugt et al. [310] developed a population-based MCMC algorithm that allows for the exchange of information among multiple chains to enhance the efficiency of MCMC sampling. Kavetski et al. [303] and Kavetski and Kuczera [304] showed that some computational complexities can be removed by smoothing the objective function in parameter optimizations of hydrological model calibration in accelerating the Bayesian posterior sampling. A multiple-try MCMC algorithm [312] was designed for a hydrological and environmental simulation model by making better use of the information generated in a costly run of the model. The authors used multiple evaluations of the posterior density in the less computationally expensive subspace of error model parameters.

Furthermore, in the same spirit of two-stage procedures [287, 292, 293, 296], Ginting, Pereira, and Rahunanthan introduced a multi-stage Bayesian prediction framework for subsurface flows in [298]. The authors described a predictive procedure in a Bayesian framework, which uses a single-phase flow model for characterization aiming at making prediction for a two-phase flow model. The quality of the characterization of the underlying formations was accessed through the prediction of future fluid flow production. They also considered parallelizing the generation of MCMC chains to speed-up the posterior exploration in [297, 299]. In [297] the authors addressed this issue using several parallel MCMC chains for flow prediction. In [299] the authors parallelize single MCMC chain using a pre-fetching technique implemented on GPUs and showed that the parallelization can make the Bayesian approach computationally tractable for subsurface characterization and prediction of porous media flows. single

MCMC chain using a pre-fetching technique implemented on GPUs and showed that the parallelization can make the Bayesian approach computationally tractable for subsurface characterization and prediction of porous media flows.

The original contribution of the present work is the introduction of the concept of multi-physics MCMC (MP-MCMC) methods. In our strategy a family of computationally inexpensive preconditioners are constructed based on simpler physics as well as on surrogate models such that the number of fine-grid simulations of the problem of interest is drastically reduced in the whole MCMC calculation. Moreover, we assess the quality of the characterization step by considering Monte Carlo simulations for prediction. We use partial (in time) data from production wells to characterize permeability and porosity fields. A set of accepted proposals is then sent to the numerical model to run the forward problem and predict the remaining portion of measured production data by aggregating the solutions of the forward problem [300]. We refer to this prediction stage as the Monte-Carlo (MC) step of our Bayesian framework.

We focus on the development of MP-MCMC methods that may incorporate ad-hoc characterization procedures of use in engineering practice (for example, tracer tests and huff puff procedures [283]) in a mathematically and computationally sound framework. We remark that frequently a geological model is constructed by geologists and geophysicists based on seismic information, well measurements, etc. The framework discussed here can take such models into account: we characterize a perturbation of such deterministic fields that allow us to match simulation results to existing dynamic data.

The development of MP-MCMC methods naturally refers to a hierarchy of models for porous media flows, from full compositional multiphase flow to the simple tracer flow problem. In order to explain our framework we will refer mainly to two-phase, immiscible, incompressible displacement and tracer flows.

This report on Task 8 activities is organized as follows. We discuss the current state of practice for subsurface characterization in section 2. In this section a parametrization of uncertainty using the Karhunen-Loève expansion [306, 311] for unknown permeability and porosity fields is discussed. The parametrization is followed by a discussion of MCMC sampling for quantifying uncertainty in both permeability and porosity fields. We then recall a two-stage MCMC algorithm that uses an upscaling of the characteristics of the subsurface on a fine-grid to a computationally quicker coarse-grid; the novel MP-MCMC reduces to this procedure as a particular case. In section 3 we introduce a multi-physics MCMC algorithm for efficient and effective subsurface characterization. In the simulation studies in section 4 we implement MCMCs aiming at making predictions in an reservoir/aquifer and compare MCMC algorithms. Next our figures are presented followed by our conclusions that appear at the end of this report.

2 Current state of practice

2.1 Physical and mathematical Modeling

We consider a heterogeneous aquifer/oil reservoir which is confined in a domain Ω. The reservoir contains an injection and two production wells. Water/CO_2 is discharged at the injection well to displace the trapped oil/brine towards the production wells (see Fig. 1). The dynamics of the movement of the fluids in the reservoir is categorized as an immiscible two-phase system. The discussion applies to carbon dioxide-brine or water-oil systems. In describing the basic flow and transport models we will refer to water and oil (denoted by w and o, respectively). As indicated above, we remark that at the

end of this report we will discus an application of the new framework introduced here for a CO_2 injection study. Capillary pressure is not included in the model. To further simplify the model, we assume a gravity-free environment with no sources or sinks, and water and oil fill the pore space. The injection and production wells are modeled through boundary conditions.

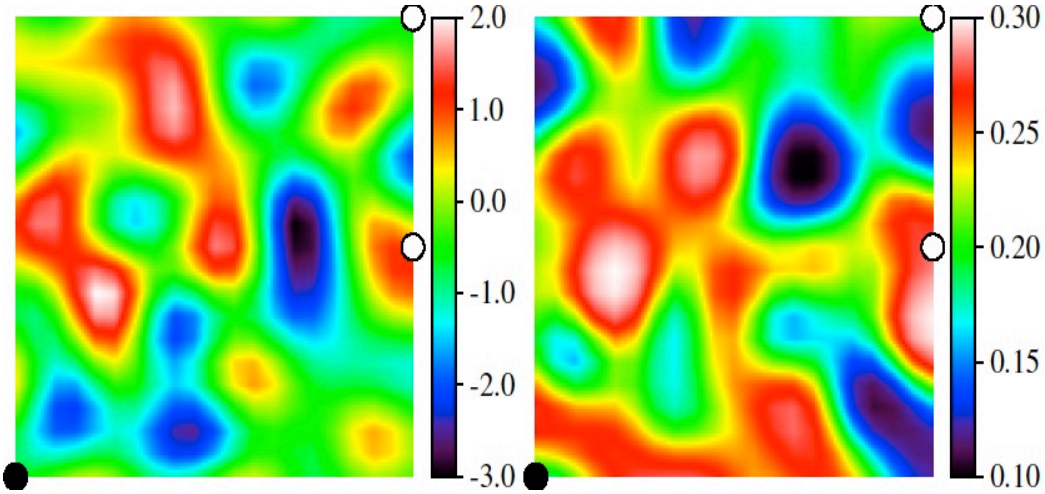

Figure 1: Permeability (in logarithmic scale) and porosity distribution of the reference field on the left and right, respectively. Closed and open circles denote the location of injection and production wells, respectively.

Darcy's law with a statement of conservation of mass allow us to write the governing equations of the flow as

$$\nabla \cdot \mathbf{u} = 0, \text{ where } \mathbf{u} = -\lambda(s)k(\mathbf{x})\nabla p, \tag{1}$$

and

$$\phi(\mathbf{x})\frac{\partial s}{\partial t} + \nabla \cdot (f(s)\mathbf{u}) = 0, \tag{2}$$

where $\mathbf{u}$ is the Darcy velocity, s is the water saturation, k is the absolute permeability and ϕ is the porosity. The total mobility $\lambda(s)$ and the flux function $f(s)$ are respectively given by

$$\lambda(s) = \frac{k_{rw}}{\mu_w} + \frac{k_{ro}}{\mu_o}, \quad f(s) = \frac{k_{rw}(s)/\mu_w}{\lambda(s)}, \tag{3}$$

where k_{rj}, $j = w,o$, is the relative permeability of the phase j [286].

We sample rock permeability and porosity of the oil reservoir using partial fractional flow data. For each production boundary the fractional flow $F(t)$ is defined as the fraction of oil in the produced fluid, which depends on dimensionless time t (in PVI):

$$F(t) = 1 - \frac{\int_{\partial\Omega_{\text{out}}} \mathbf{u}_n f(s)\ \mathrm{d}l}{\int_{\partial\Omega_{\text{out}}} \mathbf{u}_n\ \mathrm{d}l}, \tag{4}$$

and

$$\mathrm{PVI} = \int_0^T V_p^{-1} \int_{\partial\Omega_{\mathrm{in}}} \mathbf{u}_n \, \mathrm{d}l \, \mathrm{d}\tau, \tag{5}$$

where $\partial\Omega_{\mathrm{out}}$ ($\partial\Omega_{\mathrm{in}}$) denotes outflow (inflow) boundary, $\mathbf{u}_n$ is normal velocity field, V_p is the total pore-volume of the reservoir, and T denotes the time taken for injection of water.

The pressure and saturation equations, (1) and (2), are coupled together by the Darcy velocity $\mathbf{u}$ and water saturation s. For a better computational efficiency in solving these equations, we employ an operator splitting technique (see for example [284, 285, 290]). This technique allows us to use very larger time steps for solving (1) than the time steps for solving (2), which are governed by the CFL condition. We thus introduce a variable time step Δt_s for the saturation calculation, and a longer time step Δt_p for the pressure calculation. The pressure and thus the Darcy velocity are approximated at times $t^m = m\Delta t_p$, where $m = 0,1,\ldots$; the saturation is approximated at times $t^{m,k} = t^m + \sum_{i=1}^{k} (\Delta t_s)_i$ for $t^m < t^{m,k} \le t^{m+1}$. We specify the water saturation at $t = 0$. We refer the reader to [308, 309] for further discussion on the numerical schemes used in solving the forward problem possibly taking advantage of GPU hardware for high performance computing.

2.2 Parametrization of uncertainty

In this subsection for completeness we recall the Karhunen-Loève (KL) expansion [306, 311] that has been discussed in the report for Task 6. This expansion is used to reduce dimension of uncertainty space for permeability and porosity. This reduction technique has been applied within a Bayesian statistical framework in [292, 296-299]. Here we reproduce the technique for the sake of completeness of the discussion.

We assume that permeability distribution is log-normal [289]. This simplification leads to $\log[k(\mathbf{x},\omega)] = Y^k(\mathbf{x},\omega)$, where $\mathbf{x}$ represents spatial location, and ω introduces randomness. The $Y^k(\mathbf{x},\omega)$ represents a field with a Gaussian distribution and a covariance function

$$R(\mathbf{x_1},\mathbf{x_2}) = \sigma_Y^2 \exp\left(-\frac{1}{2}|\mathbf{L}^{-1}(\mathbf{x}_1 - \mathbf{x}_2)|^2\right), \tag{6}$$

where, $\mathbf{L} = \mathrm{diag}(L_x, L_y)$ with the correlation lengths L_x and L_y in x- and y- direction, respectively, and $\sigma_Y^2 = E[(Y^k)^2]$, and $|\cdot|^2 = \langle\cdot,\cdot\rangle$ is the usual norm induced by the Euclidean inner product.

We assume $Y^k(\mathbf{x},\omega) \in L^2(\Omega)$ with a probability of one and $E[Y^k(\mathbf{x})] = 0$. This leads to the Karhunen-Loève expansion

$$Y^k(\mathbf{x},\omega) = \sum_{i=1}^{\infty} \sqrt{\lambda_i}\, \theta_i^k(\omega) \varphi_i(\mathbf{x}), \tag{7}$$

where φ_i and λ_i satisfy

$$\int_\Omega R(\mathbf{x}_1;\mathbf{x}_2)\varphi_i(\mathbf{x}_2)\mathbf{d}\mathbf{x}_2 = \lambda_i\varphi_i(\mathbf{x}_1),\ i=1,2,..., \tag{8}$$

where $\lambda_i = E[(Y_i^k)^2] > 0$.

The L^2 basis functions $\varphi_i(\mathbf{x})$ in (8) are deterministic and resolve the spatial dependence of the permeability field and in particular its correlation structure. The scalar random variables θ_i^k represent uncertainty in permeability. We order the eigenvalues $\{\lambda_i\}_{i=1}^{\infty}$ in the KL expansion (7) (i.e., $\lambda_1 \geq \lambda_2 \geq ...$). This permits us to keep the leading order terms (quantified by the magnitude of λ_i), which capture most of the energy of the stochastic process $Y^k(\mathbf{x},\omega)$. For a N_k-term KL expansion we write

$$Y_{N_k}^k = \sum_{i=1}^{N_k}\sqrt{\lambda_i}\theta_i^k\varphi_i. \tag{9}$$

In Fig. 2 we show a decay of eigenvalues. In this case we can sample $Y^k(\mathbf{x},\omega)$ from the truncated KL expansion (7) with 80 eigenvalues.

We now focus on the KL expansion for porosity. Let us assume that both spatial correlation structures for permeability and porosity are similar. This enable us to employ the same Karhunen-Loève basis functions (8). Following the same reduction technique for the permeability field, we use a N_ϕ-term KL expansion

$$Y_{N_\phi}^\phi(\mathbf{x},\omega) = \sum_{i=1}^{N_\phi}\sqrt{\lambda_i}\theta_i^\phi(\omega)\varphi_i(\mathbf{x}). \tag{10}$$

The porosity values should fall between $\phi_{\min}$ and $\phi_{\max}$, where $\phi_{\min}$ and $\phi_{\max}$ are the lower and upper limits of the porosity distribution of subsurface. Therefore, we define the porosity as

$$\phi(\mathbf{x}) = \frac{\phi_{\min} + \phi_{\max}e^{Y_{N_\phi}^\phi}}{1+e^{Y_{N_\phi}^\phi}},\ \phi_{\min} \text{ and } \phi_{\mathbf{max}} \in (0,1). \tag{11}$$

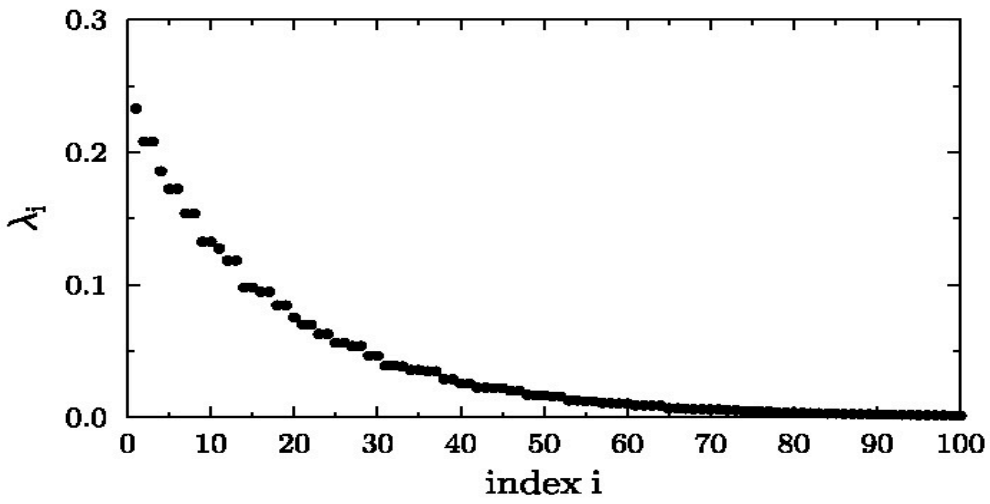

Figure 2: Decay of eigenvalues for the Gaussian covariance with $L_x = L_y = 0.1$ and $\sigma_Y^2 = 4$

2.3 Bayesian inference

In this subsection we introduce a Bayesian framework to sample the permeability and porosity fields conditioned on measured production data F_m. We sample from the conditional distribution $P(\boldsymbol{\psi} \mid F_m)$. The $\boldsymbol{\psi}$ represents the field generated by the vectors $\boldsymbol{\theta}^k$ and $\boldsymbol{\theta}^\phi$, which contain the random coefficients in the KL expansions (9) and (10), respectively. i.e., $\boldsymbol{\psi} = [\boldsymbol{\theta}^k \; \boldsymbol{\theta}^\phi]$. With Bayes' theorem we can write

$$P(\boldsymbol{\psi} \mid F_m) \propto P(F_m \mid \boldsymbol{\psi}) P(\boldsymbol{\psi}), \tag{12}$$

where $P(F_m \mid \boldsymbol{\psi})$ represents the likelihood function (that requires the forward solution of the two-phase flow) and $P(\boldsymbol{\psi})$ is the prior distribution of $\boldsymbol{\psi}$. We assume that the likelihood function follows a Gaussian distribution

$$P(F_m \mid \boldsymbol{\psi}) \propto \exp(-\langle F_m - F_{\boldsymbol{\psi}}, \Sigma(F_m - F_{\boldsymbol{\psi}}) \rangle), \tag{13}$$

where $F_{\boldsymbol{\psi}}$ represents simulated production data that is obtained by solving the forward problem with known permeability k and porosity ϕ, in other words with known $\boldsymbol{\psi}$, and Σ is the covariance matrix representing the measurement errors. $\Sigma = I / 2\sigma_F^2$, where I is the identity matrix and σ_F^2 is the precision associated with the measurement F_m and numerical solution F.

To avoid using an ad-hoc correlation between porosity and permeability, we assume that $\boldsymbol{\theta}^k$ and $\boldsymbol{\theta}^\phi$ are independent of each other.

2.3.1 Markov chain Monte Carlo method

We now discuss the standard Metropolis-Hasting MCMC algorithm for exploring the posterior for the underlying field. In this algorithm we rely on the construction of a Markov chain with an equilibrium distribution equal to the posterior distribution of interest. At each iteration, $\boldsymbol{\psi} = [\boldsymbol{\theta}^k \ \boldsymbol{\theta}^\phi]$ is drawn from an instrumental distribution $q(\boldsymbol{\psi} \mid \boldsymbol{\psi}_{j-1})$, where $\boldsymbol{\psi}_{j-1}$ is the previous state/iterate in the chain. It is then proceeded by solving the forward problem to get $F_{\boldsymbol{\psi}}$ which in turn is used in the calculation of (13). The likelihood values along with the prior information are the basis for the decision making of either to reject or accept $\boldsymbol{\psi}$. See Algorithm 1 for a detailed procedure.

Algorithm 1 Single-stage MCMC

Given the covariance function R, generate KLE parametrization $\{\lambda_n, \varphi_n\}_{n=1}^N$

Set initial state $\boldsymbol{\psi}_0 = [\boldsymbol{\theta}_0^k \ \boldsymbol{\theta}_0^\phi]$

for $j = 1$ to M_{mcmc}

(1) At state $\boldsymbol{\psi}_{j-1}$, generate $\boldsymbol{\psi} = [\boldsymbol{\theta}^k \ \boldsymbol{\theta}^\phi]$ from $q(\boldsymbol{\psi} \mid \boldsymbol{\psi}_{j-1})$

(2) With $\boldsymbol{\psi}$, compute k and ϕ using KLE and solve the forward problem on the fine-scale to get $F_{\boldsymbol{\psi}}$

(3) Accept $\boldsymbol{\psi}$ with probability

$$\Pr = \alpha(\boldsymbol{\psi}_{j-1}, \boldsymbol{\psi}) = \min\left(1, \frac{q(\boldsymbol{\psi}_{j-1} \mid \boldsymbol{\psi}) P(\boldsymbol{\psi} \mid F_m)}{q(\boldsymbol{\psi} \mid \boldsymbol{\psi}_{j-1}) P(\boldsymbol{\psi}_{j-1} \mid F_m)}\right),$$

i.e., $\boldsymbol{\psi}_j = \boldsymbol{\psi}$ with probability $\Pr$ or $\boldsymbol{\psi}_j = \boldsymbol{\psi}_{j-1}$ with probability $1 - \Pr$

end for

2.3.2 Two-stage Markov chain Monte Carlo method

We discuss a two-stage MCMC algorithm that aims at reducing computational cost on proposals that are most likely rejected after the fine-scale simulation. The detailed algorithm has been described in [287] for recovering resistor values in a electrical network, and for characterization of subsurface in [292]. We explain the main idea of the algorithm in the context of our problem of interest. We introduce a screening process to compare the measured production curves against inexpensive simulated production curves obtained on a coarse-grid. In the coarse-grid simulation we solve the equations (1) and (2) on the coarse-grid whose discretization is done in a similar fashion as in the fine-scale simulation. For the coarse-grid simulation we need to know the permeability and porosity distributions on the coarse-grid. However, we have the distributions of permeability and porosity on the fine-grid. Therefore, the permeability and porosity information should carefully be transferred on the coarse-grid. For transferring the information, we use an upscaling procedure such that effective permeability and porosity fields on the coarse-grid produce a similar average response as that of the fine-grid problem locally. As described in [291, 300] we find the effective permeability on the coarse-grid cells. We then solve (1) on the coarse-grid with $\bar{k}$ replacing k to get the upscaled Darcy's velocity. In a similar way, we solve (2) on the coarse-grid with an upscaled porosity computed as the arithmetic average over each coarse-grid cell. See Algorithm 2.

Algorithm 2 Two-stage MCMC

Given the covariance function R, generate KLE parametrization $\{\lambda_n, \varphi_n\}_{n=1}^{N}$

Set initial state $\boldsymbol{\psi}_0 = (\boldsymbol{\theta}_0^k, \boldsymbol{\theta}_0^\phi)$

for $j = 1$ to M_{mcmc}

(1) At $\boldsymbol{\psi}_{j-1}$, generate $\boldsymbol{\psi} = [\boldsymbol{\theta}^k \ \boldsymbol{\theta}^\phi]$ from $q(\boldsymbol{\psi} \mid \boldsymbol{\psi}_{j-1})$

(2) With $\boldsymbol{\psi}$, compute k and ϕ using KLE and solve the forward problem on the coarse-scale to get $F_{\boldsymbol{\psi}}^c$

(3) Accept $\boldsymbol{\psi}$ with probability

$$\alpha_c(\boldsymbol{\psi}_{j-1}, \boldsymbol{\psi}) = \min\left(1, \frac{q(\boldsymbol{\psi}_{j-1} \mid \boldsymbol{\psi}) P_c(\boldsymbol{\psi} \mid F_m)}{q(\boldsymbol{\psi} \mid \boldsymbol{\psi}_{j-1}) P_c(\boldsymbol{\psi}_{j-1} \mid F_m)}\right)$$

(4) If $\boldsymbol{\psi}$ is rejected, go back to (1), else use $\boldsymbol{\psi}$ in the fine-scale simulation to get $F_{\boldsymbol{\psi}}^f$

(5) Take $\boldsymbol{\psi}$ with probability

$$\Pr = \alpha_f(\boldsymbol{\psi}_{j-1}, \boldsymbol{\psi}) = \min\left(1, \frac{P_f(\boldsymbol{\psi} \mid F_m) P_c(\boldsymbol{\psi}_{j-1} \mid F_m)}{P_f(\boldsymbol{\psi}_{j-1} \mid F_m) P_c(\boldsymbol{\psi} \mid F_m)}\right),$$

i.e., $\boldsymbol{\psi}_j = \boldsymbol{\psi}$ with probability $\Pr$ or $\boldsymbol{\psi}_j = \boldsymbol{\psi}_{j-1}$ with probability $1 - \Pr$

end for

3 Development of the multi-physics Markov chain Monte Carlo method (MP-MCMC)

In this section we develop a new effective algorithm for the characterization of the subsurface. For the discussion below we focus on multiphase flows in rigid porous media and that take advantage of the fact that fluid flow problems in porous media with increasing complexity share the same coefficients (e.g., permeability and porosity fields) in the governing systems of partial differential equations. The overall framework would also be applicable to multiphase flows coupled with geomechanical rock deformation that will be addressed elsewhere. Typical characterization procedures of reservoir engineering (such as tracer tests) are combined in a multi-stage, multi-physics Bayesian framework that reduces drastically the computational cost of the classical Metropolis-Hastings MCMC algorithms when applied to porous media flow problems. Distinct applications might need different combination of preconditioners such that the available data is properly used to inform the simulation models. Consider, as an example, the injection of CO_2 in a deep saline aquifer. One may have only one injection well along with a few monitoring wells. This is a situation where one could try several huff puff procedures, with tracers and other fluids with several viscosities. Each huff puff procedure would generate a production curve of the injected fluid that could be used in a preconditioning step in conjunction with saturation measurements at monitoring wells.

We now discuss an algorithm for MP-MCMCs. The algorithm takes into account a family (N_d) of physically-based auxiliary flow problems, production data and posterior distributions. We denote the

flow problems, production data, and posterior distributions by $\{FP_i^*\}_{i=1}^{N_d}$, $\{F_{m,i}^*\}_{i=1}^{N_d}$, and $\{\pi_i^*(\psi \mid F_{m,i}^*)\}_{i=1}^{N_d}$, respectively. In the algorithm $Q_i(\cdot|\cdot)$ is an effective instrumental distribution.

Algorighm 3 Multi-physics MCMC

for $j=1$ to M_{mcmc}

(A) At state ψ_j, generate a trial ψ_0^t from $Q_0(\psi_0^t \mid \psi_j) = q(\psi_0^t \mid \psi_j)$

for $i=1$ to N_d

(1) With ψ_{i-1}^t, solve the forward problem FP_i^* to get F_i^*

(2) Within stage i take

$$\psi_i^t = \begin{cases} \psi_{i-1}^t \text{ with probability } \alpha_i \\ \psi_j \text{ with probability } 1-\alpha_i \end{cases}$$

$$\alpha_i = \min\left(1, \frac{Q_{i-1}(\psi_j \mid \psi_{i-1}^t)\pi_i^*(\psi_{i-1}^t \mid F_{m,i}^*)}{Q_{i-1}(\psi_{i-1}^t \mid \psi_j)\pi_i^*(\psi_j \mid F_{m,i}^*)}\right)$$

(3) If

$$\psi_i^t = \begin{cases} \psi_{i-1}^t \text{ go to } i=i+1 (B) \text{ if } i < N_d \ (i = N_d) \\ \psi_j \text{ go back to (A)} \end{cases}$$

end for

(B) With ψ_0^t, solve the fine grid forward problem to get F_f

(C) Accept ψ_0^t with probability

$$\alpha_f = \min\left(1, \frac{Q_{N_d}(\psi_j \mid \psi_0^t)P(\psi \mid F_m)}{Q_{N_d}(\psi_0^t \mid \psi_j)P(\psi_j \mid F_m)}\right)$$

end for

For $i=1,\cdots,N_d$

$$\begin{aligned} Q_i(\psi_i^t \mid \psi_j) &= \alpha_i(\psi_j, \psi_i^t)Q_{i-1}(\psi_i^t \mid \psi_j) \\ &\quad + (1 - \int \alpha_i(\psi_j, \psi_i^t)Q_{i-1}(\psi_i^t \mid \psi_j)d\psi_i^t)\delta_{\psi_j}(\psi_i^t). \end{aligned}$$

It can be shown that

$$Q_i(\psi_j \mid \psi_i^t) = \frac{\pi_i^*(\psi_j \mid F_{m,i}^*)}{\pi_i^*(\psi_i^t \mid F_{m,i}^*)} Q_i(\psi_i^t \mid \psi_j). \tag{14}$$

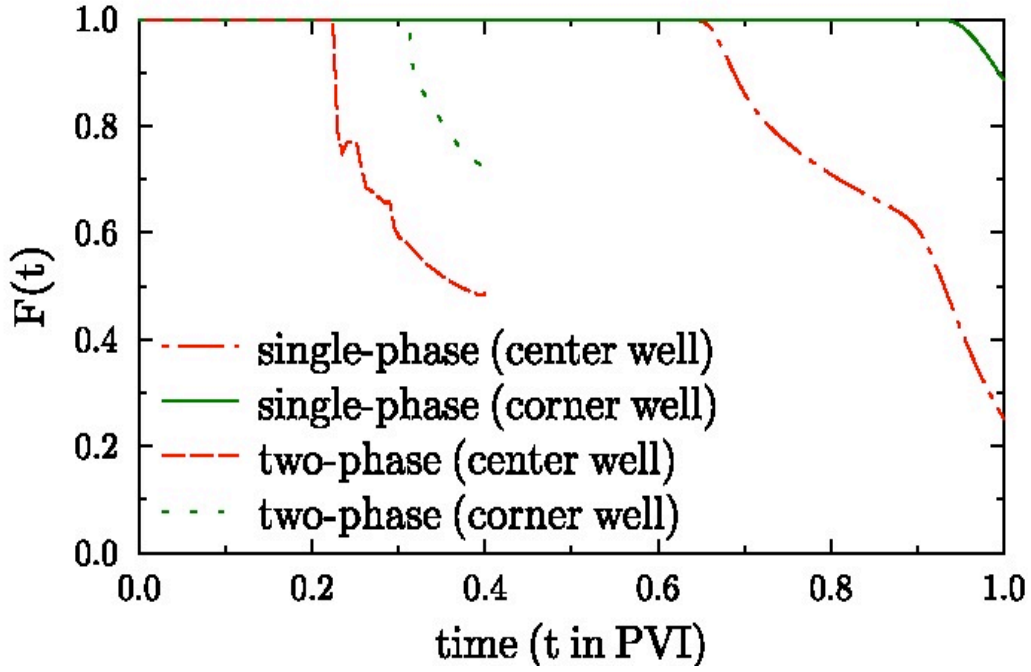

Figure 3: Synthetic measured data for single- and two-phase flows

Results and Discussion

4 Simulation studies

As an indication of the feasibility of our proposed developments we present numerical results of single- and multi-physics MCMCs. We inject tracer or water in a reservoir with the well configuration described in Fig. 1. If the injected fluid is tracer, we will have a single-phase flow problem. We will have a two-phase flow problem if we inject water. For our simulation study we have measured tracer data until 1.0 PVI and measured oil production until 0.4 PVI. See Figure 3. These $F(t)$ curves were obtained by running the flow simulator on the reference field. In the following discussion we refer the standard Metropolis-Hastings MCMC algorithm as single-stage MCMC and we abbreviate this as SMCMC.

We now consider the following two cases for multi-stage, single-physics MCMCs. For these MCMCs we use a two-phase flow model with measured data until 0.4 PVI. The first case SP-2S denotes the two-stage MCMC, where we use a grid of 32×32 for filtering. In the second case SP-3S we have two coarse-grids 32×32 and 64×64 for filtering. In Table 1 we show results for these single-physics MCMCs. Clearly by adding an extra computationally relatively inexpensive level to the two-stage procedure described above a considerable increase in the acceptance rates is observed.

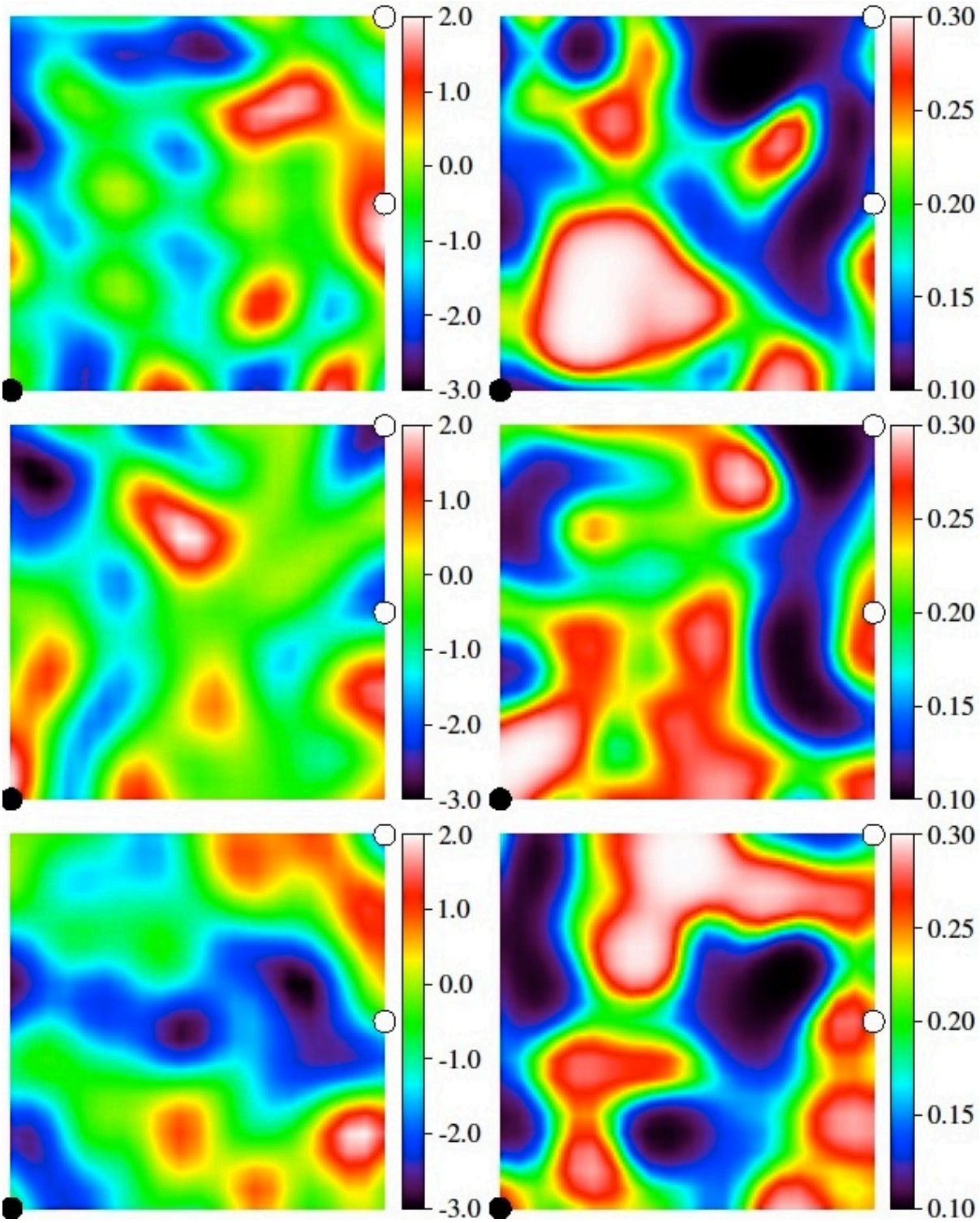

Figure 4: A set of accepted fields for single-physics MCMCs: Permeability (in logarithmic scale) and porosity distribution on the left and right, respectively. Closed and open circles denote the location of injection and production wells, respectively. Top to bottom, SMCMC, SP-2S, and SP-3S were used for characterization, respectively.

Next we consider multi-stage, two physics MCMCs. In the MCMCs, we use tracer data until 1.0 PVI for preconditioning with two-phase flow being the problem of interest. Here we consider three cases. In the first case MP-1P2P we use tracer flow until 1.0 PVI on a 32×32 grid as the filtering step. MP-1P1P2P denotes a three-stage multi-physics MCMC with tracer flow until 1.0 PVI on 32×32 and 128×128 grids for screening out proposals. In the third case MP-1P2P2P we use tracer flow until 1.0 PVI for the first stage on a grid 32×32, and two-phase flow until 0.4 PVI for the second stage on the same grid 32×32. In all the cases we run two-phase simulation on a fine-grid of 128×128 in the final stage. Again, computationally very inexpensive filtering stages based on tracer tests (that require only one elliptic solution) are quite efficient as they produce acceptance rates comparable to those of more expensive upscaled two-phase filtering stages (see Table 2).

Table 1: A comparison of accepted proposals out of 20000 proposals for single physics MCMCs

		no. of acc. proposals and acc. rate		
grid	σ_F^2	SMCMC	SP-2S	SP-3S
32×32	8×10^{-4}	—	8304 (42%)	8762 (44%)
64×64	4×10^{-4}	—	—	5978 (68%)
128×128	1×10^{-4}	4026 (20%)	3373 (41%)	3212 (54%)

Table 2: A comparison of accepted proposals out of 20000 proposals for multi-physics MCMCs

		no. of acc. proposals and acc. rate		
grid	σ_F^2	MP-1P2P	MP-1P1P2P	MP-1P2P2P
32×32 (tracer)	8×10^{-4}	—	9037 (45%)	10151 (51%)
32×32 (2-phase)	4×10^{-4}	—	—	6494 (64%)
128×128 (tracer)	4×10^{-4}	9107 (46%)	7065 (78%)	—
128×128 (2-phase)	1×10^{-4}	3033 (33%)	2251 (32%)	2607 (40%)

Now we discuss single- and multi-physics MCMCs for prediction. A set of accepted fields collected in Bayesian framework using single-physics MCMCs and multi-physics MCMCs is shown in Figure 4 and Figure 5, respectively. We run the numerical simulator until 1.4 PVI to produce the rest of production curves for each accepted field. We then take an average of the production curves and we refer the average as the prediction. As shown in Figure 6 the predictions using standard MCMC and multi-physics MCMCs are more reliable than the predictions using single-physics MCMCs. However, the standard MCMC is computationally more expensive than multi-physics MCMCs. It highlights that multi-physics MCMCs are as reliable as the standard MCMC, but computationally better than the standard MCMC.

Next we consider the case where we use the huff puff technique as a screening step in the Bayesian framework used. The huff puff procedure consists of injecting and producing the same contaminant fluid for a very small amount of time. This strategy enables us to know the characteristics of the sample near the injection wells at each realization. The first huff puff stage takes place in the injection well in Fig. 1, and the second huff puff stage occurs on the two production wells of the boundary in Fig. 1

simultaneously. If the candidate profile is accepted in the second stage as well, then we run the third stage in the fine grid.

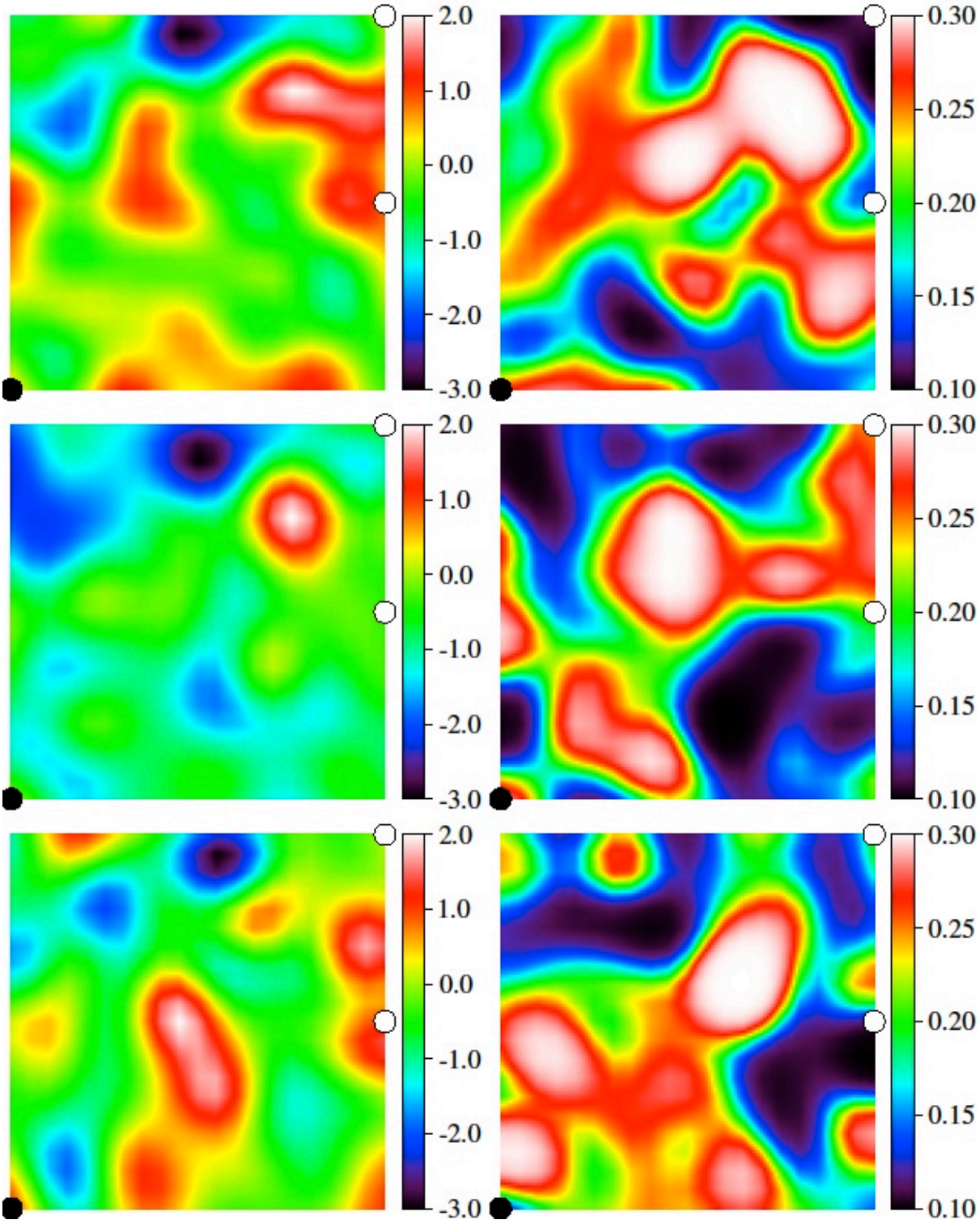

Figure 5: A set of accepted fields for multi-physics MCMCs: Permeability (in logarithmic scale) and porosity distribution on the left and right, respectively. Closed and open circles denote the location of injection and production wells, respectively. Top to bottom, MP-1P2P, MP-1P1P2P, and MP-1P2P2P were used for characterization, respectively.

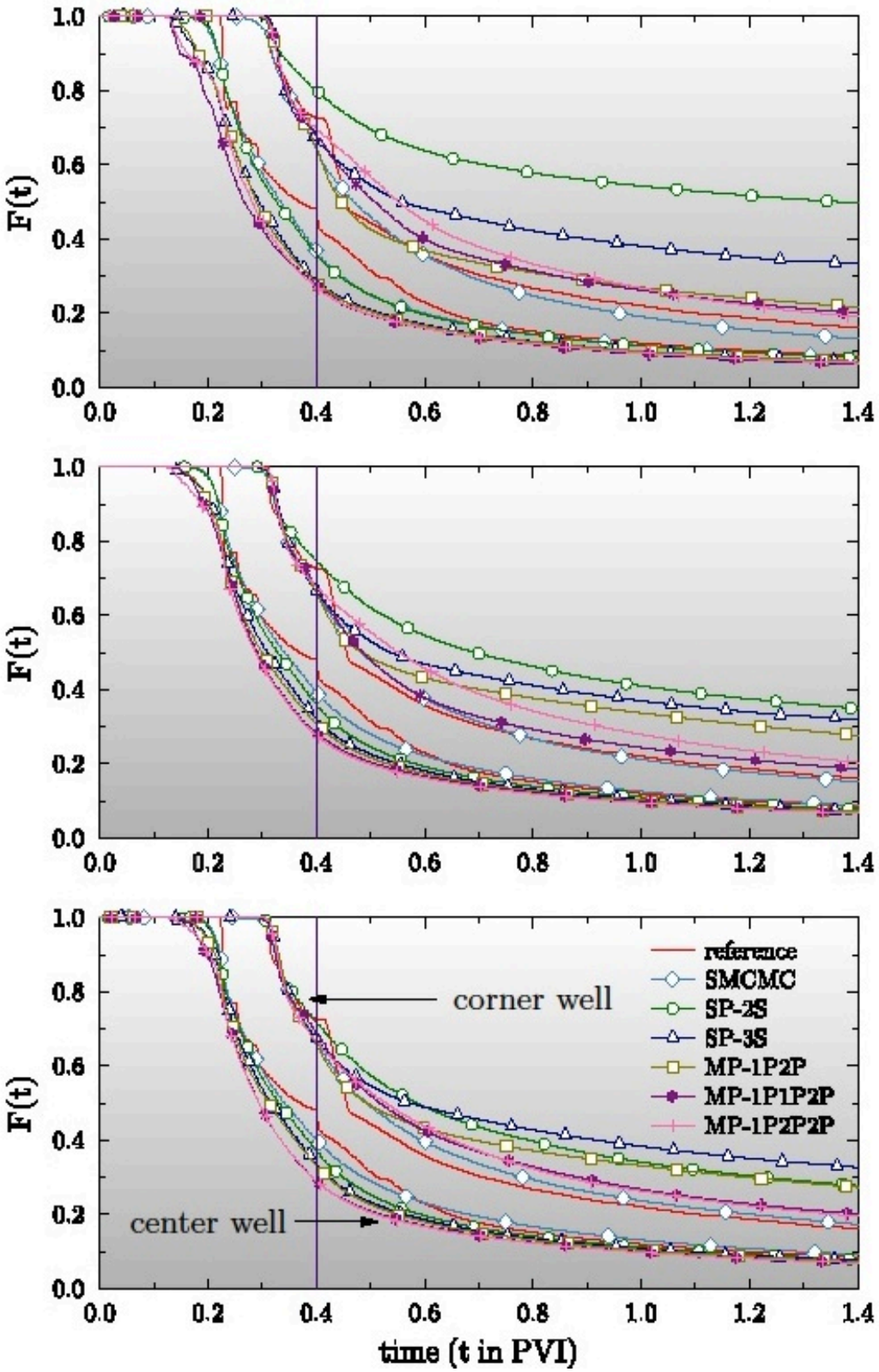

Figure 6: Prediction using single- and multi-physics MCMCs: Vertical line separates measurement and prediction data. Top to bottom 4000, 8000, and 12000 proposals were used for prediction, respectively.

Taking into account of burn-in period, 10% of accepted proposals were discarded in prediction.
To ensure computational efficiency we aim to get high acceptance rates but with the production curves of the huff puff being as small as possible, so we concentrate our studies for the case in which the huff puff production time is $T_{hp} = 0.025$ PVI. After the two huff puff stages, the third stage have measured tracer data until 1.0 PVI. In Table 3 we compare the acceptance rates for different precision parameters on first stage, $\sigma^2_{hp1} = 5\times10^{-7}$ against $\sigma^2_{hp1} = 1\times10^{-7}$.

Table 3: A comparison of accepted proposals for different press ion parameters $\sigma^2_{hp_1}$, with a huff puff production time of $T_{hp} = 0.025$. Here we have 25000 MCMCs and $\sigma^2 = 1\times10^{-4}$.

		no. of acc. proposals and acc. rate		
$\sigma^2_{hp_1}$	$\sigma^2_{hp_2}$	huff puff 1	huff puff 2	stage 3
1×10^{-7}	1×10^{-7}	13252 (53%)	7652 (57%)	2110 (27%)
5×10^{-7}	1×10^{-7}	16248 (64%)	3535 (21%)	1155 (32%)

Next we consider the application of the Multi-Physics Markov Chain Monte Carlo Method to a CO_2 injection study. We take a fine grid of size 128 vs. 128 in a computational region with one injection well at the bottom left corner (we inject supercritical CO_2 at a rate of one pore volume every six years), one production well at the upper right corner, and four monitoring wells. The problem setup is shown in Figure 7. The CO_2 injection period is one year (almost 0.17 PVI) before breakthrough. We apply a two-stage procedure, such that for the up-scaled simulation we use a coarse mesh with size 64 vs. 64. The effect of the up-scaling procedure on the saturation of CO_2 can be seen in Figure 8. In this Figure the grid is coarsened by a factor of 2 in each direction as we move from left to right and from top to bottom.

The results for a two-stage procedure aiming at speeding up the Markov Chain Monte Carlo calculation are shown in Table 4.

Table 4: The two-stage MCMC applied to a CO_2 injection project.

MCMC	proposals	HuffPuff	Upscaled	Forward	rate
single-stage	4066	-	-	385	9.47%
two-stages	8712	-	3995	734	18.37%

Note that almost half of the proposals were rejected by the up-scaling filter, indicating the effectiveness of the procedure. As indicated above other procedures may be designed, depending of the physical problem at hand, as well as the availability of monitoring wells.

The results reported above are currently being prepared to be submitted for publication in the in the form two manuscripts. The first one will present the multi-physics, multi-stage procedure developed under this task. The other one will be dedicated to the application of this new framework for aquifer characterization in CO_2 storage problems at the field scale.

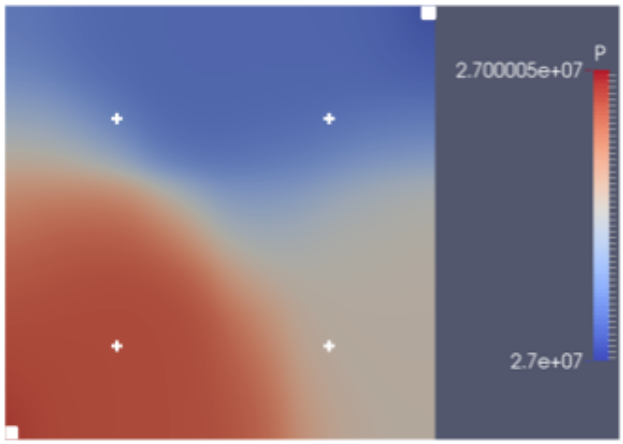

Figure 7: Problem setup for a CO_2 injection study.

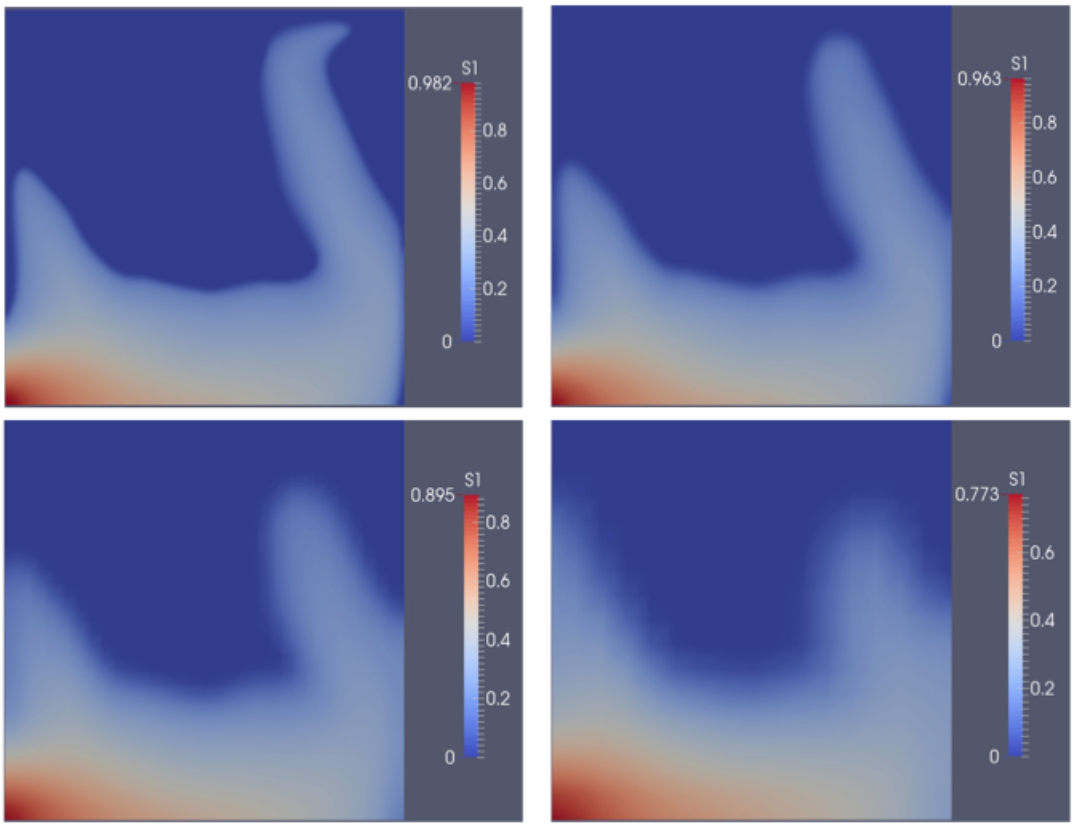

Figure 8: The effect of the up-scaling of the permeability field on the saturation of the injected CO_2.

Conclusions

We developed computationally fast and effective methods of generating MCMC chains in a Bayesian framework for subsurface characterization. We constructed a family of computationally inexpensive preconditioners based on simpler physics and we drastically reduced the number of fine-grid simulations in proposed multi-physics MCMCs.

We considered prediction in an oil reservoir to assess the quality of the proposed MCMCs. We used a two-phase flow model to describe the movement of fluid in porous media. In subsurface characterization we explored samples in single- and multi-physics MCMCs in a Bayesian framework to collect probable candidates for the underlying subsurface. In the characterization the MCMC algorithm accepts or rejects fields conditioned to measured partial oil production curves. In the multi-physics MCMCs we used tracer (single-phase) flow model on coarse-grids to screen out proposals before running expensive fine-grid, two-phase flow simulations. The accepted fields in the characterization step were used to simulate the rest of production curves. By aggregating the rest of simulated production curves we predicted the production in each MCMC. Standard Metropolis-Hastings MCMC and multi-physics MCMCs were more reliable than single-physics MCMCs in the problem we considered. However, the standard MCMC is computationally more expensive than the multi-physics MCMCs. It indicates that the multi-physics MCMCs are efficient and effective for subsurface characterization and prediction of porous media flows.

GRAPHICAL MATERIALS LIST(S)

Task 2: Measurement of mixed scCO2/brine steady-state drainage and imbibition relative permeabilities in samples from the RSU at reservoir condition.

REFERENCES

1) Span R, Wagner W. A new equation of state for carbon dioxide covering the fluid region from the triple-point temperature to 1100 K at pressure up to 800 MPa. J Phys Chem Ref Data 1996;25(6):1509–96.
2) Batzle M, Zhijing W. Seismic properties of pore fluids. Geophysics 1992;57(11):1396–408.
3) Michels A, Botzen A, Schuurman W. The viscosity of carbon dioxide between 0°C and 75°C and at pressure up to 2000 atmospheres. Physica 1957;23(1-5):95–102.
4) Bachu S, Bennion B. Interfacial tension between CO2, freshwater, and brine in the range of pressure from (2 to 27) MPa, temperature from (20 to 125)°C, and water salinity from (0 to 334000) mg.L_1. J Chem Eng Data 2009;54:765–75.
5) Piri M. Recirculating. Constant back pressure core flooding apparatus and method. W02012/082797 A1, July, 2012.
6) Lake LW. Enhanced oil recovery. New Jersey: Prentice Hall; 1989.
7) Saraji S, Lamia G, Piri M. Wettability in CO2/brine/quartz systems: an experimental study at reservoir conditions. In: SPE 160208, prepared for presentation at the SPE annual technical conference and exhibition, San Antonio, Texas; 8–10 October, 2012.
8) Spiteri EJ, Juanes R, Blunt MJ, Orr FM Jr. A new model of trapping and relative permeability hysteresis for all wettability characteristics. SPE J 2008;13(3):277-88.
9) Pentland CH, El-Maghraby R, Iglauer S, Blunt MJ. Measurements of the capillary trapping of supercritical carbon dioxide in Berea sandstone. Geophys Res Lett 2011;38:L06401.
10) Mason G, Morrow NR. Capillary behavior of a perfectly wetting liquid in irregular triangular tubes. J Coll Interf Sci 1991;144(1):262–74.
11) Piri M, Blunt MJ. Three-dimensional mixed-wet random pore-scale network modeling of two- and three-phase flow in porous media. II. Results. Phys Rev E 2005;71(2):026302:1–026302:11.
12) Duan Z, Sun R. An improved model calculating CO2 solubility in pure water and aqueous NaCl solutions from 273 to 533 K and from 0 to 2000 bar. Chem Geol 2003;193:257–71.
13) Oak MJ. Three-phase relative permeability of water-wet Berea. In: SPE 20183, proceedings of the SPE/DOE seventh symposium on enhanced oil recovery, Tulsa, Oklahoma, 22–25 April, 1990.
14) Oak MJ, Baker LE, Thomas DC. Three-phase relative permeability of Berea sandstone. J Pet Technol 1990;42(8):1054–61.
15) Campbel-Stone Erin, Raine Lynds, Carol Frost, Thomas P. Becker, Bridget Diem, The Wyoming carbon underground storage project: Geologic characterization of Moxa Arch and Rock Springs Uplift, Energ. Procedia 2011;4:4656-663.
16) Span R, Wagner W. A new equation of state for carbon dioxide covering the fluid region from the triple-point temperature to 1100 K at pressure up to 800 MPa, J. Phys. Chem. Ref. Data 1996;25(6):1509-96.
17) Ihmels EC, Lemmon EW, Gmehling J. An equation of state and compressed liquid and supercritical densities for sulfur dioxide, Fluid Phase Equilib. 2003;207:111-30.
18) Miller PJ, Atten CV, Bradley MJ. North American Power Plant Air Emissions, Commission for Environmental Cooperation of North America, 2004.
19) Lloyd Evan. North American Power Plant Air Emissions, Comission for Environmental Cooperation of North America, 2011.
20) Reddy KJ, Weber H, Bhattacharyya P, Argyle M, Taylor D, Christensen M, Foulke T, Fahlsing P. Instantaneous capture and mineralization of flue gas carbon dioxide: Pilot scale study, Nature Precedings 2010,doi:10.1038/npre.2010.5404.1.
21) Sayegh SG, Najman J. CO2-SO2-brine phase behavior studies, Petroleum Recovery Institute, Alberta Department of Energy Library Services, 1984.

22) Tan SP, Yao Y, Piri M. A PC-SAFT/PMSA model for the solubility of SO2+ CO2mixtures in brine at elevated pressures and temperatures, Ind. Eng. Che. Res. 2013;52:10864-72.
23) Bachu S, Bennion B. Interfacial tension between CO2, freshwater, and brine in the range of pressure from (2 to 27) MPa, temperature from (20 to 125)°C, and water salinity from (0 to 334000) mg.L-1, J. Chem. Eng. Data 2009;54:765-75.
24) Batzle M, Zhijing W. Seismic properties of pore fluids, Geophysics 1992;57(11):1396-408.
25) Chiquet P, Draidon J-L, Broseta D, Thibeau S. CO2/water interfacial tension under pressure and temperature conditions of CO2 geological storage, Energy Convers. Manage. 2007;48:736-44.
26) Saraji S, Goual L, Piri M, Plancher H. Wettability of sc-CO2/brine/quartz systems: Simultaneous measurement of contact angle and interfacial tension at reservoir conditions, Langmuir 2013;29(23):6856-66,doi:10.1021/la3050863.
27) Saraji S, Piri M, Goual L. The effect of brine salinity, SO2 contamination, pressure, and temperature on contact angle and interfacial tension of sc-CO2/brine/quartz systems, Under review in Int. J. Greenh. Gas Con. 2014.
28) Fenghour A, Wakeham WA, Vesovic V. The viscosity of the carbon dioxide, J. Phys. Che. Ref. Data 1998;27(1):31-44, doi:10.1021/la3050863.
29) Piri M. Recirculating. Constant back pressure core flooding apparatus and method. US2012/0211089 A1, August, 2012.
30) Akbarabadi M, Piri M. Relative permeability hysteresis and capillary trapping characteristics of supercritical CO2/brine system: An experimental study at reservoir conditions, Adv. Water Resour. 2013;52:190-206.
31) Anderson WG. Wettability literature survey-Part 4: Effects of wettability on capillary pressure, J. Petrol. Technol. 1987;39(10):1283-300.
32) Spiteri EJ, Juanes R, Blunt MJ, Orr Jr FM. A new model of trapping and relative permeability hysteresis for all wettability characteristics, SPE J. 2008;13(3):277-88.
33) Land CS. Calculation of imbibition relative permeability for two- and three-phase flow from rock properties, SPE J. 1968;8:149-56.
34) Pini R, Krevor SCM, Benson SM. Capillary pressure and heterogeneity for the CO2/water system in sandstone rocks at reservoir conditions, Adv. Water Resour. 2012;38:48-59.
35) Nogueira M, Mamora DD. Effect of flue gas impurities on the process of injection and storage of CO2 in depleted gas reservoirs, J. Energ. Resour. Technol. 2008;30:2339-53.
36) Bachu S, Bennion B. Effects of in-situ conditions on relative permeability characteristics of CO2-brine systems, Environ. Geol. 2008;54:1707-22.
37) Bennion B, Bachu S. Drainage and imbibition relative permeability relationships for supercritical CO2/brine and H2S/Brine systems in intergranular sandstone, carbonate, shale and anhydrite rocks, SPE Resev. Eval. Eng. 2008;11(3):487-96.
38) Okabe H, Tsuchiya Y. Experimental investigation of residual CO2 saturation distribution in carbonate rocks, International symposium of the Society of the Core Analysts in Abu Dhabi, 29 October- 2 November, 2008.
39) El-Maghraby RM, Blunt MJ. Residual CO2 trapping in Indiana limestone, Environ. Sci. Tech. 2013;2(1):58-64.
40) Bennion B, Bachu S. Relative permeability characteristics for supercritical CO2 displacing water in a variety of potential sequestration zones in western Canada sedimentary basin, SPE 95547 ;Presented at the SPE technical conference and Exhibition, Dallas, TX, 9-12 Oct.2005, DOI:10.2118/95547-MS.
41) Perrin JC, Krause M, Kuo CW, Milijkovic L, Charoba E, Benson SM. Core-scale experimental study of relative permeability properties of CO2 and brine in reservoir rocks, Energy Procedia 2009;1:3515-22.
42) Krevor SCM, Pini R, Li B, Benson SM. Capillary heterogeneity trapping of CO2 in a sandstone rock at reservoir condition, Geophys. Res. Lett. 2011;38:L15401.

43) Krevor SCM, Pini R, Zou L, Benson SM. Relative permeability and trapping of CO2 and water in sandstone rocks at reservoir conditions, Water Resour. Res. 2012;48:W02532, doi:10:1029/2011WR010859.
44) Bennion B, Bachu S. Drainage and imbibition CO2/brine relative permeability curves at reservoir conditions for carbonate formations; In proceedings of the SPE Annual Technical Conference and Exhibition, Florence, Italy, September 19-22, 2010.
45) Oak MJ, Baker LE, Thomas DC. Three-phase relative permeability of Berea sandstone, J. Pet. Technol. 1990;42(8):1054-61.
46) Benson S, Pini R, Reynolds C, Krevor S. Relative permeability analysis to describe multi-phase flow in CO2 storage reservoirs, Global CCS Institute Targeted Report No. 2, 2013.
47) Leas WJ. Relative permeability to gas, Transactions of the American Institute of Mining and Metallurgical and Petroleum Engineers 1950;189:65-72.
48) Ramakrishnan T, Capiello A. A new technique to measure static and dynamic properties of a partially saturated porous medium, Chem. Eng. Sci. 1991;16(4):1157-63.
49) Pini R, Benson SM. Simultaneous determination of capillary pressure and relative permeability curves from core-flooding experiments with various fluid pairs, Water Resour. Res. 2013;49:3516-30, doi:10.1002/wrcr.20274.
50) Chiquet P, Broseta D, Thibeau S. Wettability alteration of caprock minerals by carbon dioxide, Geofluids 2007;7:112-22.
51) Chalbaud C, Robin M, Lombard J-M, Martin F, Egermann P, Bertin H. Interfacial tension measurements and wettability evaluation for geological CO2 storage, Adv. Water Resour. 2009;32:98-109.
52) Be A. (2011), Multiphase Flow in Porous Media with Emphasis on CO2 Sequestration, PhD Dissertation, University of Bergen, Norway.
53) P. Chiquet, D. Broseta, and S. Thibeau, "Wettability alteration of caprock minerals by carbon dioxide," Geofluids, vol. 7, no. 2, pp. 112–122, May 2007.
54) D. N. Espinoza and J. C. Santamarina, "Water-CO2 -mineral systems: Interfacial tension, contact angle, and diffusion-Implications to CO2 geological storage," Water Resour. Res., vol. 46, no. 7, p. W07537, Jul. 2010.
55) P. K. Bikkina, "Contact angle measurements of CO2–water–quartz/calcite systems in the perspective of carbon sequestration," Int. J. Greenh. Gas Control, vol. 5, no. 5, pp. 1259–1271, Sep. 2011.
56) C. Chalbaud, M. Robin, J.-M. Lombard, F. Martin, P. Egermann, and H. Bertin, "Interfacial tension measurements and wettability evaluation for geological CO2 storage," Adv. Water Resour., vol. 32, no. 1, pp. 98–109, Jan. 2009.
57) J. L. Dickson, G. Gupta, T. S. Horozov, B. P. Binks, and K. P. Johnston, "Wetting phenomena at the CO2/water/glass interface.," Langmuir, vol. 22, no. 5, pp. 2161–70, Feb. 2006.
58) D. Yang, Y. Gu, and P. Tontiwachwuthikul, "Wettability determination of the reservoir brine - reservoir rock system with dissolution of CO2 at high pressures and elevated temperatures," Energy & Fuels, no. 22, pp. 504–509, 2008.
59) Y. Sutjiadi-Sia, P. Jaeger, and R. Eggers, "Interfacial tension of solid materials against dense carbon dioxide," J. Colloid Interface Sci., vol. 320, pp. 268–274, 2008.
60) S. Wang, I. M. Edwards, and A. F. Clarens, "Wettability phenomena at the CO2-brine-mineral interface: implications for geologic carbon sequestration.," Environ. Sci. Technol., vol. 47, no. 1, pp. 234–41, Jan. 2013.
61) W. Plug, H. E. P. B. V, S. Mazumder, and J. Bruining, "Capillary Pressure and Wettability Behavior of CO 2 Sequestration in Coal at Elevated Pressures," SPE J., pp. 455–464, 2008.
62) W.-J. Plug and J. Bruining, "Capillary pressure for the sand–CO2–water system under various pressure conditions. Application to CO2 sequestration," Adv. Water Resour., vol. 30, no. 11, pp. 2339–2353, Nov. 2007.

63) Y. Kim, J. Wan, T. J. Kneafsey, and T. K. Tokunaga, "Dewetting of silica surfaces upon reactions with supercritical CO2 and brine: pore-scale studies in micromodels.," Environ. Sci. Technol., vol. 46, no. 7, pp. 4228–35, Apr. 2012.
64) J. Jung and J. Wan, "Supercritical CO2 and ionic strength effects on wettability of silica surfaces : equilibrium contact angle measurements," Energy and Fuels, no. 26, pp. 6053–6059, 2012.
65) R. Farokhpoor, B. J. a. Bjørkvik, E. Lindeberg, and O. Torsæter, "Wettability behaviour of CO2 at storage conditions," Int. J. Greenh. Gas Control, vol. 12, pp. 18–25, Jan. 2013.
66) D. Broseta, N. Tonnet, and V. Shah, "Are rocks still water-wet in the presence of dense CO2 or H2S?," Geofluids, vol. 12, no. 4, pp. 280–294, Nov. 2012.
67) K. Michael, a. Golab, V. Shulakova, J. Ennis-King, G. Allinson, S. Sharma, and T. Aiken, "Geological storage of CO2 in saline aquifers—A review of the experience from existing storage operations," Int. J. Greenh. Gas Control, vol. 4, no. 4, pp. 659–667, Jul. 2010.
68) E. J. Wilson, T. L. Johnson, and D. W. Keith, "Regulating the ultimate sink: managing the risks of geologic CO2 storage.," Environ. Sci. Technol., vol. 37, no. 16, pp. 3476–83, Aug. 2003.
69) T. K. Tokunaga and J. Wan, "Capillary pressure and mineral wettability influences on reservoir CO2 capacity," Rev. Mineral. Geochemistry, vol. 77, no. 1, pp. 481–503, Nov. 2013.
70) S. Wang, Z. Tao, S. M. Persily, and A. F. Clarens, "CO2 adhesion on hydrated mineral surfaces.," Environ. Sci. Technol., vol. 47, no. 20, pp. 11858–65, Oct. 2013.
71) J. Mccaughan, S. Iglauer, and F. Bresme, "Molecular dynamics simulation of water/ CO2-quartz interfacial properties : application to subsurface gas injection," Energy Procedia, vol. 37, pp. 5387–5402, 2013.
72) S. Iglauer, M. S. Mathew, and F. Bresme, "Molecular dynamics computations of brine– CO2 interfacial tensions and brine–CO2–quartz contact angles and their effects on structural and residual trapping mechanisms in carbon geo-sequestration," J. Colloid Interface Sci., no. 386, pp. 405–414, 2012.
73) C. M. Tenney and R. T. Cygan, "Molecular simulation of carbon dioxide, brine, and clay mineral interactions and determination of contact angles.," Environ. Sci. Technol., vol. 48, no. 3, pp. 2035–42, Feb. 2014.
74) P. Chiquet, J.-L. Daridon, D. Broseta, and S. Thibeau, "CO2/water interfacial tensions under pressure and temperature conditions of CO2 geological storage," Energy Convers. Manag., vol. 48, no. 3, pp. 736–744, Mar. 2007.
75) V. Shah, D. Broseta, G. Mouronval, and F. Montel, "Water/acid gas interfacial tensions and their impact on acid gas geological storage," Int. J. Greenh. Gas Control, vol. 2, no. 4, pp. 594–604, Oct. 2008.
76) P. J. Miller and C. Van Atten, "North American Power Plant Emissions," 2004.
77) J. Mahadevan, "Comments on the paper titled 'Contact angle measurements of CO2–water-quartz/calcite systems in the perspective of carbon sequestration': A case of contamination?," Int. J. Greenh. Gas Control, vol. 7, pp. 261–262, Mar. 2012.
78) D. N. Espinoza and J. C. Santamarina, "Water-CO2 -mineral systems: Interfacial tension, contact angle, and diffusion-Implications to CO 2 geological storage," Water Resour. Res., vol. 46, no. 7, p. n/a–n/a, Jul. 2010.
79) A. W. Neumann, Applied Surface Thermodynamics, 2nd ed. CRC Press, 2011, p. 743.
80) S. Bachu, "Screening and ranking of sedimentary basins for sequestration of CO2 in geological media in response to climate change," Environ. Geol., vol. 44, no. 3, pp. 277–289, Jun. 2003.
81) S. Saraji, L. Goual, M. Piri, and H. Plancher, "Wettability of supercritical carbon dioxide/water/quartz systems: simultaneous measurement of contact angle and interfacial tension at reservoir conditions.," Langmuir, vol. 29, no. 23, pp. 6856–66, Jun. 2013.
82) S. Iglauer, A. Salamah, M. Sarmadivaleh, K. Liu, and C. Phan, "Contamination of silica surfaces: Impact on water–CO2–quartz and glass contact angle measurements," Int. J. Greenh. Gas Control, vol. 22, pp. 325–328, Mar. 2014.

83) P. K. Bikkina, "Contact angle measurements of CO2–water–quartz/calcite systems in the perspective of carbon sequestration," Int. J. Greenh. Gas Control, vol. 5, no. 5, pp. 1259–1271, Sep. 2011.
84) J. Mills, M. Riazi, and M. Sohrabi, "Wettability of common rock-forming minerals in a CO2-brine system at reservoir conditions," SCA2011-06, pp. 1–12, 2011.
85) H. Tavana, N. Petong, a. Hennig, K. Grundke, and a. W. Neumann, "Contact Angles and Coating Film Thickness," J. Adhes., vol. 81, no. 1, pp. 29–39, Feb. 2005.
86) A. Kalantarian, R. David, and A. W. Neumann, "Methodology for high accuracy contact angle measurement.," Langmuir, vol. 25, no. 24, pp. 14146–54, Dec. 2009.
87) J. R. Davis, ASM specialty handbook: Nickel, Cobalt, and their alloys, 2nd ed. ASM International, 2007.
88) K. K. Mohanty, "Fluids in porous media: two-phase distribution and flow," Univ. of Minnesota, 1981.
89) G. Hirasaki, "Interfacial phenomena in oil recovery," N. Morrow, Ed. Marcel Dekker Inc., 1990.
90) R. Span and W. Wagner, "A New Equation of State for Carbon Dioxide Covering the Fluid Region from the Triple-Point Temperature to 1100 K at Pressures up to 800 MPa," J. Phys. Chem. Ref. Data, vol. 25, no. 6, p. 1509, 1996.
91) A. Hebach, A. Oberhof, and N. Dahmen, "Density of water + carbon dioxide at elevated pressures: Measurements and correlation," J. Chem. Eng. Data, vol. 49, no. 4, pp. 950–953, 2004.
92) A. Hebach, A. Oberhof, N. Dahmen, A. Ko, and H. Ederer, "Interfacial Tension at Elevated Pressures s Measurements and Correlations in the Water + Carbon Dioxide System," no. 2, pp. 1540–1546, 2002.
93) P. Chiquet, D. Broseta, and S. Thibeau, "Wettability alteration of caprock minerals by carbon dioxide," Geofluids, vol. 7, no. 2, pp. 112–122, 2007.
94) J.-W. Jung and J. Wan, "Supercritical CO2 and ionic strength effects on wettability of silica surfaces: Equilibrium contact angle measurements," Energy and Fuels, vol. 26, no. 9, pp. 6053–6059, 2012.
95) A. Vishnyakov, Y. Y. Shen, and M. S. Tomassone, "Interactions of silica nanoparticles in supercritical carbon dioxide," J. Chem. Phys., vol. 129, no. 17, p. No. 174704, 2008.
96) T. K. Tokunaga, "DLVO-based estimates of adsorbed water film thicknesses in geologic CO2 reservoirs.," Langmuir, vol. 28, no. 21, pp. 8001–9, May 2012.
97) N. V Churaev, "Surface forces in wetting films," Adv. Colloid Interface Sci., vol. 103, no. 3, pp. 197–218, 2003.
98) L. Boinovich and A. Emelyanenko, "Wetting and surface forces.," Adv. Colloid Interface Sci., vol. 165, no. 2, pp. 60–9, Jul. 2011.
99) D. Koschel, J.-Y. Coxam, L. Rodier, and V. Majer, "Enthalpy and solubility data of CO2 in water and NaCl(aq) at conditions of interest for geological sequestration," Fluid Phase Equilib., vol. 247, no. 1–2, pp. 107–120, Sep. 2006.
100) S. Bachu and D. B. Bennion, "Interfacial Tension between CO2 , Freshwater , and Brine in the Range of Pressure from (2 to 27) MPa , Temperature from (20 to 12) °C, and Water Salinity from (0 to 334 000) mg· L-1," J. Chem. Eng. Data, no. 54, pp. 765–775, 2009.
101) T. L. Tarbuck and G. L. Richmond, "Adsorption and Reaction of CO2 and SO2 at a Water Surface," J. Am. Chem. Soc., no. 128, pp. 3256–3267, 2006.
102) Dullien, F. A. L. (1992), *Porous Media: Fluid Transport and Pore Structure*, 2nd ed., Academic Press, San Diego.
103) Sahimi, M. (2010), *Flow and Transport in Porous Media and Fractured Rock*, 2nd ed., Wiley-VCH, Los Angeles.
104) Koshizuka, S., H. Tamako, and Y. Oka (1995), A particle method for incompressible viscous flow with fluid fragmentation, *Computational Fluid Dynamics Journal*, *4(1)*, 2946.

105) Premoze, S., T. Tasdizen, J. Bigler, A. Lefohn, and R. Whitaker (2003), Particle-based simulation of fluids, *Computer Graphics Forum*, *22*, 3.
106) Ovaysi, S., and M. Piri (2010), Direct pore-level modeling of incompressible fluid flow in porous media, *Journal of Computational Physics*, *229*, 7456-7476.
107) Ovaysi, S., and M. Piri (2011), Pore-scale modeling of dispersion in disordered porous media, *Journal of Contaminant Hydrology*, *124*, 68-81.
108) Zhu, Y., P. J. Fox, and J. P. Morris (1999), A pore-scale numerical model for flow through porous media, *International Journal for Numerical and Analytical Methods in Geomechanics*, *23*, 881-904.
109) Tartakovsky, A., and P. Meakin (2005), A smoothed particle hydrodynamics for miscible flow in three-dimensional fractures and two-dimensional Rayleigh-Taylor instability, *Journal of Computational Physics*, *207*, 610-624.
110) Gingold, R., and J. Monaghan (1997), Smoothed particle hydrodynamics: theory and application to non-spherical stars, *Monthly Notices of the Royal Astronomical Society*, *181*, 375-389.
111) Inamuro, T., T. Ogata, S. Tajima, and N. Konishi (2004), A Lattice Boltzmann method for incompressible two-phase flows with large density differences, *Journal of Computational Physics*, *198*, 628-644.
112) Li, H., C. Pan, and C. Miller (2005), Pore-scale investigation of viscous coupling effects for two-phase flow in porous media, *Physical Review E*, *72*, 026705.
113) Fourie, W., R. Said, P. Young, and D. Barnes (2007), The simulation of pore scale fluid flow with real world geometries obtained from X-ray computed tomography, *Proceedings of the COMSOL Conference, Boston*.
114) Øren, P. E., S. Bakke, and O. J. Arntzen (1998), Extending predictive capabilities to network models, *SPE Journal*, *3(4)*, 324-336.
115) Patzek, T. W., and D. B. Silin (2001), Shape factor and hydraulic conductance in noncircular capillaries. I. One-phase creeping flow, *Journal of Colloid and Interface Science*, *236(2)*, 295-304.
116) Blunt, M. J., M. D. Jackson, M. Piri, and P. H. Valvatne (2002), Detailed physics, predictive capabilities and macroscopic consequences for pore-network models of multiphase flow, *Advances in Water Resources*, *25(8-12)*, 1069-1089.
117) Piri, M., and M. J. Blunt (2005a), Three-dimensional mixed-wet random pore-scale network modeling of two- and three-phase flow in porous media. I. Model description, *Physical Review E*, *71(026301)*, doi:10.1103/PhysRevE.71.026,301.
118) Piri, M., and M. J. Blunt (2005b), Three-dimensional mixed-wet random pore-scale network modeling of two- and three-phase flow in porous media. II. Results, *Physical Review E*, *71(026302)*, doi:10.1103/PhysRevE.71.026,302.
119) Fatt, I. (1956a), The network model of porous media I. Capillary pressure characteristics, *Transactions of the American Institute of Mining, Metallurgical, and Petroleum Engineers*, *207*, 144-159.
120) Fatt, I. (1956b), The network model of porous media II. Dynamic properties of a single size tube network, Transactions of the American Institute of Mining, Metallurgical, and Petroleum Engineers, 207, 160-163.
121) Fatt, I. (1956c), The network model of porous media III. Dynamic properties of networks with tube radius distribution, *Transactions of the American Institute of Mining, Metallurgical, and Petroleum Engineers*, *207*, 164-181.

122) Øren, P. E., and S. Bakke (2003), Reconstruction of Berea sandstone and pore-scale modelling of wettability effects, *Journal of Petroleum Science and Engineering*, *39*, 177-199.
123) Valvatne, P. H., and M. J. Blunt (2004), Predictive pore-scale modeling of two-phase flow in mixed wet media, *Water Resources Research*, *40*.
124) Mayer, R. P., and R. A. Stowe (1965), Mercury porosimetry-breakthrough pressure for penetration between packed spheres, *Journal of Colloid Science*, *20*, 893-911.
125) Princen, H. M. (1969a), Capillary phenomena in assemblies of parallel cylinders I. Capillary rise between two cylinders, *Journal of Colloid and Interface Science*, *30(1)*, 69-75.
126) Princen, H. M. (1969b), Capillary phenomena in assemblies of parallel cylinders II. Capillary rise in systems with more than two cylinders, *Journal of Colloid and Interface Science*, *30(3)*, 359-371.
127) Hui, M. H., and M. J. Blunt (2000), Effects of wettability on three-phase flow in porous media, *Journal of Physical Chemistry B*, *104(16)*, 3833-3845.
128) Amestoy, P. R., J. K. I. S. Duff, and J.-Y. L'Excellent (2001), A fully asynchronous multifrontal solver using distributed dynamic scheduling, *SIAM Journal of Matrix Analysis and Applications*, *23(1)*, 15-41.
129) Amestoy, P. R., A. Guermouche, J.-Y. L'Excellent, and S. Pralet (2006), Hybrid scheduling for the parallel solution of linear systems, *Parallel Computing*, *32(2)*, 136-156.
130) Aghaei, A., and M. Piri (2014), Direct pore-to-core up-scaling of displacement processes: Experimentation and dynamic pore network modeling, *Journal of Hydrology*, *(under review)*
131) Alizadeh, A. H., and M. Piri (2014), The effect of saturation history on three-phase relative permeability: An experimental study, *Water Resources Research*, *50*, doi:10.1002/2013WR014914.
132) Oak, M. J. (1990), Three-phase relative permeability of water-wet Berea, *Paper SPE 20183, Proceedings of the SPE/DOE Seventh Symposium on Enhanced Oil Recovery, Tulsa, Oklahoma, 22-25 April*.
133) Lerdahl, T. R., P. E. Øren, and S. Bakke (2000), A predictive network model for three-phase flow in porous media, *Paper SPE 59311, Proceedings of the SPE/DOE Symposium in Improved Oil Recovery, Tulsa, Oklahoma, 3-5 April*, doi:10.2118/59311-MS.
134) Ji, X.; Tan, S.P.; Adidharma, H.; Radosz, M. Statistical Associating Fluid Theory Coupled with Restricted Primitive Model Extended to Bivalent Ions. SAFT2: 2. Brine/Seawater Properties Predicted. J. Phys. Chem. B. 2006, 110, 16700-16706.
135) Tan, S.P.; Yao, Y.; Piri, M. Modeling the Solubility of SO2+CO2 Mixtures in Brine at Elevated Pressures and Temperatures. Ind. Eng. Chem. Res. 2013, 52, 10864-10872.
136) Kleiner, M.; Sadowski, G. Modeling of Polar Systems Using PCP-SAFT: An Approach to Account for Induced-Association Interactions. J. Phys. Chem. C. 2007, 111, 15544-15553.
137) Kontogeorgis, G.M.; Voutsas, E.C.; Yakoumis, I.V.; Tassios, D.P. An Equation of State for Associating Fluids, Ind. Eng. Chem. Res. 1996, 35, 4310–4318.
138) Wu J.; Prausnitz, J.M. Phase Equilibrium for Systems Containing Hydrocarbons, Water and Salt: An Extended Peng-Robinson Equation of State. Ind Eng Chem Res. 1998, 37, 1634-1643.

139) Inchekel, R.; de Hemptinne, J.-C.; Fürst, W. The Simultaneous Representation of Dielectric Constant, Volume and Activity Coefficients Using an Electrolyte Equation of State. Fluid Phase Equilib., 2008, 271, 19-27.
140) Lin, Y.; Thomsen, K.; de Hemptinne, J.-C. Multicomponent Equations of State for Electrolytes. AIChE J., 2007, 53, 989-1005.
141) Inchekel, R. Développement d'une équation d'état applicable aux systèmes d'électrolytes eau-alcool-sels-hydrocarbures. Dissertation, Mines Paris Tech, 2008, Table 25 (p. 117).
142) Kontogeorgis, G.M.; Folas, G.K. Thermodynamic Models for Industrial Applications: From Classical and Advanced Mixing Rules to Association Theories; John Wiley & Sons, Ltd.: Chichester, U.K., 2010.
143) Schwartz, S.E.; White, W.H. "Solubility Equilibria of the Nitrogen Oxides and Oxyacids in Dilute Aqueous Solution" in Advances in Environmental Science and Engineering, Vol. 4. Plafflin, J.R. and Zeigler, E.N. (Eds.), Gordon and Breach Science Publishers: New York, 1981; pp 1-45.
144) Joshi, J.B.; Mahajani, V.V.; Juvekar, V.A. Absorption of NOx Gases. Chem. Eng. Commun. 1985, 33, 1-92.
145) Thiemann, M.; Scheibler, E.; Wiegand, K.W. Nitric Acid, Nitrous Acid, and Nitrogen Oxides in Ullmann's Encyclopedia of Industrial Chemistry; Wiley-VCH Verlag GmbH & Co. KGaA., 2000.
146) Burdick, C.L.; Freed, E.S. The Equilibrium between Nitric Oxide, Nitrogen Peroxide and Aqueous Solution of Nitric Acid. J. Am. Chem. Soc. 1921, 43, 518-530.
147) Tereschchenko, L.Ya; Panov, V.P.; Pozin, M.E. Equilibrium between Nitrogen Oxides and Nitric Acid Solutions. Zh. Prikl. Khim. 1968, 41, 487-492.
148) Carberry, J.J. Some remarks on chemical equilibrium and kinetics in the nitrogen oxides – water system. Chem. Eng. Sci. 1959, 9, 189-194.
149) Sweeney, A.J.; Liu, Y.A. Use of Simulation to Optimize NOx Abatement by Absorption and Selective Catalytic Reduction. Ind. Eng. Chem. Res. 2001, 40, 2618-2627.
150) Stern, S.A.; Mullhaupt, J.T.; Kay, W.B. The Physicochemical Properties of Pure Nitric Acid. Chem. Rev. 1960, 60, 185-207.
151) Reamer, H.H.; Corcoran, W.H.; Sage, B.H. Volumetric Behavior of Nitric Acid. Ind. Eng. Chem. 1953, 45, 2699-2704.
152) Duffy, C.H.; Corcoran, W.H.; Sage, B.H. Volumetric and Phase Behavior in the Nitric Acid –Water System. Ind. Eng. Chem. 1956, 48, 431-433.
153) Reamer, H.H.; Mason, D.M.; Sage, B.H. Volumetric Behavior of Red and White Fuming Nitric Acid. Ind. Eng. Chem. 1953, 45, 1094-1097.
154) Corcoran, W.H.; Reamer, H.H.; Sage, B.H. Volumetric and Phase Behavior in the Nitric Acid – Nitrogen Dioxide System. Ind. Eng. Chem. 1954, 46, 2541-2546.
155) Reamer, H.H.; Corcoran, W.H.; Sage, B.H. Volumetric and Phase Behavior in the Nitric Acid – Nitrogen Dioxide – Water System. Ind. Eng. Chem. Chem. Eng. Data Series 1956, 1, 24-29.
156) Reamer, H.H.; Sage, B.H. Volumetric and Phase Behavior in Part of the Nitric Acid – Nitrogen Dioxide – Water System. Ind. Eng. Chem. Chem. Eng. Data Series 1958, 3, 245-252.
157) Gross, J.; Sadowski, G. Perturbed-Chain SAFT: An Equation of State Based on a Perturbation Theory for Chain Molecules. Ind. Eng. Chem. Res. 2001, 40, 1244-1260.

158) Tan, S.P.; Adidharma, H.; Radosz, M. Recent Advances and Applications of Statistical Associating Fluid Theory. Ind. Eng. Chem. Res. 2008, 47, 8063–8082.
159) Forsythe, W.R.; Giauque, W.F. The Entropies of Nitric Acid and its Mono- and Tri-hydrates. Their Heat Capacities from 15 to 300 K. The Heats of Dilution at 298.1 K. The Internal Rotation and Free Energy of Nitric Acid Gas. The Partial Pressures over its Aqueous Solutions. J. Am. Chem. Soc. 1942, 64, 48-61.
160) Tereschchenko, L.Ya; Panov, V.P.; Pozin, M.E.; Zubov, V.V. Analytical Method for Calculating Reaction Processes of Nitric Oxide with Nitric Acid Solutions. Zh. Prikl. Khim. 1968, 41, 2103-2113.
161) Tereschchenko, L.Ya; Pozin, M.E.; Panov, V.P. Method of Calculating Equilibrium and Interaction Conditions in the Reaction of Nitrogen Oxides with Nitric Acid Solutions. Zh. Prikl. Khim. 1968, 41, 702-709.
162) Pozin, M.E.; Kopylev, B.A.; Tereschchenko, L.Ya; Bel'chenko, G.V. Calculation of the Equilibrium Composition of Nitrose Gas over Nitric Acid Solutions. Zh. Prikl. Khim. 1963, 36, 16-24.
163) Smith, J.M.; Van Ness, H.C.; Abbott, M.M. Introduction to chemical engineering thermodynamics. 7th ed. Boston: McGraw-Hill, 2005.
164) Sanderson, R.V.; Chien, H.H.Y. Simultaneous Chemical and Phase Equilibrium Calculation. Ind. Eng. Chem. Process Des. Develop. 1973, 12, 81- 85.
165) Huang, S.H.; Radosz, M. Equation of State for Small, Large, Polydisperse, and Associating Molecules. Ind. Eng. Chem. Res. 1990, 29, 2284-2294.
166) James, D.W.; Marshall, R.C. An Electron Spin Resonance Study of the Dinitrogen Tetroxide – Nitrogen Dioxide System. J. Phys. Chem. 1968, 72, 2963-2966.
167) Belkadi, A.; Llovell, F.; Gerbaud, V.; Vega, L.F. Modeling the vapor-liquid equilibrium and association of nitrogen dioxide/dinitrogen tetroxide and its mixtures with carbon dioxide. Fluid Phase Equilib. 2008, 266, 154-163.
168) Kohler, F. Dimerization and Thermodynamic Properties of Nitric Oxide. J. Mol. Liquids 1995, 67, 105-123.
169) Zhou, Z.; Todd, B.D.; Travis, K.P.; Sadus, R.J. A molecular dynamics study of nitric oxide in water. Diffusion and structure. J. Chem. Phys. 2005, 123, 054505.
170) Adidharma, H.; Radosz, M. SAFT1 for Associating Fluids: Alkanols. J. Phys. Chem. B. 2001, 105, 9822-9827.
171) Held, C.; Cameretti, L.F.; Sadowski, G. Modeling aqueous electrolyte solutions. Part 1. Fully dissociated electrolytes. Fluid Phase Equilib. 2008, 270, 87–96.
172) Rumpf, B.; Maurer, G. Solubilities of hydrogen cyanide and sulfur dioxide in water at temperatures from 293.15 to 413.15 K and pressures up to 2.5 MPa. Fluid Phase Equilib. 1992, 81, 241-260.
173) Rabe, A.E.; Harris, J.F. Vapor Liquid Equilibrium Data for the Binary System, Sulfur Dioxide and Water. J. Chem. Eng. Data 1963, 8, 333-336.
174) Spall, B.C. Phase Equilibria in the System Sulphur Dioxide-Water from 25-300 C. Can. J. Chem. Eng. 1963, 41, 79-83.
175) Wiebe, R.; Gaddy, V.L. The Solubility in Water of Carbon Dioxide at 50, 75 and 100º, at Pressures to 700 Atmospheres. J. Am. Chem. Soc. 1939, 61, 315-318.
176) Rumpf, B.; Nicolaisen, H.; Ocal, C.; Maurer, G. Solubility of Carbon Dioxide in Aqueous Solutions of Sodium Chloride: Experimental Results and Correlation. J. Solution Chem. 1994, 23, 431-448.

177) Koschel, D.; Coxam, J.-Y.; Rodier, L.; Majer, V. Enthalpy and solubility data of CO2 in water and NaCl(aq) at conditions of interest for geological sequestration. Fluid Phase Equilib. 2006, 247, 107-120.
178) Kiepe, J.; Horstmann, S.; Fischer, K.; Gmehling, J. Experimental Determination and Prediction of Gas Solubility Data for CO2 + H2O Mixtures Containing NaCl or KCl at Temperatures between 313 and 393 K and Pressures up to 10 MPa. Ind. Eng. Chem. Res. 2002, 41, 4393-4398.
179) Zawisza, A.; Malesinska, B. Solubility of Carbon Dioxide in Liquid Water and of Water in Gaseous Carbon Dioxide in the Range 0.2-5 MPa and at Temperatures up to 473 K. J. Chem. Eng. Data. 1981, 26, 388-391.
180) Cummings, L.W.T. High-pressure Rectification. I- Vapor-Liquid Equilibrium Relations at High Pressures. Ind. Eng. Chem. 1931, 23, 900-902.
181) Daubert, T. E.; Danner, R. P. Physical and Thermodynamic Properties of Pure Chemicals: Data Compilation; New York: Hemisphere Pub. Corp., 1989.
182) Tan, S.P., Yao, Y.; Piri, M. Modeling the Solubility of SO2 + CO2 Mixtures in Brine at Elevated Pressures and Temperatures. Ind. Eng. Chem. Res. 2013, 52, in print. http://dx.doi.org/10.1021/ie4017557
183) Tan, S.P.; Kargel, J.S.; Marion, G.M. Titan's Atmosphere and Surface Liquid: New Calculation using Statistical Associating Fluid Theory. Icarus 2013, 222, 53-72.
184) McKeown, A.B.; Belles, F.E. Nitric Acid – Nitrogen Dioxide – Water System. Vapor Pressures and Related Properties. Ind. Eng. Chem. 1955, 47, 2540-2543.
185) Boublik, T.; Kuchynka, K. Vapor-liquid Equilibria XXII. Pressure dependence of Azeotropic Compositions for the Nitric Acid-Water System. Collect. Czech. Commun. 1960, 25, 579-582.
186) Chapoy, A.; Mohammadi, A.H.; Tohidi, B.; Richon, D. Gas Solubility Measurement and Modeling for the Nitrogen + Water System from 274.18 K to 363.02 K. J. Chem. Eng. Data. 2004, 49, 1110.
187) Rigby, M.; Prausnitz, J. M. Solubility of Water in Compressed Nitrogen, Argon, and Methane. J. Phys. Chem. 1968, 72, 330-334.
188) Winkler, L.W. The solubility of gases in water. Ber. Dtsch. Chem. Ges. 1901, 34, 1408-1422.
189) Levchuk, N.F.; Sukmanov, B.N.; Trubnikov, V.P. Liquid-vapor phase equilibrium in the nitrogen dioxide – nitric acid system. Vestsi Akad. Navuk BSSR, Ser. Fiz. Energ. Navuk. 1989, 4, 21-27.
190) Scheunemann, U.; Wagner, H.G. An apparatus for the determination of low-temperature liquid-vapor equilibria and measurements in the nitrogen-nitric oxide (N2 – NO) system. Ber. Bunsenges. Phys. Chem. 1985, 89, 1285-1292.
191) Selleck, F.T.; Reamer, H.H.; Sage, B.H. Volumetric and Phase Behavior of Mixtures of Nitric Oxide and Nitrogen Dioxide. Ind. Eng. Chem. 1953, 45, 814-819.
192) Pitzer, K.S.; Peiper, J.C.; Busey, R.H. Thermodynamic Properties of Aqueous Sodium Chloride Solutions. J.Phys. Chem. Ref. Data. 1984, 13, 1-102.
193) Duffy, C.H.; Corcoran, W.H.; Sage, B.H. Volumetric and Phase Behavior in the Nitric Acid –Water System. Ind. Eng. Chem. 1956, 48, 431-433.
194) Yan, W.; Huang, S.; Stenby, E.H. Measurement and modeling of CO2 solubility in NaCl brine and CO2–saturated NaCl brine density. International Journal of Greenhouse Gas Control. 2011, 5, 1460–1477.

195) Folas, G.K.; Kontogeorgis, G.M.; Michelsen, M.L.; Stenby, E.H. Application of the Cubic-Plus-Association Equation of State to Mixtures with Polar Chemicals and High Pressures. Ind. Eng. Chem. Res. 2006, 45, 1516–1526.
196) Tsivintzelis, I.; Kontogeorgis, G.M.; Michelsen, M.L.; Stenby, E.H. Modeling Phase Equilibria for Acid Gas Mixtures Using the CPA Equation of State. Part II: Binary mixtures with CO2. Fluid Phase Equilib. 2011, 306, 38-56.
197) Akbarabadi M., Piri M.: Relative permeability hysteresis and capillary trapping characterestics of supercritical CO_2/brine system: An Experimental Study at Reservoir Conditions. Advances in Water Resources 52, 190-206 (2013)
198) Ameri, A., Shojai Kaveh, N., Rudolph, E. S. J., Wolf, K.-H., Farajzadeh, R., Bruining, J.: Interactions among crude oil-brine-sandstone rock-CO_2 by contact angle measurements. Energy Fuels 27(2), 1015-1025 (2013)
199) Barenblatt, G.A.: Scaling, Self-Similarity and Intermediate Asymptotics. Cambridge Texts in Applied Mathematics. Cambridge University Press (2006)
200) Bachu, S., Bennion, B.: Effects of in-situ conditions on relative permeability characteristics of CO2-brine systems. Environmental Geology 54(8), 1707-1722 (2008)
201) Bear, J.: Dynamics of Fluids in Porous Media. Environmental Science Series. Elsevier, New York. Reprinted with corrections. Dover, New York (1988)
202) Eftekhari, A. A., Van Der Kooi, H., Bruining, J.: Exergy analysis of underground coal gasification with simultaneous storage of carbon dioxide. Energy 45(1), 729-745 (2012)
203) deSouza, A. J., Marchesin, D., Bedrikovetsky, P., Krause, P.: A simple model for three-phase flow with hysteresis. Matemática Contemporânea 19, 153-185 (2000)
204) Farajzadeh, R., Meulenbroek, B., Daniel, D., Riaz, A, Bruining, J.: An empirical theory for gravitationally unstable flow in porous media. Computational Geosciences 17(3), 515-527 (2013)
205) Flett M., Gurton R., Taggart I.: The function of gas-water relative permeability hysteresis in the sequestration of carbon dioxide in saline formations. SPE 88485, presented at SPE Asia Pacific Oil and Gas Conference and Exhibition, Perth, Australia, October 18-20 (2004)
206) Golding, M.J., Neufeld, J.A., Hesse, M.A., Huppert, H.E.: Two-phase gravity currents in porous media. J. Fluid Mech. 678, 248-270 (2011)
207) Hesse, M.A., Orr, F.M., Tchelepi, H.A.: Gravity currents with residual trapping. J. Fluid Mech. 611, 35-60 (2008)
208) Huppert, H.E., Woods, A.W.: Gravity-driven flows in porous layers. J. Fluid Mech. 292, 55-69 (1995)
209) Juanes R., Spiteri E. J., Orr Jr., F. M., Blunt, M. J.: Impact of relative permeability hysteresis on geological CO_2 storage. Water Resour. Res. 42, W12418 (2006)
210) Juanes R., MacMinn C.W., Szulczewski, M.L.: The footprint of the CO2 plume during carbon dioxide storage in saline aquifers: storage efficiency for capillary trapping at the basin scale. Trans. Porous Med. 82(1), 19-30 (2010)
211) Killough J.E.: Reservoir simulation with history-dependent saturation functions. Old SPE Journal 16(1), 37-48 (1976)
212) Kumar A., Noh M., Pope G.A., Sepehrnoori K., Bryant S., Lake L. W.: Reservoir simulation of CO_2 storage in deep saline aquifers. SPEJ 10(3), 336-348 (2005)

213) Kurganov A., Noelle S., Petrova G.: Semi-discrete central-upwind schemes for hyperbolic conservation laws and Hamilton-Jacobi equations. SIAM J. Sci. Comput. 23(3), 707–740 (2001)
214) Kurganov A., Tadmor E.: New high-resolution central schemes for nonlinear conservation laws and convection-diffusion equations. J. of Computational Physics 160, 241–282 (2000)
215) Land C.S.: Calculation of imbibition relative permeability for two- and three-phase flow from rock properties. Old SPE Journal 8(2), 149-156 (1968)
216) MacMinn, C.W., Szulczewski, M.L., Juanes, R.: CO_2 migration in saline aquifers. Part 1. Capillary trapping under slope and groundwater flow. J. Fluid Mech. 662, 329-351 (2010)
217) MacMinn, C.W., Szulczewski, M.L., Juanes, R.: CO_2 migration in saline aquifers. Part 2. Capillary and solubility trapping. J. Fluid Mech. 688, 321-351 (2011)
218) Marchesin D., Plohr B.: Wave Structure in WAG Recovery. SPEJ 6(2), 209-219, SPE-71314 (2001)
219) Meulenbroek, B., Farajzadeh, R., Bruining, J.: The effect of interface movement and viscosity variation on the stability of a diffusive interface between aqueous and gaseous CO_2. Phys. Fluids 25, 074103 (2013) http://dx.doi.org/10.1063/1.4813072
220) Mo S., Zeweigel P., Lindeberg E., Akervoll I.: Effect of geologic parameters on CO_2 storage in deep saline aquifers. SPE 93952, presented at SPE Europec/EAGE Annual Conference, Madrid, Spain, June 13-16 (2005)
221) Obi E.-O. I., Blunt M. J.: Streamline-based simulation of carbon dioxide storage in a North Sea aquifer. Water Resour. Res. 42, W03414 (2006)
222) Ozah R. C., Lakshminarasimhan S., Pope G. A., Sepehrnoori K., Bryant S.: Numerical simulation of the storage of pure CO_2 and CO_2-H_2S gas mixtures in deep saline aquifers. SPE 97255, presented at SPE Annual Tech. Conf., Dallas, October 9-12 (2005)
223) Piri M. Recirculating. Constant back pressure core flooding apparatus and method. Patent, W02012/082792 A1 (2012)
224) Plohr B., Marchesin D., Bedrikovetsky P. M., Krause, P.: Modeling hysteresis in porous media via relaxation. Computational Geosciences 5, 225-256 (2001)
225) Plug, W. J., Bruining, J.: Capillary pressure for the sand-CO_2-water system under various pressure conditions; application to CO_2 sequestration. Advances in Water Resources 30, 2339-2353 (2007)
226) Qi R., LaForce T. C., Blunt M. J.: Design of carbon dioxide storage in aquifers. Int. J. Greenhouse Gas Control 3, 195-205 (2009)
227) Salimi, H., Wolf, K.-H., Bruining, J.: The influence of capillary pressure on the phase equilibrium of the CO_2-water system: Application to carbon sequestration combined with geothermal energy. Int. J. Greenhouse Gas Control 11, 47-66 (2012)
228) Schaerer C. E., Marchesin D., Sarkis, M., Bedrikovetsky, P.: Permeability hysteresis in gravity counterflow segregation. SIAM J. Appl. Math. 66(5), 1512-1532 (2006)
229) Span R., Wagner W.: A new equation of state for carbon dioxide covering the fluid region from the triple-point temperature to 1100 K at pressure up to 800 MPa. Journal of Physical and Chemical Reference Data 25(6), 1509-1596 (1996)
230) Spiteri E.J., Juanes R.: Impact of relative permeability hysteresis on the numerical simulation of WAG injection. J. Pet. Sci. Eng. 50(2), 115-139 (2006)

231) Spiteri E.J., Juanes R., Blunt M.J., Orr F.M.Jr.: Relative permeability hysteresis: Trapping models and application to geological CO_2 sequestration. SPE 96448, presented at SPE Annual Tech. Conf., Dallas, October 9-12 (2005)

232) Spiteri E.J., Juanes R., Blunt M.J., Orr F.M.Jr.: A new model of trapping and relative permeability hysteresis for all wettability characteristics. SPE J 13(3), 277-88 (2008)

233) Taku Ide S., Jessen K., Orr F.M.Jr.: Storage of CO_2 in saline aquifers: Effects of gravity, viscous, and capillary forces on amount and timing of trapping. Int. J. Greenhouse Gas Control 1, 481-491 (2007)

234) E. Abreu, J. Douglas, Jr., F. Furtado, D. Marchesin and F. Pereira. Three-phase immiscible displacement in heterogeneous petroleum reservoirs. Mathematics and Computers in Simulation, 73(1):2–20, 2006.

235) J. Bear. Hydraulics of groundwater. MCGRAW-HILL, 1979.

236) G. Chavent, and J. Roberts. A unified physical presentation of mixed, mixed-hybrid finite elements and standard finite difference approximations for the determination of velocities in waterflow problems. Adv. Water Resour., 14(6):329–348, 1991.

237) A. Chisten and C. Fox. MCMC using an approximation. J Comput Graph Stat, 14(4):795–810, 2005.

238) S. Cotter, G. Roberts, A. Stuart and D. White. MCMC Methods for Functions: Modifying Old Algorithms to Make Them Faster. Statist. Sci., 28(3):424–446, 2013.

239) C. Douglas, Y. Efendiev, R. Ewing, V. Ginting and R. Lazarov. Dynamic Data Driven Simulations in Stochastic Environments. Computing, 77(4):321–333, 2006.

240) Z. Duan and R. Sun. An improved model calculating CO_2 solubility in pure water and aqueous NaCl solutions from 273 to 533 K and from 0 to 2000 bar. Chemical Geology, 193:257–271, 2003.

241) Zhenhao Duan, Jiawen Hu, Dedong Li and Shide Mao. Density of the CO2-H_2O and CO2-H_2O-NACL systems up to 647 k and 100 mpa. Energy Fuels, 22:1666-1674, 2008.

242) E. Wong. Stochastic Processes in Information and Dynamical Systems. McGraw-Hill, New York, 1971.

243) Y. Efendiev, A. Datta-Gupta, V. Ginting, X. Ma and B. Mallick. An efficient two-stage Markov chain Monte Carlo method for dynamic data integration. Water Resour. Res., 41(W12423), 2005.

244) Y. Efendiev, T. Hou and W. Luo. Preconditioning Markov chain Monte Carlo simulations using coarse-scale models. SIAM J. Sci. Comput., 28(2):776–803, 2006.

245) G. Dagan. Flow and transport in porous formations. Springer-Verlag, 1989.

246) V. Ginting, F. Pereira, M. Presho, and S. Wo. Application of the two-stage Markov chain Monte Carlo method for characterization of fractured reservoirs using a surrogate flow model. Comput. Geosci., 15(4):691–707, 2011.

247) D. Gourgouillon, H.M.N.T Avelino, J.M.N.A Fareleira and M.N da Ponte. Simultaneous viscosity and density measurement of supercritical CO_2-saturated peg 400. The Journal of Supercritical Fluids, 3:177-185, 1998.

248) J. Douglas Jr., F. Furtado and F. Pereira. On the numerical simulation of waterflooding of heterogeneous petroleum reservoirs. Comp. Geosciences, 1:155–190, 1997.

249) W. K. Hastings. Monte Carlo sampling methods using Markov chains and their applications. Biometrika, 57:97–109, 1970.
250) A. Kurganov and E. Tadmor. New high-resolution central schemes for nonlinear conservation laws and convection-diffusion equations. J. of Computational Physics, 160:241–282, 2000.
251) A. M. M. Leal. Flash equilibrium method for CO_2 and H_2S storage in brine aquifers with parallel gpu implementation. Masters thesis, Math Department, University of Wyoming. 2010.
252) M. Liebmann. Efficient PDE Solvers on Modern Hardware with Applications in Medical and Technical Sciences. PhD thesis, University of Graz, 2009.
253) M. Loève. Probability theory. Springer, Berlin, 1977.
254) G. Qin. PhD thesis, Department of Chemical and Petroleum Engineering, University of Wyoming, 1995.
255) B. Rumpf, H. Nicolaisen, C. Ocal and G. Maurer. Solubility of carbon dioxide in aqueous solutions of sodium chloride: Experimental results and correlations. Journal of solution chemistry, 23:431-448, 1994.
256) J. A. Trangenstein and J. B. Bell. Mathematical structure of the black oil model for petroleum reservoir simulation. SIAM Journal on Applied Mathematics, 49:746-783, 1989.
257) X. Ma, M. Al-Harbi, A. Datta-Gupta and Y. Efendiev. An efficient two-stage sampling method for uncertainty quantification in history matching geological models. SPE Journal, :77-87, March, 2008.
258) A. Francisco, V. Ginting, F. Pereira, J. Rigelo (2014), Design and Implementation of a Multiscale Mixed Method for Porous Media Flows. Mathematics and Computers in Simulation, 99, 125-138.
259) E. Obi and M. Blunt. Streamline-based simulation of carbon dioxide storage in a north sea aquifer. Water Resour. Res., 42:W03414, April 2006.
260) K. Pruess and N. Muller. Formation dry-out from co2 injection into saline aquifers: 1. Effects of solids precipitation and their mitigation. Water Resour. Res., 45:W03402, April 2009.
261) Y. Xiao, T. Xub, and K. Pruess. The effects of gas-fluid-rock interactions on co2 injection and storage: Insights from reactive transport modeling. Energy Procedia, 1:1783–1790, April 2009.
262) J. Rutqvist, J. Birkholzer, and F. Cappa. Estimating maximum sustainable injection pressure during geological sequestration of co2 using coupled fluid flow and geomechanical fault-slip analysis. Energy Conversion and Management, 48(6):1798–1807, April 2007.
263) C. D. Hawkes, S. Bachu, and P. J. McLellan. Geomechanical factors affecting geological storage of co2 in depleted oil and gas reservoirs. Journal of Canadian Petroleum Technology, 44(10):52–61, April 2005.
264) M. Ferronato and G. Gambolato. Poro-mechanical modeling of CO_2 sequestration in exploited gas field. In H.L. Ling, editor, Proceedings of the 4th Biot Conference on Poromechanics, pages 171–176, 2009.
265) T. Bjornara, E. Akere, and E. Skurtiveit. Coupled flow and geomechanical model for co2 injection. In H.L. Ling, editor, Proceedings of the 4th Biot Conference on Poromechanics, pages 183–188, 2009.

266) H. Soltanzadeha and D. Christopher. Assessing fault reactivation tendency within and surrounding porous reservoirs during fluid production or injection. International Journal of Rock Mechanics and Mining Sciences, 46(1):1–7, April 2009.
267) H. Soltanzadeha and C. D. Hawkes. Semi-analytical models for stress change and fault reactivation induced by reservoir production and injection. Journal of petroleum science and engineering, 60(2):71–85, April 2008.
268) H. Soltanzadeha and C. D. Hawkes. Semi-analytical models for stress change and fault reactivation induced by reservoir production and injection. Journal of petroleum science and engineering, 60(2):71–85, April 2008.
269) C. Arnes, H. Lillejord, and A. Vieler. Simulation forecasts complex flow streams from ekofisk. Oil & Gas Journal, 94(44):69–75, October 1996.
270) D. G. Fredlund and H. Rahardjo. Soil mechanics for unsaturated soils. John Wiley & Sons Canada, Ltd. (AUG 17 1993), 1993.
271) D. G. Fredlund and N. R. Morgenstern. Stress state variables for unsaturated soils. ASCE Geothec Eng., 103:447–446, 1977.
272) E. E. Alonso, A. Gens, and A. Josa. A constitutive model for partially saturated soils. Geotechnique, 40(3):405–430, September 1990.
273) G. Bolzon, B. A. Schrefler, and O. C. Zienkiewicz. Elastoplastic soil constitutive laws generalized to partially saturated states. Geotechnique, 46(2):279–289, June 1996.
274) A. W. Bishop. The principle of effective stress. Teknisk Ukeblad, 106:859–863, 1959.
275) D. G. Fredlund and H. Rahardjo. Soil mechanics for unsaturated soils. John Wiley & Sons Canada, Ltd. (AUG 17 1993), 1993.
276) A. Settari and D. Walters. Advances in coupled geomechanical and reservoir modeling with applications to reservoir compaction. SPE Reservoir Simulation Symposium, pages 14–17, January 1999.
277) R. H. Dean, X. Gai, C. M. Stone, and S. E. Minkoff. A comparison of techniques for coupling porous flow and geomechanics. SPE JOURNAL, 11, 1:132–140, 2006.
278) R. Charlier and P. Samier. Numerical simulation of the coupled behavior of faults during the depletion of a high-pressure/high-temperature reservoir. In SPE/ISRM Rock Mechanics Conference, pages number 78199–MS, 2002.
279) B. A. Schrefler and X. Y. Zhan. A fully coupled model for water-flow and air-flow in deformable porous-media. Water Resources Research, 29(1):155–167, January 1993.
280) S. Olivella, A. Gens, J. Carrera, and E. E. Alonso. Numerical formulation for a simulator (code bright) for the coupled analysis of saline media. Engineering Computations, 13(7):87, 1996.
281) J. Kim, H. Tchelepi, and R. Juanes. Stability, accuracy and efficiency of sequential methods for coupled flow and geomechanics. SPE 119084, 2009.
282) M. Mendes, M. Murad and F. Pereira, (2012), A New Computational Strategy for Solving Two-Phase Flow in Strongly Heterogeneous Poroelastic Media of Evolving Scales. International Journal for Numerical and Analytical Methods in Geomechanics, 36(15):1683-1716.
283) A. Abedini and F. Torabi. Oil recovery performance of immiscible and miscible CO2 huff-and-puff processes. Energy & Fuels, 28(2):774–784, 2014.
284) E. Abreu, J. Douglas Jr., F. Furtado, and F. Pereira. Operator splitting based on physics for flow in porous media. Int. J. of Computational Science, 2(3):315–335, 2008.

285)E. Abreu, J. Douglas Jr., F. Furtado, and F. Pereira. Operator splitting for three-phase flow in heterogeneous porous media. Communications in Computational Physics, 6(1):72–84, 2009.
286)Z. Chen, G. Huan, and Y. Ma. Computational methods for multiphase flows in porous media. SIAM, Philadelphia, PA, 2006.
287)J.A. Christen and C. Fox. Markov chain Monte Carlo using an approximation. Journal of Computational and Graphical Statistics, 14(4):795–810, 2005.
288)M. Christie, V. Demyanov, and D. Erbas. Uncertainty quantification for porous media flows. Journal of Computational Physics, 217:143–158, 2006.
289)G. Dagan. Flow and transport in porous formations. Springer-Verlag, 1989.
290)J. Douglas Jr., F. Furtado, and F. Pereira. On the numerical simulation of waterflooding of heterogeneous petroleum reservoirs. Comp. Geosciences, 1:155–190, 1997.
291)L.J. Durlofsky. Numerical calculation of equivalent grid block permeability tensors for heterogeneous porous media. Water Resour. Res., 27(5):699–708, 1991.
292)Y. Efendiev, A. Datta-Gupta, V. Ginting, X. Ma, and B. Mallick. An efficient two-stage Markov chain Monte Carlo method for dynamic data integration. Water Resour. Res., 41(W12423), 2005.
293)Y. Efendiev, T. Hou, and W. Luo. Preconditioning Markov chain Monte Carlo simulations using coarse-scale models. SIAM J. Sci. Comput., 28(2):776–803, 2006.
294)C. Fox and G. Nicholls. Sampling conductivity images via MCMC. In University of Leeds, pages 91–100, 1997.
295)Jianlin Fu and J.Jaime Gomez-Hernandez. A blocking Markov chain Monte Carlo method for inverse stochastic hydrogeological modeling. Mathematical Geosciences, 41(2):105–128, 2009.
296)V. Ginting, F. Pereira, M. Presho, and S. Wo. Application of the two-stage Markov chain Monte Carlo method for characterization of fractured reservoirs using a surrogate flow model. Computational Geosciences, 15(4):691–707, 2011.
297)V. Ginting, F. Pereira, and A. Rahunanthan. Multiple Markov chains Monte Carlo approach for flow forecasting in porous media. Procedia Computer Science, 9:707 – 716, 2012.
298)V. Ginting, F. Pereira, and A. Rahunanthan. A multi-stage Bayesian prediction framework for subsurface flows. International Journal for Uncertainty Quantification, 3(6):499–522, 2013.
299)V. Ginting, F. Pereira, and A. Rahunanthan. A pre-fetching technique for prediction of porous media flows. Computational Geosciences, 2014. To Appear.
300)V. Ginting, F. Pereira, and A. Rahunanthan. Rapid quantification of uncertainty in permeability and porosity of oil reservoirs for enabling predictive simulation. Mathematics and Computers in Simulation, 99:139–152, 2014.
301)J. Glimm and D. H. Sharp. Prediction and the quantification of uncertainty. Phys. D, 133(1-4):152–170, 1999.
302)D. Higdon, H. Lee, and Z. Bi. A Bayesian approach to characterizing uncertainty in inverse problems using coarse and fine-scale information. IEEE Transactions on Signal Processing, 50:389–399, 2002.
303)D. Kavetski, G. Kuczera, and S.W. Franks. Calibration of conceptual hydrological models revisited: 1. overcoming numerical artifacts. Journal of Hydrology, 320(1ï¿½2):173–186, 2007.

304) D. Kavetski and G. Kuczera. Model smoothing strategies to remove microscale discontinuities and spurious secondary optima in objective functions in hydrological calibration. Water Resources Research, 43:1–9, 2007.
305) Herbert Lee, David Higdon, Zhuoxin Bi, Marco Ferreira, and Mike West. Markov random field models for high-dimensional parameters in simulations of fluid flow in porous media. Technical report, Technometrics, 2002.
306) M. Loève. Probability theory. Springer, Berlin, 1977.
307) D.S. Oliver, L.B. Cunha, and A.C. Reynolds. Markov chain Monte Carlo methods for conditioning a permeability field to pressure data. Mathematical Geology, 29(1):61–91, 1997.
308) F. Pereira and A. Rahunanthan. Numerical simulation of two-phase flows on a GPU. In 9th International meeting on High Perfomance Computing for Computational Science (VECPAR '10), Berkeley, CA, June 2010.
309) F. Pereira and A. Rahunanthan. A semi-discrete central scheme for the approximation of two-phase flows in three space dimensions. Mathematics and Computers in Simulation, 81(10): 2296–2306, 2011.
310) J.A. Vrugt, H. V. Gupta, W. Bouten, and S. Sorooshian. A shuffled complex evolution Metropolis algorithm for optimization and uncertainty assessment of hydrologic model parameters. Water Resources Research, 39(8):1201–1217, 2003.
311) E. Wong. Stochastic Processes in Information and Dynamical Systems. McGraw-Hill, New York, 1971.
312) H. Xie, J.W. Eheart, Y. Chen, and B.A. Bailey. An approach for improving the sampling efficiency in the Bayesian calibration of computationally expensive simulation models. Water Resources Research, 45:1–14, 2009.